

**INVESTIGATION AND CONTROL OF
MAGNETIZATION DYNAMICS IN
FERROMAGNETIC/NONMAGNETIC BI-
LAYER SYSTEMS**

**THESIS SUBMITTED FOR THE DEGREE OF
DOCTOR OF PHILOSOPHY (SCIENCE)
IN
PHYSICS (EXPERIMENTAL)**

**BY
ARNAB GANGULY**

**DEPARTMENT OF PHYSICS
UNIVERSITY OF CALCUTTA
2016**

To Tani...

Acknowledgement

It is great pleasure for me to acknowledge Prof. Anjan Barman for giving me an opportunity to work in his wonderful laboratory under his supervision in course of my Ph.D. I am also thankful to him for his support and encouragement and valuable suggestions whenever I face problems in my research. I first met him while doing a summer project in course of my M.Sc. Later I did few more projects with him before joining in Ph.D. Initially I expected that he would be a reserved person like some other professors. Later on I found him very frank and patient to his students. He is an extremely helpful person with full of humanity to whom you can trust and share your academic, official or even personal difficulties. His hard work, dedication to research, sense of responsibility, vastness of knowledge and innovation power inspires me a lot. I like to convey my heartfelt gratitude and thanks to him for all his efforts during last five years to make my research a success.

I like to thank my parents for unconditional love, support, guidance and encouragement that keeps me going through the successful journey of my research. They sacrifice a lot for me. I could not spend a long time with them during the course my Ph.D. but they never complained. They are the biggest inspiration of my life. I also like to thank my wife for her encouragement which boosts me up for doing the best research. She made useful discussions about the memory and logical operation of a computer which helps me in writing the thesis. I am also thankful to her for helping me in proof checking.

I would like to express my sincere gratitude to Prof. Yoshi Chika Otani and his group of Quantum Nano-Scale Magnetism Laboratory, RIKEN, Japan for providing me the opportunity of doing spin torque ferromagnetic resonance experiment in his laboratory under the DST-JST collaborative project. Special thanks to Dr. K. Kondou for sample preparation and useful discussion.

I would also like to express my heartiest thanks to Prof. Del Atkinson and his group, department of physics, Durham University, UK for providing me samples and doing x-ray reflectivity experiments under the DST-UKIERI collaborative project. Special thanks to Dr. J. A. King, S. Azzawi and R. M. Rowan-Robinson for sample preparation and discussion.

Thanks to Dr. Saswati Barman for teaching me micromagnetic simulation. She helped me a lot in doing projects and publishing a number of papers outside this thesis.

I also thank my friends and colleagues. Specifically, Dr. Semanti Pal helped me in learning TR-MOKE technique. Dr. Jaivardhan Sinha gave some useful suggestion about my research and make me aware about some contemporary research activities. Dr. Bipul Kr. Mahato and Debanjan Polley had some nice interaction with me on various topics including science, sports and politics. Special thanks to the other lab members like Santanu, Sucheta, Kartik, Chandrima and Neha for some direct and indirect help in my research.

Finally, I thank the fellowship of S. N. Bose National Centre for Basic Sciences for giving me an opportunity to work. Thanks to the common research facilities of the institute under the technical cell which was helpful for basic characterization of the samples. I also acknowledge to the financial support from Department of Science and Technology, Government of India under Grant No. INT/JP/JST/P-23/09, Department of Information Technology Government of India under Grant No. 1(7)/2010/M&C, Japan Science and Technology Agency Strategic International Cooperative Program under Grant No. 09158876 and the British Council for the DST-UKIERI joint project: Grant No. DST/INT/UK/P-44/2012.

Arnab Ganguly,

S. N. Bose National Centre for Basic Sciences

Salt Lake, Kolkata, India.

List of Publications

Included in This Thesis

- [1] Azzawi, A., Ganguly, A., Tokac, M., Rowan-Robinson, R. M., Sinha, J., Hindmarch, A. T., Barman, A. & Atkinson, D. Evolution of damping in ferromagnetic/non-magnetic thin film bilayers as a function of non-magnetic thickness. *Phys. Rev. B* **93**, 054402 (2016).
- [2] Ganguly, A., Azzawi, S., Saha, S., King, J. A., Rowan-Robinson, R. M., Hindmarch, A. T., Sinha, J., Atkinson, D. & Barman, A. Tunable magnetization dynamics in interfacially modified Ni₈₁Fe₁₉/Pt bilayer thin film microstructures. *Sci. Rep.* **5**, 17596 (2015).
- [3] Ganguly, A., Kondou, K., Sukegawa, H., Mitani, S., Kasai, S., Niimi, Y., Otani, Y. & Barman, A. Thickness dependence of spin torque ferromagnetic resonance in Co₇₅Fe₂₅/Pt bilayer films. *Appl. Phys. Lett.* **104**, 072405 (2014).
- [4] Ganguly, A., Rowan-Robinson, R., Haldar, A., Jaiswal, S., Sinha, J., Hindmarch, A., Atkinson, D. & Barman, A. Time-domain detection of current controlled magnetization damping in Pt/Ni₈₁Fe₁₉ bilayer and determination of Pt spin Hall angle. *Appl. Phys. Lett.* **105**, 112409 (2014).
- [5] King, J. A., Ganguly, A., Burn, D. M., Pal, S., Sallabank, E. A., Hase, T. P. A., Hindmarch, A. T., Barman, A. & Atkinson, D. Local control of magnetic damping in ferromagnetic/non-magnetic bilayers by interfacial intermixing induced by focused ion-beam irradiation. *Appl. Phys. Lett.* **104**, 242410 (2014).

Not Included in This Thesis

- [6] Barman, S., Ganguly, A. & Barman, A. Configuration and polarization dependent transverse domain wall motion and domain wall switching in ferromagnetic nanowire. *Spin* **3**, 1350001 (2013).
- [7] Polley, D., Ganguly, A., Barman, A. & Mitra, R. K. Polarizing effect of aligned nanoparticles in terahertz frequency region. *Opt. Lett.* **38**, 2754 (2013).
- [8] Barman, S., Ganguly, A. & Barman, A. Phonon heat conduction in Al_xGa_{1-x}N film. *Europhys. Lett.* **97**, 36011 (2012).

- [9] Mahato, B., Ganguly, A., Rana, B. & Barman, A. Magnetization reversal in chemically synthesized hexagonal cobalt microplatelets. *J. Phys. Chem. C* **116**, 22057 (2012).
- [10] Rana, B., Ganguly, A. & Barman, A. Magnetic shape anisotropy in chemically synthesized chains of nickel nanoparticles. *IEEE Trans. Magn.* **47**, 2859 (2011).

Abstract

Existing technologies of electronic data storage and memory devices employ ferromagnets with controlled magnetic properties. Emergent technologies including spintronics and magnonics also search for engineered magnetic materials and metamaterials. There are two ways of controlling the magnetic properties for this purpose a) by searching new materials or b) by active control of existing material by external means. In this thesis we engineer magnetization dynamics by injecting spin current, modifying interface properties by ion irradiation or using suitable combination of materials forming the interface.

Unlike charge current, which is a direct consequence of flow of charge, spin current solely deals with the spin degree of freedom of an electron giving rise to a new technology over the existing charge based technology, known as spintronics. For a pure spin current there are a lot of advantages including no net flow of charge and hence no stray Oersted field, minimum power dissipation, tunable magnetic damping, or reduction of noise due to thermal fluctuation in nanomagnetic devices. All these exciting features, however, have been bottlenecked by the insufficiency of spin current density required to drive spintronic devices. Hence substantial research is required to enhance the conversion efficiency between charge current and spin current known as spin Hall angle (θ_{SH}). The content of this thesis is to investigate θ_{SH} of ferromagnetic/nonmagnetic bi-layer systems using different measurement techniques like spin-torque ferromagnetic resonance (ST-FMR) and modulation of damping technique. We shall study spin orbit interaction, impurity scattering, spin Hall effect, spin diffusion length, spin pumping, generation and injection of spin current across the interface, which can play a crucial role in controlling the magnetization dynamics and spin transport properties of the ferromagnetic layer. This will enable an external control of the effective damping of a material by tuning the applied charge current density.

The detection principle is based spin torque ferromagnetic resonance technique which relies on anisotropic magnetoresistance of the ferromagnet. The spectrum shape, amplitude, line width and resonance position are very important measurable quantity for this experiment, which gives us information about Gilbert damping, precession frequency, and also θ_{SH} .

However, damping measurement using FMR is not very precise because of instrumental linewidth and various extrinsic effects. Hence, we directly measure the Gilbert damping using

an all-optical time-resolved MOKE microscope for comparison. To have a better understanding and control over the dynamical properties we study the effect on the various measurable quantities by varying different experimental and material parameters including rf power, bias field angle and film thickness as well as interface properties.

Recently, focused ion beam (FIB) is regularly used for direct nanoscale patterning and milling to fabricate nanostructures with high precision. It may also be used to locally manipulate and control magnetic properties, domain structures as well as magnetization and domain wall dynamics on the micro and nanoscale. This opens new opportunities for interesting scientific investigations and has potential in future applications of nanoscale magnetic structures, such as sensors, memory and logic devices. In this thesis we will investigate the local magnetic property manipulation by low dose FIB irradiation of ferromagnetic/nonmagnetic bilayer thin film systems. A systematic investigation are made on patterned 30 μm dots of $\text{Ni}_{80}\text{Fe}_{20}$ (10 nm)/nonmagnetic-metal [Au, Cr, Cu, Pt] bi-layers as a function of very low dose focused gallium ion irradiation (upto 5 $\text{pC}/\mu\text{m}^2$). The dynamics are be measured by using an all-optical time-resolved MOKE microscope. We characterize the variation of Gillbert damping and precession frequency of magnetization with irradiation dose and also investigate the underlying phenomena occurring at the interface. The results are further supported by measurements of structural and compositional changes at the interface. Possible intermixing of the layers as a function of ion beam dose, in terms of interfacial broadening, roughening and development of a nanoscale compositionally graded alloy is discussed to explain the precession frequency and damping in such systems.

Contents

List of Figures.....	XIV
Chapter 1: Introduction	1
References	8
Chapter 2: Theoretical Overview.....	12
2.1. Electron Spin	12
2.2. Spin Continuity Equation	12
2.3. Spin Polarization	14
2.4. Spin Current and Charge Current	15
2.5. Time Reversal Symmetry of Spin Current	16
2.6. Hall Effect	17
2.6.1. Ordinary Hall Effect	17
2.6.2. Anomalous Hall Effect	19
2.6.3. Spin Hall Effect	20
2.6.4. Skew Scattering.....	22
2.6.5. Side Jump	23
2.7. Spin Pumping	24
2.8. Anisotropic Magnetoresistance	26
2.9. Giant Magnetoresistance	28
2.9.1. Two Current Model	29
2.9.2. Spin Dependent Scattering	30
2.9.3. How GMR Works.....	31
2.10. Tunneling Magnetoresistance.....	32
2.11. Magnetization.....	33
2.12. Maxwell's Equations	34
2.13. Classification of Magnetic Materials.....	35

2.13.1.	Langevin Theory of Diamagnetism	36
2.13.2.	Langevin Theory of Paramagnetism.....	37
2.13.3.	Weiss Theory of Ferromagnetism	38
2.14.	Origin of molecular field (The exchange interaction).....	39
2.15.	Antiferromagnetic and Ferrimagnetic Materials	40
2.16.	Fundamental Energies in Ferromagnetism.....	41
2.16.1.	Zeeman energy:	41
2.16.2.	Exchange Energy:.....	41
2.16.3.	Anisotropy Energy:	42
2.16.4.	Demagnetizing Energy:	43
2.17.	Timescales of Magnetization Dynamics.....	43
2.18.	Ultrafast Demagnetization.....	44
2.18.1.	The Three Temperature Model.....	45
2.18.2.	Elliott-Yafet (EY) Spin Flip Scattering	46
2.18.3.	Spin-flip Coulomb Scattering.....	47
2.19.	Landau-Lifshitz-Gilbert Equation	47
2.20.	Spin-Orbit Coupling.....	50
2.21.	Origin of Damping	51
2.22.	Ferromagnetic Resonance	52
	References	56
Chapter 3: Experimental Techniques.....		63
3.1.	Thin Film Deposition	63
3.1.1.	Magnetron Sputtering Process.....	64
3.1.2.	E-beam Evaporation	65
3.2.	Optical Lithography.....	66
3.3.	Focused Ion Beam	68
3.3.1.	Effect of Ion Irradiation.....	70
3.4.	Scanning Electron Microscope.....	72
3.5.	X-ray Reflectivity.....	73

3.6.	Vibrating Sample Magnetometer	75
3.7.	Atomic Force Microscope	76
3.8.	Static Magneto-optical Kerr Effect Microscope.....	78
3.9.	Time-resolved Magneto-optical Kerr Effect Microscope.....	80
3.9.1.	Primary Components of the Setup.....	81
3.9.1.1.	Laser	81
3.9.1.2.	Second Harmonic Generator (SHG).....	84
3.9.2.	Experimental Setup	85
3.9.3.	Some Routine Alignments.....	87
3.10.	Spin Torque Ferromagnetic Resonance.....	88
	References	91
Chapter 4: Local Control of Magnetic Damping in Ferromagnetic/non-		
magnetic Bi-layers by Interfacial Intermixing Induced by Focused Ion-beam		
Irradiation.....		
		93
4.1.	Introduction	93
4.2.	Sample Preparation and Experimental Details	95
4.3.	Results and Discussion	96
4.4.	Summary	102
	References	102
Chapter 5: Tunable Magnetization Dynamics in Interfacially Modified Ni₈₁Fe₁₉		
Bi-Layer Thin film Microstructures		
		106
5.1.	Introduction	106
5.2.	Sample Description	108
5.3.	Methods	109
5.3.1.	Fabrication.....	109
5.3.2.	Measurement Technique	109
5.4.	Results and Discussion	110
5.4.1.	Time-resolved Scanning Kerr Images	111
5.4.2.	Precession Frequency and Damping.....	111

5.4.3.	Spin Relaxation Times	117
5.5.	Summary	118
	References	119
Chapter 6: Role of Heavy Metal Capping Layer and Interface in Controlling the Damping of Ferromagnet/Nonmagnet Bi-layer.....		
123		
6.1.	Introduction	123
6.2.	Experimental	124
6.3.	Results and Discussion.....	126
6.4.	Summary	132
	References	132
Chapter 7: Thickness Dependence of Spin-torque Ferromagnetic Resonance in Co₇₅Fe₂₅/Pt Bi-layer Films and Estimation of Spin Hall Angle of Pt		
135		
7.1.	Introduction	135
7.2.	Experimental Details	136
7.3.	Underlying Theory	137
7.4.	Results and Discussion.....	140
7.5.	Summary	145
	References	145
Chapter 8: Time-domain Detection of Current Controlled Magnetization Damping in Pt/Ni₈₁Fe₁₉ Bi-layer and Determination of Pt Spin Hall Angle....		
148		
8.1.	Introduction	148
8.2.	Experimental Details	149
8.3.	Theory	150
8.4.	Results and Discussion.....	151
8.5.	Summary	155
	References	156

Chapter 9: Role of Interface in Current Induced Modulation of Damping in Ion Irradiated Ni₈₁Fe₁₉/Pt Bi-layers.....	158
9.1. Introduction	158
9.2. Sample Preparation.....	159
9.3. Experimental Technique.....	161
9.4. Results	163
9.5. Discussion	170
9.6. Summary and Future Prospective.....	171
References	172
Chapter 10: Evolution of Damping in Ferromagnetic/nonmagnetic Thin Film Bi-layers As a Function of Nonmagnetic Layer Thickness.....	174
10.1. Introduction	174
10.2. Formalism for Analysis of Damping	176
10.3. Experimental Details	177
10.4. Results	178
10.5. Discussion	182
10.6. Conclusion.....	186
References	187
Chapter 11: Summary and Future Prospectives.....	190
11.1. Summary	190
11.2. Future Prospective	192

List of Figures

Figure Caption	Page
Figure 2.1. Schematic representation of time reversal in case of (a) charge current and (b) spin current. The bottom figure in each case represents the equivalent picture.	17
Figure 2.2. Schematic illustration of ordinary Hall effect.	19
Figure 2.3. Schematic diagram of spin Hall effect.	22
Figure 2.4. Hall geometries; (a) ordinary Hall effect, (b) anomalous Hall effect and (c) spin Hall effect.	22
Figure 2.5. Skew scattering effect.	23
Figure 2.6. Schematic illustration of spin pumping using density of states.	26
Figure 2.7. Variation of resistance with magnetic field in Fe/Cr superlattice (reference 37).	29
Figure 2.8. Variation of the number of up and down spin electrons per atom with layer numbers for (a) Co/Cu/Co and (b) Fe/Cr/Fe structures along with schematic illustrations of scattering mechanism.	31
Figure 2.9. Schematic illustration of GMR by using equivalent circuit.	32
Figure 2.10. Illustration of magnetic configuration in ferromagnetic, antiferromagnetic and ferrimagnetic materials.	40
Figure 2.11. Magnetization dynamics of various timescales.	44
Figure 2.12. Precessional motion of magnetization in presence of damping and spin transfer torque.	50
Figure 2.13. Some standard shapes with co-ordinate convention.	56
Figure 3.1. Schematic diagram of balanced and unbalanced magnetron sputtering.	65
Figure 3.2. Schematic illustration of photolithography process.	68
Figure 3.3. Experimental arrangement of FIB system; (left) imaging mode and (right) irradiation mode.	70
Figure 3.4. NiFe (20 nm)/Au (3 nm) surface structure after the irradiation of $1 \times 1 \mu\text{m}$ windows with doses a) 3.1, b) 6.3, c) 12.5, d) 31.2, e) 62.5 and f) $625 \times 10^{15} \text{ Ga}^+/\text{cm}^2$ at normal incidence with a beam current of 1.5 pA and an acceleration voltage of 30 keV (see reference 9).	71
Figure 3.5. Ion irradiation induced intermixing of interface forming compositionally graded alloy (a schematic illustration).	72
Figure 3.6. Experimental arrangement for scanning electron microscope.	73

Figure 3.7. Schematic illustration of the working principle of XRR.	75
Figure 3.8. Experimental arrangement for vibrating sample magnetometer.	76
Figure 3.9. Atomic force microscope setup (a schematic diagram).	78
Figure 3.10. A schematic diagram of static magneto-optical Kerr effect (Static MOKE) magnetometer setup (top) and the inside electronics of optical bridge detector along with a typical hysteresis loop obtained from static MOKE in case of NiFe(10 nm)/Pt(3 nm) bi-layer (bottom).	80
Figure 3.11. Schematic diagram of Millennia laser head. The figure is reproduced from reference 16.	82
Figure 3.12. A schematic of the beam path inside the folded cavity of Tsunami. The figure is reproduced from reference 14.	83
Figure 3.13. The four prism arrangement used for dispersion compensation in Tsunami laser.	84
Figure 3.14. Schematic diagram of the time resolved magneto-optical Kerr effect (TRMOKE) microscope.	86
Figure 3.15. (a) Typical time-resolved Kerr rotation data from Pt(6.8 nm)/Ni ₈₁ Fe ₁₉ (12.7 nm)/MgO(2.4 nm) sample at a bias field of 1.4 kOe., (b) precessional oscillation part of the time resolved data and (c) fast Fourier transform of figure 3.15(b).	87
Figure 3.16. A standard reflectivity signal obtained from a Si(100) wafer as a function of the time delay between the pump and the probe beams.	88
Figure 3.17. Schematic of the ST-FMR measurement set up and the mechanism of FMR absorption.	90
Figure 3.18. A typical ST-FMR spectrum (black) along with its symmetric (red) and asymmetric components (blue).	90
Figure 4.1. Examples of the background-corrected magnetization oscillations measured using TR-MOKE for NiFe/Au bi-layered microstructures as a function of low-to-moderate Ga ⁺ ion irradiation dose at $H = 1.5$ kOe.	97
Figure 4.2. (a) The damping coefficient, α , (note: error bars are smaller than data points) and (b) the precessional frequencies obtained from the TRMOKE data of a NiFe/Au bi-layer as a function of FIB dose at $H = 1.5$ kOe. (c) The precessional frequency dependence of the damping determined by varying H , for irradiation doses of 0.1 (triangle), 1.7 (circle), and 3.2 (square) pC/ μm^2 .	98
Figure 4.3. Examples of the background-corrected magnetization oscillations measured for NiFe/Cr microstructures as a function of low Ga ⁺ ion irradiation dose at $H = 1.5$ kOe.	98
Figure 4.4. (a) The damping coefficient, α , and (b) the precessional frequencies obtained from the TR-MOKE data of a NiFe/Cr bi-layer as a function of FIB dose at $H = 1.5$ kOe.	99

(c) The precessional frequency dependence of the damping determined by varying H , for irradiation doses of 0.13 (triangle), 0.40 (circle), and 1.00 (square) $\text{pC}/\mu\text{m}^2$.	
Figure 5.1. (a) Schematic illustration of ion beam irradiation of a bi-layer circular structure. (b) TR-MOKE trace from a sample irradiated with ion dose $d = 3.1 \text{ pC}/\mu\text{m}^2$. Note changes in the time base. (c) Time-resolved Kerr images of the sample at three time delays.	111
Figure 5.2. (a) Comparison of TR-MOKE traces between NiFe/Pt ($d = 0.3 \text{ pC}/\mu\text{m}^2$) and NiFe films. Symbols correspond to experimental data while the solid curves are fits to equation 5.2. (b) Power spectra of NiFe/Pt sample at different bias field values H . (c) Frequency vs. bias magnetic field for the NiFe/Pt ($d = 0.3 \text{ pC}/\mu\text{m}^2$) sample. Here the symbols represent experimental data points and the solid curve is a fit to equation 5.3.	113
Figure 5.3. (a) TR-MOKE traces at three different doses. Here, symbols correspond to the experimental data and solid curves are fits to Equation 5.2. (b) Damping is plotted as a function of dose. The shaded box represents the transition between two regions. (c) Variation of damping with dose in the lower dose regime for NiFe/Pt (filled circles) and NiFe/Cu (filled triangles). Here, symbols are the experimental results and solid lines are linear fits. The data shown in figure 5.3(a) - (c) correspond to $H = 1.8 \text{ kOe}$. (d) Variation of damping with precession frequency at three different doses.	116
Figure 5.4. (a) FFT power spectra of the TR-MOKE data of ion irradiated NiFe/Pt samples at three different doses at $H = 1.8 \text{ kOe}$. (b) Variation of frequency f as a function of dose at $H = 1.8 \text{ kOe}$. Symbols are the experimental data and solid lines are linear fits. The shaded box represents the transition between two regions. (c) Magnetization relaxation times τ_1 and τ_2 are plotted as a function of dose. Here the symbols are obtained from experimental data while the solid lines are only guides to the eye.	118
Figure 6.1. Schematic diagram of the experimental setup explaining increase in ferromagnetic resonance (FMR) line-width due to spin pumping effect.	125
Figure 6.2. (a) Variation of damping in CoFeB/Pt system with Pt layer thickness and (b) spin diffusion length as a function of CoFeB layer thickness. (c) Variation of damping in CoFeB/Ta system with Ta layer thickness. (d) Comparison of damping variation between CoFeB/Pt and CoFeB/Ta with nonmagnetic layer thickness.	127
Figure 6.3. (a) Inverse of ferromagnetic layer thickness dependence of damping for CoFeB/NM systems (NM = Pt, Ta) and (b) variation of line-width with frequency for the same samples.	129
Figure 6.4. (a) NM layer thickness dependence of damping for the combination of FM (6 nm)/NM bi-layers, with FM = CoFe and CoFeB, NM = Pt, Ta. (b) Comparison of damping with inverse of FM layer thickness for those samples.	132
Figure 7.1. (a) Schematic illustration of the experimental setup and the sample along with	138

the directions of the applied rf current and bias magnetic field; (b) FMR spectra measured at different excitation frequencies (f); and (c) variation of resonance frequency (f) with the bias magnetic field for CoFe (6.5 nm)/Pt (5.8 nm) sample and the extraction of saturation magnetization from the Kittel fit.	
Figure 7.2. (a) Variation of J_S / J_C as a function of Pt thickness in CoFe/Pt bi-layers with different CoFe thickness. Inset shows the variation of spin diffusion length (l_S) of Pt with CoFe thickness. (b) MOD as a function of current density in the Pt layer for two different orientations of the bias magnetic field in CoFe(3.4 nm)/Pt(5.8 nm) bi-layer. (c) Comparison of θ_{SH} as a function of CoFe thickness obtained from ST-FMR and MOD measurements.	141
Figure 7.3. FM layer thickness dependency of θ_{SH} in CoFe/Pt and Py/Pt systems obtained from (a) ST-FMR measurement and (b) MOD measurement ($d = 5.8$ nm). (c) ST-FMR spectrum of CoFe(4.7 nm)/Pt(7 nm) bi-layer film is shown by black circle. Green and blue solid lines are the symmetric and asymmetric components, respectively. Red circles in the main graph as well as in inset show ST-FMR like spectrum in single CoFe(4.7 nm) layer. (d) CoFe thickness dependency of effective damping coefficient α_{eff} . For the Py/Pt system, the ST-FMR data in figure 7.3(a) and the MOD data in figure 7.3(b) are taken from references 7 and 19, respectively.	143
Figure 8.1. Schematic diagram of the sample and the experimental geometry.	150
Figure 8.2. (a) Time-resolved Kerr rotation data for Pt/Ni ₈₁ Fe ₁₉ bi-layer film at $H \sim 1.4$ kOe, $I_{dc} = 0$ and at $\theta = 0^\circ$. (b) Precessional part of the time-resolved data. (c) Fast Fourier transform (FFT) spectrum of figure 8.2(b). (d) Time-resolved Kerr rotation data from a single Ni ₈₁ Fe ₁₉ layer of equal dimensions as that in the bi-layer film.	152
Figure 8.3. (a) Time-resolved Kerr rotation for Pt/Ni ₈₁ Fe ₁₉ bi-layer film at different bias field values (H) at $I_{dc} = 0$ and $\theta = 0^\circ$. (b) The corresponding FFT spectra. (c) Variation of experimental precession frequency (f) with H (symbol) and fit to the Kittel formula (solid line). (d) Variation of α as a function of f .	153
Figure 8.4. (a) Time-resolved magnetization precession at different dc charge current densities, J_C , for $\theta = 90^\circ$ obtained from the TR-MOKE experiment. Symbols represent the experimental data points, and solid lines are the theoretical fits. (b) The variation of α with J_C for magnetic fields oriented at angle $\theta = 0^\circ, 45^\circ$ and 90° with respect to the current direction. (c) Variation of the precessional frequency f with J_C for $\theta = 45^\circ$, and 90° .	154
Figure 9.1. Schematic diagram of the ion irradiated Ni ₈₁ Fe ₁₉ /Pt bi-layer sample.	160
Figure 9.2 Microscopic image of ion irradiated spots on the sample.	161

Figure 9.3. Photographic image of the sample with electrical connection arranged on a sample holder.	162
Figure 9.4. Photograph of the excitation and detection part of the TR-MOKE setup illustrating the experimental arrangement for this experiment.	163
Figure 9.5. (a-e) Time-resolved Kerr rotation data for unirradiated Ni ₈₁ Fe ₁₉ /Pt bi-layer at different applied current. The black circles denote experimental data points and the red lines are the fitted data.	164
Figure 9.6. Damping is plotted as a function of applied current for un-irradiated Ni ₈₁ Fe ₁₉ /Pt bi-layer sample.	165
Figure 9.7 (a-e) Time-resolved Kerr rotation data of Ni ₈₁ Fe ₁₉ /Pt bi-layer at an irradiation dose $d = 0.8 \text{ pC}/\mu\text{m}^2$ for different applied current. The black circles denote experimental data points and the red lines are the fitted data.	166
Figure 9.8. Damping is plotted as a function of applied current for the sample with irradiation dose $d = 0.8 \text{ pC}/\mu\text{m}^2$.	166
Figure 9.9. (a-e) Time-resolved Kerr rotation data of Ni ₈₁ Fe ₁₉ /Pt bi-layer for an irradiation dose of $d = 2 \text{ pC}/\mu\text{m}^2$ for different applied current. The black circles denote experimental data points and the red lines are the fitted data. (f) Variation of damping as a function of applied current corresponding to figure 9.9 (a-e).	167
Figure 9.10. (a-f) Time-resolved Kerr rotation data of Ni ₈₁ Fe ₁₉ /Pt bi-layer for irradiation dose $d = 3.6 \text{ pC}/\mu\text{m}^2$ for different applied current. The black circles denote experimental data points and the red lines are the fitted data. (g) Variation of damping as a function of applied current corresponding to figure 9.10 (a-f).	168
Figure 9.11. (a-f) Time-resolved Kerr rotation data of Ni ₈₁ Fe ₁₉ /Pt bi-layer for irradiation dose $d = 5 \text{ pC}/\mu\text{m}^2$ for different applied current. The black circles denote experimental data points and the red lines are the fitted data. (g) Variation of damping as a function of applied current corresponding to figure 9.11 (a-f).	169
Figure 10.1. (a) Examples of x-ray reflectivity data and the best-fitting simulations for Co (10 nm)/Pt (t_{Pt}). (b) Background subtracted time-resolved magneto-optic Kerr rotation data for Co/Pt with two different Pt layer thicknesses and the best-fitting damped sinusoids.	178
Figure 10.2. [(a) and (c)] α_{eff} as a function of t_{NM} for Co/Pt and Ni ₈₁ Fe ₁₉ /Pt, respectively. (b) Frequency and saturation magnetization as a function of t_{NM} and $\sim 1.4 \text{ kOe}$ of magnetic field strength; it shows a similar trend in their variations. The shaded bar indicates the Pt thickness where the Pt became continuous.	181

<p>Figure 10.3. Damping coefficient α_{eff} as a function of precessional frequency for 10 nm Co films capped with 0.6 nm and 2 nm Pt. The extrinsic damping decreases with the increasing Pt thickness until reaches to negligible extrinsic effect at $t_{NM} = 2$ nm.</p>	182
<p>Figure 10.4. Schematic illustration of the growth of discontinuous to continuous NM capping layer. (a) Experimental damping data for Co/Pt and Co/Au as a function of t_{NM}. The circular point is a literature value for pure cobalt. (b) Theoretical variation in damping data for Co/Pt and Co/Au adapted from reference 3. as a function of t_{NM}.</p>	185

Chapter 1

Introduction

Magnetism is commonly known as a force generated in some specific materials due to which it attracts matter of similar type. The history of magnetism is quite old starting from the dates earlier than 600 BC. Magnetic material was probably first discovered from naturally occurring iron oxide known as loadstone. However, scientific understanding and application of magnetism started much later. In the twelfth century magnetic compass was known to be used for navigation. Dr. William Gilbert first published a systematic study on magnetism, “*The Magnete*”, in the year of 1600. On 1819, Oersted discovered deflection of magnetic needle by current carrying wire which essentially bridges between electricity and magnetism triggering a series of inventions leading to the development of modern electromagnetism. Around 1880 magnetic hysteresis loop was first observed in iron. In 1895 Curie law was proposed. Theories of diamagnetism and paramagnetism were developed in 1905 by Langevin followed by the theory of ferromagnetism by Weiss on 1906. Landau and Lifshitz theorized the dynamics of magnetic moments in 1935[1], which was further modified by Gilbert in 1955[2]. The theory of spin wave was developed in 1930 by Bloch[3]. In the year of 1988-89, the history of magnetism reached another milestone when professors Fert[4] and Grunberg[5] first experimentally observed giant magnetoresistance effect in Fe/Cr multilayer system for which they were awarded Noble prize in 2007. This investigation finds huge application in magnetic read write devices triggering a new dimension of research called spintronics[6] along with considerable interest in interlayer spin transport and magnetization dynamics in ferromagnetic (FM)/nonmagnetic (NM) bi-layer or multilayer systems. Here we see spintronics evolve beyond fundamental magnetism and venture into exciting applications in different magnetic systems. In that sense spintronics and magnetism should not be considered as two isolated branches of research, rather they are intimately related to each other. The purpose of this thesis is to study some properties which bridge between these two branches.

Nowadays, we are used to in handling gigabytes or terabytes of data in electronic gadgets like smartphone, tablets and personal computer. A new addition in that list is cloud computation which offers individual storing and manipulating data in the web. Even few years back the scenario was completely different. Such a sophisticated computation and freedom of memory were simply beyond one’s imagination. So it will be interesting looking back into the history

of recording evolving to our present hard drive technology before we discuss about its future prospective.

In the nineteenth and earlier twentieth century, before the advent of magnetic recording, punched cards were widely used as a recording medium. It was first implemented in mechanised textile loom in 1725. In early digital computers punch cards were introduced as primary input method for programs and data. These are basically paper cards containing punched holes at suitable places to represent data. They are also known as Hollerith cards and IBM cards. These cards allow the user to save and access information by inserting it into the computer. The data was read by determining the position of the holes. The technique becomes obsolete after 1970s being replaced by more efficient magnetic recording technique.

In 1932 G. Taushek discovered a magnetic recording technique called drum memory which is an early stage of magnetic hard drives. It looks like a cylinder or drum with ferromagnetic layer coated at the outer surface. Read and write head was mounted few microns apart. Data can be written by applying short electric pulse in the rotating drum and the change of polarization of magnetization at a particular point of the magnetic surface is detected by the read head. It had a typical storage capacity of 10 KB. It was widely used in computers in 1950s and 60s.

The first hard disc drive (HDD) was introduced by IBM in 1956. It was a bulky hard drive with weight around 250 kg consisting of 50 discs of 24 inch diameter and storage capacity of ~5 MB. In 1980 IBM introduced hard drive (IBM 3310) with more than 2.5 GB memory but still very large in size. Later the use of GMR and TMR technology in HDD made the life much easier. Present hard drives are very fast, handy and can store Terabytes of data. But how does such a miracle become possible? The answer lies in its working principle. It has a number of thin magnetic disks called platter mounted on a spindle which can rotate at thousands of rpm. The data can be stored in both sides of the platter provided magnetic layer and read write heads are present on each side. Co Based alloy is used as a magnetic material. A sophisticated engineering makes it possible to float the read-write head only few nanometres apart from the film plane. Such a narrow gap helps to reduce the size of each data element and thus increase storage density. The head can have a very accurate movement in the film plane by Lorentz force with small applied current. A tiny electric field is used to write the data in the magnetic disk. A GMR or TMR based read head detect small change in flux corresponding to the data bit.

There are different other types of data storage medium and some of them are obsolete like magnetic tape, floppy disk while some are still being used like magneto-optical (MO) disks, flash drives and data cards. In MO disks local heating due to pulsed laser is used for writing data. This technique is known as heat assisted magnetic recording (HAMR)[7]. The laser pulse of $1\mu\text{m}$ diameter falls on the disk and increases the local temperature. As a result the coercivity of the material decreases from its original value at the spotted region. Now, the magnetization of the region can be switched easily by applying a suitable field without affecting the other part of the disc. The field value should be chosen intermediate to the coercivity of heated and outside region. When the laser spot moves, temperature decreases with a subsequent increase in coercivity. This essentially freezes the magnetization orientation. The data is read by the same laser spot using magneto-optical Kerr effect.

It is clear that the storage density increases with the reduction of bit size. However, the particle size for storing one bit of data can be reduced down to a certain limit called superparamagnetic limit. For a single domain particle the magneto-crystalline anisotropy energy is given by $E = \frac{1}{2}KV \sin^2 \theta$ where K is the anisotropy constant, V is the volume and θ is the angle between easy direction and magnetization. The minimum energy or the most favourable state can be obtained for two opposite orientation of magnetization given by $\theta = 0^\circ$ and 180° . If magnetization tries to hop from one state to the other it has to cross the energy barrier of KV . Hence, the barrier is important because it restrains the loss of spin memory. The thermal fluctuation in the environment determined by $K_B T$ (K_B = Boltzman constant and T = temperature) acts as a source of perturbation energy for random switching of magnetization. Hence, for thermal stability the ratio between KV and $K_B T$ should be larger than a certain value. The critical value of $KV/ K_B T$ depends on various properties of the medium like saturation magnetization, grain size distribution and inter-granular coupling which can typically vary between 40 to 80[8-11]. Now if we want to reduce the volume (V) of data bit, K has to be large enough for maintaining the barrier height. Hence high anisotropy material can be a solution for higher storage density. However, the increase of K is limited by the required field to be produced to write in the medium. The maximum write field is around 400 kA/m, correspond to a minimum grain diameter of approximately 11–12 nm by ensuring thermal stability in CoCrPt-based longitudinal media[8,11]. Hence from the discussion we understand that the storage capacity can be increased by increasing anisotropy of the material only up to a certain limit.

From earlier discussion we understand that the recording head has to apply a field larger than the coercive field of the writing medium. This essentially put a limitation on anisotropy and thereby in storage capacity. But interestingly there exist another scheme where one can have saturation recording with writing field much smaller than the coercivity of the medium. This is called microwave assisted magnetic recording (MAMR)[12-14]. The idea is based on ferromagnetic resonance (FMR). Initially magnetization of a system is oriented along the easy direction. A transverse ac field is applied in presence of a pulsed magnetic field along the easy axis opposite to the initial magnetization. At resonance, energy is absorbed and precession angle increases. If absorption of energy overcomes the damping, the gyration will increase and finally causes gyro reversal of magnetization providing the reversing field pulse to sustain for sufficiently long time. The threshold field value for magnetization reversal depends on the duration of pulse, damping and ac frequency. The scheme promises storage density over 1TB/in²[12].

Apart from magnetic properties and recording technique, storage capacity depends on the geometry of writing. It can be written in the plane of the film or perpendicular to the film plane which requires in-plane magnetized or perpendicularly magnetized materials, respectively. The first one is called longitudinal recording [9,11,15-19] and the latter is known as perpendicular recording[20-24]. Longitudinal recording was more conventional earlier. Later perpendicular recording has been proposed due to certain advantages. In perpendicular recording the areal density of data is higher and the bit patterns are magnetostatically more stable as compared to the longitudinal recording. Therefore, it is less affected by thermal fluctuation and other spurious fields. Earlier literature reveals that longitudinal recording can have maximum storage capacity of 100 GB/in²[17]whereas for transverse recording it can be up to 340GB/in²[24]. In addition to that, the switching mechanism is much sharper having lower level of noise. These make the transverse recording a hot area of research at present.

Another interesting field is patterned magnetic media[25] where periodic array of dots acting as data bits are supposed to be a possible solution for high density storage media. A 50 nm periodicity of such dots correspond to a storage density of 260 GB/in². In this case the feature size is very small which is in nanometre scale. Hence, instead of photolithography electron beam lithography is used. An advanced lithographic technique can produce even smaller feature which may lead to even higher storage capacity[26]. Another important aspect of this scheme is the bits have a defined boundary which is physically separated from each other and not by the domain wall boundary in a continuous medium. As a result transition noise can be

eliminated resulting in a better performance of the device. Unlike thin films, dots of a patterned media are coupled to each other behaving like a single magnetic domain. As a result thermal stability criteria correspond to the volume and anisotropy of the entire magnetic elements which make the system thermally very stable. One major problem of this arrangement is synchronization which means the read-write head should be very small and addresses the exact location of the dot.

The concept of spin wave is relatively old which was introduced by F. Bloch in 1930[27]. However, it is equally relevant to the present technology due to its tremendous applicability. A collective excitation of spins with phase propagating in a continuous or confined magnetic medium is known as spin wave. The quanta of spin waves are called magnons. A periodically varying medium where propagation of magnons is studied is called magnonic crystal. By changing the physical parameters of a magnonic crystal like size, shape, unit cell arrangement and lattice constant one can modulate band structures and thereby magnonic band gaps which can be applied as components for data communication devices such as filters. Kostylev *et al.* first demonstrated spin wave based logic gates using Mach-Zehnder-type current-controlled interferometer[28]. It is important to note that spin waves can be classified into various modes depending on the relative orientation between propagation vector and applied magnetic field. There exists one variant of spin waves which are localized in the surface called surface spin wave or Damon-Eshbach mode. This mode has a nonreciprocal behaviour in the spin wave amplitude for opposite direction of wave vector[29-32]. The value of nonreciprocity is not a constant but depends on external magnetic field. Using this nonreciprocal behaviour one can construct spin wave logic[33] which can be potentially important to replace our existing semiconductor based logic devices due to its exciting features. The surface spin waves have a large group velocity of ~few tens of micron/nm. Hence, the logic gate can well operate in the GHz frequency range. Such devices are scalable up to a feature size of few nanometres. In terms of power consumption spin wave propagation is not associated with any charge transfer. Hence, they are energetically very efficient.

For fast logic operation of a computer a special type of memory is required which can be accessed (read or write) randomly by a program. This is known as random access memory (RAM). In contrast there exist memories which can be serially accessed called serial access memory (SAM) like recording tape. It works well as a buffer memory e.g., video card but not as programmable memory because to find a particular data in SAM each memory shell needs to be checked serially which makes the operation complex and much slower. In case of

RAM, memory cells are located at the junction of two dimensional grids and can be addressed instantly by the row and column numbers. Our present technology offers semiconductor based RAM driven by charge current. Dynamic random access memory (DRAM)[34] is a common variant of RAM, where information is stored using an integrated circuit which contains transistors and capacitors. The transistor acts as a controlling switch and the capacitor holds the data in form of electrical charge. But the main drawback of DRAM is volatility that is the storage capacitor cannot hold its charge over an extended period of time and will lose the stored data bit unless its charge is refreshed periodically. That is the reason why it is called dynamic. As a substitute to DRAM magnetoresistive random access memory (MRAM)[35-37] comes into picture which is non-volatile. It relies on spin valves. A unit structure has a hard magnetic layer with fixed spin orientation and a soft magnetic layer separated by a thin insulating spacer. The parallel or anti-parallel configuration of the soft magnetic layer with respect to pinned layer results in a low or high resistance due to tunnelling magnetoresistance (TMR) effect denoting “1” or “0” state respectively. Recently MRAM is proposed with spin transfer torque (STT) based switching called STT-MRAM. Fast switching time, low programming current, scalability and non-volatile nature of this memory qualify itself as a possible alternative to the present RAM. Configuration wise TMR elements with perpendicular anisotropy (P-TMR) are even more interesting because of its small cell size as well as high anisotropy assuring a good thermal stability. Such STT-MRAM[38-39] based on P-TMR elements is known as P-STT-MRAM. In such devices programming current reduces rapidly with the reduction of the size of the element. Hence, it is naturally scalable. Switching probability increases with write current. The critical current needed for magnetization switching is proportional to the damping of the system. It means lower the damping is smaller will be the current for writing. Smaller damping can also be useful in other applications such as spin wave based devices where low loss transmission and processing of signal via magnetization waves are required. Recently, it is observed that STT can completely compensate the damping torque resulting in an un-damped precession of magnetization called auto oscillation[40] that unfolds the opportunity of electromagnetic signal being transferred through a magnetic medium without decay. One step further, negative damping with sufficiently large STT can enable us to construct a new type of nano-oscillator based on self-excitation of magnetization[40]. On the other hand, large damping causes the suppression of magnetization which is desirable for nano-scale magnetic devices due to higher reversal rate and coherent rotation of magnetization. It also helps in reduction of noise due to thermal fluctuation and hence, we have a better signal to noise ratio. The operation of a device and its

speed can depend on the frequency modes of magnetization oscillation. Hence, the key message turns out from the discussion is that optimization or active control of magnetic properties is crucial for the performance of various devices. Let us talk about a FM/NM bi-layer system which is considered to be a promising unit structure for many future devices. Magnetic parameters of such structures can be optimized in several ways like designing the interface with selective combination of materials, variation of layer thicknesses and also active controls like injection of spin current or interface modification by low dose ion irradiation.

The concept of spin current[41] came from electrons having two degrees of freedom namely charge and spin degrees of freedom which are normally associated with each other but separable in space under certain experimental conditions. Unlike charge current which is a direct consequence of flow of charge, spin current solely deals with the spin degree of freedom of an electron giving rise to a new technology over the existing charge based technology known as spintronics. For a pure spin current[41-42] there are a lot of advantages like no net flow of charge and hence no stray Oerstead field, minimum power dissipation, tunable magnetic damping[40,43-45], by which one can achieve loss less propagation of electromagnetic waves [44], or reduction of noise due to thermal fluctuation[44] as mentioned earlier. All these exciting features, however, have been bottlenecked by the insufficiency of spin current density required to drive spintronic devices. Hence, a lot of research is required to enhance the conversion efficiency between charge current and spin current known as spin Hall angle[45-48](θ_{SH}). One important aspect of this thesis is to investigate θ_{SH} of FM/NM bi-layer samples using different measurement techniques like spin torque ferromagnetic resonance and modulation of damping techniques. We will discuss spin-orbit interaction, impurity scattering, spin Hall effect, spin diffusion length, spin pumping, generation and injection of spin current across the interface, which can play a crucial role in controlling the magnetization dynamics, spin wave and spin transport properties of the ferromagnetic layer. The discussion will be included in chapters 6-10.

Recently, focused ion beam (FIB) is commonly used for direct nanoscale patterning[49] and milling to fabricate nanostructures with high precision. It may also be used to locally manipulate magnetic properties, domain structures[50] as well as magnetization and domain wall dynamics[51-52] on the micro and nanoscale. This opens new opportunities for interesting scientific investigations and has potential in future applications of nanoscale magnetic structures, such as sensors, memory and logic devices. In this thesis, we have studied active con-

trol of dynamic magnetic properties by interface engineering[53-54] using FIB irradiation which will be included in chapters 4, 5 and 9.

References

- [1] Landau, L. D. & Lifshitz, E. On the theory of the dispersion of magnetic permeability in ferromagnetic bodies. *Phys. Z. Sowjetunion* **8**, 101 (1935).
- [2] Gilbert, T. L. A phenomenological theory of damping in ferromagnetic materials. *IEEE Trans. Magn.* **40**, 3443 (2004).
- [3] Bloch, F. Zur theorie des ferromagnetismus. *Zeitschrift für Physik* **61**, 206 (1930).
- [4] Baibich, M. N. *et al.* Giant magnetoresistance of (001) Fe/(001) Cr magnetic superlattices. *Phys. Rev. Lett.* **61**, 2472 (1988).
- [5] Binasch, G., Grünberg, P., Saurenbach, F. & Zinn, W. Enhanced magnetoresistance in layered magnetic structures with antiferromagnetic interlayer exchange. *Phys. Rev. B* **39**, 4828 (1989).
- [6] Wolf, S. *et al.* Spintronics: a spin-based electronics vision for the future. *Science* **294**, 1488 (2001).
- [7] Rottmayer, R. E. *et al.* Heat-assisted magnetic recording. *IEEE Trans. Magn.* **42**, 2417 (2006).
- [8] Weller, D. & Doerner, M. F. Extremely high-density longitudinal magnetic recording media. *Annual review of materials science* **30**, 611 (2000).
- [9] Moser, A. & Weller, D. Thermal processes and stability of longitudinal magnetic recording media. *IEEE Trans. Magn.* **35**, 2808 (1999).
- [10] Weller, D. & Moser, A. Thermal effect limits in ultrahigh-density magnetic recording. *IEEE Trans. Magn.* **35**, 4423 (1999).
- [11] Bertram, H. N., Zhou, H. & Gustafson, R. Signal to noise ratio scaling and density limit estimates in longitudinal magnetic recording. *IEEE Trans. Magn.* **34**, 1845 (1998).
- [12] Wang, Y., Tang, Y. & Zhu, J.-G. Media damping constant and performance characteristics in microwave assisted magnetic recording with circular ac field. *J. Appl. Phys.* **105**, 07B902 (2009).
- [13] Zhu, J.-G., Zhu, X. & Tang, Y. Microwave assisted magnetic recording. *IEEE Trans. Magn.* **44**, 125 (2008).

-
- [14] Zhu, J. G. & Wang, Y. Microwave assisted magnetic recording utilizing perpendicular spin torque oscillator with switchable perpendicular electrodes. *IEEE Trans. Magn.* **46**, 751 (2010).
- [15] Abarra, E. *et al.* Longitudinal magnetic recording media with thermal stabilization layers. *Appl. Phys. Lett.* **77**, 2581 (2000).
- [16] Chen, T. & Yamashita, T. Physical origin of limits in the performance of thin-film longitudinal recording media. *IEEE Trans. Magn.* **24**, 2700 (1988).
- [17] Choe, G. *et al.* Highly in-plane oriented CoCrPtB longitudinal media for 130-Gb/in² recording. *IEEE Trans. Magn.* **39**, 633 (2003).
- [18] Coffey, K. R., Parker, M. & Howard, J. K. High anisotropy L1₀ thin films for longitudinal recording. *IEEE Trans. Magn.* **31**, 2737 (1995).
- [19] Piramanayagam, S. Longitudinal Recording Media. *Developments in Data Storage: Materials Perspective*, 33 (John Wiley & Sons, Inc., 2011).
- [20] Iwasaki, S. & Ouchi, K. Co-Cr recording films with perpendicular magnetic anisotropy. *IEEE Trans. Magn.* **14**, 849 (1978).
- [21] Piramanayagam, S. Perpendicular recording media for hard disk drives. *J. Appl. Phys.* **102**, 011301 (2007).
- [22] Iwasaki, S. Perpendicular magnetic recording. *IEEE Trans. Magn.* **16**, 71 (1980).
- [23] Albrecht, M. *et al.* Recording performance of high-density patterned perpendicular magnetic media. *Appl. Phys. Lett.* **81**, 2875 (2002).
- [24] Hsu, Y. *et al.* Challenges for perpendicular write heads at high recording density. *IEEE Trans. Magn.* **43**, 605 (2007).
- [25] Ross, C. A. Patterned magnetic recording media. *Annu. Rev. Mat. Res.* **31**, 203 (2001).
- [26] Sato, H. & Homma, T. Fabrication of magnetic nanodot arrays for patterned magnetic recording media. *J. Nanosci. Nanotechnol.* **7**, 225 (2007).
- [27] Bloch, F. Zur theorie des ferromagnetismus. *Z. Phys.* **61**, 206 (1930).
- [28] Kostylev, M. *et al.* Spin-wave logical gates. *Appl. Phys. Lett.* **87**, 153501 (2005).
- [29] Damon, R. & Eshbach, J. Magnetostatic modes of a ferromagnetic slab. *J. Appl. Phys.* **31**, S104 (1960).
- [30] Schneider, T. *et al.* Phase reciprocity of spin-wave excitation by a microstrip antenna. *Phys. Rev. B* **77**, 214411 (2008).
- [31] Amiri, P. K., Rejaei, B., Vroubel, M. & Zhuang, Y. Nonreciprocal spin wave spectroscopy of thin Ni-Fe stripes. *Appl. Phys. Lett.* **91**, 062502 (2007).

- [32] Sekiguchi, K. *et al.* Nonreciprocal emission of spin-wave packet in FeNi film. **97** 022508 (2010).
- [33] Jamali, M. *et al.* Spin wave nonreciprocity for logic device applications. *Sci. Rep.* **3** 3160 (2013).
- [34] Horiguchi, F. *Dynamic Random Access Memory*. (Wiley-VCH Verlag GmbH & Co. KGaA, 2010).
- [35] Nishimura, N. *et al.* Magnetic tunnel junction device with perpendicular magnetization films for high-density magnetic random access memory. *J. Appl. Phys.* **91**, 5246 (2002).
- [36] Tehrani, S. *et al.* Magnetoresistive random access memory using magnetic tunnel junctions. *Proc. IEEE* **91**, 703 (2003).
- [37] Parkin, S. *et al.* Exchange-biased magnetic tunnel junctions and application to nonvolatile magnetic random access memory. *J. Appl. Phys.* **85**, 5828 (1999).
- [38] Khvalkovskiy, A. *et al.* Basic principles of STT-MRAM cell operation in memory arrays. *J. Phys. D: Appl. Phys.* **46**, 74001 (2013).
- [39] Kishi, T. *et al.* Lower-current and fast switching of a perpendicular TMR for high speed and high density spin-transfer-torque MRAM. *Electron Devices Meeting, 2008. IEDM 2008. IEEE International*, 1 (2008).
- [40] Demidov, V. E. *et al.* Magnetic nano-oscillator driven by pure spin current. *Nat. Mater.* **11**, 1028 (2012).
- [41] Takahashi, S. & Maekawa, S. Spin current, spin accumulation and spin Hall effect. *Sci. Technol. Adv. Mater.* **9**, 014105 (2008).
- [42] Bader, S. & Parkin, S. Spintronics. *Annu. Rev. Condens. Matter Phys.* **1**, 71 (2010).
- [43] Ando, K. *et al.* Electric manipulation of spin relaxation using the spin Hall effect. *Phys. Rev. Lett.* **101**, 036601 (2008).
- [44] Demidov, V. E. *et al.* Control of magnetic fluctuations by spin current. *Phys. Rev. Lett.* **107**, 107204 (2011).
- [45] Liu, L., Moriyama, T., Ralph, D. & Buhrman, R. Spin-torque ferromagnetic resonance induced by the spin Hall effect. *Phys. Rev. Lett.* **106**, 036601 (2011).
- [46] Kondou, K. *et al.* Evaluation of spin Hall angle and spin diffusion length by using spin current-induced ferromagnetic resonance. *Appl. Phys. Express* **5**, 073002 (2012).

- [47] Mosendz, O. *et al.* Quantifying spin Hall angles from spin pumping: Experiments and theory. *Phys. Rev. Lett.* **104**, 046601 (2010).
- [48] Ganguly, A. *et al.* Thickness dependence of spin torque ferromagnetic resonance in Co₇₅Fe₂₅/Pt bilayer films. *Appl. Phys. Lett.* **104**, 072405 (2014).
- [49] Fassbender, J. & McCord, J. Magnetic patterning by means of ion irradiation and implantation. *J. Magn. Magn. Mater.* **320**, 579 (2008).
- [50] Aziz, A. *et al.* Angular dependence of domain wall resistivity in artificial magnetic domain structures. *Phys. Rev. Lett.* **97**, 206602 (2006).
- [51] Burn, D. & Atkinson, D. Control of domain wall pinning by localised focused Ga⁺ ion irradiation on Au capped NiFe nanowires. *J. Appl. Phys.* **116**, 163901 (2014).
- [52] Lavrijsen, R. *et al.* Controlled domain-wall injection in perpendicularly magnetized strips. *Appl. Phys. Lett.* **96**, 222502 (2010).
- [53] King, J. *et al.* Local control of magnetic damping in ferromagnetic/non-magnetic bilayers by interfacial intermixing induced by focused ion-beam irradiation. *Appl. Phys. Lett.* **104**, 242410 (2014).
- [54] Ganguly, A. *et al.* Tunable Magnetization Dynamics in Interfacially Modified Ni₈₁Fe₁₉/Pt Bilayer Thin Film Microstructures. *Sci. Rep.* **5** 17596 (2015).

Chapter 2

Theoretical Overview

In this chapter we present an overview of the theories relevant to this thesis. In the first part we describe electron spin in a quantum mechanical approach from which the concept and properties of spin current will be discussed. We also discuss the underlying theories of different spintronic phenomena like spin Hall effect, spin pumping and various magnetoresistance effects. The second part of this chapter begins with the discussion of the theoretical background and origin of magnetism. Later we focus on magnetization dynamics, spin waves and related phenomena including the underlying physics of magneto-optical Kerr effect and ferromagnetic resonance.

2.1. Electron Spin

Electron is a negatively charged subatomic particle commonly known to us over a long time. Itinerant electrons in a metal wire can carry current when an electrical voltage is applied. The negative charge is a fundamental property of electron, as is its small charge to mass ratio. In addition to charge and mass, electrons have a third property called spin that is often overlooked. However, more recently it is realized that spin of an electron can be utilized to drive electronic based devices like memory and logic devices with added functionality.

2.2. Spin Continuity Equation

We know that electron is a Fermionic particle with $\frac{1}{2}$ integer spin and therefore constrained by Pauli exclusion principle. Spin of an electron is a quantum mechanical observable angular momentum of which is expressed by an operator as

$$\hat{S} = \frac{\hbar}{2} \hat{\sigma} \tag{2.1},$$

where \hbar is the Plank's constant and $\hat{\sigma}$ is Pauli spin matrices given by

$$\hat{\sigma}_x = \begin{pmatrix} 0 & 1 \\ 1 & 0 \end{pmatrix}, \hat{\sigma}_y = \begin{pmatrix} 0 & -i \\ i & 0 \end{pmatrix} \text{ and } \hat{\sigma}_z = \begin{pmatrix} 1 & 0 \\ 0 & -1 \end{pmatrix} \quad (2.2).$$

In quantum mechanical formalism the state of an electron is described by a spinor $\psi(r, t)$ as

$$\psi(r, t) = a|\uparrow\rangle + b|\downarrow\rangle \equiv \begin{pmatrix} a \\ b \end{pmatrix} \quad (2.3),$$

where $|\uparrow\rangle$ and $|\downarrow\rangle$ are the two eigenstates of \hat{S} known as “spin up” and “spin down” respectively corresponding the eigenvalues $\pm\hbar/2$ while a and b are the complex quantities. The probability density of $\psi(r, t)$ is $\rho(r, t) = \psi^\dagger(r, t)\psi(r, t) = a^2 + b^2$. In case of an electron charge density ρ_C spin density ρ_s with quantization along \hat{S} can be expressed as

$$\rho_C(r, t) = \psi^\dagger(r, t)Q\psi(r, t) \text{ and } \rho_s(r, t) = \psi^\dagger(r, t)\hat{S}\psi(r, t) \quad (2.4),$$

where $Q = -eI_2$ is the charge operator, $-e$ is the charge of an electron and I_2 is a two dimensional identity matrix. Now, charge can be defined as a ratio of charge density and probability density i.e., $\rho_C(r, t) / \rho(r, t)$. Using similar intuition one can define spin charge as

$$s(r, t) = \frac{\rho_s(r, t)}{\rho(r, t)} = \frac{\psi^\dagger(r, t)\hat{S}\psi(r, t)}{\psi^\dagger(r, t)\psi(r, t)} = \phi^\dagger(r, t)\hat{S}\phi(r, t) \quad (2.5),$$

where $\phi(r, t)$ is the normalized spinor which is related to $\psi(r, t)$ as $\phi(r, t) = \rho(r, t)^{-1/2}\psi(r, t)$.

Now using equation 2.1 in equation 2.5 we get

$$s(r, t) = \frac{\hbar}{2} \phi^\dagger(r, t)\hat{\sigma}\phi(r, t) = \frac{\hbar}{2} p(r, t) \quad (2.6).$$

Here, $p(r, t)$ is called polarization vector[1] corresponding to the spinor $\phi(r, t)$. The polarization vector as well as spin charge of an electron is unit real pseudovector in three-dimensional space and can be observed experimentally. It determines the spin precession of an electron. Bloch introduced this concept in the discussion of nuclear induction[2].

In quantum mechanics, the fundamental probability continuity equation in steady state is given by

$$\frac{\partial \rho}{\partial t} + \vec{\nabla} \cdot \vec{j} = 0 \quad (2.7),$$

where j is the probability current density. As we define spin charge density as $\rho_{\vec{s}}(r,t) = \rho(r,t) \cdot s(r,t)$, the continuity equation in case of spin current[3] turns out to be

$$\begin{aligned} \vec{s} \left(\frac{\partial \rho}{\partial t} + \vec{\nabla} \cdot \vec{j} \right) &= 0 \\ \frac{\partial (\rho \vec{s})}{\partial t} + \vec{\nabla} \cdot (\vec{j} \vec{s}) - \rho \frac{\partial \vec{s}}{\partial t} - \vec{j} \cdot \vec{\nabla} \vec{s} &= 0 \end{aligned} \quad (2.8),$$

where $(\vec{j} \vec{s})$ is a second order tensor.

2.3. Spin Polarization

So far we have seen that spin of an electron can be considered as a degree of freedom similar to charge which follows continuity equation and can be defined by the polarization vector. But what do we actually mean by spin polarization of an ensemble of electron? A system is said to be polarised if the two spin states have unequal distribution of population. In other words spins have a preferential orientation which is analogous to the polarization of light where the electric field vectors are preferentially orientated along a particular direction. An electron beam is called fully polarized if all the spins are in same state. If the majority of spin belong to a particular state then the beam is polarized to that state and if they are equally distributed then the beam is called un-polarized. The spin polarization of electron is important in many aspects. In theoretical studies spin polarization makes it easier to calculate parameters like initial and final energy state of an electron system undergoing spin dependent processes. Hence, we need not to bother about what happens to the individual spins. It brings the concept of pure spin current and spin polarized current on which spintronics stand. Spin current can exert torque on magnetization and thereby control magnetization dynamics and magnetization reversal and domain wall motion. Some unique examples will be discussed in chapter 7-9.

It is not straight forward to polarize an electron beam by separating spins in space. In 1922 Otto Stern and Walther Gerlac took the first initiative by polarizing neutral silver atoms passing through an inhomogeneous magnetic field[4-5]. The atoms have a magnetic moment related to their angular momentum. Hence, magnetic field deflects the atoms from their straight path. A screen placed at a distance shows discrete points rather than a continuous distribution. The experiment first reveals the quantum nature of spin angular momentum, and is considered to be important step towards the development of spin physics. However, the scheme cannot be used for the separation of charged particles like electron. Lorentz force acting on electrons combined with uncertainty criteria prevents the separation of opposite spins. However, more recently it is known that electron spins can be separated in space using spin Hall effect which gives rise to spin current. The detailed mechanism will be discussed in later part of this chapter.

2.4. Spin Current and Charge Current

As we have seen earlier the probability density of $\psi(r,t)$ can be expressed as $a^2 + b^2$. Here, a^2 and b^2 signifies the probability densities of “spin up” and “spin down” states which in classical picture corresponds to the carrier densities of those states denoted by n_{\uparrow} and n_{\downarrow} respectively that adds up to the total carrier density n . Hence we get, $a^2 + b^2 = n_{\uparrow} + n_{\downarrow} = n$. Now by applying charge operator Q and spin operator \hat{S} (equation 2.1) on wave function $\psi(r,t)$ and choosing quantization along \hat{S}_z without loss of generality equation 2.4 yields

$$\begin{aligned}\rho_c &= -e\psi^\dagger(r,t)\psi(r,t) = -e(a^2 + b^2) = -e(n_{\uparrow} + n_{\downarrow}) \\ \text{and } \rho_s &= \frac{\hbar}{2}\psi^\dagger(r,t)\hat{\sigma}_z\psi(r,t) = \frac{\hbar}{2}(a^2 - b^2) = \frac{\hbar}{2}(n_{\uparrow} - n_{\downarrow})\end{aligned}\quad (2.9).$$

It is important to note that in the right hand side of equation 2.9 we obtain pre-factors as $-e$ and $\hbar/2$ in case of ρ_c and ρ_s respectively which signifies that electron acts as a carrier of charge as well as angular momentum. Now, from the concept of classical mechanics it is easy to understand that volume charge density ρ_c multiplied with the carrier velocity v gives the charge current density ($J_c = \rho_c v$). Similarly, one can define spin current density as $J_s = \rho_s v$

and the current densities of individual carrier will be $J_{\uparrow(\downarrow)} = -en_{\uparrow(\downarrow)}v$. Hence, using equation 2.9 we get

$$J_c = (J_{\uparrow} + J_{\downarrow}) \text{ and } J_s = -\frac{\hbar}{2e}(J_{\uparrow} - J_{\downarrow}) \quad (2.10).$$

Hence, we can conclude that charge current can be denoted by the sum of currents due to two different carriers whereas spin current is the difference of that[3,6-7]. It is important to note that the units of charge current and spin current are not the same. We know that in SI system the unit of charge current J_c is A/m^2 . From equation 2.10 we get the unit of J_{\uparrow} and J_{\downarrow} as A/m^2 and hence the unit of spin current J_s becomes $(\hbar/e)A$.

2.5. Time Reversal Symmetry of Spin Current

In this context we shall discuss about how spin current behave under time reversal. Earlier it is mentioned that pure spin current is dissipation less which is considered as one of the most important advantages of spin current. On the contrary charge current is associated with heat dissipation. The argument suggests that spin current is time invariant whereas, charge current changes sign under time reversal. Time reversal is defined as an operation where time changes sign due to which velocity (v), spin (\hat{S}) and charge (q) transforms as $\vec{v} \rightarrow -\vec{v}$, $\hat{S} \rightarrow -\hat{S}$ and $q \rightarrow -q$. Now we know that the charge and spin current densities can be expressed in terms of v , \hat{S} and q as $J_c = \rho_c v$ and $J_s = \rho_s v$. The schematic diagram of the time reversal in case of charge and pure spin current are shown in figure 2.1 (a) and (b) respectively. Equivalent diagrams are shown at the bottom of each figures from which it is clear that charge current changes sign under time reversal but spin current does not.

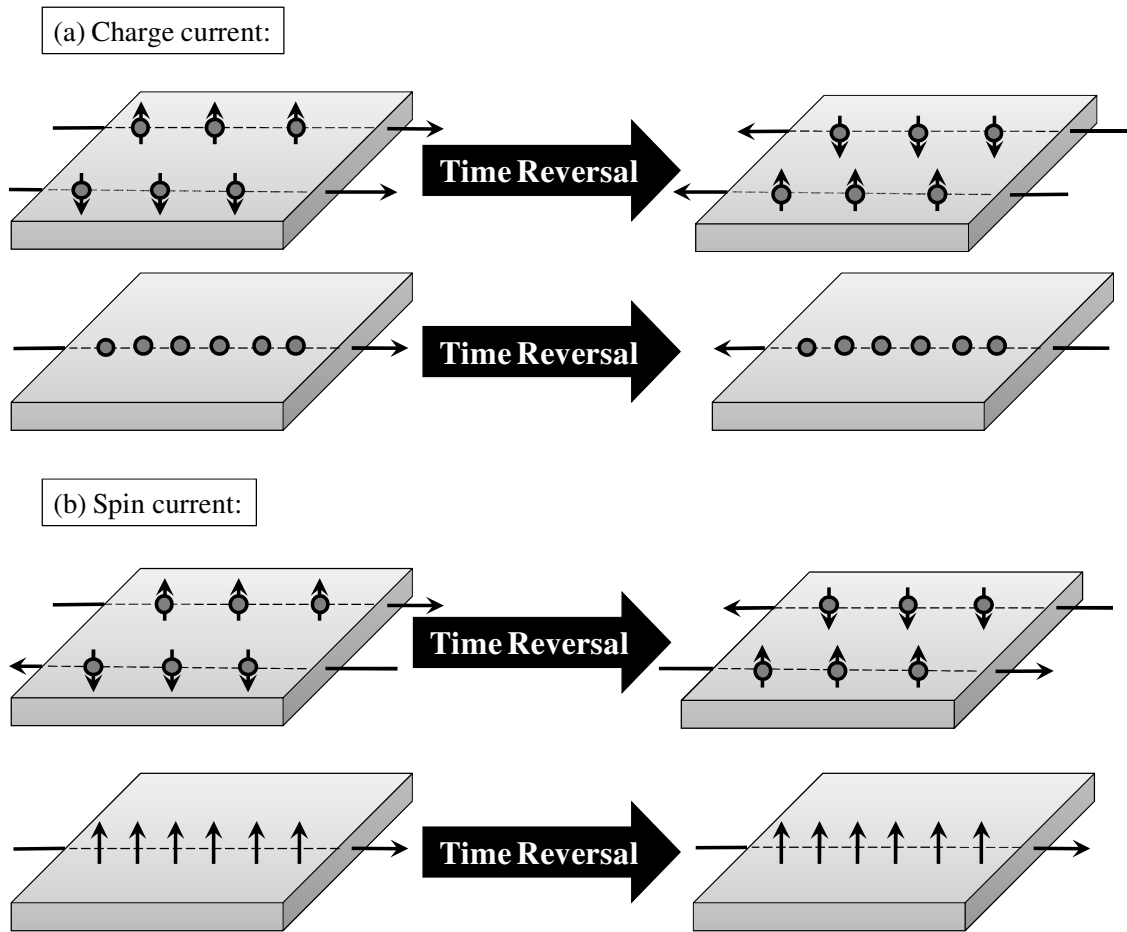


Figure 2.1. Schematic representation of time reversal in case of (a) charge current and (b) spin current. The bottom figure in each case represents the equivalent picture.

2.6. Hall Effect

Hall effect was first observed by Edwin H. Hall in the year of 1879, 18 years before the discovery of electron[8]. If a nonmagnetic conductor carries charge current, in presence of a transverse magnetic field, an electric field is developed within the conductor in a direction perpendicular to both current and magnetic field. The phenomenon is referred to as Hall effect or ordinary Hall effect.

2.6.1. Ordinary Hall Effect

Let us consider a piece of conductor carrying current I along x-direction placed in an external magnetic field \vec{B} applied along y-direction as shown in figure 2.2. The current carriers

will be deflected by the Lorentz force, given by $\vec{F} = q(\vec{v} \times \vec{B})$, along z-direction causing an accumulation of charge on the top surface. Here, q is the charge and \vec{v} is the average velocity of the carrier. When the charge carrier is electron (for metal or n-type semiconductor) the top surface will be negatively charged with respect to the bottom surface while in case of hole (for p-type semiconductor) the picture is opposite. The accumulation of charge gives rise to an electric field (Hall field, \vec{E}_H) that exerts a force on the charge carriers opposite to the Lorentz force. The two opposing forces cancel each other when equilibrium is achieved. Hence, in steady state the force equation for an electron can be expressed by as

$$e\vec{E}_H = e(\vec{v} \times \vec{B}) \quad (2.11).$$

Using equation 2.11 and the expression for current as $I = nyzve$, one obtain the expression for Hall voltage as

$$V_H = E_H z = vBz = IB / nye \quad (2.12).$$

Here, V_H , n , y and z indicate Hall voltage, number density of electron, width and thickness of the conductor. In this case the total electric field in the system is $E_T = \sqrt{E_A^2 + E_H^2}$ where, \vec{E}_A is the applied electric field along x-direction which drives the current. The angle between \vec{E}_A and \vec{E}_T is called Hall angle θ_H given by the expression in equation 2.13.

$$\theta_H = \tan^{-1}(E_H / E_A) = Bv / E_A = B\mu_c \quad (2.13).$$

Here, μ_c denotes the mobility of electron.

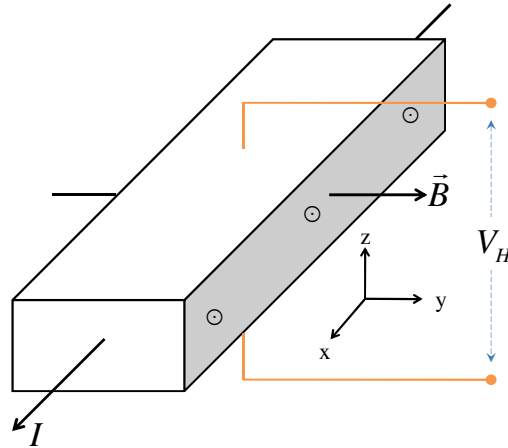


Figure 2.2. Schematic illustration of ordinary Hall effect.**2.6.2. Anomalous Hall Effect**

Anomalous Hall effect (AHE)[9-11] is one of the most interesting transport phenomenon which refers to the appearance of a large Hall voltage in a magnetic system in response to an applied electric current. The total Hall resistance in a ferromagnetic material is contributed from two different effects. One is proportional to applied B which corresponds to the ordinary Hall effect. The other part is anomalous which is often proportional to the magnetization (M) of the system as given by equation 2.14

$$R_H = R_O B + R_A M \quad (2.14),$$

where R_O and R_A are the ordinary and anomalous Hall coefficients, respectively. At normal temperature R_O is much higher than R_A . However, at lower temperature they are comparable[12]. Despite its century long history of research the microscopic origin of AHE is still a matter of debate. Primarily three mechanisms can be identified as contributing factors to AHE namely, intrinsic effect, skew scattering and side jump mechanism. The last two effects fall in the extrinsic category which is related to spin asymmetric scattering in presence of impurity. These two effects will be discussed later in further detail. The intrinsic effect can be observed in a pure system with no impurity scattering involved. Rather, it can be described in terms of k-space (momentum-space) Berry phase of occupied Bloch states. Recently, Yao *et al.*[13] proposed a scheme for the calculation of Anomalous Hall conductivity in terms of Berry phase. If we consider a cubic magnetic material with magnetization along z-direction, the nonzero component of Berry curvature along that direction can be expressed in the form as equation 2.15 which comes from Kubo formula derivation

$$\Omega_n^z(\mathbf{k}) = \sum_{n' \neq n} \frac{2\hbar \text{Im} \langle \psi_{nk} | v_x | \psi_{n'k} \rangle \langle \psi_{n'k} | v_y | \psi_{nk} \rangle}{(E_{n'} - E_n)^2} \quad (2.15),$$

where $|\psi_{nk}\rangle$ and E_n are the eigen states and eigen values of Bloch Hamiltonian respectively and v is velocity operator. The sum of Berry curvature over occupied bands are

$$\Omega^z(\mathbf{k}) = \sum_n f(n)\Omega_n^z(\mathbf{k}) \quad (2.16).$$

Here, $f(n)$ denotes the equilibrium Fermi-Dirac distribution function. The integration of equation 2.16 over Brillouin zone (BZ) gives us the AHC as shown in equation 2.17.

$$\sigma_{xy} = -\frac{e^2}{\hbar} \int_{BZ} \frac{d^3\mathbf{k}}{(2\pi)^3} \Omega^z(\mathbf{k}) \quad (2.17)$$

In this context it is worth to discuss the quantum Hall effect (QHE)[14] which is considered as a quantized version of the intrinsic AHE. QHE was discovered by Klitzing *et al.*[15] in the year of 1980. They found that in a two dimensional electron gas Hall conductivity is quantized in the units of e^2/h .

$$\sigma = n \frac{e^2}{h} \quad (2.18)$$

Here, n is known as filling factor which can take either integer or fractional values. Thus QHE can be classified in two parts namely integer QHE and fractional QHE[16-18] depending on the value of n . The first one is the usual case which can be understood in terms of Landau quantization. The latter one is more complicated which relies on the collective behavior of 2D electron gas. Robert Laughlin, Horst Störmer and Daniel Tsui were awarded Nobel prize in physics in the year of 1998 for this discovery[19].

2.6.3. Spin Hall Effect

The Spin Hall effect was first predicted by Dyakonov and Perel in 1971[20]. It was experimentally observed much later in 2004-05 in semiconductors[21-22]. This eventually opens new possibilities for spintronic based devices as a replacement to our present electronic technology triggering a lot of research interest and industrial drive.

The spin Hall Effect can be described as the scattering of electron with opposite spin polarity in the two lateral boundaries of a nonmagnetic metallic wire (like Pt, Ta) due to the application of a charge current along the length. Figure 2.3 schematically illustrates the effect in case of a rectangular and cylindrical wire. For a rectangular wire opposite spins are accumulated in the opposite boundaries perpendicular to the current while in case of a cylinder spins wind around the surface. The strength of spin accumulation is proportional to the applied current

and the polarity of spin accumulation changes sign while the direction of current is reversed. The heavy metal itself determines the polarity and strength of spin accumulation denoted by spin Hall angle (θ_{SH}) which is usually intrinsic to the material. For example, in case of Pt and Ta spin accumulation is opposite. Hence the polarity of θ_{SH} is different. Here accumulation of opposite spins, transverse to charge current, gives rise to spin current which is somewhat similar to ordinary Hall effect where separation of charge gives rise to a transverse charge current. The reciprocal phenomenon is also allowed in nature where spin current gives rise to a transverse charge current called inverse spin Hall effect. The mechanism is similar to the spin Hall effect. In figure 2.4 the spin Hall effect geometry is compared with other Hall geometries. Here we notice a major difference that spin Hall effect does not involve any external magnetic field or magnetization as opposed to other Hall effects.

The physical origin of this effect[23] lies in the coupling of the charge and spin currents due to spin-orbit interaction. Impurity induced spin asymmetric scattering causes spin Hall effect which can be explained by two different mechanisms known as skew scattering and side jump discussed below.

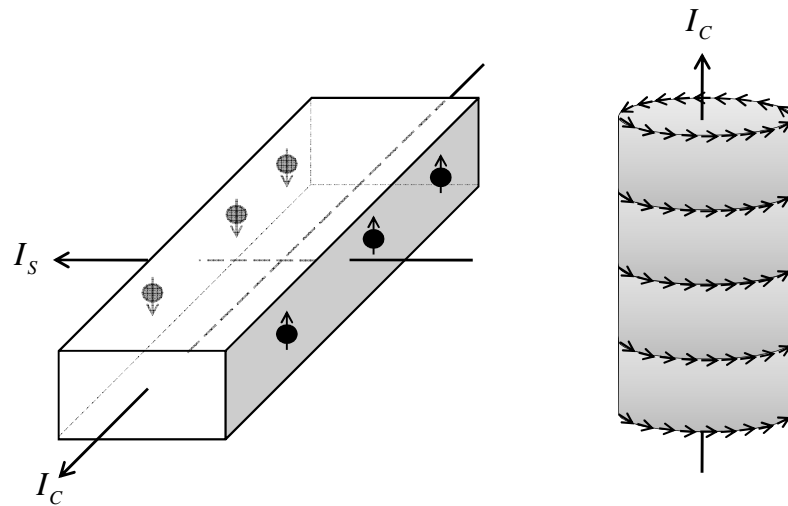


Figure 2.3. Schematic diagram of spin Hall effect.

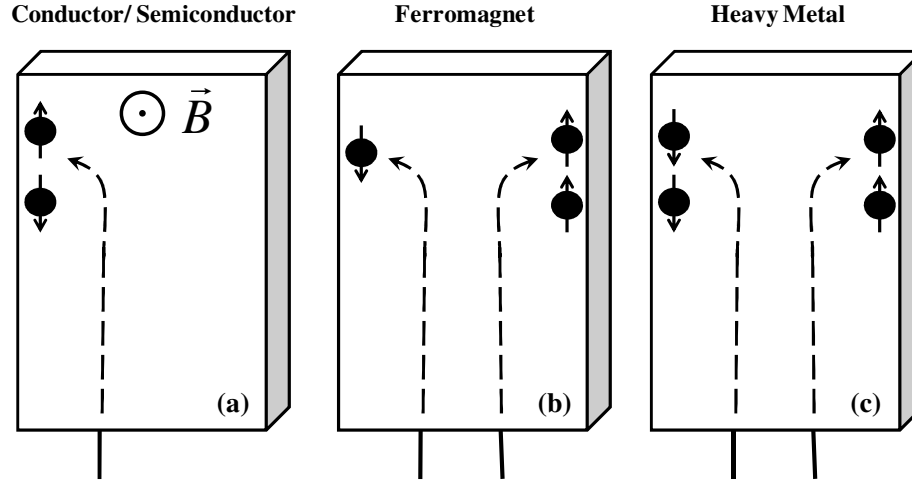


Figure 2.4. Hall geometries; (a) ordinary Hall effect, (b) anomalous Hall effect and (c) spin Hall effect.

2.6.4. Skew Scattering

The concept of skew scattering was proposed by N. F. Mott in the year of 1929 which suggests that polarized electrons are asymmetrically scattered due to spin orbit interaction[24-25]. Itinerant electrons with opposite spin polarity deflect in opposite directions while approaching a local impurity present in the propagation medium. Let us consider the interaction of electrons with such an impurity having negative electric charge as shown by the schematic in figure 2.5. When an electron passes through the electric field (induced by the impurity), a magnetic field $\vec{B} \sim \vec{v} \times \vec{E}$ is experienced by spin in the moving frame of electron. From figure 2.5 one can easily make the following observations that \vec{B} acts perpendicular to the plane of scattering and the sign is opposite for electrons passing from the left and right side of the impurity. The \vec{B} field is inhomogeneous over space due to the non uniformity of \vec{E} field as well as the space dependent \vec{v} in the electron trajectory. Hence, electron experience a force of deflection due to Zeeman effect given by $\hbar\mu_B / \nabla \cdot (\vec{B} \cdot \vec{\sigma})$ which depends on the polarity of spin. This is known as Mott effect or skew scattering effect.

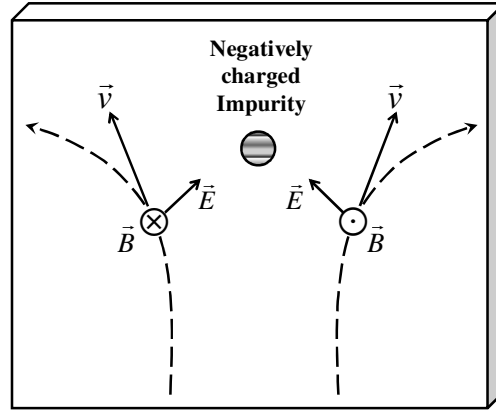


Figure 2.5. Skew scattering effect.

2.6.5. Side Jump

In quantum mechanical formalism free electrons are considered as wave packets travelling with an average constant velocity along a straight line. Now, let us consider the case of scattering of electron by a central potential at time $t=0$. From the principle of quantum mechanics one can argue that at a finite time t ($t \gg 0$) after scattering the trajectory will again be a straight line. When spin-orbit interaction plays a role in the system, the symmetry of the problem is low. It suggests that there is no reason why the linear trajectories of electron before and after collision should coincide. Hence, two possibilities come into the picture. Either the two straight lines will make an angle θ with each other or they make a lateral shift Δy parallel to each other. The second one is known as side jump mechanism.

Side jump is believed to be a purely quantum mechanical process where its physical significance is debated over a long time. When a plane wave is scattered by an impurity in presence spin orbit interaction, a spherical wave is generated with its centre shifted laterally with respect to propagation. An anomalous velocity of electron occurs which depends on the polarity of spin. Starting from Pauli Hamiltonian (H) with consideration of spin-orbit (SO) interaction one can obtain the anomalous velocity as

$$\begin{aligned}
 H &= p^2 / 2m + eV + V_{so}, [V_{so} = \frac{\hbar}{4m^2 c^2} (\vec{\sigma} \times \vec{\nabla} V) \cdot \vec{p}] \\
 \Rightarrow \vec{v} &= \frac{\partial H}{\partial \vec{p}} = \frac{\vec{p}}{m} - \frac{e\hbar}{4m^2 c^2} (\vec{\sigma} \times \vec{E})
 \end{aligned} \tag{2.19},$$

where, $\vec{\sigma}$ is the spin polarity and \vec{E} is the electric field corresponding to the potential V .

2.7. Spin Pumping

Spin current can exert spin transfer torque on magnetization vector resulting in a switching or modification of magnetization dynamics in a ferromagnetic material. The reverse process is also allowed in nature where precessing magnetization gives rise to spin current transported into an adjacent normal metal at the cost of its own angular momentum. As a result the amplitude of precession suffers a faster decay leading to an enhancement of damping. The magnetization precession can be described by the Landau-Lifshitz-Gilbert (LLG) equation as shown in equation 2.20.

$$\frac{d\hat{m}}{dt} = -\gamma\hat{m} \times [H_{eff} + \frac{\lambda}{(\gamma m)^2} \frac{d\hat{m}}{dt}] \quad (2.20)$$

Here, \hat{m} is the magnetization, γ is the gyromagnetic ratio, H_{eff} is the effective magnetic field and $\alpha = \lambda/\gamma m$ is the Gilbert damping coefficient. We will have a detailed discussion about the origin of this in section 2.19. The first term of the right hand side of this equation represents the torque responsible for the precession of magnetization which is physically related to the volume injection of spin current. When the spin current is allowed to leak through an adjacent nonmagnetic material damping increases. In other words an external excitation induces magnetization precession due to which angular momentum is transferred from ferromagnetic to the nonmagnetic layer in form of spin current which is analogous to a physical pumping mechanism, hence known as spin pumping effect. Spin pumping and a consequent enhancement of damping can be described analytically in terms of scattering matrix at Fermi energy of the ferromagnetic thin film in contact with normal metal reservoir suggested by Berger[26] [78] and Tserkovnyak *et al.* [27]. The effect is analogous to the parametric pumping of charge current in mesoscopic systems[28] which is governed by periodically varying two independent parameters of a system. The enhancement of damping also depends on the type of normal material used. For instance, Pt acts as a better spin sink than Cu resulting in a larger enhancement of Gilbert damping[29]. The spin absorption efficiency can be estimated by the inverse of spin flip relaxation time (τ_{sf}) which is again proportional to Z^4 , where Z is the atomic number. Hence, a stronger spin pumping is expected in presence a of heavy metal layer adjacent to the ferromagnet. Tserkovnyak et al. theoretically calculated spin pumping and explained the behavior of damping using time dependent scattering theory in case of ferromagnetic sandwich structures (N/F/N; N=nonmagnet, F=ferromagnet) as experimentally ob-

tained from FMR line width by Mizukami *et al.*[30] The spin current can be expressed in the form of equation 2.21.

$$I_S^{Pump} = \frac{\hbar}{4\pi} (A_r m \times \frac{dm}{dt} - A_i \frac{dm}{dt}) \text{ where, } A_r = 1/2 \sum_{mn} \{ |r_{mn}^\uparrow - r_{mn}^\downarrow|^2 + |t_{mn}^\uparrow - t_{mn}^\downarrow|^2 \}$$

$$\text{and } A_i = \text{Im} \sum_{mn} \{ r_{mn}^\uparrow (r_{mn}^\downarrow)^* + t_{mn}^\uparrow (t_{mn}^\downarrow)^* \} \quad (2.21)$$

Here, r_{mn}^\uparrow , r_{mn}^\downarrow are the reflection coefficients and t_{mn}^\uparrow , t_{mn}^\downarrow are the transmission coefficients for spin up and spin down electrons. Considering the conservation of angular momentum in case of spin pumping the magnetization dynamics can be represented by the LLG equation (Equation 2.20) where α and γ are modified as

$$\alpha = \frac{\gamma}{\gamma_0} [\alpha_0 + g(A_i^C + A_i^S) / 4\pi M] \text{ and } \frac{1}{\gamma} = \frac{1}{\gamma_0} [1 + g(A_i^C + A_i^S) / 4\pi M] \quad (2.22),$$

where γ is the gyromagnetic ratio, M is the total magnetic moment, the superscripts C and S indicate the capping and seed normal metal layer and the subscript 0 denotes the bulk value. Now let us consider density of states of conduction electrons in a ferromagnet during spin pumping (see figure 2.6). Initially the bands corresponding to spin up and spin down electrons (red and blue) are filled up to Fermi level with relative shift equal to exchange energy (figure 2.6 left). A change in magnetization orientation causes a further shift in the energy level by allowing electrons above Fermi energy which will relax via spin flip process to fill the lower energy spin band. An additional relaxation process takes place in presence of an adjacent nonmagnetic layer via spin pumping followed by a spin flip in the nonmagnetic layer (figure 2.6 middle) until the equilibrium is achieved (figure 2.6 right).

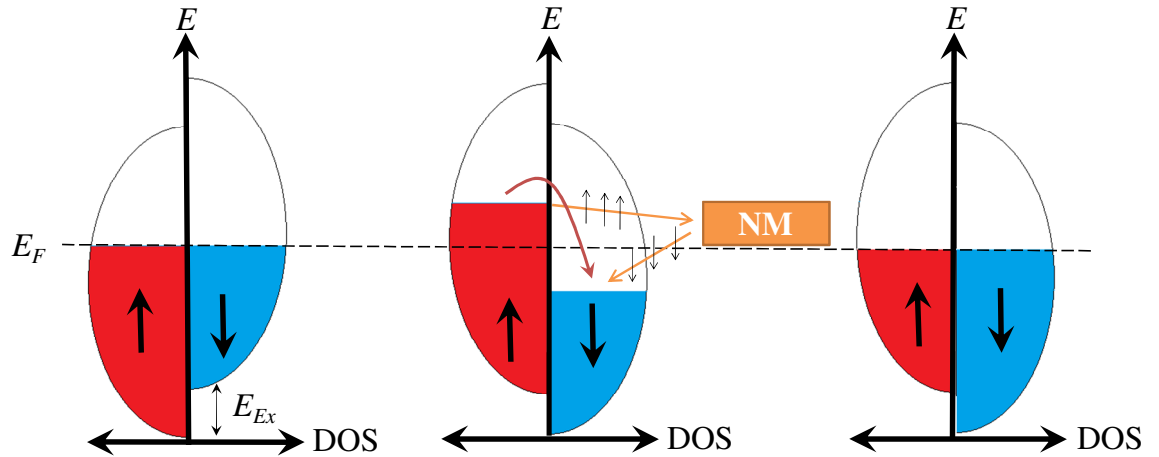


Figure 2.6. Schematic illustration of spin pumping using density of states.

2.8. Anisotropic Magnetoresistance

Anisotropic magnetoresistance[31] (AMR) is one of the most fundamental phenomena which relates electricity with magnetism and forms the basis of spintronics. The fact that electrical resistivity (ρ) of a magnetic system depends on the relative angle (θ) between applied charge current and magnetization direction is known as anisotropic magnetoresistance. The strength of this effect is determined by the AMR ratio defined as follows.

$$\frac{\Delta\rho}{\rho_{\perp}} = \frac{\rho_{\parallel} - \rho_{\perp}}{\rho_{\perp}} \quad (2.23)$$

In this equation ρ_{\parallel} and ρ_{\perp} are the resistivity with current parallel and perpendicular to the magnetization, respectively. Let us consider a rectangular strip of polycrystalline ferromagnetic material where current is applied along the length. In such case ρ can be expressed in terms of θ as shown in equation 2.24 considering resistivity as a rank two tensor[32].

$$\rho(\theta) = \rho_{\perp} + \Delta\rho \cos^2 \theta \quad (2.24)$$

Here, $\Delta\rho$ denotes the differential resistivity for longitudinal and transverse magnetization orientation. It has also been observed that the effect has a significant dependence on layer thickness. A rapid decrease of the AMR ratio is observed when the thickness is reduced below 6 nm. This effect can be attributed to the enhancement of the resistivity at lower thickness while $\Delta\rho$ remains constant. However, recently a reduction of $\Delta\rho$ with decreasing thickness is also observed contributing to this effect[33]. The AMR effect is originated from s - d scattering of the ferromagnetic electron and influenced by the spin density of states at Fermi energy. The AMR can take both positive and negative values[34]. Strong ferromagnets like face centred cubic (FCC) Fe, Co with mostly filled d -bands shows positive AMR whereas half metallic ferromagnets having significant DOS at one spin state and zero DOS at other shows negative AMR. In case of Fe_3O_4 of the half metallic ferromagnets, the sign of AMR switches from negative to positive with increasing temperature.

A theoretical description for the explanation of AMR deals with the s - d interaction where the scattering of conduction band electrons into localized d states by impurities are considered.

The d bands are spin mixed due to the spin orbit interaction given by $\lambda \vec{L} \cdot \vec{S}$ where λ , L and S are the spin orbit coupling constant, and orbital and spin angular momentum, respectively. Under this framework Campbell–Fert and Jaoul derived an expression for AMR ratio for strong ferromagnets shown in equation 2.25 known as CFJ model[34-35].

$$\frac{\Delta\rho}{\rho} = \frac{3}{4} \left(\frac{\lambda}{H_{Ex}} \right)^2 \left(\frac{\rho_{s \rightarrow d \downarrow}}{\rho_{s \uparrow}} - 1 \right) \quad (2.25)$$

In this equation H_{Ex} is the exchange field, $\rho_{s\sigma}$ denotes the resistivity of the conduction electron with spin polarity σ while $\rho_{s \rightarrow d \sigma'}$ takes care of the s - d scattering effect where conduction s electrons are scattered by the impurities into the d states of σ' spin. The scattering processes considered in the CFJ model are $s \uparrow \rightarrow s \uparrow$, $s \uparrow \rightarrow d \downarrow$ and $s \downarrow \rightarrow d \downarrow$. Later Malozemoff generalized the model by incorporating other scattering processes and found the expression for AMR applicable for both strong as well as weak ferromagnet as given by the following expression[34,36].

$$\frac{\Delta\rho}{\rho} = \frac{\gamma(\rho_{s \rightarrow d \downarrow} - \rho_{s \rightarrow d \uparrow})^2}{(\rho_s + \rho_{s \rightarrow d \uparrow})(\rho_s + \rho_{s \rightarrow d \downarrow})} \quad (2.26)$$

2.9. Giant Magnetoresistance

The giant magnetoresistance (GMR) is one of the most remarkable inventions of the last century which offers a huge scope of application in magnetic data storage and sensor devices. Now a days the data storage industry focus towards increasing the storage capacity by writing each data bit in a smaller region of a magnetic disc. As a consequence the magnetic signal corresponding to a data bit becomes weaker. GMR device can sense very small change of magnetic flux that is why it can be used in present hard drives. It can be used as sensors for example, machine speed controller, motion and position tracker, automotive engine control, proximity sensor and tag reader. The GMR is also a potential candidate for the replacement of semiconductor random access memory (RAM) by magnetoresistive random access memory (MRAM) which is not affected by power disruption.

In the year of 1988-89, the team of professor Fert[37] and of Grunberg[38] first experimentally observed giant magnetoresistance (GMR) effect in Fe/Cr superlattices. The two adjacent ferromagnetic layers of the system separated by a nonmagnetic spacer are usually antiferromagnetically coupled to each other by an indirect exchange interaction. In presence of an external magnetic field the moments of the magnetic layers align themselves in the same direction resulting in a significant drop in the electrical resistance of the system. The word “giant” here signifies that the percentage change in resistance with respect to bias field is much larger as compared to other magnetoresistance effects like AMR. As for instance around 50% change in the GMR value is observed for the above system while the AMR for Fe is only a few percent. Figure 2.7 shows the magnetoresistance curves for the Fe/Cr superlattice at 4.2 K with current and field applied in the same direction in the plane of the sample. Here we observe that the resistivity drops with applied field and stabilizes after a certain field called saturation field, H_s . In this context it is important to discuss two fundamental and interrelated concepts of spintronics on which GMR stands. One is spin dependent scattering and the other is two current model.

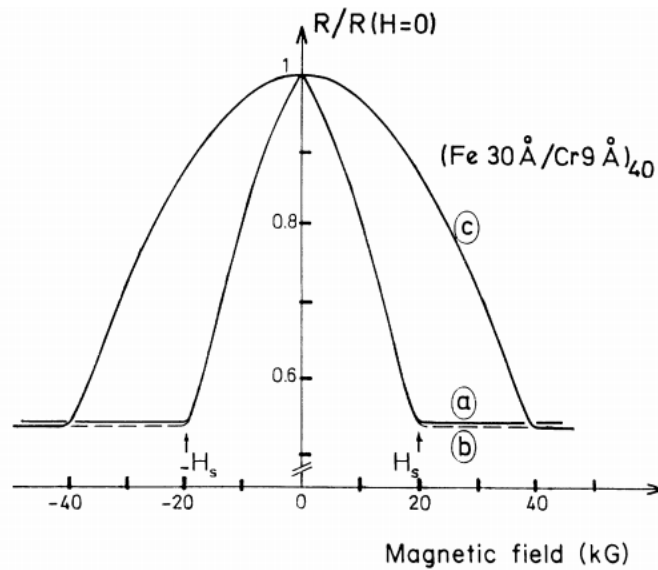


Figure 2.7. Variation of resistance with magnetic field in Fe/Cr superlattice (reference 37).

2.9.1. Two Current Model

The two current model was proposed in the year of 1936 by N. F. Mott where a sudden drop in the resistivity of ferromagnetic metal below Curie temperature in presence of a magnetic

field was explained[39]. In this model conduction electrons spins are considered parallel and antiparallel to the magnetization and the probability of spin flip process during scattering is considered to be negligible. Below Curie temperature when the ferromagnet attains saturation magnetization the unoccupied shells (or holes) in the d band align themselves antiparallel to the magnetization. In that case only half of the conduction electrons are allowed to make transition to the d band. On the other hand, above Curie temperature d band transition for all conduction electrons is possible as the unoccupied states in the d band have both the spin states. As conduction electron population determines the conductivity, the model explains a decrease in resistance in presence of magnetization. Later in 1968 A. Fert and I. A. Campbell experimentally observed two current conduction in dilute nickel based alloy at low temperature[40]. They found that spin up and spin down electrons carry current in parallel with different resistivity giving rise to an effective resistivity of the system. The model considers different relaxation times for opposite spin states as τ_{\uparrow} and τ_{\downarrow} . It also incorporates spin flip and electron scattering processes by another relaxation time as $\tau_{\uparrow\downarrow}$. The Boltzman equation for the two spin channel is solved for a coupled system from which the expression for the effective resistivity can be obtained as shown in equation 2.27.

$$\rho_{eff} = \frac{\rho_{\uparrow}\rho_{\downarrow} + \rho_{\uparrow\downarrow}(\rho_{\uparrow} + \rho_{\downarrow})}{\rho_{\uparrow} + \rho_{\downarrow} + 4\rho_{\uparrow\downarrow}} \quad (2.27)$$

Here, $\rho_{\zeta} = m / ne^2 \tau_{\zeta}$ ($\zeta \Rightarrow \uparrow, \downarrow, \uparrow\downarrow$) with m , e , n being the mass, charge and number of electrons.

2.9.2. Spin Dependent Scattering

It is observed that in some specific systems itinerant electrons with a certain polarity of spin scatter more strongly than the other. This phenomenon is known as spin dependent scattering[41-44]. From the first principle analysis of electronic structures it can be understood that the primary contribution to spin dependent scattering comes from the uniformity of spin dependent atomic potential in a magnetic alloy or multilayered system. The matching of a spin channel lowers the density of states at Fermi energy. Korringa-Kohn-Rostoker coherent potential approximation technique provides us first-principles electronic structure calculations for a random disordered alloy which basically introduces an effective periodicity replac-

ing the random disorder. The scheme enables us to calculate cohesive energy, ground state properties and conductivity of the system[45-46]. A more recent modification to this theory allows us to calculate the conductivity of a layered structure with varying composition[47]. Now let us consider a trilayer system with NM layer sandwiched between two FM layers as shown in figure 2.8[48]. In the first case Cu is sandwiched between Co (figure 2.8(a)) and in the second case Cr is embedded in between two Fe layers (figure 2.8(b)). In both the cases strong GMR can be observed. The graphs describe the variation number of up and down spin electrons per atom with layer numbers. Note in this study magnetization in the adjacent FM layer is considered to be parallel. A discontinuity or irregularity in the number of electrons in a specific spin channel can be considered as atomic potential or defects in the system. To an itinerant electron such discontinuity appears as a barrier due to which it encounters scattering at the interfaces leading to a loss of velocity and a consequent increase in the effective resistivity. In Co/Cu/Co an up spin electron does not experience a significant change in the number of electrons per atom across the interface. In other words, the matching in the majority spin channel makes lattice potential smooth due to which an up spin electron faces minimum resistance while passing through the system. On the contrary, down spin electron faces a large difference in potential between Co and Cu. Hence it is more likely to scatter in both the interfaces. Thus the resistance in the minority spin channel is large. Conversely in Fe/Cr/Fe system scattering occurs in the up spin channel causing larger resistance while the down spin channel is short circuited (see schematic diagrams of figure 2.8).

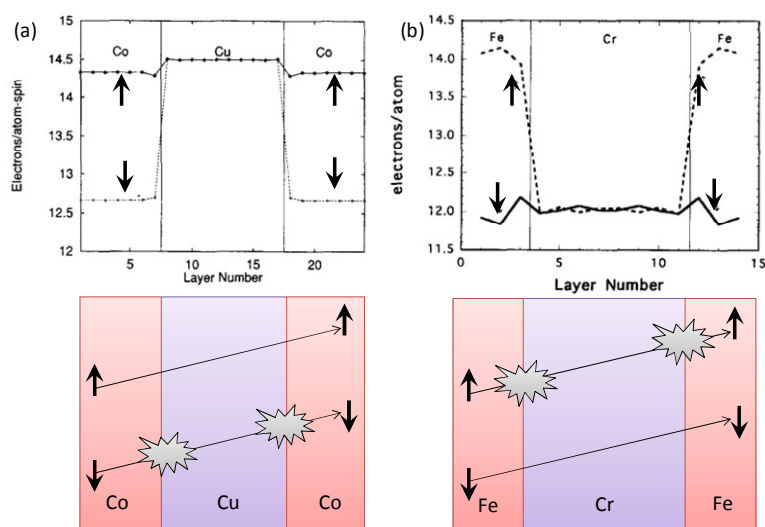


Figure 2.8. Variation of the number of up and down spin electrons per atom with layer numbers for (a) Co/Cu/Co and (b) Fe/Cr/Fe structures along with schematic illustrations of scattering mechanism.

2.9.3. How GMR Works

Let us now go back to the discussion of GMR and consider the case of Co/Cu/Co trilayer system. In absence of a magnetic field the two adjacent Co layers are antiferromagnetically coupled as shown in figure 2.9(a). In case of an up spin electron the resistance in the first interface is negligible while it is large in the second interface. For a down spin electron the case is the opposite i.e., high resistance in the first and negligible resistance in the second interface. Hence, in this configuration the current is almost equally distributed between two spin channels. Now when an external magnetic field is applied the magnetization in the Co layers becomes parallel (see figure 2.9(b)). Hence, the up spin channel acts as electrically short due to small resistance in both the interfaces while the down spin channel becomes highly resistive resulting in a large decrease in the effective resistance. An example of such decrease in magnetoresistance with external field curve is shown in figure 2.7 as obtained by Baibich *et al.*[37] in case of Fe/Co superlattices at 4.2 K. Here H_s denotes the field value above which the minimum resistance can be achieved. The GMR can be increased by increasing the number of repeats. It is weaker when the nonmagnetic layer is thicker or the temperature is higher because in both the cases the probability of spin flip scattering increases in the nonmagnetic layer resulting in a mixing in the spin channels.

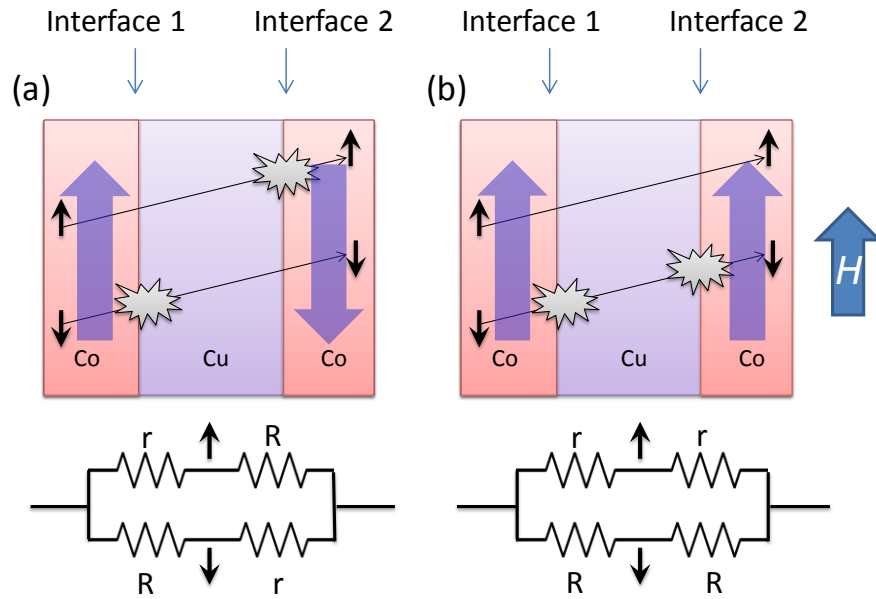


Figure 2.9. Schematic illustration of GMR by using equivalent circuit.

2.10. Tunneling Magnetoresistance

The remarkable success and application possibilities of GMR fuels up the interest in spin dependent transport phenomena in magnetic tunnel junctions[49] (MTJ). The magnetoresistance effect similar to GMR can be observed in MTJ known as tunneling magnetoresistance (TMR). The structure of a MTJ consists of two ferromagnetic layers separated by an insulating barrier. Specifically, the insulating layer has to be very thin which can be a few atomic layers in thickness to allow a significant tunneling conductivity between the ferromagnetic layers. The TMR can be explained as a change of electrical resistance perpendicular to the film plane depending on the relative configuration of the magnetizations of the adjacent ferromagnetic layers. For parallel configuration the possibility of electron tunneling through the insulating barrier becomes larger, resulting in a large tunneling current. Conversely tunneling current is less of antiparallel configuration.

The TMR is purely a quantum mechanical process which cannot be explained classically because tunneling of electron through an insulating potential barrier is not allowed in classical picture. In the year of 1975 a theoretical model was proposed by Julliere to explain TMR in terms of spin polarization ratio of ferromagnetic electrons (P) calculated from spin dependent density of states (D) at Fermi energy (E_F) as shown in equation 2.28[50].

$$P = \frac{D_{\uparrow}(E_F) - D_{\downarrow}(E_F)}{D_{\uparrow}(E_F) + D_{\downarrow}(E_F)} \quad (2.28)$$

Here the subscript \uparrow or \downarrow denotes spins parallel or antiparallel to the magnetization. Now P_1 and P_2 being the polarization ratio for the two adjacent ferromagnetic layers the TMR is given by

$$\text{TMR} = \frac{R_{AP} - R_P}{R_P} = \frac{P_1 P_2}{1 - P_1 P_2} \quad (2.29),$$

where R_P and R_{AP} are the electrical resistances in parallel and anti-parallel configuration of the ferromagnets. The equation shows that for spin polarization close to 1 the TMR ratio becomes very high which can act as a switch having very small or large resistance depending on the moments. In Fe/MgO/Fe (001) system experimentally observed TMR[51-53] is obtained of the order of 300% whereas theoretical prediction shows more than 1000% of TMR can be achieved in similar systems[54-55]. The TMR is a promising candidate for application in magneto-resistive devices like MRAM[53,56-59] and hard disc read head [60-65].

2.11. Magnetization

So far we have discussed how electron and spin can control different spintronic phenomena. The underlying physics of magnetism also stems from the evolution of electron round the atomic nucleus and also spin of an electron about its own axis. The unpaired electrons in an atom are associated with an intrinsic dipole moment. Considering the orbital motion of an electron as a current loop the moment can be defined as $\mu_l = I.A$ where $I = \frac{e}{2\pi / \omega}$ and

$A = \pi r^2$ are the current and area of the orbit. Now, using the ground state of orbital angular momentum as $|\vec{l}| = m\omega r^2 = \hbar$ in the above expression we get $\mu_l = e\hbar / 2m$ which is called Bohr magneton (μ_B). In absence of an external bias field the moments are randomly oriented due to thermal fluctuation. As a result there is no net magnetic moment or magnetization in the system. Now with an applied magnetic field the dipoles tend to orient themselves along the bias field direction resulting in a net magnetic moment in the system. The phenomenon is known as magnetization. The magnetization \vec{M} is vector quantity which is defined as a den-

sity of magnetic dipole moment at a point volume. Mathematically this is expressed as follows.

$$\vec{M} = \lim_{\Delta V \rightarrow 0} \frac{1}{\Delta V} \sum_{i=1}^N \vec{m}_i \quad (2.30)$$

Here, N is the total number of dipoles present in a small volume ΔV and \vec{m}_i indicate the moment corresponding to the i^{th} dipole.

2.12. Maxwell's Equations

The concept of electromagnetism stands on four famous equations known as Maxwell's equations given below.

$$\begin{aligned} \nabla \cdot \vec{D} &= \rho & \nabla \times \vec{E} &= -\frac{\partial \vec{B}}{\partial t} \\ \nabla \cdot \vec{B} &= 0 & \nabla \times \vec{H} &= \vec{J} + \frac{\partial \vec{D}}{\partial t} \end{aligned} \quad (2.31)$$

Here, \vec{D} , \vec{B} , ρ , \vec{E} , \vec{H} and \vec{J} denote Electric displacement vector, Magnetic induction, charge density, Electric field, magnetic field and charge current density, respectively. The general concept of magnetism can be obtained from the electromagnetic theory by considering the process to be quasistatic with no electric field and current involved. Hence, this is specialized case where the following conditions are applicable on the Maxwell's equation to describe magnetism as shown by the expressions below

$$\frac{\partial}{\partial t} \rightarrow 0, \vec{J} \rightarrow 0 \text{ and } \vec{E} \rightarrow 0 \quad (2.32).$$

Thus the new set of Maxwell's equation is obtained as follows.

$$\nabla \cdot \vec{B} = 0 \text{ and } \nabla \times \vec{H} = 0 \quad (2.33)$$

2.13. Classification of Magnetic Materials

Let us consider magnetic induction \vec{B} which can be expressed as

$$\vec{B} = \mu_0(\vec{H} + \vec{M}) \quad (2.34).$$

The magnetization \vec{M} and magnetic field \vec{H} are closely related to each other. However, the relationship is material dependent. In most of the cases \vec{M} is proportional to \vec{H} up to a certain value. Such a class of material is called linear material which can be expressed as follows.

$$\vec{M} = \chi\vec{H} \quad (2.35)$$

Here χ is a dimensionless scalar quantity known as magnetic susceptibility. As a result a linear relationship between \vec{B} and \vec{H} can be obtained as equation 2.36 by substituting equation 2.35 into 2.34

$$\vec{B} = \mu_0(1 + \chi)\vec{H} = \mu\vec{H} \quad (2.36),$$

where $\mu = \mu_0(1 + \chi)$ is the permittivity of the material. The linear magnetic materials can be divided in two categories one with $\chi < 0$ and the other with $\chi > 0$. The former is known as diamagnetic whereas the latter is called paramagnetic material. The diamagnetic material is weakly repelled by the external field and the paramagnets are weakly attracted by the field. In the following table we have some examples of diamagnetic and paramagnetic materials along with their susceptibilities relevant to this thesis.

Paramagnetic		Diamagnetic	
Material	χ	Material	χ
Ta	1.78×10^{-2}	Au	3.5×10^{-5}
Pt	2.9×10^{-4}	Si	4.2×10^{-6}
Cr	2.7×10^{-4}	Cu	9.8×10^{-6}

There is another set of materials where a nonlinear response of M with H is observed. In other words χ or μ is no more a constant rather a function of H . In such materials a larger positive value of χ can be obtained due to its strong response with external field. Such a class of materials is called ferromagnet. Examples of such element and alloys as studied in this thesis are Co, CoFe, CoFeB and NiFe. They have different magnetic properties and can show interesting phenomena in combination with diamagnetic and paramagnetic systems.

2.13.1. Langevin Theory of Diamagnetism

The Langevin theory of diamagnetism is based on the electronic motion around the nucleus. Let us consider an electron of charge $-e$ and mass m with precession radius r . Thus the magnetic moment developed is $\vec{m} = \frac{e\omega}{2} r^2$.

$$\vec{m} = \text{Current} \cdot \text{Area} = -\frac{e\omega}{2\pi} \pi r^2 = -\frac{e\omega}{2} r^2 \quad (2.37)$$

The centripetal force acting on electron is given by $m\omega^2 r$. In presence of a magnetic field there will be an additional force $\vec{F}_L = e(\vec{v} \times \vec{B})$ known as Lorentz force due to which the angular frequency changes by $\Delta\omega$. Hence the force equation takes the form as shown in equation 2.38.

$$m(\omega + \Delta\omega)^2 r = m\omega^2 r + e\omega r B \quad (2.38)$$

From equation 2.38 we obtain $\Delta\omega = eB/2m = \gamma B$ (γ =gyromagnetic ratio) which is known as Larmour frequency. Hence a corresponding change in magnetic moment is observed. If there is Z atomic orbitals and n number of atoms per unit volume, then the total induced magnetization can be expressed as

$$\vec{M} = -nZe^2 \bar{r}^2 \vec{B} / 6m \quad (2.39),$$

where \bar{r}^2 is the mean square radius of the orbitals. So the diamagnetic susceptibility per unit volume is given by

$$\chi = \vec{M} / \vec{H} = -\mu_0 n Z e^2 \bar{r}^2 / 6m \quad (2.40).$$

It is important to note that expression of χ in case of a diamagnetic material is negative and independent of temperature and applied field.

2.13.2. Langevin Theory of Paramagnetism

In this theory a molecular gas is considered having n atoms per unit volume. The total potential energy of a dipole in presence of a field can be expressed as $U = -\vec{m} \cdot \vec{B}$. According to the Boltzman distribution the number of dipoles within the energy range between U and $U + \Delta U$ is given by

$$dn = C.e^{U/KT} dU = C.e^{mB\cos\theta/KT} mB\sin\theta d\theta \quad (2.41).$$

Here θ is the angle between moment and magnetization, C is a constant to be determined and K is the Boltzman constant. The value of C is obtained by integrating the equation 2.41 over all θ and we get

$$dn = \frac{n.e^{mB\cos\theta/KT} \sin\theta d\theta}{\int_0^\pi e^{mB\cos\theta/KT} \sin\theta d\theta} \quad (2.42)$$

Hence, the dipole moment per unit volume will give the magnetization expressed as follows.

$$M = \int_0^\pi m \cos\theta dn \quad (2.43)$$

From equations 2.42 and 2.43 the expression of M is obtained as

$$M = nm(\coth\alpha - 1/\alpha) = M_s L(\alpha), \quad [\alpha = mB / KT] \quad (2.44),$$

where M_s is the saturation magnetization and $L(\alpha)$ is known the Langevin function. Now the $L(\alpha)$ can be approximated as $\alpha/3$ for small value of alpha. Thus we get the susceptibility as shown in equation 2.45.

$$\chi = M / H = m^2 n \mu_0 / 3KT \quad (2.45)$$

In this case the susceptibility is inversely proportional to the temperature which is known as Curie law.

2.13.3. Weiss Theory of Ferromagnetism

In ferromagnetic materials magnetic dipoles are connected to each other via a quantum mechanical interaction called exchange interaction. As a result a large group of neighboring dipoles are aligned parallel to each other and undergo coherent rotation during magnetization reversal. Thus they form a magnetic domain which can be considered as a single macrospin in magnetization calculation. The boundary of the domain is called domain wall. When the sample is not magnetized the domains are randomly oriented. Hence, the magnetic moments cancel each other resulting in zero net magnetic moment in the system. With the application of the external field domain wall is displaced or rotated through a quasistatic dynamical process called domain wall dynamics and we have a net moment along the applied field. The process is not fully reversible. Hence such a material shows magnetic hysteresis.

P. Weiss first proposed the theory of ferromagnetism which is basically an extension of Langevin theory of paramagnetism. Here, apart from external magnetic field molecular field due to the interaction of the neighboring dipoles is considered which is proportional to the magnetization. Hence, the effective magnetic field can be expressed by the equation below.

$$H_{eff} = \vec{H} + \gamma\vec{M} \quad (2.46)$$

Here, γ is the proportionality constant independent of temperature called Weiss constant. From Langevin theory (equation 2.44) we know $M / M_s = L(\alpha)$ where $\alpha = mB / KT$. Here, replacing B by $\mu_0 H_{eff}$ we get

$$M / M_s = L(\alpha'), \quad \alpha' = \frac{\mu_0 m}{KT} (H + \gamma M) \quad (2.47)$$

Now from the above equation we can see that at zero applied field we can have magnetization in a ferromagnetic sample called spontaneous magnetization. Hence, for $H = 0$, M / M_s can be obtained as

$$M / M_s = \alpha' T / 3\theta, \quad \theta = \mu_0 \gamma n m / 3K \quad (2.48)$$

So, magnetization at a particular temperature can be obtained by the general solution of equation 2.47 and 2.48. For $T < \theta$ finite solution of M can be obtained that means we are in the

ferromagnetic regime. Above Curie temperature no general solution can be obtained. It suggests that no spontaneous magnetization can be obtained in this region i.e., it acts like a paramagnet. In this region the susceptibility is proportional to $1/(T-\theta)$ which is known as Curie-Weiss law.

2.14. Origin of molecular field (The exchange interaction)

The molecular field introduced in Weiss theory is nothing but the exchange interaction which is a consequence of Coulomb interaction and Pauli exclusion principle. Heisenberg theorized the direct exchange interaction based on Heitler-London model for hydrogen molecule where overlap between two electronic wave functions is considered. The Pauli exclusion principle suggests that the resultant wavefunction must be antisymmetric. If we consider electron wavefunction having spatial and spin components as $\psi = \phi(r)\chi(s)$, the asymmetric part of the resultant wavefunction can be written in two ways.

$$\begin{aligned}\psi_a &= \phi_s(r_1, r_2)\chi_a(s_1, s_2) \\ \text{or, } \psi_a &= \phi_a(r_1, r_2)\chi_s(s_1, s_2)\end{aligned}\quad (2.49)$$

Here, the subscripts a and s correspond to asymmetric and symmetric wavefunction whereas the numbers corresponds to individual electrons. From this, one can obtain the singlet and triplet states, the energy corresponding to which can be obtained as follows.

$$E_{\text{Singlet}} \propto (K_{12} + J_{12}) \text{ and } E_{\text{Triplet}} \propto (K_{12} - J_{12}) \quad (2.50)$$

Here, K_{12} and J_{12} are the Coulomb interaction energy and exchange integral, respectively. Apart from direct exchange we can have indirect exchange interaction in rare earth ferromagnets and antiferromagnetic oxides called superexchange. In metals, conduction electrons can take part in such interaction known as RKKY interaction.

2.15. Antiferromagnetic and Ferrimagnetic Materials

In some special cases of magnetic materials the neighbouring spins are oriented antiparallel to each other due to the exchange interaction. In such cases, the exchange integral J_{12} takes a negative value. As a consequence we have a zero or negligible magnetization because a pair

of neighbouring magnetic moments cancel each other as illustrated in figure 2.10. For example, metals such as Cr and alloys like FeMn are known to have such antiferromagnetic behaviour.

Let us now consider two neighbouring moments of different magnitudes are oriented opposite to each other due to negative exchange interaction. In that case we have a partial cancellation of moments leading to a net magnetization along the larger moment. It is of course smaller than that of ferromagnetic material of similar type. Such a material is called ferrimagnetic material. This is possible when the sublattices consist of two different materials or different ions of a particular material.

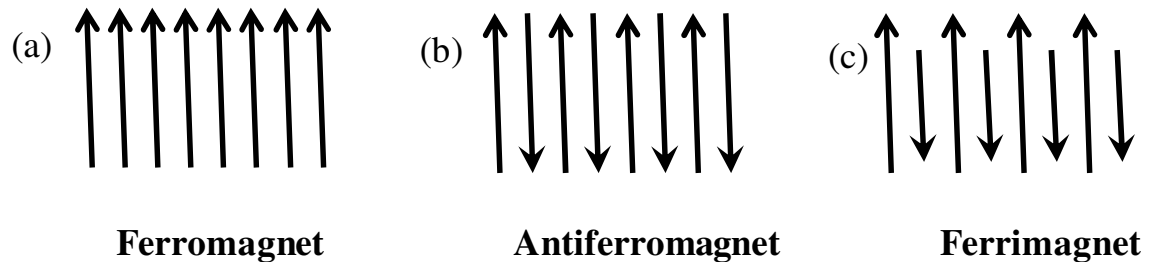


Figure 2.10. Illustration of magnetic configuration in ferromagnetic, antiferromagnetic and ferrimagnetic materials.

2.16. Fundamental Energies in Ferromagnetism

Ferromagnetism deals with four fundamental energies which basically governs the static and dynamical magnetic properties of a ferromagnetic system. In this section we discuss about the energy terms listed below

1. Zeeman energy: external field induced energy
2. Exchange energy: quantum mechanical interaction between dipoles
3. Anisotropy energy: originates from crystal anisotropy of a material
4. Demagnetizing energy: developed due to the changes of magnetization at the boundary.

2.16.1. Zeeman energy:

Let us consider a magnetic dipole in presence of an applied magnetic field H . The energy stored in the dipole is

$$\mathcal{E}^{Zee} = -\mu_0 m H \cos \theta \quad (2.51).$$

Here, m is the dipole moment and θ is the angle between the moment and the magnetic field. This energy is known as Zeeman energy. If there is n number of dipoles in volume V we have the total Zeeman energy as

$$E^{Zee} = -\mu_0 \sum_{i=1}^n \vec{m}_i \cdot \vec{H} \quad (2.52).$$

Generalizing the above equation under continuum approximation we have the general expression of Zeeman energy as follows.

$$E^{Zee} = -\mu_0 \int_V \vec{M} \cdot \vec{H} dV \quad (2.53)$$

2.16.2. Exchange Energy:

In the earlier section we have discussed the exchange interaction which can be described by the overlapping of two electronic wavefunctions. Here we present the exchange Hamiltonian for a system with spin S and uniform exchange constant as J .

$$H^{Ex} = -2J \sum_{i \neq j} \vec{S}_i \cdot \vec{S}_j \quad (2.54)$$

Under continuum approximation the Hamiltonian takes the form as follows:

$$E^{Ex} = A \int_V (\nabla \vec{m})^2 dV \quad (2.55)$$

Here m is a unitary vector along the moment. A is the exchange stiffness constant which is a material property and can be expressed as $A = 2JS^2 / a$ where a is the lattice constant of the material. We know that exchange interaction is a short range interaction. The length scale corresponding to the interaction is called exchange length which is related to the exchange stiffness constant by the expression below (SI)

$$l_{Ex} = \sqrt{\frac{2A}{\mu_0 M_s^2}} \quad (2.56),$$

where M_s is the saturation magnetization of the material. In the following table we calculate exchange length for some ferromagnetic materials discussed in this thesis.

Table 2.2. Calculation of exchange length.			
Material	A (J/m)	M_s (A/m)	l_{Ex} (nm)
Co	1.8×10^{-11}	1.4×10^6	3.8
NiFe	1×10^{-11}	8×10^5	5

2.16.3. Anisotropy Energy:

Magnetization of many crystalline materials are not isotropic i.e., they have a preferred orientation of magnetization. The energy associated to such anisotropic behaviour of a material is known as anisotropy energy. The preferential direction can be indicated by the anisotropy vector K which is called as easy axis. Conversely, the crystallographic axis along which it is very hard to orient the magnetization is called hard axis.

For a hexagonal crystal like Co the long axis is the easy axis. If magnetization makes an angle with the easy axis the energy can be expressed by equation 2.57 after ignoring higher orders of $\sin^2 \theta$.

$$E_K = \int_V (K \sin^2 \theta) dV \quad (2.57)$$

This is called uniaxial anisotropy energy.

For cubic structures like FCC (Ni) or BCC (Fe), the anisotropy energy is given by

$$E_K = \int_V (K_0 + K_1(\alpha_1^2 \alpha_2^2 + \alpha_2^2 \alpha_3^2 + \alpha_3^2 \alpha_1^2)) dV \quad (2.58),$$

where α represents the direction cosine of magnetization with respect to crystal axes. This is known as cubic anisotropy energy.

2.16.4. Demagnetizing Energy:

The distribution of magnetization gives rise to an intrinsic field inside the sample known as demagnetizing field H_d . The magnetization in presence of H_d gives rise to an energy similar to Zeeman energy as discussed in section 2.16.1. This is known as demagnetizing energy which can be expressed as follows.

$$E^d = -\frac{\mu_0}{2} \int_V \vec{M} \cdot \vec{H}_d dV \quad (2.59)$$

Here, the demagnetizing energy stems from the magnetization itself. Hence they are interrelated. To take care of this fact an additional factor $\frac{1}{2}$ comes in the energy term as compared Zeeman energy because in that case the external field is independent of magnetization.

2.17. Timescales of Magnetization Dynamics

The evolution of magnetization can occur at different timescales ranging from microseconds (μs) to femtoseconds (fs) which determines the speed of the magnetization dynamics. The processes with their characteristic times are schematically represented in figure 2.11. The slowest one is the domain wall dynamics which typically occurs between few nanoseconds (ns) to few μs . Precession of magnetization is a relatively faster process [66] occurring between 10-100 picoseconds (ps) before it gets damped in sub-ns to tens of ns resulting in a propagation of spin-waves in ferromagnetic material. The vortex core switching has its characteristic time of few tens of ps to several ns. Magnetization reversal dynamics which is commonly known for its application in magnetic recording covers the time scale of few ps to few hundreds of ps. Moreover, there are processes which are even faster than that, for example, fundamental exchange interaction (~ 10 fs), SO coupling and spin-transfer-torque (~ 10 fs – 1 ps) and laser induced ultrafast demagnetization (100s of fs). When a femtosecond laser pulse falls on a magnetized sample, an ultrafast demagnetization is observed [67]. The origin of this effect is still unclear and debated over a long time. However, it can be understood in terms of the excitation of Stoner pairs [68], SO coupling [69], coupling with the electromagnetic field via a terahertz emission [70], and scattering of spins with impurity centers or phonons [71]. The demagnetization is followed by a partial recovery of magnetization within 1-10 ps. This occurs due to the exchange of energy from hot electrons and spins to the lattice which can be phenomenologically described by a three temperature

model [67,72]. The faster recovery is followed by a slower recovery of magnetization due to the diffusion of electron and lattice energy to the environment [73-74].

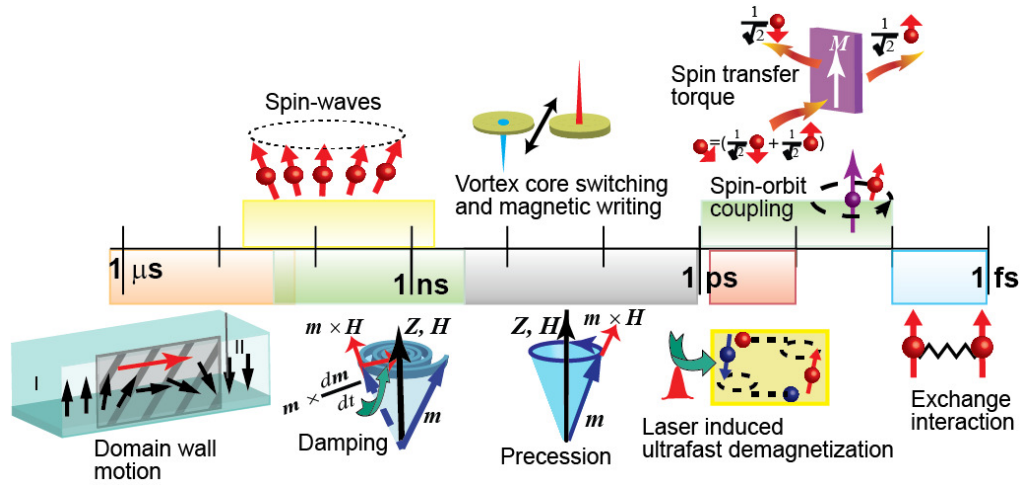


Figure 2.11. Magnetization dynamics of various timescales.

2.18. Ultrafast Demagnetization

The two colour pump-probe based technique using ultra short laser pulses has opened the territory of the magnetization dynamics to the experimentalist in femtosecond time scale. As a most remarkable consequence the ultrafast demagnetization was first observed in 1996 [67] in Ni films which fuels up a huge research interest due to its applicability in high speed recording devices. At the same time it resulted in new challenges like modeling the magnetization dynamics in an extremely non-equilibrium regime and controlling the material properties in similar timescale. Although various theories have been proposed the topic remains highly debated over the years. Here we discuss some of the models which best explain this phenomenon.

2.18.1. The Three Temperature Model

In the year of 1974 S. I. Anisimov *et al.* [75] investigated electron-lattice relaxation kinetics due to ultrashort laser excitation in metal by considering transfer of electron energy to the lattice and subsequent change in temperature corresponding to lattice and electron gas known as two temperature model. The three temperature model is basically one step extension to that where the thermodynamics of spin has been considered. The first experimental observation of

the ultrafast demagnetization in Ni under the excitation of a 60 fs laser pulse is explained phenomenologically by this model [67]. It assumes that the system consists of three thermalized reservoirs namely, the electron, lattice and spin with corresponding temperatures T_e , T_l and T_s respectively between which the exchange of energy is allowed.

Initially the sample is magnetized in presence of a bias magnetic field. When the laser pulse is incident on the sample coherent interaction between the photon, charge and spin occurs. In this regime the angular momentum of light gets nonlinearly modified within about 50 fs. In the next step incoherent process starts which means the phase relation of electron wavefunction with respect to excitation has been destroyed. In this timescale thermalized electrons and spins are excited to the conduction band leading to a demagnetization in the system. After that, energy exchange between charge and spin with lattice takes place resulting in a fast re-magnetization. This process involves a significant change in the macroscopic thermodynamic quantities due to a change in the spin correlation length near Curie temperature. A slower relaxation is followed by the faster relaxation when the energy is dissipated from the lattice to the surrounding. The ultrafast demagnetization dynamics can be formulated in terms of three temperatures T_s , T_e and T_l corresponding to spin, electron and lattice as shown by the three coupled equations as follows

$$C_e(T_e) \frac{dT_e}{dt} = -g_{el}(T_e - T_l) - g_{es}(T_e - T_s) + P(t) \quad (2.60),$$

$$C_s(T_s) \frac{dT_s}{dt} = -g_{es}(T_s - T_e) - g_{sl}(T_s - T_l) \quad (2.61),$$

$$\text{and } C_l(T_l) \frac{dT_l}{dt} = -g_{el}(T_l - T_e) - g_{sl}(T_l - T_s) \quad (2.62)$$

with C_e = electronic specific heat of the material concerned,

C_s = magnetic contribution to the specific heat,

C_l = lattice contribution to the specific heat,

g_{el} = electron-lattice interaction constant,

g_{sl} = spin-lattice interaction constant,

g_{es} = electron-spin interaction constant,

and $P(t)$ = laser source term.

2.18.2. Elliott-Yafet (EY) Spin Flip Scattering

The Elliott-Yafet (EY) spin flip scattering[76] describes the laser excited ultrafast transfer of angular momentum from electron spin degrees of freedom to the electronic orbital degrees of freedom or the atomic orbital moments of the lattice. The scattering of hot electrons excited by a phonon changes its probability to be found in up or down spin state. That is how the angular momentum is delivered from the electronic system to the lattice. The sum over all electronic states corresponding to spin up or down is associated with magnetic moment of same size. The population difference between the states can be denoted by $D = N_{\uparrow} - N_{\downarrow}$, where N_{\uparrow} and N_{\downarrow} are the number of electrons in spin up and spin down states, respectively. Here, D is proportional to the total magnetization of the system. Now $W_{\uparrow,\downarrow}$ and $W_{\downarrow,\uparrow}$ being the number of transitions per unit time from spin up to down and down to up states, the rate equation can be expressed as

$$\frac{dD}{dt} = 2[W_{\uparrow,\downarrow}(\tau) - W_{\downarrow,\uparrow}(\tau)] \quad (2.63),$$

where τ is the spin relaxation time. The factor 2 on the right hand side appears as spin flip process changes the population difference between the states by a factor of 2. Y. Yafet considers the system close to equilibrium with equilibrium Fermi energy ε_F^0 and a deviation from the equilibrium can be accounted for by two different Fermi energies for both the spin channels as $\varepsilon_{F\uparrow}(t) \neq \varepsilon_F^0$ and $\varepsilon_{F\downarrow}(t) \neq \varepsilon_F^0$. Now by considering time and space invariance, equation (2.73) turns out to be

$$\frac{dD}{dt} = D - D^0 / T \quad (2.64).$$

Here, T is the spin relaxation time which according to Elliott and Yafet is further related to the relaxation of electrical resistivity, τ by the expression below

$$T = \tau / pb^2 \quad (2.65),$$

where p is a material specific parameter and b^2 denotes the degrees of spin mixing between involved states.

2.18.3. Spin-flip Coulomb Scattering

The spin flip Coulomb scattering is primarily based on the EY interactions. In the earlier discussion of the EY interactions we have discussed laser induced ultrafast demagnetization due to the interaction between electron and phonon. In the present model electron-electron Coulomb scattering[77] in presence of spin orbit interaction is exclusively considered as a key factor behind the demagnetization process. As opposed to electron-phonon interaction, the electron-electron scattering is not a (quasi)elastic process. So, the probability of phase space transitions from minority to majority bands is much larger in this case as compared to the electron-phonon scattering which can only cause transitions near points in the Brillouin zone when the bands are energetically close. The model analytically describes the scattering dynamics by Boltzmann scattering integrals for the momentum-dependent dynamical distribution functions in various bands.

2.19. Landau-Lifshitz-Gilbert Equation

The magnetization dynamics has a quantum mechanical background. Let us start with the time variation of spin which can be expressed by the commutation of spin and Hamiltonian operator as shown in equation 2.66.

$$i\hbar \frac{d}{dt} \langle \vec{S} \rangle = [\vec{S}, H] \quad (2.66)$$

Now in presence of an external magnetic field B , the interaction potential between S and B determine the Hamiltonian which takes the form as follows.

$$H = \frac{-g\mu_B}{\hbar} \vec{S} \cdot \vec{B} \quad (2.67)$$

Here, μ_B is the Bohr magnetron and g is the gyromagnetic ratio for free electron. Using equation 2.67, the commutator $[S, H]$ can be calculated as follows.

$$[\vec{S}, H] = ig\mu_B(\vec{S} \times \vec{B}) \quad (2.68)$$

Thus substituting equation 2.68 in 2.66 we get the equation of motion for a single spin as shown in equation 2.69.

$$\frac{d}{dt}\langle \vec{S} \rangle = \frac{g\mu_B}{\hbar}(\vec{S} \times \vec{B}) \quad (2.69)$$

In macrospin model the magnetization of the system is supposed to be uniform through the sample expressed as \vec{M} which is related to \vec{S} as

$$\vec{M} = \frac{g\mu_B}{\hbar}\langle \vec{S} \rangle \quad (2.70).$$

Thus from equation 2.69 and 2.70 the equation of motion of magnetization dynamics turns out to be as follows

$$\frac{d\vec{M}}{dt} = -\gamma(\vec{M} \times \vec{H}) \quad (2.71),$$

where $\gamma = \frac{g\mu_B}{\hbar}$, is the gyromagnetic ratio. This equation is known as Landau-Lifshitz (LL) equation[78]. A more generalized form of the equation can be obtained by introducing an effective field on the sample like anisotropy, dipolar and exchange field in addition to the applied bias field H , denoted by \vec{H}_{eff} . Thus the generalized LL equation can be written as equation 2.72 and the right hand side part of the equation is called precessional torque (PT) term.

$$\frac{d\vec{M}}{dt} = -\gamma(\vec{M} \times \vec{H}_{eff}) \quad (2.72)$$

However, the LL equation as above cannot describe the equation of motion of magnetization completely because it does not incorporate damping. It implies that the magnetization vector precesses around the effective magnetic field in a conical trajectory for infinitely long time with an angular frequency $\omega = \gamma H_{eff}$. The real situation is somewhat different. The magnetization loses momentum during precession due to the magnetic viscosity of the material. Hence the tip of the magnetization vector follows a spiral path as shown in figure 2.12 and

finally gets aligned along \vec{H} . Therefore, an additional damping torque (DT) term ($\vec{D}(\vec{M}, \vec{H}_{eff})$) should be added with the LL equation[36].

$$\frac{d\vec{M}}{dt} = -\gamma(\vec{M} \times \vec{H}_{eff}) + \vec{D}(\vec{M}, \vec{H}_{eff}) \quad (2.73)$$

Gilbert proposed[79]

$$\vec{D}(\vec{M}, \vec{H}_{eff}) = \frac{\alpha}{M_s} (\vec{M} \times \frac{d\vec{M}}{dt}) \quad (2.74).$$

Thus incorporating the Gilbert damping term in the LL equation we get the following equation of motion (equation 2.75) describing the magnetization dynamics which is famously known as Landau-Lifshitz-Gilbert equation.

$$\frac{d\vec{M}}{dt} = -\gamma(\vec{M} \times \vec{H}_{eff}) + \frac{\alpha}{M_s} (\vec{M} \times \frac{d\vec{M}}{dt}) \quad (2.75)$$

In this equation α is a dimensionless constant known as Gilbert damping constant which determines how rapidly the magnetization comes back to the equilibrium after excitation. This parameter is important for data storage and spintronics application.

The dynamics of magnetization becomes further complicated when we have spin injection into a ferromagnetic system because spin current can exert torque on magnetization. In that case we have to consider another torque term in the LLG equation in addition to PT and DT called spin transfer torque (STT) and the modified equation takes the form as follows[80].

$$\frac{d\vec{M}}{dt} = -\gamma(\vec{M} \times \vec{H}_{eff}) + \frac{\alpha}{M_s} (\vec{M} \times \frac{d\vec{M}}{dt}) + \frac{\hbar}{2e\mu_0 M_s t} J_s (\vec{M} \times \vec{\sigma} \times \vec{M}) \quad (2.76)$$

Here, t , J_s and $\vec{\sigma}$ denote ferromagnetic layer thickness, spin current density and polarity of spin respectively. From vector analysis it can be shown that STT is collinear with DT i.e., either parallel or antiparallel to DT depending on $\vec{\sigma}$. Hence STT has a key role in controlling the effective damping of the system.

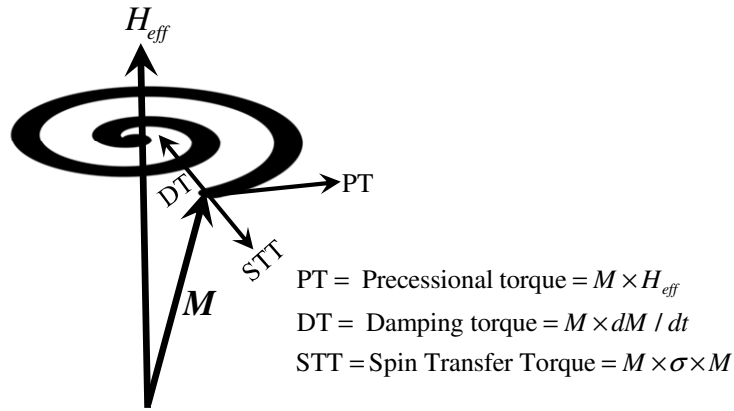


Figure 2.12. Precessional motion of magnetization in presence of damping and spin transfer torque.

2.20. Spin-Orbit Coupling

Electron has both orbital and spin angular momentum denoted by \vec{L} and \vec{S} , respectively. The interaction between them is known as spin orbit (S-O) interaction. This interaction breaks the degeneracy of the energy levels of electrons corresponding to same orbital having opposite spin, thus responsible for the fine structures in the atomic spectra. It also plays a role in magnetic damping by transfer of momentum. This is a quantum mechanical process where angular momentum is quantized. Hence, it can take some particular values. The eigenvalues of $|\vec{L}|^2$, $|\vec{S}|^2$ and $|\vec{J}|^2$ can be expressed as follows.

$$\begin{aligned}
 |\vec{L}|^2 &= \hbar^2 l(l+1), \quad l \in \{0, 1, 2, \dots\} \\
 |\vec{S}|^2 &= \hbar^2 s(s+1), \quad s \in \{+1/2, -1/2\} \\
 |\vec{J}|^2 &= \hbar^2 j(j+1), \quad j \in \{1/2, 1, 3/2, \dots\} \quad [j = |l \pm s|]
 \end{aligned} \tag{2.77}$$

The total angular momentum is the vector sum of orbital and spin angular momentum as

$$\vec{J} = \vec{L} + \vec{S} \tag{2.78}$$

Let us take dot product of \vec{J} with itself. Then we have

$$\begin{aligned}
|\vec{J}|^2 &= |\vec{L}|^2 + |\vec{S}|^2 + 2\vec{L}\vec{S} \\
\text{or, } \vec{L}\vec{S} &= \frac{1}{2}(|\vec{J}|^2 - |\vec{L}|^2 - |\vec{S}|^2)
\end{aligned} \tag{2.79}$$

The energy corresponding to S-O interaction is given by

$$\begin{aligned}
V_{L,S} &= \frac{a}{\hbar^2}(\vec{L}\vec{S}) \\
&= \frac{a}{2\hbar^2}(|\vec{J}|^2 - |\vec{L}|^2 - |\vec{S}|^2) \text{ [using equation 2.79]}
\end{aligned} \tag{2.80}$$

Here, a is a constant having dimension of energy called spin-orbit coupling constant. Now replacing the operators with corresponding eigenvalues we get

$$V_{L,S} = \frac{a}{2}[j(j+1) - l(l+1) - s(s+1)] \tag{2.81}$$

This equation corresponds to the energy splitting due to S-O interaction.

2.21. Origin of Damping

The LLG equation describing magnetization precession provides us with important information about a magnetic system. This attracts a considerable attention to research over decades due to its importance in information storage and spintronics applications. Specifically, the damping constant (α) can play a crucial role in controlling processes like magnetization switching in spin valves[81], spin injection and detection[80], current-induced magnetization reversal[81], and spin wave propagation in magnetic media[82].

The basic concept of α is simple which comes from the relaxation of magnetization precession in absence of an external stimulus. However, a concrete understanding about its origin is still due. A combination of spin orbit (S-O) interaction[83] and s - d scattering into ferromagnetic band electrons[84] by phonon is believed to be the origin of magnetic relaxation giving rise to an intrinsic α of the LLG type. Different processes like spin flip scattering or ordinary scattering between spin dependent band levels are introduced to analyze the phenomena. Magnonic modes relaxing through an exchange interaction with conduction s electrons via s - d coupling accompanied by a spin flip of the s -electrons can explain the origin of α . On the

other hand, defect induced extrinsic two magnon scattering[85-86] may lead to an enhancement in α as well as a shift in precession frequency in thin film ferromagnets. The phenomenon can be visualized by generation of high frequency spin waves, degenerate with ferromagnetic resonance (FMR) mode, in presence of dipolar coupling between spins. Defects scatter energy from FMR mode to the spin waves leading to a relaxation of de-phasing character. The situation is even more complicated in case of bi-layer or multilayer thin films where α is sensitive to interface hybridization[87-88] as well as spin pumping[27,89] effect. Although a number of theoretical models exist for explaining damping analytically, experimental evidences for those are quite challenging because a combined effect contributes to the experimentally observed α . In this scenario distinction and regulation of several intrinsic and extrinsic factors contributing to experimentally observed α have become a need of the moment, which are extensively explored in this thesis in case of ferromagnetic (FM)/nonmagnetic (NM) bi-layer systems.

2.22. Ferromagnetic Resonance

The word ‘resonance’ is commonly used in acoustics which comes from the word resound or echo. In string instruments such resonance sound can be heard due to an indirect interaction of vibrating strings in absence of direct excitation. The principle of resonance lies in transfer of energy between modes. To be specific, when a system is driven at one of its own natural frequencies the energy absorption from the excitation source is favoured as compared to other non natural frequencies resulting in an enhancement of vibration amplitude in the system. This phenomenon is known as resonance. Although the natural frequency is a property of the system it can be tuned by varying external parameters. For example one can tune the natural frequency of a string by applying suitable tensile strain on it.

Interestingly resonance can occur in precessing magnetization of a ferromagnetic material called ferromagnetic resonance (FMR) and the principle is similar to that observed in case of a vibrating string. In this case a steady external bias magnetic field is applied to orient the magnetization along the field direction which is analogous to the tensile strain of the string. Thus varying the strength of the bias field one can tune the frequency of magnetic resonance modes of a system. As an excitation source usually a radio frequency (rf) current is applied which produces an alternating magnetic field to the system. Either rf is swept at a constant

bias field or the bias field is varied at a constant rf to excite the resonance modes. At resonance condition the amplitude of oscillation increases. It is associated with dissipation of energy per cycle resulting in damping as discussed earlier in LLG equation in section 2.19. For an alternate way to describe damping we go back to the example of a string where the relaxation rate corresponding to resonance depends on the viscosity which is an intrinsic property of the vibrating medium. Similarly in ferromagnetic medium intrinsic magnetic viscosity exists for controlling the dynamical magnetization relaxation processes which is nothing but the damping of the medium. Hence, the two primary information one can extract from FMR about a magnetic system are i) the behaviour of resonance modes and their frequencies and ii) damping.

FMR was first experimentally observed by J. Griffiths [90]. However, it is found that the resonance frequency (ω_0) cannot be simply expressed by the Larmor frequency $\omega_L = \gamma B_{eff}$. To resolve anomaly Charles Kittel [91-92] proposed that one should consider the dynamical coupling caused by the demagnetizing field while he approximated the magnetization to be uniform throughout the sample and can be considered as a macrospin.

Let us consider a ferromagnetic specimen with demagnetization factors N_x, N_y, N_z along three principal axes. A bias magnetic field H_0 is applied along x-axis. The static and dynamic field can be expressed as follows:

$$\vec{H}(r) = \vec{H}_0(r) + \vec{H}_d(r) \quad (2.82)$$

$$\text{and,} \quad \vec{h}(r,t) = \vec{h}_{rf}(r,t) + \vec{h}_d(r,t) \quad (2.83)$$

Here, the subscript d denotes demagnetization. Hence, the effective field and magnetization can be given as follows.

$$\vec{H}(r,t) = \vec{H}_0 + \vec{H}_d + \vec{h}_{rf} + \vec{h}_d = \begin{pmatrix} H_0 \\ 0 \\ 0 \end{pmatrix} + \begin{pmatrix} -N_x M_s \\ 0 \\ 0 \end{pmatrix} + \begin{pmatrix} 0 \\ h_y \\ h_z \end{pmatrix} + \begin{pmatrix} 0 \\ h_y \\ h_z \end{pmatrix} = \begin{pmatrix} H_0 - N_x M_s \\ h_y - N_y m_y \\ h_z - N_z m_z \end{pmatrix} \quad (2.84)$$

$$\text{and } \vec{M}(r,t) = \begin{pmatrix} M_s \\ m_y \\ m_z \end{pmatrix}$$

The time variation of field and magnetization can be expressed as

$$\begin{aligned} h(r,t) &= h(r)e^{-i\alpha t} \\ \text{and } m(r,t) &= m(r)e^{-i\alpha t} \end{aligned} \quad (2.85).$$

Now substituting equation 2.83 and 2.84 in the LLG equation and ignoring the nonlinear terms under approximation of small precession angle we get

$$\begin{pmatrix} h_y \\ h_z \end{pmatrix} = \frac{1}{\omega_m} \begin{pmatrix} \gamma[H_0 + (N_y - N_x)M_s] - i\alpha\omega & i\omega \\ -i\omega & \gamma[H_0 + (N_z - N_x)M_s] - i\alpha\omega \end{pmatrix} \begin{pmatrix} m_y \\ m_z \end{pmatrix} = \chi^{-1} \begin{pmatrix} m_y \\ m_z \end{pmatrix} \quad (2.86),$$

where $\omega_m = \gamma M_s$. This equation tells us that the transverse components of magnetization are not the same due to the different demagnetization factors. Hence the precession of magnetization is not necessarily circular rather elliptical. Now we calculate the susceptibility tensor from equation 2.86 which can be expressed as

$$\chi = \frac{\omega_m \begin{pmatrix} \gamma[H_0 + (N_z - N_x)M_s] - i\alpha\omega & -i\omega \\ i\omega & \gamma[H_0 + (N_y - N_x)M_s] - i\alpha\omega \end{pmatrix}}{[\gamma\{H_0 + (N_z - N_x)M_s\} - i\alpha\omega][\gamma\{H_0 + (N_y - N_x)M_s\} - i\alpha\omega] - \omega^2} \quad (2.87).$$

The x component corresponding to the susceptibility tensor is zero because bias field is applied along this direction and the magnetization oscillation is taking place in the y - z plane. However, the transverse susceptibility components are very large because magnetization of a ferromagnet system is much larger than electronic or nuclear paramagnet for a particular magnetic field. The resonance condition can be achieved by using $\chi \rightarrow \infty$ and $\alpha \rightarrow 0$ in equation 2.87 which under linear approximation take the form as follows

$$\omega = \gamma \sqrt{[H_0 + (N_z - N_x)M_s][H_0 + (N_y - N_x)M_s]} \quad (2.88).$$

The above dispersion relation gives a better estimation of resonance frequency of a ferromagnetic system solving the previous anomaly which is known as Kittel formula. The expressions for the resonance frequency for some standard shaped ferromagnetic systems (under the co-ordinate system convention as shown in figure 2.13) are listed below [91,93]:

Table 2.3. Expression for resonance frequency for some standard shaped ferromagnetic systems.					
Shape	Magnetization direction	Demagnetizing Factors			Resonance frequency
		N_x	N_y	N_z	
Infinitely thin plane	Tangential	0	4π	0	$\omega_0 = \gamma[H_z(H_z + 4\pi M_z)]^{1/2}$
	Normal	0	0	4π	$\omega_0 = \gamma[H_z - 4\pi M_z]$
Infinitely thin cylinder	Longitudinal	2π	2π	0	$\omega_0 = \gamma(H_z + 2\pi M_z)$
	Transverse	2π	0	2π	$\omega_0 = \gamma[H_z(H_z - 2\pi M_z)]^{1/2}$
Sphere	-	$4\pi/3$	$4\pi/3$	$4\pi/3$	$\omega_0 = \gamma H_z$

In this context it is interesting to note that the transverse susceptibility χ (equation. 2.87) is a complex quantity which has a real and imaginary component indicating relative phase difference.

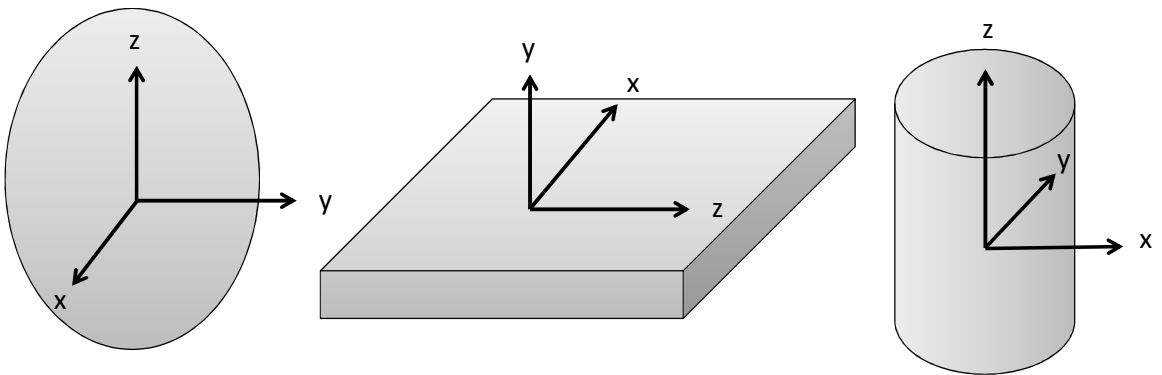


Figure 2.13. Some standard shapes with co-ordinate convention.

References

- [1] Robson, B. A. *The theory of polarization phenomena*. (Oxford Univ Pr, 1974).
- [2] Bloch, F. Nuclear induction. *Physical review* **70**, 460 (1946).
- [3] Zhou, X., Zhang, Z. & Hu, C.-Z. Spin continuity equation and definition of spin current. *arXiv:0904.3796* (2009).
- [4] Gerlach, W. & Stern, O. Der experimentelle Nachweis der Richtungsquantelung im Magnetfeld. *Zeitschrift für Physik* **9**, 349 (year).
- [5] Gerlach, W. & Stern, O. Das magnetische Moment des Silberatoms. *Zeitschrift für Physik* **9**, 353.(year)
- [6] Takahashi, S. & Maekawa, S. Spin current, spin accumulation and spin Hall effect. *Sci. Technol. Adv. Mater.* **9**, 014105 (2008).
- [7] Czeschka, F. D. *Spin currents in metallic nanostructures*, Technische Universität München, (2011).
- [8] Hall, E. H. On a new action of the magnet on electric currents. *American Journal of Mathematics* **2**, 287 (1879).
- [9] Sinitsyn, N. Semiclassical theories of the anomalous Hall effect. *J. Phys. Condens. Matter* **20**, 023201 (2008).
- [10] Nagaosa, N. *et al.* Anomalous hall effect. *Rev. mod. phys.* **82**, 1539 (2010).
- [11] Jungwirth, T., Niu, Q. & MacDonald, A. Anomalous Hall effect in ferromagnetic semiconductors. *Phys. Rev. Lett.* **88**, 207208 (2002).
- [12] Karplus, R. & Luttinger, J. Hall effect in ferromagnetics. *Phys. Rev.* **95**, 1154 (1954).
- [13] Yao, Y. *et al.* First principles calculation of anomalous Hall conductivity in ferromagnetic bcc Fe. *Phys. Rev. Lett.* **92**, 037204 (2004).
- [14] Stone, M. *Quantum Hall Effect*. (World Scientific, 1992).
- [15] Klitzing, K. v., Dorda, G. & Pepper, M. New method for high-accuracy determination of the fine-structure constant based on quantized Hall resistance. *Phys. Rev. Lett.* **45**, 494 (1980).
- [16] Laughlin, R. B. Anomalous quantum Hall effect: an incompressible quantum fluid with fractionally charged excitations. *Phys. Rev. Lett.* **50**, 1395 (1983).
- [17] Stormer, H. *et al.* Fractional quantization of the Hall effect. *Phys. Rev. Lett.* **50**, 1953 (1983).

-
- [18] Tsui, D. C., Stormer, H. L. & Gossard, A. C. Two-dimensional magnetotransport in the extreme quantum limit. *Phys. Rev. Lett.* **48**, 1559 (1982).
- [19] Schwarzschild, B. Physics Nobel Prize Goes to Tsui, Stormer and Laughlin for the Fractional Quantum Hall Effect. *Phys. Today* **51**, 17 (1998).
- [20] Dyakonov, M. & Perel, V. Current-induced spin orientation of electrons in semiconductors. *Phys. Lett. A* **35**, 459 (1971).
- [21] Kato, Y., Myers, R., Gossard, A. & Awschalom, D. Observation of the spin Hall effect in semiconductors. *Science* **306**, 1910 (2004).
- [22] Wunderlich, J., Kaestner, B., Sinova, J. & Jungwirth, T. Experimental observation of the spin-Hall effect in a two-dimensional spin-orbit coupled semiconductor system. *Phys. Rev. Lett.* **94**, 047204 (2005).
- [23] Takahashi, S. & Maekawa, S. Spin current, spin accumulation and spin Hall effect. *Sci. Technol. Adv. Mater.* **9**, 014105 (2008).
- [24] Mott, N. F. The scattering of fast electrons by atomic nuclei. *Proc. R. Soc. Lond. A* **124**, 425 (1929).
- [25] Mott, N. F. & Massey, H. S. W. *The theory of atomic collisions*. Vol. 35 (Clarendon Press Oxford, 1965).
- [26] Berger, L. Emission of spin waves by a magnetic multilayer traversed by a current. *Phys. Rev. B* **54**, 9353 (1996).
- [27] Tserkovnyak, Y., Brataas, A. & Bauer, G. E. Enhanced Gilbert damping in thin ferromagnetic films. *Phys. Rev. Lett.* **88**, 117601 (2002).
- [28] Brouwer, P. Scattering approach to parametric pumping. *Phys. Rev. B* **58**, R10135 (1998).
- [29] Tserkovnyak, Y., Brataas, A. & Bauer, G. E. W. Enhanced Gilbert Damping in Thin Ferromagnetic Films. *Phys. Rev. Lett.* **88**, 117601 (2002).
- [30] Mizukami, S., Ando, Y. & Miyazaki, T. Ferromagnetic resonance linewidth for NM/80NiFe/NM films (NM= Cu, Ta, Pd and Pt). *J. Magn. Magn. Mater.* **226**, 1640 (2001).
- [31] Smit, J. Magnetoresistance of ferromagnetic metals and alloys at low temperatures. *Physica* **17**, 612 (1951).
- [32] De Ranieri, E. *et al.* Lithographically and electrically controlled strain effects on anisotropic magnetoresistance in (Ga, Mn) As. *New J. Phys.* **10**, 065003 (2008).

- [33] Rowan-Robinson, R., Hindmarch, A. & Atkinson, D. Enhanced electron-magnon scattering in ferromagnetic thin films and the breakdown of the Mott two-current model. *Phys. Rev. B* **90**, 104401 (2014).
- [34] Kokado, S., Tsunoda, M., Harigaya, K. & Sakuma, A. Anisotropic magnetoresistance effects in Fe, Co, Ni, Fe₄N, and half-metallic ferromagnet: A systematic analysis. *J. Phys. Soc. Jpn.* **81**, 024705 (2012).
- [35] Campbell, I. A., Fert, A. & Jaoul, O. The spontaneous resistivity anisotropy in Ni-based alloys. *J. Phys. C: Solid State Phys.* **3**, S95 (1970).
- [36] Malozemoff, A. Anisotropic magnetoresistance of amorphous and concentrated polycrystalline iron alloys. *Phys. Rev. B* **32**, 6080 (1985).
- [37] Baibich, M. N. *et al.* Giant magnetoresistance of (001) Fe/(001) Cr magnetic superlattices. *Phys. Rev. Lett.* **61**, 2472 (1988).
- [38] Binasch, G., Grünberg, P., Saurenbach, F. & Zinn, W. Enhanced magnetoresistance in layered magnetic structures with antiferromagnetic interlayer exchange. *Phys. Rev. B* **39**, 4828 (1989).
- [39] Mott, N. F. The electrical conductivity of transition metals. *Proc. R. Soc. Lond. A* **153**, 699 (1936).
- [40] Fert, A. & Campbell, I. Two-current conduction in nickel. *Phys. Rev. Lett.* **21**, 1190 (1968).
- [41] Dieny, B. Classical theory of giant magnetoresistance in spin-valve multilayers: influence of thicknesses, number of periods, bulk and interfacial spin-dependent scattering. *J. Phys. Condens. Matter* **4**, 8009 (1992).
- [42] Johnson, B. & Camley, R. Theory of giant magnetoresistance effects in Fe/Cr multilayers: Spin-dependent scattering from impurities. *Phys. Rev. B* **44**, 9997 (1991).
- [43] Parkin, S. Origin of enhanced magnetoresistance of magnetic multilayers: Spin-dependent scattering from magnetic interface states. *Phys. Rev. Lett.* **71**, 1641 (1993).
- [44] Van Peski-Tinbergen, T. & Dekker, A. Spin-dependent scattering and resistivity of magnetic metals and alloys. *Physica* **29**, 917 (1963).
- [45] Butler, W. H. Theory of electronic transport in random alloys: Korringa-Kohn-Rostoker coherent-potential approximation. *Phys. Rev. B* **31**, 3260 (1985).

-
- [46] Stocks, G. M., Temmerman, W. M. & Gyorffy, B. L. Complete Solution of the Korringa-Kohn-Rostoker Coherent-Potential-Approximation Equations: Cu-Ni Alloys. *Phys. Rev. Lett.* **41**, 339 (1978).
- [47] Butler, W., Zhang, X. G., Nicholson, D. & MacLaren, J. Theory of transport in inhomogeneous systems and application to magnetic multilayer systems. *J. Appl. Phys.* **76**, 6808 (1994).
- [48] Butler, W., Zhang, X.-G., Nicholson, D. & MacLaren, J. Spin-dependent scattering and giant magnetoresistance. *J. Magn. Magn. Mater.* **151**, 354 (1995).
- [49] Zhu, J.-G. J. & Park, C. Magnetic tunnel junctions. *Mater. Today* **9**, 36 (2006).
- [50] Julliere, M. Tunneling between ferromagnetic films. *Phys. Lett. A* **54**, 225 (1975).
- [51] Yuasa, S. *et al.* Giant room-temperature magnetoresistance in single-crystal Fe/MgO/Fe magnetic tunnel junctions. *Nat. mater.* **3**, 868 (2004).
- [52] Parkin, S. S. *et al.* Giant tunnelling magnetoresistance at room temperature with MgO (100) tunnel barriers. *Nat. mater.* **3**, 862 (2004).
- [53] Gallagher, W. J. & Parkin, S. S. P. Development of the magnetic tunnel junction MRAM at IBM: From first junctions to a 16-Mb MRAM demonstrator chip. *IBM Journal of Research and Development* **50**, 5 (2006).
- [54] Mathon, J. & Umerski, A. Theory of tunneling magnetoresistance of an epitaxial Fe/MgO/Fe (001) junction. *Phys. Rev. B* **63**, 220403 (2001).
- [55] Butler, W., Zhang, X.-G., Schulthess, T. & MacLaren, J. Spin-dependent tunneling conductance of Fe/MgO/Fe sandwiches. *Phys. Rev. B* **63**, 054416 (2001).
- [56] Tehrani, S. *et al.* Recent developments in magnetic tunnel junction MRAM. *IEEE Trans. Magn.* **36**, 2752 (2000).
- [57] Kim, H. J. *et al.* Development of magnetic tunnel junction for toggle MRAM. *IEEE Trans. Magn.* **41**, 2661 (2005).
- [58] Au, E. K. S. *et al.* A switched-current sensing architecture for a four-state per cell magnetic tunnel junction MRAM. *Ieee T Circuits-I* **51**, 2113 (2004).
- [59] Au, E. K. S. *et al.* A novel current-mode sensing scheme for magnetic tunnel junction MRAM. *IEEE Trans. Magn.* **40**, 483 (2004).
- [60] Marongmued, K. & Sa-Ngiamsak, C. How Does Electrostatic Discharge Event Not Cause Polarity Flip in TMR Read Heads? *IEEE Trans. Magn.* **48**, 3555 (2012).

- [61] Miyatake, M., Kugiya, F. & Kodama, N. Read Performance Reliability in TMR Head. *Ieee Trans. Dev. Mater. Rel.* **12**, 24 (2012).
- [62] Sapozhnikov, V., Gao, K. Z. & Chen, Y. G. Intrinsic asymmetry and angular dependence of the junction resistance for high TMR read sensors. *J. Appl. Phys.* **105** (2009).
- [63] Kautzky, M. C. *et al.* Atomic Layer Deposition Al₂O₃ Films for Permanent Magnet Isolation in TMR Read Heads. *IEEE Trans. Magn.* **44**, 3576 (2008).
- [64] Smith, N., Katine, J. A., Childress, J. R. & Carey, M. J. Thermal and spin-torque noise in CPP (TMR and/or GMR) read sensors. *IEEE Trans. Magn.* **42**, 114 (2006).
- [65] McKinstry, K. D. & Dee, R. H. TMR window measurements with thin film write MR read heads on metal particle tape including erase bands. *IEEE Trans. Magn.* **34**, 1958 (1998).
- [66] van Kampen, M. *et al.* All-Optical Probe of Coherent Spin Waves. *Phys. Rev. Lett.* **88**, 227201 (2002).
- [67] Beaurepaire, E., Merle, J. C., Daunois, A. & Bigot, J. Y. Ultrafast Spin Dynamics in Ferromagnetic Nickel. *Phys. Rev. Lett.* **76**, 4250 (1996).
- [68] Knorren, R., Bennemann, K. H., Burgermeister, R. & Aeschlimann, M. Dynamics of Excited Electrons in Copper and Ferromagnetic Transition Metals: Theory and Experiment. *Phys. Rev. B* **61**, 9427 (2000).
- [69] Zhang, G. P. & Hübner, W. Laser-induced Ultrafast Demagnetization in Ferromagnetic Metals. *Phys. Rev. Lett.* **85**, 3025 (2000).
- [70] Beaurepaire, E. *et al.* Coherent Terahertz Emission from Ferromagnetic Films Excited by Femtosecond Laser Pulses. *Appl. Phys. Lett.* **84**, 3465 (2004).
- [71] Koopmans, B., Ruigrok, J. J. M., Longa, F. D. & Jonge, W. J. M. d. Unifying Ultrafast Magnetization Dynamics. *Phys. Rev. Lett.* **95**, 267207 (2005).
- [72] Koopmans, B. *et al.* Explaining the Paradoxical Diversity of Ultrafast Laser-induced Demagnetization. *Nat. Mater.* **9**, 259 (2010).
- [73] Laraoui, A. *et al.* Ultrafast Spin Dynamics of an Individual CoPt₃ Ferromagnetic Dot. *Eur. Phys. J. D* **43**, 251 (2007).
- [74] Laraoui, A. *et al.* Study of Individual Ferromagnetic Disks With Femtosecond Optical Pulses. *J. Appl. Phys.* **101**, 09C105 (2007).

- [75] Anisimov, S. I., Kapeliovich, B. L. & Perel'man, T. L. Electron Emission from Metal Surface Exposed to Ultrashort Laser Pulses. *Zh. Eksp. Teor. Fiz.* **66**, 776 (1974).
- [76] Steiauf, D. & Fähnle, M. Elliott-Yafet mechanism and the discussion of femtosecond magnetization dynamics. *Phys. Rev. B* **79**, 140401(R) (2009).
- [77] Krauß, M. *et al.* Ultrafast demagnetization of ferromagnetic transition metals: The role of the Coulomb interaction. *Phys. Rev. B* **80**, 180407 (2009).
- [78] Landau, L. D. & Lifshitz, E. On the theory of the dispersion of magnetic permeability in ferromagnetic bodies. *Phys. Z. Sowjetunion* **8**, 101 (1935).
- [79] Gilbert, T. L. A phenomenological theory of damping in ferromagnetic materials. *IEEE Trans. Magn.* **40**, 3443 (2004).
- [80] Ganguly, A. *et al.* Time-domain detection of current controlled magnetization damping in Pt/Ni₈₁Fe₁₉ bilayer and determination of Pt spin Hall angle. *Appl. Phys. Lett.* **105**, 112409 (2014).
- [81] Schumacher, H., Chappert, C., Sousa, R. & Freitas, P. Current-induced precessional magnetization reversal. *Appl. Phys. Lett.* **83**, 2205 (2003).
- [82] Xi, H. & Xue, S. Spin-wave propagation and transmission along magnetic nanowires in long wavelength regime. *J. Appl. Phys.* **101**, 123905 (2007).
- [83] He, P. *et al.* Quadratic Scaling of Intrinsic Gilbert Damping with Spin-Orbital Coupling in L₁₀ FePdPt Films: Experiments and Ab Initio Calculations. *Phys. Rev. Lett.* **110**, 077203 (2013).
- [84] Ingvarsson, S. *et al.* Role of electron scattering in the magnetization relaxation of thin Ni₈₁Fe₁₉ films. *Phys. Rev. B* **66**, 214416 (2002).
- [85] Arias, R. & Mills, D. Extrinsic contributions to the ferromagnetic resonance response of ultrathin films. *Phys. Rev. B* **60**, 7395 (1999).
- [86] Lenz, K. *et al.* Two-magnon scattering and viscous Gilbert damping in ultrathin ferromagnets. *Phys. Rev. B* **73**, 144424 (2006).
- [87] Grange, W. *et al.* Experimental and theoretical x-ray magnetic-circular-dichroism study of the magnetic properties of Co₅₀Pt₅₀ thin films. *Phys. Rev. B* **62**, 1157 (2000).
- [88] Nakajima, N. *et al.* Perpendicular magnetic anisotropy caused by interfacial hybridization via enhanced orbital moment in Co/Pt multilayers: magnetic circular x-ray dichroism study. *Phys. Rev. Lett.* **81**, 5229 (1998).

- [89] Rezende, S. *et al.* Enhanced spin pumping damping in yttrium iron garnet/Pt bilayers. *Appl. Phys. Lett.* **102**, 012402 (2013).
- [90] Griffiths, J. Anomalous High-frequency Resistance of Ferromagnetic Metals. *Nature* **158**, 670 (1946).
- [91] Kittel, C. On the Theory of Ferromagnetic Resonance Absorption. *Phys. Rev.* **73**, 155 (1948).
- [92] Kittel, C. Interpretation of Anomalous Larmor Frequencies in Ferromagnetic Resonance Experiment. *Phys. Rev.* **71**, 270 (1947).
- [93] Gurevich, A. & Melkov, G. *Magnetization Oscillations and Waves*. (CRC Press, 1996).

Chapter 3

Experimental Techniques

In this chapter we shall focus on sample preparation, characterization and measurement techniques used in this thesis. We start with thin film deposition using dc/rf magnetron sputtering and e-beam evaporation. The discussion is followed by micro-fabrication techniques in clean room which are used for patterning the samples, electrode and waveguide. The discussion also includes an overview of optical and e-beam lithography. In this context we describe a novel technique to achieve controlled intermixing of atoms at the interface of a bi-layer by Ga^+ ion irradiation using focused ion beam. Later we briefly discuss about the characterization of the samples using scanning electron microscope, vibrating sample magnetometer, x-ray refractivity, atomic force microscope and static magneto-optical Kerr effect. Finally, we describe time resolved magneto-optical Kerr microscopy and spin torque ferromagnetic resonance as investigative techniques.

3.1. Thin Film Deposition

Sample preparation is the first step to experimental research. It is crucial because unwilling imperfection in the sample may introduce noise or deviation from the physical and material properties. In our study samples are prepared using ultra high vacuum (UHV) thin film deposition and clean room micro-fabrication techniques. Thin films of different materials like NiFe, Co, CoFe, CoFeB, Pt, Cu, Ta, W, Cr, Au, SiO₂, MgO are grown on thermally oxidised non-doped Si substrate using dc/rf magnetron sputtering system in UHV chamber whereas in some cases metals like NiFe, Au, Cu are deposited using e-beam evaporation technique. NiFe, Co, CoFe and CoFeB are chosen as ferromagnetic material, Pt, Cu, Ta, W, Cr, Au are used as nonmagnetic metal and SiO₂ or MgO are usually chosen as a protective or insulating layer. The thickness of the films lies in the range of 0 to 20 nm. In case of a co-planer waveguide 50 to 150 nm thick Au is deposited and patterned on top of 5 nm of Ta layer which is used for good adhesion of Au to Si substrate.

3.1.1. Magnetron Sputtering Process

Magnetron sputtering[1] is a physical vapor deposition technique by which one can grow high quality thin films having same composition as the source material. The technique is widely used in electronic, hardware and optical industries for deposition of single or multi-layer films and various types of coating by materials having different physical properties like low friction coating, corrosion resistive coating, thermal or electrical insulation coating and anti reflection coating.

The sputtering process is done in an ultra high vacuum chamber filled with inert gas like Ar. When a high voltage is applied glow discharge plasma is created. As a result, positively charged ions driven by the electric field are accelerated to cathode and hit the negatively charged target material with sufficient force resulting in removal of target atoms from its surface, called sputtering. Then the sputtered atoms may be condensed on a nearby substrate as thin film. For conductive material dc or rf power supply can be used to create electric field whereas for insulating materials only rf works. During sputtering, secondary electrons are also emitted from the target due to ion bombardment which essentially plays a role in maintaining the plasma.

The basic sputtering process is known for a long time. However, it suffers limitations like low deposition rate, high substrate heating and low ionization of plasma. To overcome these problems magnetron sputtering comes into picture. The magnetron is used to create magnetic field parallel to the target surface so that the motion of the secondary electron are confined along the field lines in the vicinity of the target. Thus the probability of electron-atom collision increases resulting in an increase in ionization efficiency of plasma. Hence more number of ions hit the target and sputtering rate increases consequently increasing the rate of deposition. In addition to that higher ionization allows plasma to be maintained at lower voltage and lower operating pressure. The magnetron is placed below the target with one of its poles along the central axis of the target plane while the other pole symmetrically placed around the outer edge of the central pole as shown in figure 3.1. Magnetrons can be of two types; balanced magnetron and unbalanced magnetron. In the first case the strength of the two pole pieces are equal and the lines of forces are closed between the pole pieces while in the second case outer pole piece is stronger than the inner one resulting in some open lines of force. Thus

sition is negligible. This technique is most suitable for deposition of metals for their relatively lower melting point but difficult for insulators because their melting temperature are higher. This technique is very efficient for growing multilayer films with high quality interface. A multi source system allows to evaporate materials in turn or co-evaporation for the formation of alloys without breaking the vacuum throughout the growth.

3.2. Optical Lithography

Lithography is a useful technique for micro and nanoscale patterning. It can be of different type depending on type of exposure like photolithography, e-beam lithography, x-ray and ion beam lithography. Out of those, photolithography is very popular for microscale patterning. The primary advantage of this technique is parallel growth of all microstructures. A large area can be patterned in a single exposure of light using photomask. However, submicron features are difficult to resolve by this technique due to diffraction of light. The usual steps for photolithographic patterning are as follows (see figure 3.2).

- 1. Substrate cleaning:** At first a Si substrate is taken on which the sample will be grown. It has to undergo a proper cleaning process by ultrasonating it in acetone for 20 minutes. This will help to remove inorganic and organic impurity materials from the top of the substrate. The substrate is dried by a dry nitrogen flow.
- 2. Resist coating:** A uniform layer of photo resist dissolved in an organic solvent is coated on the substrate. In our case a thin layer of primer (1,1,1,3,3,3,-Hexamethyldisilazane, $C_6H_{10}NSi_2$, HDMS) is coated using spin coater. First the substrate is fixed on top of the spindle of a spin coater. A few drops of primer solution is put on the substrate and rotated at 500 rpm for 5 seconds and then 5000 rpm for 40 seconds. The centrifugal force makes the liquid uniformly distributed on the substrate. The thickness of the layer depends on the density and speed of rotation. The substrate is then baked in an oven at $80^\circ C$ for 5 minutes. Thereafter a positive photoresist (AZ-1500) is coated on top of the substrate in a similar way and baked at $80^\circ C$ for 10 min. Baking essentially removes solvent from the photoresist and increase the adhesion. With the recipe described above we obtain a typical thickness of resist $\sim 1 \mu m$.
In this context it is worth mentioning that photoresist can be of two types either positive or negative. For positive photoresist chemical changes occur at UV light expo-

sure. Hence the exposed part becomes more soluble in the developer solution. Conversely in case of negative photo resist the exposed part becomes more polymerized and less soluble.

- 3. UV light exposure and developing:** The resist coated substrate is exposed to UV light with typical energy 90mJ/mm^2 through a mask containing pattern. The resist reacts at the exposed part which becomes soluble in the developer. Then the substrate is dipped into a developer solution for 50-60 seconds followed by a rinsing in de-ionized water for about 1 minute. Then it is dried by dry nitrogen flow. The process makes the resist pattern visible at the unexposed part.
- 4. Lift off and etch back process:** Single or multilayer thin films are deposited on the whole substrate and then treated with acetone for 1 minute to remove the residual resist. Thus we obtain a patterned single or multilayer thin film. Sometimes thin films are deposited on the substrate first on top of which resist is patterned using photolithography technique as mentioned above. Then the films are etched back in the weaker part of the resist using reactive ions and the harder part remains unaffected. Finally the residual resists are removed and we get the desired patterning on the thin film.

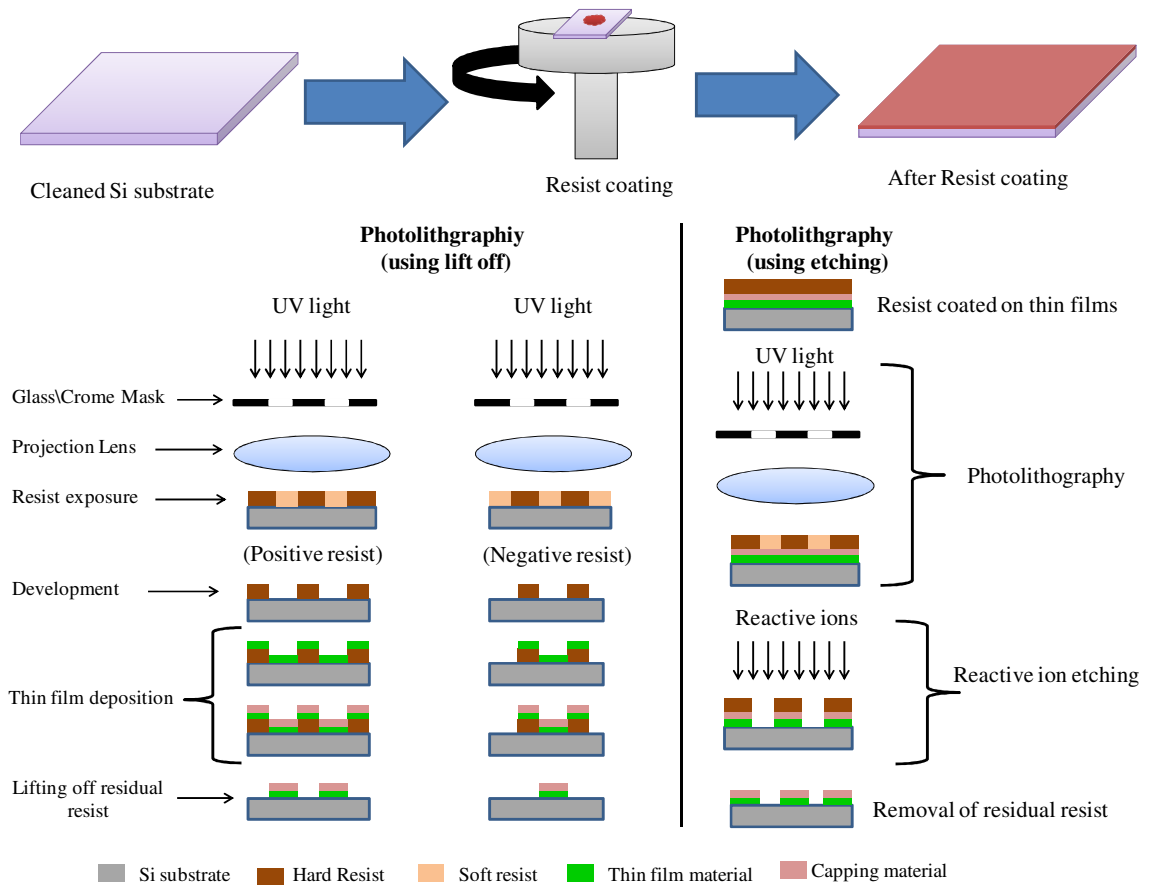


Figure 3.2. Schematic illustration of photolithography process.

3.3. Focused Ion Beam

Recently, focused ion beam (FIB) is regularly used for direct nanoscale patterning[2] and milling to fabricate nanostructures with high precision. It may also be used to locally manipulate and control magnetic properties, domain structures[3-4] as well as magnetization and domain wall dynamics[5] on the micro and nanoscale. This opens new opportunities for interesting scientific investigations and has potential in future applications of nanoscale magnetic devices, such as sensors, memory and logic devices. In this thesis we have investigated the local magnetic property manipulation by low dose FIB irradiation of ferromagnetic/nonmagnetic bi-layer thin film systems[6-7].

Here we have used the FEI Helios NanoLab Dual Beam (FIB/SEM) system. It consists of a liquid ion metal source (LIMS) with beam diameter ~5 nm and a field emission Gun (FEG)

electron source producing high resolution electron beam. Gallium is used as LIMS in our system due to certain advantages like low vapor pressure, less volatility, low melting point and good electrical conductivity. The emission characteristics of Ga^+ showing high angular intensity with a small energy spread qualifies itself as one of the fittest candidate as LIMS.

Let us now discuss about the dual beam system and how it can be used for creating antidot nano-structure or local intermixing in the sample. First the sample is placed on a stage inside the chamber. Then the vacuum is achieved below to 10^{-6} Torr. The electron gun is placed vertically downward while the ion beam source is tilted at 45° with respect to the electron gun (see figure 3.3 (left)). When the vacuum is achieved the tilt of the sample stage is adjusted at a critical angle of 52° (see figure 3.3 (right)) so that both the ion and electron beam can be focused exactly at the same position of the sample. This is called the eucentric point. This critical position of the stage enables us to image as well as irradiate the same part of the sample at the same time. The energetic ion beam raster scan and mills out the sample by local sputtering following a user defined pattern loaded earlier in the system's program. The purpose of the electron beam is to visualize the sample so that we can align and get the features at the desired location. It also helps us to understand the topographic quality of patterning. Secondary and back scattered electrons reflected from the sample produce the image. The mechanism is same as scanning electron microscopy. The imaging could be done by Ga^+ beam as well. However, electron beam is preferred because Ga ion can damage the sample during imaging. Moreover when the two beams are aligned at the eucentric point, it is better to use electron beam for aligning the sample before irradiation to limit the Ga^+ exposure and allow better positioning of irradiation. At eucentric point we have a slanted view of the sample although one can have a top view by rotating sample stage perpendicular to the electron source.

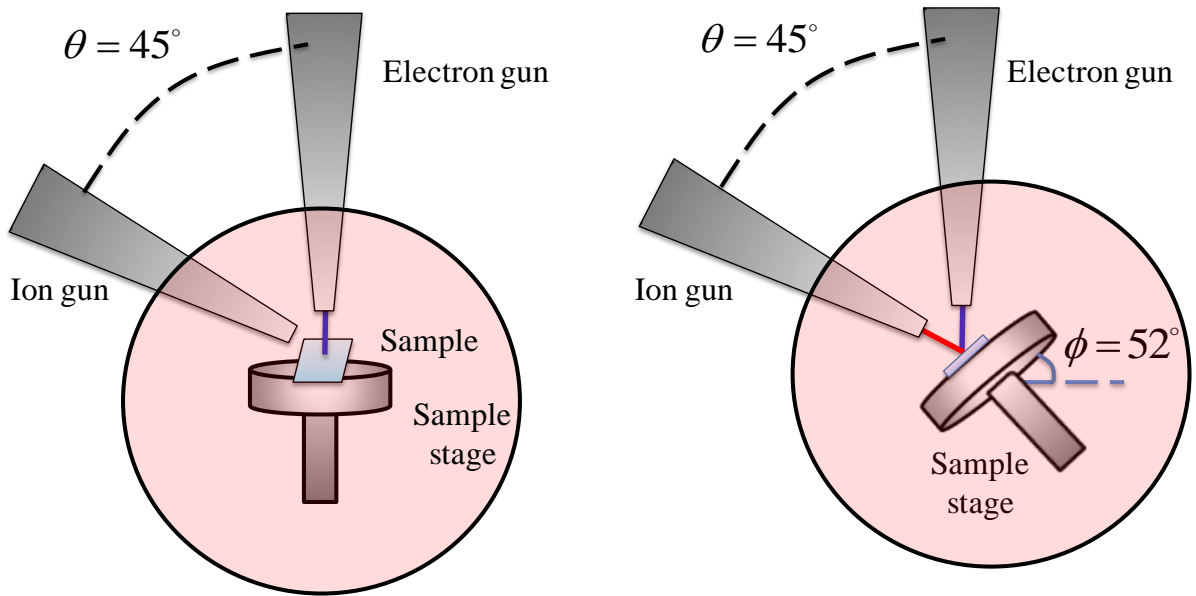


Figure 3.3. Experimental arrangement of FIB system; (left) imaging mode and (right) irradiation mode.

3.3.1. Effect of Ion Irradiation

The effect of ion irradiation on thin films, specifically at the low dose regime, stimulates a lot of research interest due to its potential in controlling various magnetic properties of a system. Recently it is established that low dose irradiation causes structural changes at the interface of a bi-layer[6,8-9] film. A detailed investigation on such structural change of NiFe/Au bi-layer has been performed by D. Burn in his Ph.D. thesis (see reference 9). Now the question is what is physically indicated by dose and what is its critical value below which one can expect interesting structural changes without having significant sputtering from top surface of a thin film? Dose indicates the strength of ion irradiation applied on a sample. It is determined by the number of Ga^+ ions exposed per unit area. In this thesis we shall express dose in the unit of $\text{pC}/\mu\text{m}^2$. To determine critical dose we can refer to figure 3.4 showing scanning electron microscopic image of NiFe (20 nm)/Au (3 nm) bi-layer with increasing irradiation dose from (a) to (f). At lower dose ((a)-(c)) faint contrast is observed due to surface roughness created by ions and at higher dose ((d)-(f)) the effect of sputtering is clearly observed. In this thesis we restrict irradiation dose up to $5 \text{ pC}/\mu\text{m}^2$ to avoid structural deformation or damage in our sample. We study dynamical magnetic properties like ultrafast relaxation, frequency and damping of magnetization precession in FM/NM ion irradiated bi-layers.

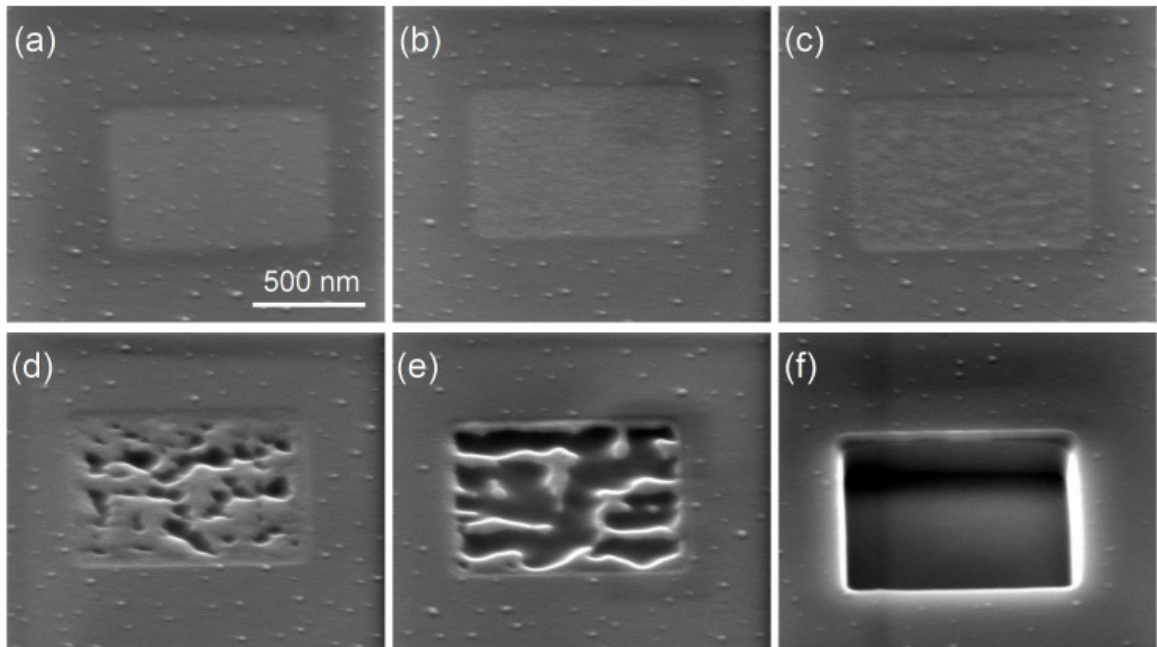


Figure 3.4 NiFe (20 nm)/Au (3 nm) surface structure after the irradiation of $1 \times 1 \mu\text{m}$ windows with doses a) 3.1, b) 6.3, c) 12.5, d) 31.2, e) 62.5 and f) $625 \times 10^{15} \text{Ga}^+/\text{cm}^2$ at normal incidence with a beam current of 1.5 pA and an acceleration voltage of 30 keV (see Reference 9).

During ion irradiation Ga ions get implanted into the sample and distributed down to a depth of 10 nm from the surface. The density of implanted Ga^+ increases with dose. However, in our study doping from Ga is less than 1-2% which is unlikely to create magnetic changes in the system. Transfer of energy from the incident ions to the capping layer causing displacement of atoms at the interface is a more significant effect. The re-orientation of intermixed atoms initially located around the interfaces and the intermixed region broadens across the thickness with increasing dose as shown in figure 3.5. Intermixing may lead to a formation of compositionally graded alloy, change in effective grain size by expansion or contraction of lattice, local stress relaxation, amorphization, increase of scattering defects, loss of magnetic moment, change in hybridization, spin transport and dynamical magnetization properties. Earlier literature[10] shows simulated results on relative concentration of atoms across the thickness of NiFe/Au bi-layer due to irradiation using TRYDYN software which supports the formation of compositionally graded interface broadening with increasing dose.

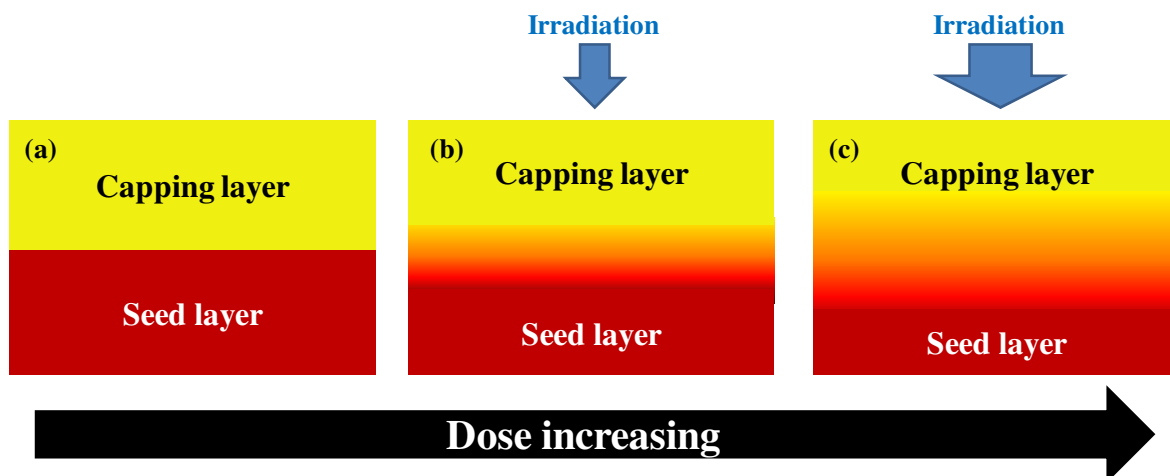


Figure 3.5. Ion irradiation induced intermixing of interface forming compositionally graded alloy (a schematic illustration).

3.4. Scanning Electron Microscope

The scanning electron microscope (SEM) uses high-energy beam of electrons to produce a magnified image of a specimen with detailed information about surface topography and morphology. It is an indispensable tool for the characterization of micro and nanostructures. Here we used SEM to check size, shape and morphology of our sample, electrode contacts, uniformity of the irradiated spot and identified their location in bi-layer film.

For the emission of electron beam two types of phenomena can be used. One is thermionic emission and the other is electric field induced emission. Both types of SEM are used in course of this thesis. For the first case, an electron gun fitted with a tungsten filament cathode acts as electron source, whereas, in the latter case electron beam is emitted from a field emission cathode. The beam profile is narrower in case of field emission resulting in a better spatial resolution. The energy of electrons can be varied from few hundreds eV to few tens of keV. A nonuniform electric field is used to accelerate the emitted electrons. The beam is focused by electromagnetic lenses, called condenser lens and then passes through an electromagnetic scanning coil and finally, is focused onto the sample (figure 3.6) [11]. The scanning coil deflects the beam laterally due to which it performs a raster scan over a rectangular area of the sample surface. When electron beam hits the sample different types of electrons like secondary electrons, backscattered electrons and Auger electrons are generated due to elastic

and inelastic collisions along with the emission of X-rays and visible light (cathodoluminescence). The secondary electrons, produced by inelastic scattering of electrons are collected by a detector. By comparing the intensity of these secondary electrons to the scanning primary electron beam, an image of the sample surface is produced and displayed on a monitor. The samples are generally fixed on a metal stub by a sticky carbon tape. There can be accumulation of charge at the sample surface which increases brightness and affects the image quality. Hence, the samples should be electrically conductive at the surface as well as grounded to avoid charge accumulation. We have used “FEI QUANTA 200” and “FEI Helios NanoLab 600” SEMs to characterize our samples.

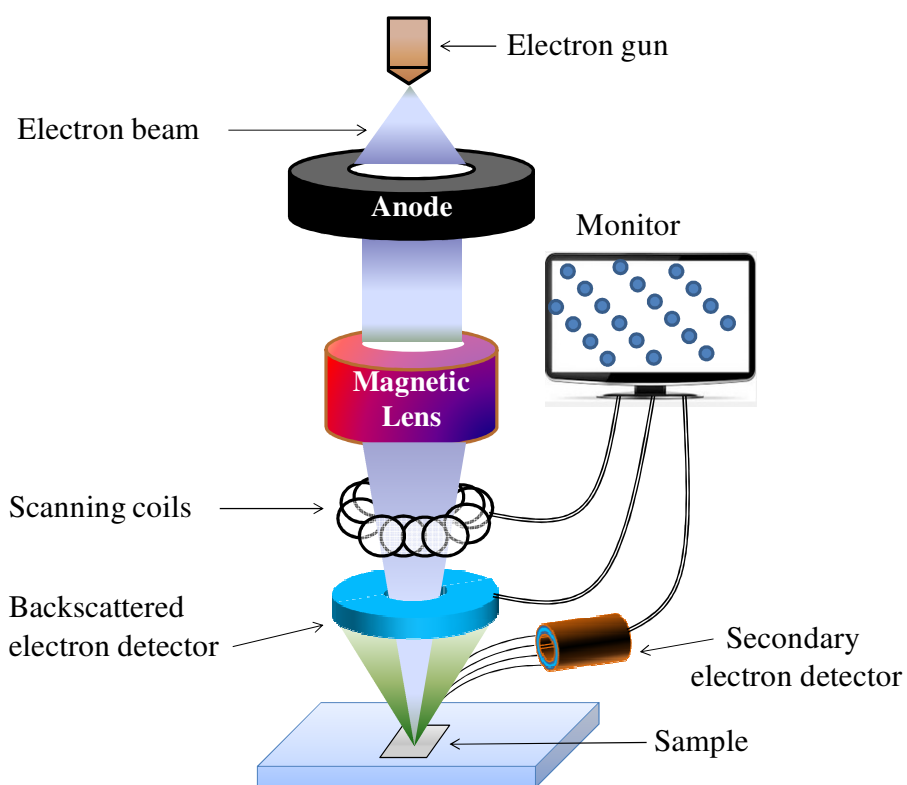


Figure 3.6. Experimental arrangement for scanning electron microscope.

3.5. X-ray Reflectivity

X-ray reflectivity is a powerful technique to characterize structural properties like electron density, interface roughness, thickness of single or multilayered thin films. The technique is based on reflection of x-ray from the surface or interface of a sample (see figure 3.7). Inside

the instrument usually we have a fixed x-ray source and the angle of incidence (θ) of x-ray beam falling on the sample surface is varied by rotating the sample stage. The angle of incidence is small which is called grazing angle. An x-ray detector is also rotated and placed at an angle 2θ with respect to the incident beam for measuring the intensity of the x-ray reflected from the sample. The refractive index of sample for x-ray is slightly less than 1. Hence a total external reflection (up to a critical angle θ_c) is observed and x-ray barely penetrates into the sample. In this region the reflectivity curve is ideally flat. However, it can be influenced by the size and roughness of the top surface. Beyond θ_c x-ray starts to penetrate into the material and the penetration depth increases with θ . Consequently the intensity of the specularly reflected radiation decreases. The critical angle depends on the electron density at the surface. When an interface is formed, electron density changes locally along the thickness. Hence, a part of the x-ray gets reflected from the interface plane. The remaining part passes through the interface and may then encounter another interface from where another reflection occurs. The intensity of x-ray reflected from each interface depends on the roughness at the interface, difference in electron density across the interface and how sharply it changes along the thickness. Now the reflected x-rays come out of the sample at the same angle and collected by the detector. The reflected beams are coherent in nature but with a constant phase with each other. So, instead of simply adding up they form interference pattern on the detector. The periodicity of the maxima and minima depends on the phase which is largely dependent on the distance between the reflection planes which is nothing but the layer thickness. Thus from reflectivity curve we can precisely measure individual layer thicknesses of multilayer thin films.

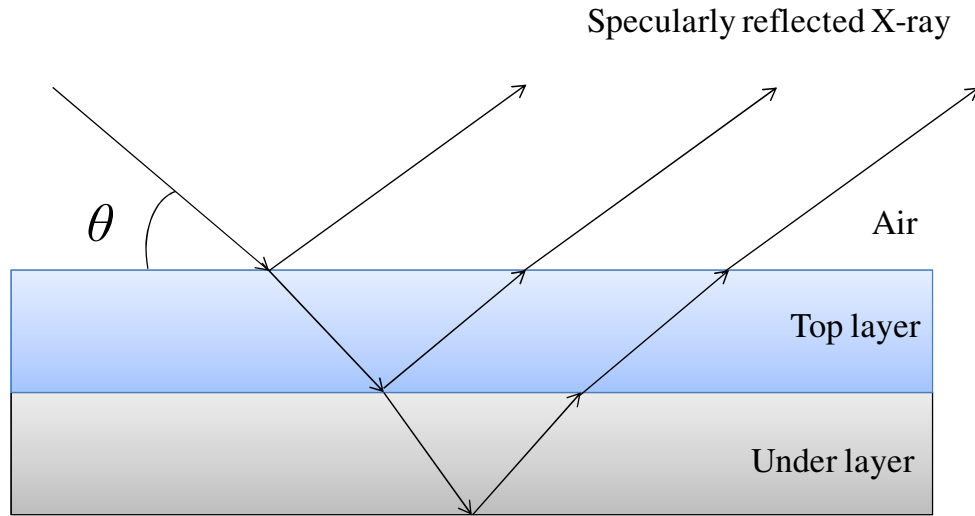


Figure 3.7. Schematic illustration of the working principle of XRR.

3.6. Vibrating Sample Magnetometer

Vibrating sample magnetometer (VSM) is commonly used for the basic characterization of magnetic samples. It enables us to study static magnetic properties of a system by precise measurement of magnetic moment (magnetization) as a function of magnetic field and temperature. The mechanism of VSM stands on the Faraday's law, which states that whenever there is a change in magnetic flux through a coil, an electromotive force (*emf*) is induced in the coil. Mathematically, it can be expressed as follows.

$$E = -NA \frac{dB}{dt} \quad (3.1)$$

Here E is the induced *emf*, A and N are the area and number of turns of the coil. Now replacing B by $H + 4\pi M$ in equation 3.1 and considering constant field applied on the sample we get,

$$E = -NA \frac{dM}{dt}, [H = \text{constant}] \quad (3.2).$$

Equation 3.2 implies that the *emf* generated in the coil is proportional to the magnetization of the sample provided initial magnetization is much smaller than field induced magnetization of the sample.

In VSM there are two pole pieces and the sample is placed in a uniform magnetic field produced by the pole pieces. The sample is mounted in between the pole pieces by a vertical nonmagnetic plastic or quartz rod connected to a piezoelectric transducer. A sinusoidal electrical signal produced by an oscillator is fed into a piezoelectric transducer where it is converted into a mechanical vibration. As a result the sample starts to vibrate in vertical direction inducing voltage in the pickup coil proportional to its magnetization. The voltage is measured by a lock-in amplifier using piezoelectric frequency as reference. A Hall sensor is placed close to a pickup coil to measure the applied field. In this thesis we used VSM to study $M-H$ curves of difference samples. A schematic illustration of the VSM setup is shown in figure 3.8.

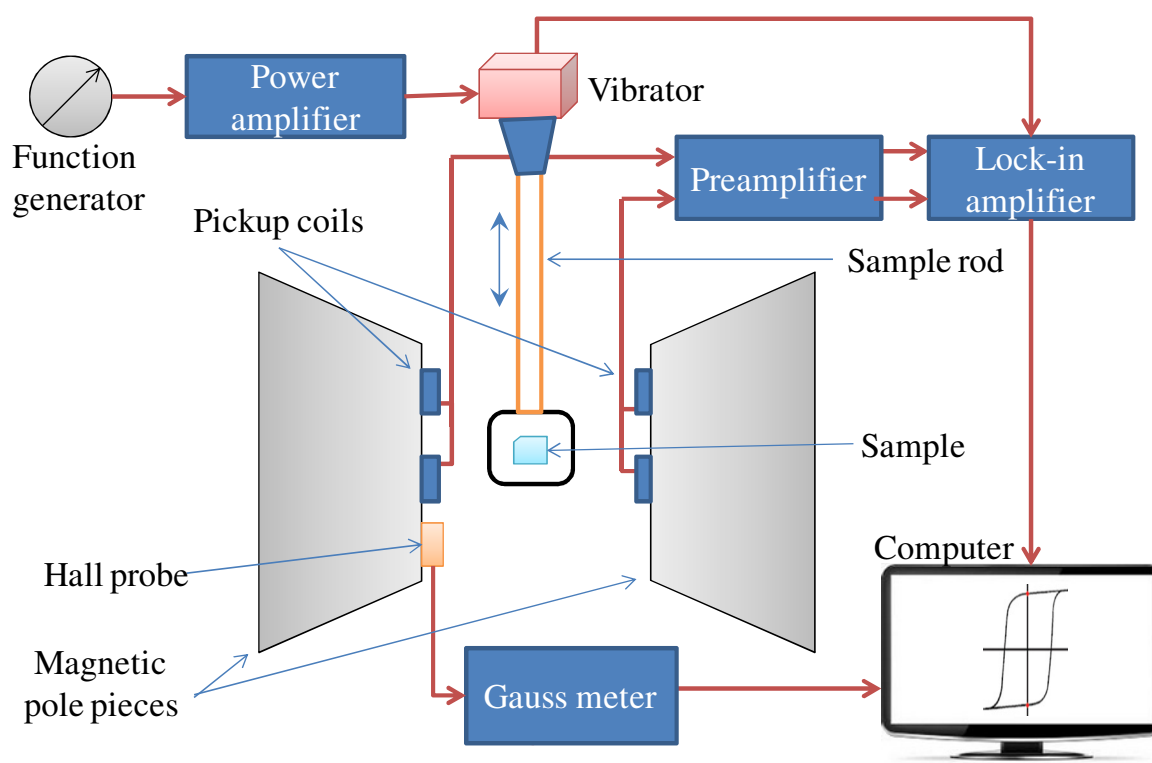


Figure 3.8. Experimental arrangement for vibrating sample magnetometer.

3.7. Atomic Force Microscope

Atomic force microscope (AFM) is an instrument which can map the surface topography of a sample with atomic scale resolution. Typically it can have lateral and vertical resolution down to 10 nm and 0.1 nm, respectively. It works on the principle of inter atomic Van der

Walls forces between sample surface and a sharp tip of the AFM instrument. The tip is attached to one end of a cantilever while the other end remains fixed. According to Hooke's law the cantilever bends due to small force (F) acted on the tip and the deflection (S) at the free end can be calculated as $S = F/K$. Here, K is the spring constant of the cantilever which should be very small for having sufficiently large S . The deflection is monitored by a laser beam focused on the cantilever reflecting to a quadrant photodetector (QPD). The head is scanned over the surface with the help of a piezoelectric tube which can physically bend or stretch in all directions depending on the signal of a feedback controller connected to the QPD (figure 3.9).

The inter-atomic interaction can be described by Lennard-Jones potential (LJ potential) which is a combination of van der Waals attraction and Pauli repulsion mathematically expressed as follows.

$$\phi = -\frac{A}{r^6} + \frac{B}{r^{12}} \quad (3.3)$$

For larger separation the nature of interaction is attractive due to the van der Waals force and for very close separation the interaction is dominated by a strong and short range electrostatic repulsion due to the overlap of electron cloud between atoms called Pauli repulsion.

AFM can be operated in three different modes namely contact, non contact and tapping mode. In contact mode the tip physically touches the sample and scanned over the surface. The imaging is done in the repulsive regime of the potential function (equation 3.3). The bending of the cantilever head causes deflection of the laser spot in the QPD which corresponds to a change in voltage. The signal is used for mapping sample topography as well as adjusting the height of the cantilever. Contact mode AFM offers high scanning speed as well as very good atomic resolution for samples with hard surface. However, it is not appropriate for soft and sticky samples because it may damage the sample and the tip due to their direct contact. In non contact AFM the tip vibrates near its resonant frequency while scanning the sample and it does not physically touches the sample surface. The system keeps the amplitude or frequency constant using feedback. As a result, the average height of the tip is maintained during scanning. In tapping mode the tip vibrates at larger amplitude, which is kept

constant. In this mode the tip can touch the sample only at its lowest position. Hence, it is called intermittent contact mode.

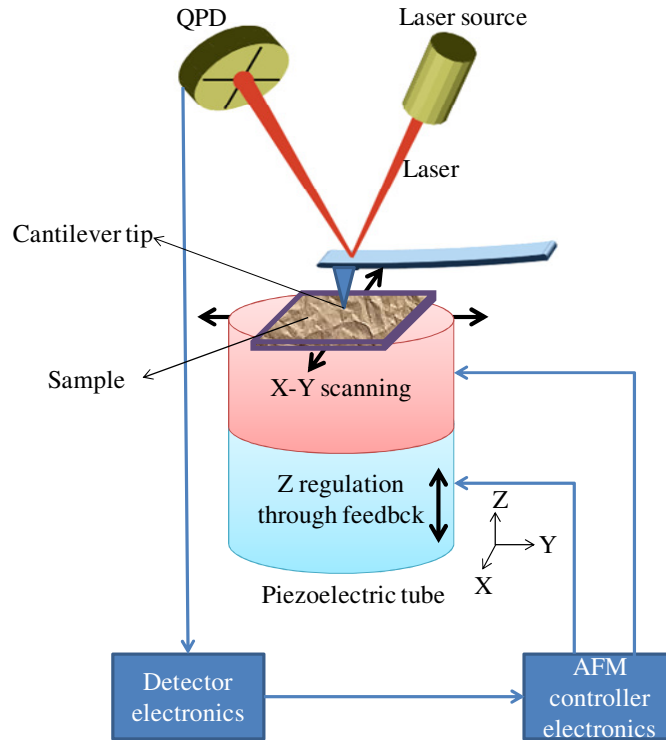


Figure 3.9. Atomic force microscope setup (a schematic diagram).

3.8. Static Magneto-optical Kerr Effect Microscope

Static magneto-optical Kerr effect (MOKE) is an optical technique to measure static magnetization properties of ferromagnetic systems like single or multilayer thin films, dot and anti-dot nanostructures or nanoparticles. The technique works on the principle of MOKE effect which is basically the rotation of plane of polarization of a plane polarized light in presence of magnetization. MOKE can be measured in three different geometries namely polar, longitudinal and transverse geometries. In polar geometry magnetization vector (\vec{M}) is parallel to the plane of reflection but perpendicular to the sample surface. In longitudinal geometry \vec{M} lies in the sample plane parallel to the plane of reflection whereas in the transverse case \vec{M} is in the plane of the sample transverse to the plane of reflection. In our lab we set up our exper-

iment in longitudinal MOKE geometry to measure Kerr rotation as a function of applied magnetic field (hysteresis loop).

In the experimental setup a He-Ne laser of wavelength (λ) = 632 nm is used as light source. The beam passes through a polarizer. The output beam is linearly polarized (*s*-polarization) which is focused on to a magnetic sample by a converging lens or long working distance microscope objective. The reflected beam having Kerr rotation information is collected by another lens and fed into an optical bridged detector. High reflecting mirrors are used to guide the laser beam from the source to the detector. A variable attenuator is placed in the path of the beam to control the intensity of the laser. A combination of lock-in amplifier and optical chopper is used for phase sensitive detection to achieve better signal to noise ratio. Bias magnetic field is applied along the sample plane by an electromagnet, while the field is varied by changing the current in its coil (figure 3.10).

Initially in absence of magnetization, the balanced condition of the detector is achieved by rotating the axis of a polarized beam splitter of the OBD (analyzer) at 45° with respect to the pass axis of the polarizer. At that point the beam will be split into two orthogonal components (A and B) with equal intensities (*i.e.*, $A = B$). Hence, the differential signal ($A - B$) becomes zero. In presence of magnetization the reflected beam becomes elliptically polarized and split in two unequal components resulting in a nonzero value of ($A - B$) (figure 3.10 (bottom)). The value of ($A - B$) is proportional to the magnetization of the sample for small angle of rotation. Hence, a suitable multiplication factor converts the lock-in voltage to Kerr rotation or magnetization which can be plotted as a function of the bias magnetic field. In this way the hysteresis loop is obtained from which we get information like coercivity, remanence, saturation magnetization, domain property and anisotropy useful for the sample characterization. A typical static MOKE hysteresis loop obtained from NiFe(10 nm)/Pt(3 nm) bi-layer is shown in figure 3.10 (bottom).

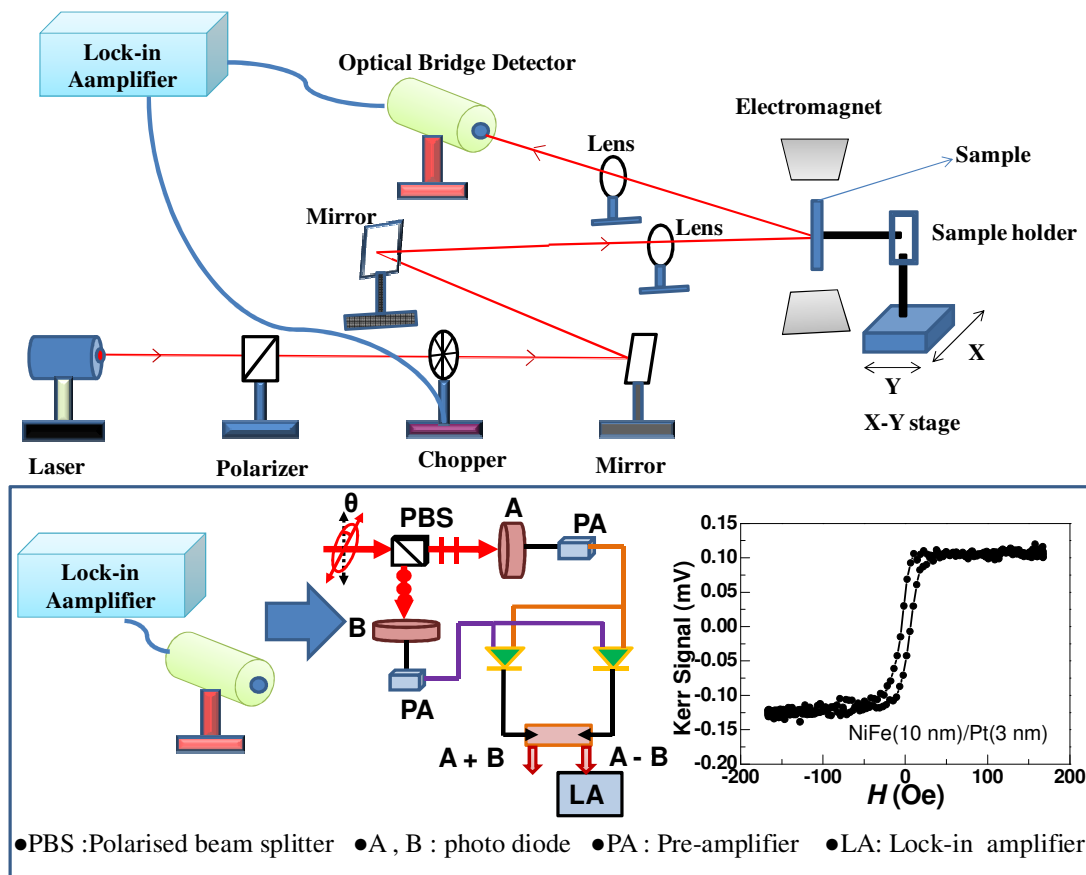


Figure 3.10. A schematic diagram of static magneto-optical Kerr effect (Static MOKE) magnetometer setup (top) and the inside electronics of optical bridge detector along with a typical hysteresis loop obtained from static MOKE in case of NiFe(10 nm)/Pt(3 nm) bi-layer (bottom).

3.9. Time-resolved Magneto-optical Kerr Effect Microscope

The most common application of magneto-optical Kerr effect is static MOKE measurement technique which allows us to investigate the static magnetization properties of a ferromagnetic system by studying hysteresis loop as discussed in the earlier section. Apart from that MOKE can also be used to study the magnetization dynamics of similar system at a very fast time scale and the technique is called time-resolved magneto-optical Kerr effect microscopy[12]. Since its first discovery in 1991[13] TR-MOKE has become a powerful

technique for studying ultrafast magnetization phenomena. The main advantages of this technique are as follows.

1. This is an all-optical technique (i.e., both excitation and detection are done optically) which allow us to investigate of magnetization dynamics at timescales of sub-100 fs.
 - a. Measurement of ultrafast demagnetization occurring at 100s of fs.
 - b. Fast relaxation of magnetization occurring between 1 and 100 ps.
 - c. Precession of magnetization and damping occurring between 10 ps and 1ns).
2. Sample fabrication procedure is straight forward. No additional waveguide structures are required as required in case of ferromagnetic resonance (FMR).
3. This is a local measurement technique.
4. This is a non-invasive measurement technique.

Let us now discuss about the setup, its components, how it works and how to align it prior to a measurement.

3.9.1. Primary Components of the Setup

3.9.1.1. Laser

The Lasing system for this setup involves three lasers in a row. An array of diode lasers pump a solid state laser. The output of the solid state laser is used to pump a Ti-sapphire oscillator with maximum power 10 W and wavelength $\lambda = 532$ nm. Regenerative acousto-optic mode locking mechanism is used inside the Ti-sapphire oscillator called “Tsunami” (Spectra-Physics). At the output of “Tsunami” we have laser pulses of ~ 80 fs pulse-width at 80 MHz repetition rate. The wavelength of the oscillator is tunable from 700–1080 nm. In our experiment we keep the wavelength constant at around 800 nm because our Si-based detectors are most sensitive near that wavelength. A brief discussion the individual lasers are as follows [14-18].

- **Diode Laser**

The CW output of the diode laser bars, consisting of twenty diode lasers, is collimated with a cylindrical micro-lens of high numerical aperture (N.A.). The output beam is coupled into an

optical fiber bundle. Typically 85-90% light of diode laser is coupled into the fiber bundle and directed to the solid state laser [16].

- **Diode Pumped Solid State Laser (Millenia)**

In diode pump solid state laser (Millenia) (figure 3.11) Nd^{3+} ions doped in a Yttrium Vanadate crystalline matrix (Nd:YVO_4) is used as the gain medium. The monochromatic output of the diode laser overlaps with the absorption spectra of the Nd^{3+} resulting in an efficient pumping. The efficiency of the Millenia is further improved by focusing the diode laser output on a volume in the active medium of the Millenia in such a way that it matches with the radius of TEM_{00} mode of the Millenia. The Nd^{3+} is a four level system where infrared light of wavelength (λ) = 1064 nm is emitted due to the transition of an electron from $4F_{3/2}$ level to $4I_{1/2}$ level. There are also transitions at 1319, 1338 and 946 nm. However, at room temperature they have lower gain as compared to 1064 nm. A lithium triborate (LBO) nonlinear crystal is used as a frequency doubler to convert the 1064 nm light into visible light ($\lambda = 532$ nm). As the efficiency of the LBO crystal is sensitive to temperature. Hence a temperature regulating oven is used to ensure constant λ at the output. A controller operated shutter placed outside the cavity to block the output beam whenever required.

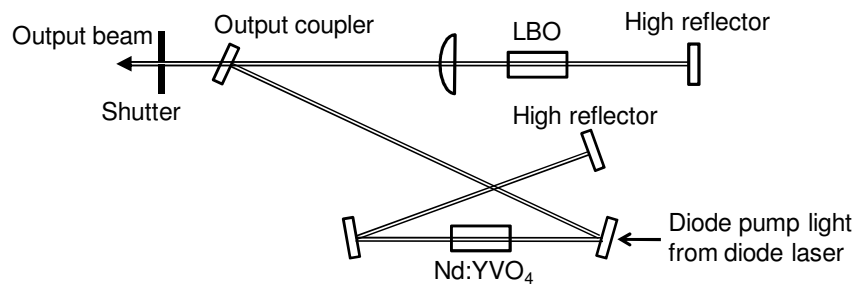


Figure 3.11. Schematic diagram of Millennia laser head. The figure is reproduced from reference 16.

- **Mode locked Ti-sapphire Laser (Tsunami)**

The lasing medium for Tsunami is titanium ions (figure 3.12) (Ti^{3+}) doped sapphire (Al_2O_3) crystal. Here the absorption occurs in the spectral range of 400-600 nm. Hence, the 532 nm laser from the output of the Millennia can efficiently pump the Tsunami. The fluorescence band also extends over a broad range from 600 nm to 1000 nm. However, the short wavelength end of fluorescence and long wavelength end of the absorption spectrum overlap with each other making lasing action possible only for $\lambda > 670$ nm.

To achieve a repetition frequency of ~ 80 MHz at the output of Tsunami it is essential to have a cavity longer than that in a CW laser. The longer cavity length is obtained by a ten-mirror folded arrangement as presented in figure 3.12 for optimizing space.

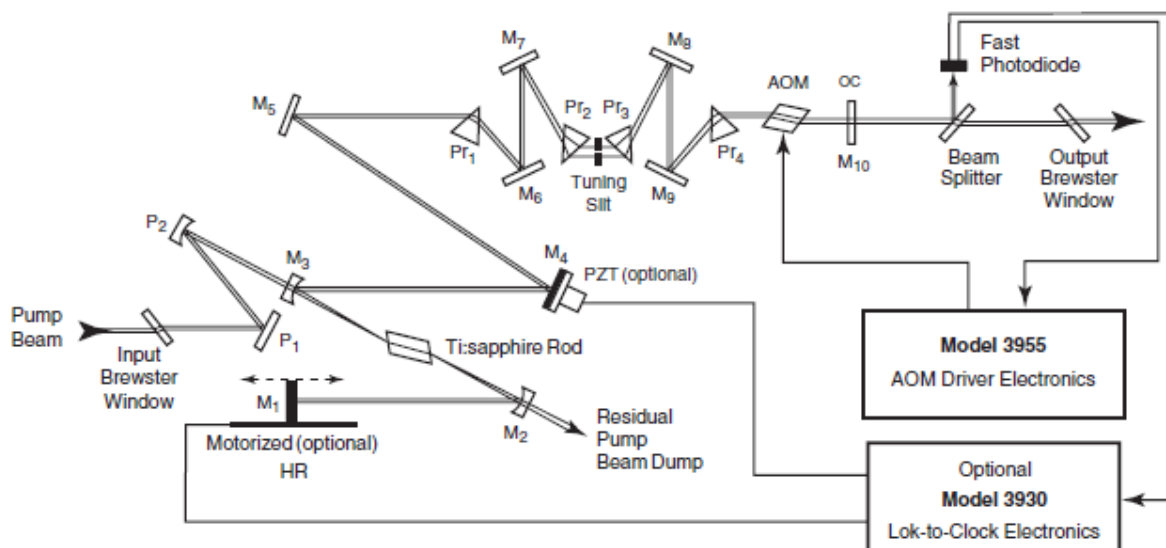


Figure 3.12. A schematic of the beam path inside the folded cavity of Tsunami. The figure is reproduced from reference 14.

The cavity is highly sensitive to the atmospheric condition like moisture, dust, chemical reaction and temperature. Hence, clean dry and less reactive nitrogen gas (99.999%) is purged to the laser head for the removal of dust and vapor. A chiller unit is also provided to keep the Ti-sapphire rod at constant temperature for long term stable performance.

Group velocity dispersion and wavelength selection: It is known that the time-bandwidth product of a Gaussian pulse is constant. Hence, for a shorter pulse, we have a larger distribution of frequency. As the refractive index (n) depends on frequency, there is a distribution of n in a pulse resulting in a variation of velocity. The variation is called as the group velocity dispersion (GVD). If lower frequencies travel faster than the higher frequencies, then that is called positive GVD and the corresponding pulse is said to be positively chirped and *vice versa* (see figure 3.13).

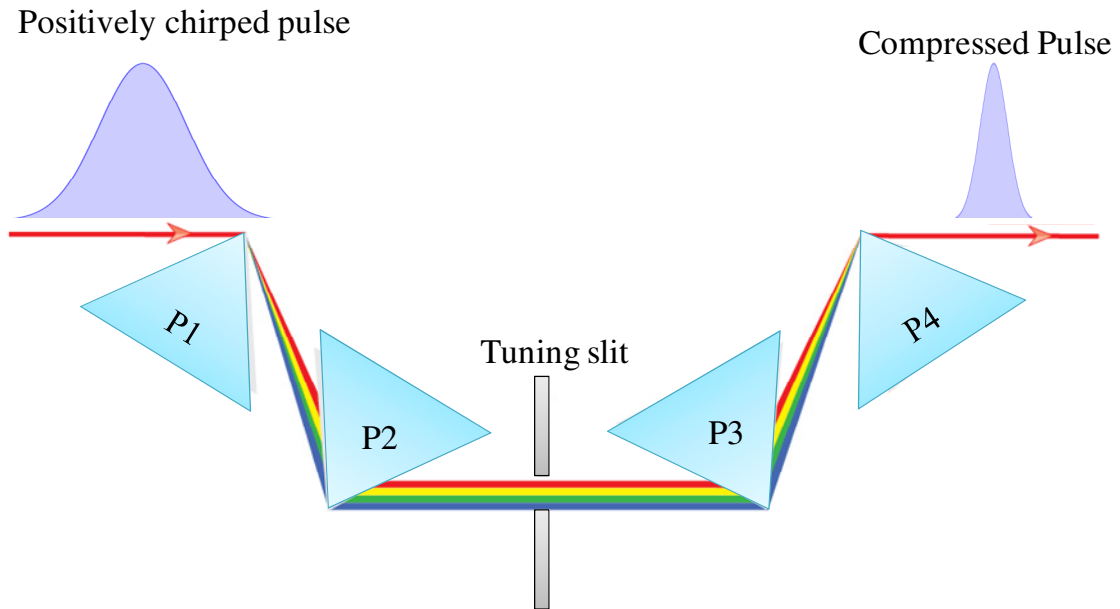


Figure 3.13. The four prism arrangement used for dispersion compensation in Tsunami laser.

In Tsunami laser, positive GVD is compensated by a four prism arrangement as shown in Fig. The net intracavity GVD is tuned by translating prisms P_2 and P_3 perpendicular to their bases. The working frequency and the bandwidth of the output laser are selected by adjusting the width and position of a slit placed between P_2 and P_3 .

3.9.1.2. Second Harmonic Generator (SHG)

Inside the second harmonic generator (SHG) cavity there is a nonlinear crystal of barium beta borate (BBO) which doubles the frequency of the laser coming from Tsunami. It produces the second harmonic beam with polarization axis perpendicular to the fundamental, whereas the

polarization of the residual fundamental beam remains unchanged. A prism separates the second harmonic from the residual fundamental beam. The high reflective coating on the prism at infrared wavelength reflects the fundamental beam while the second harmonic is diffracted. Then the beam is guided to the output by a pair of prisms which make the beam almost parallel to the fundamental. These prisms have anti-reflection (AR) coating at second harmonic wavelength to reduce the loss of output intensity by reflection.

Here the BBO crystal is used for the following advantages:

1. It minimizes pulse broadening due to group velocity dispersion (GVD).
2. No compensating crystal is required.
3. Only a single SHG crystal is required to match the phase over the entire tuning range (690 nm to 1090 nm).
4. The BBO has higher conversion efficiency as compared to LBO crystal and the crystal does not require any heater for maintaining temperature.

3.9.2. Experimental Setup

Our home built TRMOKE microscope[12], schematically shown in figure 3.14, with collinear pump-probe geometry is based upon a mode locked Ti-sapphire pulsed laser source with tunable wavelength between 700 and 1000 nm and pulse-width of about 80 fs. The fundamental beam is divided into two parts by a 7:3 beam splitter. The intense part goes through the SHG to produce the second harmonic ($\lambda = 400$ nm), which is used to pump the sample. The time-delayed fundamental is used to probe the dynamics by measuring the change in the Kerr rotation of the reflected probe beam by an optical bridge detector in a phase-sensitive manner. The time delay is created by a retro reflector fixed on an automated variable delay stage on the path of the probe beam. The probe beam is first focused on the sample surface to a diffraction limited spot size of ~ 800 nm with the help of a microscope objective (N.A. = 0.65) and an x-y-z piezoelectric scanning stage. The pump beam is made collinear with the probe beam with the help of steering mirrors and is spatially overlapped with the probe beam to a spot size of ~ 1 μm after passing through the same microscope objective. The two-color collinear pump-probe geometry enables us to achieve a very good spatio-temporal resolution and non-invasive detection sensitivity in our measurements. A bias field is applied to the sample, the direction of which was tilted slightly out of plane of the sample to have a finite

demagnetizing field along the direction of the pump pulse. A time-resolved reflectivity and magnetization data (black and green curves respectively in figure 3.14) can be obtained simultaneously using this technique.

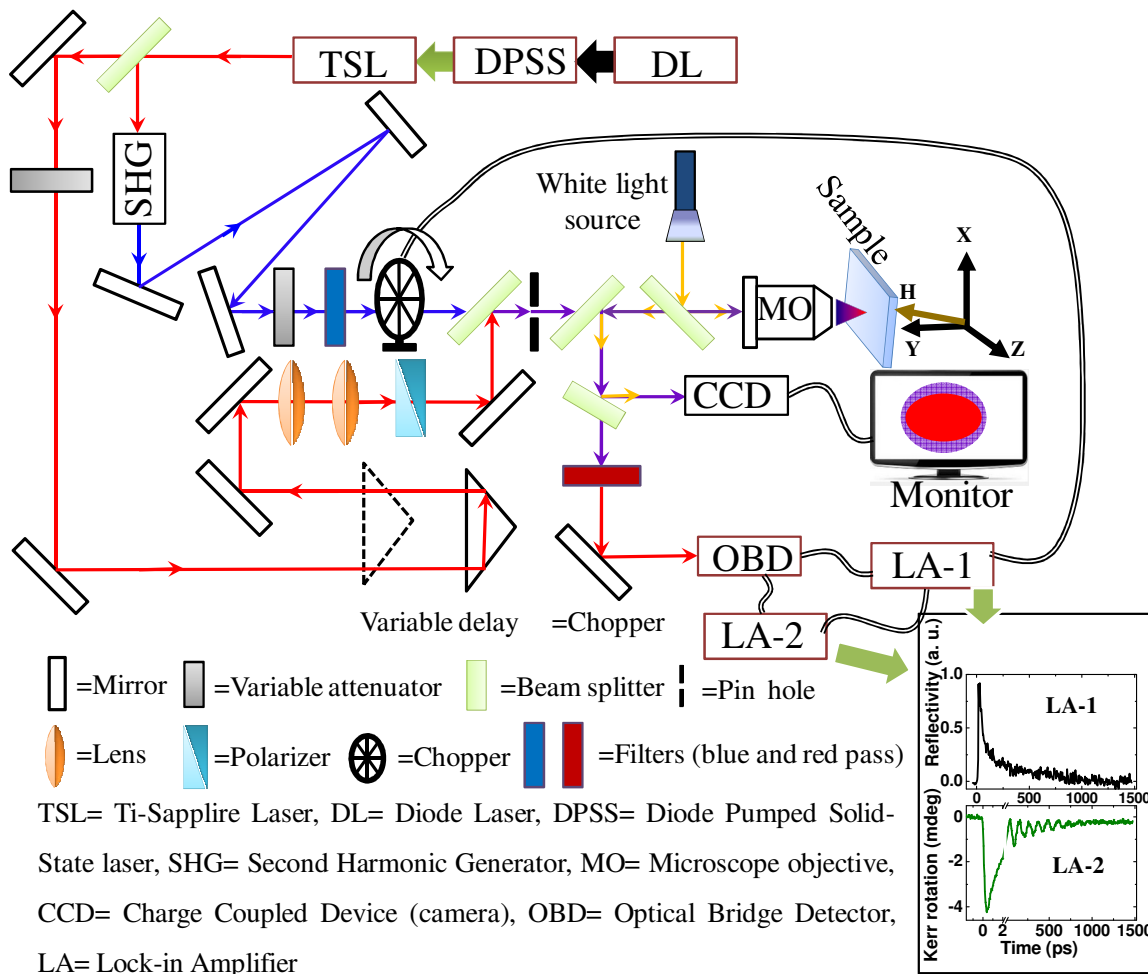


Figure 3.14. Schematic diagram of the time resolved magneto-optical Kerr effect (TRMOKE) microscope.

Figure 3.15(a) shows a typical time-resolved Kerr rotation data with three temporal regions. In Region I ($t < 0$) sample is probed before excitation which shows steady magnetization under external bias field. Region II (up to few tens of ps) shows a sharp demagnetization (500 fs) and a subsequent fast relaxation. This is followed by a slower relaxation in region III and

precession of magnetization around its new equilibrium position. Figure 3.15(b) shows a bi-exponential background subtracted precessional oscillation data fitted by a damped harmonic function for α whereas Figure 3.15(c) is the fast Fourier transform (FFT) of the same from which precession frequency (f) is obtained.

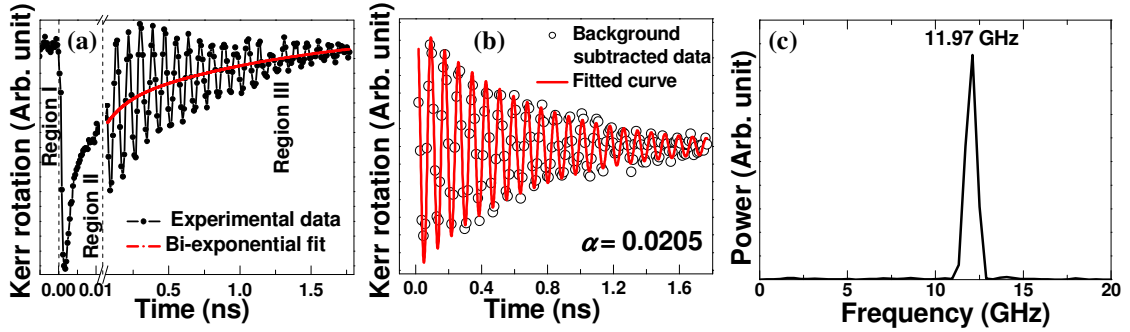


Figure 3.15. (a) Typical time-resolved Kerr rotation data from Pt(6.8 nm)/Ni₈₁Fe₁₉(12.7 nm)/MgO(2.4 nm) sample at a bias field of 1.4 kOe., (b) precessional oscillation part of the time resolved data and (c) fast Fourier transform of figure 3.15(b).

3.9.3. Some Routine Alignments

The experiment is very sensitive to the alignment of the system. Hence prior to the experiment one should follow some routine alignment procedure as follows.

1. At first, the output power and spectra of Tsunami are maximized after adjusting the central wavelength ($\lambda_0 = 800$ nm) and FWHM (~ 12 nm or more) with the help of external micrometer controllers of Tsunami.
2. The alignment of the retro-reflector (RR) is checked by placing a beam height after RR. If the beam gets shifted by moving the delay stage, mirrors before RR are adjusted to stop the shift.
3. The co-linearity of the pump and probe beams is checked by placing the beam height after the beam combiner (BC). Both beams should go through the hole on the beam height. The overlap is further confirmed by observing their images in a CCD camera. Any misalignment is fixed with the help of adjustable mirrors.
4. Next we check whether the pump and probe beams are co-axial with the MO or not. For that we check the back aperture of the microscope objective by an infrared view-

er. For fine tuning we monitor the pump and spot falling on to a substrate by a CCD camera. The MO is moved back and forth with the help of micrometer screw attached to the stage on which it is mounted. The pump and probe beams are focused and defocused repeatedly by moving the MO and we see the image on a display connected to the camera. A movement of the centre(s) of the pump and/or probe spot(s) on the screen implies that the beam(s) is (are) not co-axial with the MO. In that case, the pump and/or probe beams are made collinear with the help of two mirrors one near and one far from the MO.

5. Finally, the alignment of the OBD is confirmed by superposing the back reflected beam from OBD with the incident beam.
6. When the desired alignment is achieved the time-resolved reflectivity data from a test Si wafer is measured for about ~ 2000 ps (figure 3.16). The relaxation rate of the signal is compared with the standard data to verify the alignment condition.

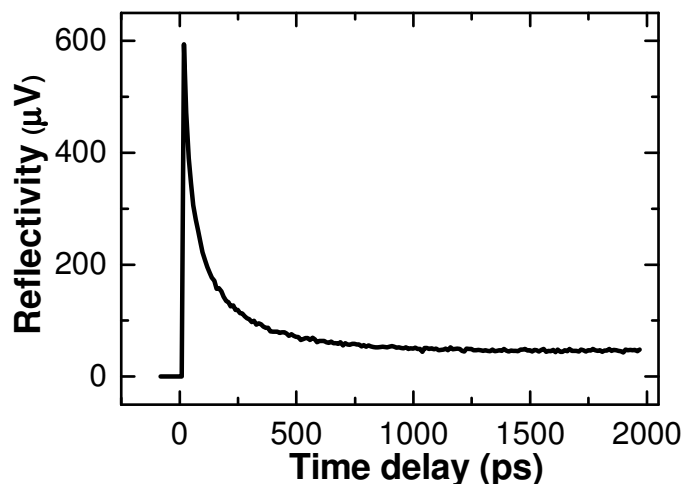


Figure 3.16. A standard reflectivity signal obtained from a Si(100) wafer as a function of the time delay between the pump and the probe beams.

3.10. Spin Torque Ferromagnetic Resonance

In this section we discuss spin torque ferromagnetic resonance (ST-FMR) which is a versatile all-electrical technique for studying the dynamical properties of a magnetic system as illustrated in figure 3.17. The technique involves rf current applied using a signal generator (MXG N5183A, Agilent) to excite a magnetic sample. The signal is launched through a

ground-signal-ground (GSG) pico-probe at a particular frequency while a bias magnetic field is applied by an electromagnet. A dc signal can also be applied with rf current along the same line in case of dc spin current induced modulation of damping experiment. The sample is designed in a rectangular shaped element acting as a part of a co-planer waveguide. The dimension of the waveguide is calculated for having 50Ω impedance. The value is conventionally chosen for a good compromise between low attenuation and power handling. The impedance is kept constant throughout the line to avoid the possibility of undesired reflections which would lead to the formation of standing waves on the trace introducing loss in the channel and noise in the spectra.

The detection technique is based on spin torque diode effect[19]. The oscillating magnetization gives rise to an oscillating resistance due to anisotropic magnetoresistance of the ferromagnet. Let us consider the applied current as $I_0 \cos \omega t$, where ω is the frequency of the rf signal. Hence, the resistance oscillates at the same frequency ω with a constant phase ϕ given by $R = R_0 + \delta R \cos(\omega t + \phi)$. Thus from Ohm's law we get the expression for voltage appearing across the sample as in equation 3.4.

$$V = I_0 R_0 \cos \omega t + \frac{I_0 \delta R}{2} \cos(2\omega t + \phi) + \frac{I_0 \delta R}{2} \cos \phi \quad (3.4)$$

The expression contains a second harmonic and a dc signal in addition to the fundamental which is comparable to the diode rectification effect. Hence, it is called spin torque diode effect. The dc part of the voltage is separated using a bias tee and fed into a nanovoltmeter or lock-in amplifier for the detection of FMR. In case of lock-in amplifier, a phase sensitive detection is used by applying low frequency amplitude modulated signal to the sample. In our study we use a bias tee, 2182A digital nanovoltmeter, low voltage meters and LI 5640 digital lock-in amplifier.

FMR spectrum can be obtained in two ways. Either the bias field is kept constant while excitation frequency is varied or vice versa. In our experiment we kept the excitation frequency constant and varied bias field applied on a sample for obtaining a spectrum. The excitation frequency usually varies between 4-12 GHz and excitation power is kept constant at +10 dBm. Bias field is varied between 0-1.8 kOe with a time constant of 3 second. The direction

of the magnetic field can also be varied by 360° in the plane of the sample by rotating the electromagnet pole pieces.

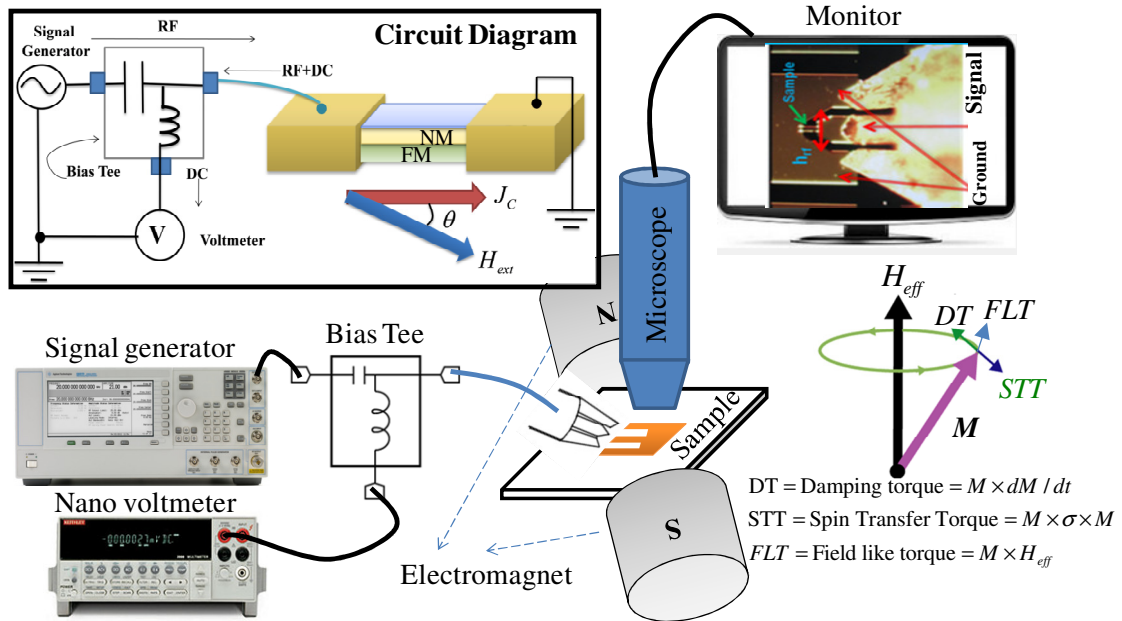


Figure 3.17. Schematic of the ST-FMR measurement set up and the mechanism of FMR absorption.

In figure 3.18 a typical ST-FMR spectrum (black) is shown with its symmetric (red) and asymmetric (blue) components corresponding to spin transfer torque and Oerstead field induced torque.

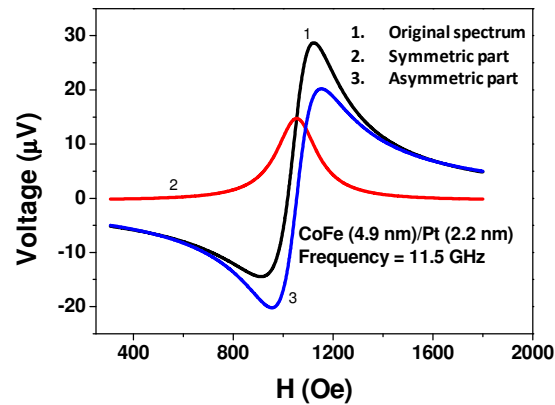


Figure 3.18. A typical ST-FMR spectrum (black) along with its symmetric (red) and asymmetric components (blue).

References

- [1] Kelly, P. J. & Arnell, R. D. Magnetron sputtering: a review of recent developments and applications. *Vacuum* **56**, 159 (2000).
- [2] Fassbender, J. & McCord, J. Magnetic patterning by means of ion irradiation and implantation. *J. Magn. Magn. Mater.* **320**, 579 (2008).
- [3] Burn, D. & Atkinson, D. Control of domain wall pinning by localised focused Ga⁺ ion irradiation on Au capped NiFe nanowires. *J. Appl. Phys.* **116**, 163901 (2014).
- [4] Aziz, A. *et al.* Angular Dependence of Domain Wall Resistivity in Artificial Magnetic Domain Structures. *Phys. Rev. Lett.* **97**, 206602 (2006).
- [5] Lavrijsen, R. *et al.* Controlled domain-wall injection in perpendicularly magnetized strips. *Appl. Phys. Lett.* **96**, 222502 (2010).
- [6] Ganguly, A. *et al.* Tunable magnetization dynamics in interfacially modified Ni₈₁Fe₁₉/Pt bilayer thin film microstructures. *Sci. Rep.* **5**, 17596 (2015).
- [7] King, J. A. *et al.* Local control of magnetic damping in ferromagnetic/non-magnetic bilayers by interfacial intermixing induced by focused ion-beam irradiation. *Appl. Phys. Lett.* **104**, 242410 (2014).

- [8] Arac, E. *et al.* Study of focused-ion-beam–induced structural and compositional modifications in nanoscale bilayer systems by combined grazing incidence x ray reflectivity and fluorescence. *J. Appl. Phys.* **111**, 044324 (2012).
- [9] Burn, D. M. Domain wall behaviour in ferromagnetic nanowires with interfacial and geometrical structuring, Ph.D. thesis, Ch. 6, 135-160 (Durham University, 2013).
- [10] Burn, D., Hase, T. & Atkinson, D. Focused-ion-beam induced interfacial intermixing of magnetic bilayers for nanoscale control of magnetic properties. *J. Phys. Condens. Matter* **26**, 236002 (2014).
- [11] McMullan, D. Scanning Electron Microscopy 1928–1965. *Scanning* **17**, 175 (1995).
- [12] Barman, A. H., A. in *Solid State Physics* Vol. 65 eds E. Camley Robert & L. Stamps Robert) 1-108 (Academic Press, 2014).
- [13] Freeman, M., Ruf, R. & Gambino, R. Picosecond pulsed magnetic fields for studies of ultrafast magnetic phenomena. *IEEE Trans. Magn.* **27**, 4840 (1991).
- [14] User's Manual, “Tsunami: Mode-locked Ti:sapphire Laser”. (*Spectra-Physics*, California, USA, 2002).
- [15] User's Manual, “Model 3980: Frequency Doubler and Pulse Selector” (*Spectra-Physics*, California, USA, 2002).
- [16] User's Manual, "Millenia Pro s-Series: Diode-Pumped, CW Visible Laser System”. (*Spectra-Physics*, California, USA, 2007).
- [17] Silfvast, W. T. *Laser Fundamentals*. (Cambridge University Press, 1996).
- [18] Svelto, O. *Principles of Lasers*. (Springer, 2009).
- [19] Tulapurkar, A. *et al.* Spin-torque diode effect in magnetic tunnel junctions. *Nature* **438**, 339 (2005).

Chapter 4

Local Control of Magnetic Damping in Ferromagnetic/non-magnetic Bi-layers by Interfacial Intermixing Induced by Focused Ion-beam Irradiation

The influence of interfacial intermixing on the picosecond magnetization dynamics of ferromagnetic/non-magnetic thin-film bi-layers was studied. Low-dose focused-ion-beam irradiation was used to induce intermixing across the interface between a 10 nm $Ni_{81}Fe_{19}$ layer and a 2–3 nm capping layer of either Au or Cr. Time-resolved magneto-optical Kerr effect was used to study magnetization dynamics as a function of ion-beam dose. With an Au cap, the damping of the un-irradiated bi-layer was comparable with native $Ni_{81}Fe_{19}$ and increased with increasing ion dose. In contrast, for $Ni_{81}Fe_{19}/Cr$ the damping was higher than that for native $Ni_{81}Fe_{19}$, but the damping decreased with increasing dose.

4.1. Introduction

Picosecond magnetization dynamics are largely controlled by damped precessional processes, and consequently, magnetic damping has received significant research attention both for the fundamental physics [1] and for technological applications [2]. For spin-transfer torque magnetoresistive random access memory (STT-MRAM) and magnonic devices, low damping facilitates a lower writing current and longer propagation of spin waves; higher damping is desirable for increasing the reversal rates and the coherent reversal of magnetic elements, as damping suppresses the precessional motion of the magnetization vector. In general, the control of magnetic properties at the micro- and nano-scale is important for technological applications. Magnetization dynamics are commonly described phenomenologically by the Landau-Lifshitz-Gilbert equation[3]

$$\frac{dM}{dt} = -\gamma M \times H_{eff} + \frac{\alpha}{M_s} M \times \frac{dM}{dt} \quad (4.1),$$

where M is the magnetization, γ is the gyromagnetic ratio, H_{eff} is the effective magnetic field, and α is the dimensionless Gilbert damping coefficient. The damping coefficient can be modified by introducing doping elements including rare earth [4-7] or transition metal [8-9] elements, with the dopant introduced by co-deposition, usually co-sputtering. A disadvantage of this approach is that the entire material is doped.

An alternative method for doping is direct irradiation with an ion beam of the desired dopant.[10] Dopants including Cr,[10] Tb,[11] Gd,[11] Ni,[12] and Fe[13] have been introduced as implanted ions. This approach can be used to introduce dopants into a localized area via lithography,[11,14] with an appropriate ion source. High-energy beams are needed to ensure adequate doping, requiring either a research accelerator or a commercially available accelerator-based ion implanter[11]. High-energy heavy-ion irradiation is not usually compatible with local patterning[15].

Dopants introduced by ion-irradiation can affect the magnetic properties by introducing specific atomic species into the material, by altering the microstructure of the magnetic material (e.g., recrystallization or amorphization) or through intermixing in multilayered structures. The saturation magnetization, magnetic anisotropy, coercivity, and damping can be modified by direct ion implantation.[12,16] Sufficient dopant can be introduced to produce significant alterations to the magnetic behavior, for example, irradiation by Cr^+ ions can cause paramagnetism in NiFe [16] and both Tb^+ and Gd^+ ions modify the damping in NiFe. These results are similar to those obtained from co-sputtering, thus indicating the effects are intrinsic to the dopants.[11] However, in the case of Cr, the damping varies according to whether the Cr is co-sputtered or ion-implanted,[10] with the biggest increase observed for implantation. With the exception of recent work on epitaxial vanadium-doped iron,[17] the addition of dopants typically increases damping.[8] Spin-wave waveguides have recently been fabricated by implanting Cr ions in selective areas of NiFe by lithographic patterning.[14] Ion beam irradiation can also modify the magnetic behavior through direct modification of the structure of the material being irradiated, without the ions acting as a dopant. Ion bombardment of a solid interface results in thousands of intermixed atoms per single ion impact[18]. Ar^+ ion irradiation has been shown to cause intermixing in Co/Pt layers, grain growth and increased interfacial

roughening, changing the magnetization from perpendicular to in-plane,[19] while intermixing in antiferromagnetic/ferromagnetic bi-layers has been shown to modify the damping.[20] Also, light ions, such as He^+ , can cause intermixing, but have been shown to end up buried in the substrate.[21] Local ion-beam-induced variations of magnetic properties have been introduced through resist-based lithographic techniques resulting in purely magnetic patterning.[14]

In contrast to mask-based ion beam patterning, focused ion-beam (FIB) irradiation allows direct nanoscale patterning without additional lithographic processes. However, although a range of ion species can be incorporated into FIBs, most commercial systems are limited to Ga^+ ions. Earlier work suggested that direct implantation of Ga^+ at high fluences is the main mechanism for modifying the magnetic properties [22] and that moderate fluences can tune the coercivity, saturation magnetization and anisotropy field in NiFe/Au bi-layers.[23] In bilayered or multilayered ferromagnetic/nonmagnetic (FM/NM) systems, low-dose FIB irradiation could be used to induce interfacial doping providing a route to locally modify the magnetic properties without substantial structural changes or damage.

Here, the magnetic damping behavior of ferromagnetic/non-magnetic thin-film bi-layers was investigated as a function of systematic intermixing of the bi-layer interface induced by low-dose focused-ion-beam irradiation. The dynamic magnetization response was measured by time resolved magneto-optic Kerr effect (TR-MOKE) microscopy. The results indicate that intermixing across the FM/NM interface, using FIB provides a mechanism for local control of the damping within the bi-layer system that may open opportunities for magnetic device applications and for creating magnonic crystal structures.

4.2. Sample Preparation and Experimental Details

Measurements were made on FM/NM bi-layer microstructures where the FM layer was $\text{Ni}_{81}\text{Fe}_{19}$ (NiFe) with a thickness of 10 nm and a thin NM cap (2–3 nm) of either Au or Cr. Arrays of 30 μm diameter circular structures were patterned from the same bi-layer, allowing many different FIB irradiation doses to be applied to the same bi-layer. The areas of the circles were small enough to irradiate relatively quickly but easy to locate and large enough for measurements of the magnetization using the TR-MOKE, the scale of structures also suggests any side-wall oxidation can be ignored.

The bi-layers were deposited on to a hydrothermally oxidized Si/SiO₂ substrate by thermal evaporation, with the deposition of the NiFe, Au and Cr from a base pressure of 1×10^{-7} Torr. Irradiation was performed using a FEI Helios Nanolab 600 FIB microscope with a 30 keV Ga⁺ ion beam at normal incidence. The circles were individually irradiated by rastering the focused ion beam over a 50 μm square area. Irradiation doses ranged from 0 to 2.5×10^{15} Ga⁺/cm² (0–4 pC/ μm^2), using a beam current of 28 pA. This current should not result in significant heating and earlier work showed that the modifications depend on the total dose and not the specific current.[24]

The dynamic magnetization behavior of individual lithographic structures was measured using an all-optical TR-MOKE system based upon a collinear two-color pump probe geometry.[25] Magnetization was pumped with femtosecond laser pulses at a wavelength of 400 nm, a pulse width of 100 fs, and a typical fluence of 10 mJ/cm² (spot size of about 1 μm). The magnetization was probed with linearly polarized 800 nm wavelength pulses, with a 70 fs pulse width, and a typical fluence of 1.5 mJ/cm² (spot size of about 800 nm). A biasing magnetic field was applied at a small angle ($5^\circ - 15^\circ$) to the sample plane during the measurements, the in-plane component of which is referred to here as H .

The raw TR-MOKE data can be divided into three temporal regimes. First, an ultrafast demagnetization was observed within the first 500 fs, this was followed by a rapid remagnetization within 10 ps and a slower remagnetization (260 ps for NiFe/Au and 1.2 ns for NiFe/Cr), superimposed on which was damped oscillatory behavior. This oscillatory behavior represents the precessional motion of the magnetization. For analysis of the data, a bi-exponential background was fitted to the decaying signal and subtracted to isolate the precessional behavior. A fast Fourier transform with a Welch window function was used to obtain the frequency spectra. The time-domain data were fitted with an exponentially damped harmonic function to obtain the relaxation time and from this the damping coefficient α [26].

4.3. Results and Discussion

Figure 4.1 shows examples of the background-corrected magnetization oscillations measured for the NiFe/Au bi-layer system as a function of low to moderate irradiation dose at $H=1.5$ kOe. In all cases, the data show damped single frequency sinusoidal behavior, allowing the

evolution of α and the precessional frequency to be determined as a function of FIB dose, see figure 4.2. For the un-irradiated bi-layer α is approximately 0.01, which is consistent with the typical values for $\text{Ni}_{81}\text{Fe}_{19}$.^[27] With increasing dose α increases, the data show some scatter but, to a first approximation, across the range investigated α increases linearly with dose at a rate of $0.0035 \mu\text{m}^2/\text{pC}$. In contrast, the precessional frequency data show less scatter and are characterized by a general decrease upon which a small peak is imposed between 1.3 and 2.0 $\text{pC}/\mu\text{m}^2$.

Figure 4.3 shows examples of the background-corrected magnetization oscillations measured for the NiFe/Cr bi-layer system as a function of low dose irradiation at $H=1.5$ kOe. Since the mass of Cr is lower than the Au the irradiation induced intermixing was expected to occur at lower doses, hence a smaller dose range was investigated. The damping coefficient α and the precessional frequencies for the NiFe/Cr bi-layers are shown as a function of ion dose in figure 4.4. In contrast to the NiFe/Au, the value of α of the un-irradiated NiFe/Cr bi-layer was significantly higher than that for the uncapped NiFe, indicating an enhancement of the damping associated with the Cr layer. With increasing dose, the damping showed significant variability but, in general, fell at a rate of $0.0054 \mu\text{m}^2/\text{pC}$.

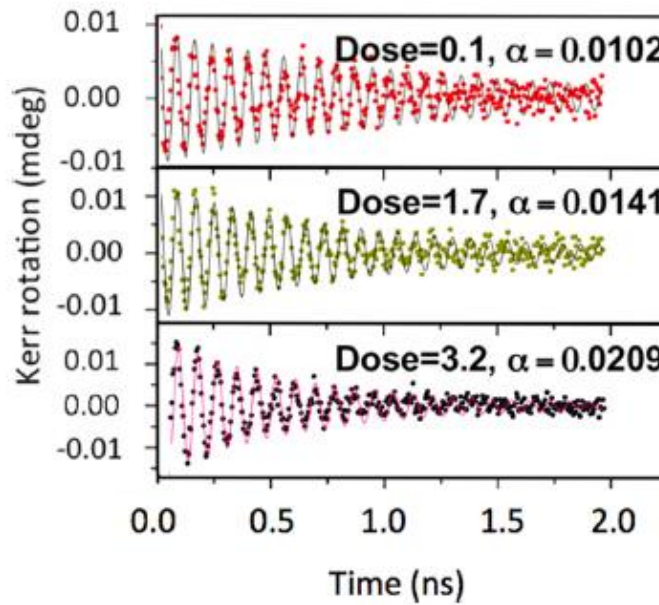


Figure 4.1. Examples of the background-corrected magnetization oscillations measured using TR-MOKE for NiFe/Au bi-layered microstructures as a function of low-to-moderate Ga^+ ion irradiation dose at $H=1.5$ kOe.

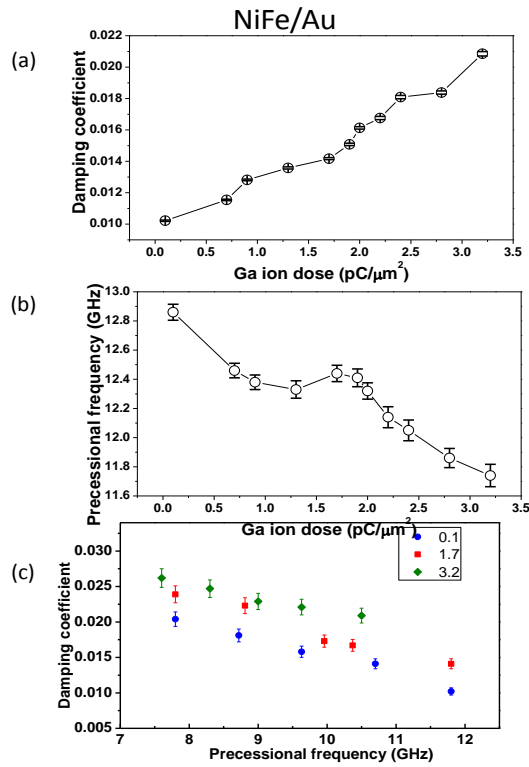


Figure 4.2. (a) The damping coefficient, α , (note: error bars are smaller than data points) and (b) the precessional frequencies obtained from the TRMOKE data of a NiFe/Au bi-layer as a function of FIB dose at $H=1.5$ kOe. (c) The precessional frequency dependence of the damping determined by varying H , for irradiation doses of 0.1 (triangle), 1.7 (circle), and 3.2 (square) $\text{pC}/\mu\text{m}^2$.

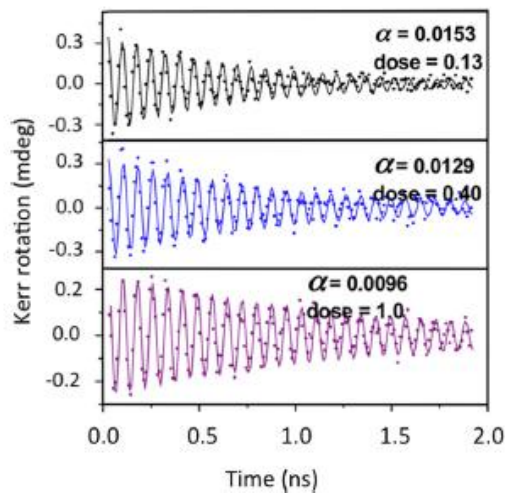


Figure 4.3. Examples of the background-corrected magnetization oscillations measured for NiFe/Cr microstructures as a function of low Ga^+ ion irradiation dose at $H= 1.5$ kOe.

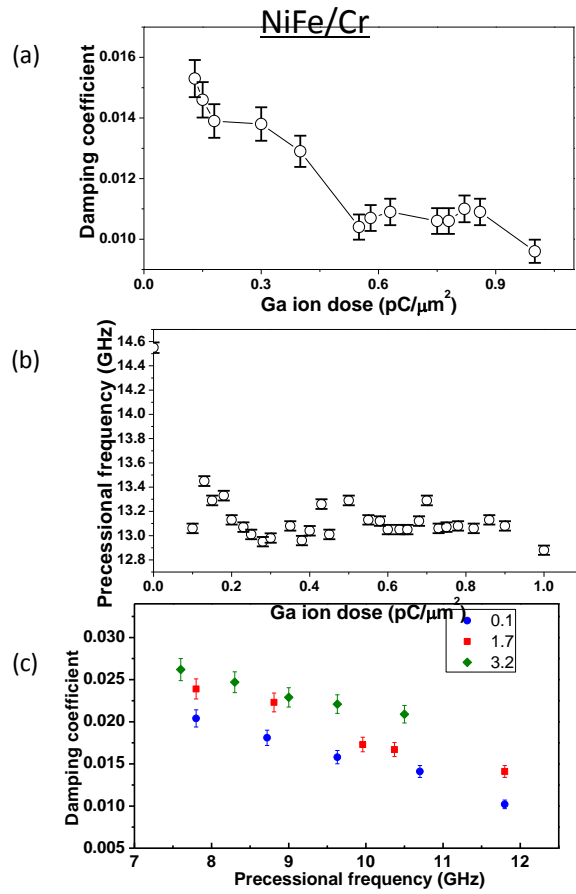


Figure 4.4. (a) The damping coefficient, α , and (b) the precessional frequencies obtained from the TR-MOKE data of a NiFe/Cr bi-layer as a function of FIB dose at $H=1.5$ kOe. (c) The precessional frequency dependence of the damping determined by varying H , for irradiation doses of 0.13 (triangle), 0.40 (circle), and 1.00 (square) $\text{pC}/\mu\text{m}^2$.

Detailed analysis of the structural changes induced by low-dose FIB irradiation in NiFe/Au bi-layers, undertaken using grazing incidence x-ray reflectivity, x-ray fluorescence, and Monte Carlo simulations,[28] showed that sputtering of material was very limited at these doses and restricted to the non-magnetic capping layer. Also, Ga^+ implantation was a very small dopant fraction (up to the order of 1%) over the relevant dose range. In contrast, intermixing at the FM/NM interface was significant, leading to a compositionally graded alloy

extending over several nanometers at the interface.[28] Furthermore, quasi-static MOKE, SQUID, and x-ray magnetic circular dichroism (XMCD) measurements of FIB irradiated NiFe/Au bi-layers revealed complex changes in the magnetization as a function of the ion beam dose[24]. For a 2.5 nm Au cap, the saturation magnetization falls rapidly in the low dose regime to a minimum around 1.3–2.0 pC/ μm^2 and recovers to a small peak before falling further with increasing irradiation.[24]

There have been significant developments in the theoretical understanding of the mechanisms for damping in Fe,[29-31] Ni,[29-31] and Co[30-31] and more generally in transition metal alloys (NiFe),[27] which have shown the significance of the effective field from spin-orbit coupling and of scattering processes. Spin-pumping across interfaces and two-magnon mediated processes in FM/NM films have also been identified as possible mechanisms for enhanced damping.[32-35] Following Woltersdorf *et al.*,[35] additional measurements were undertaken here on selected samples at different magnetic fields over range of 1.3–0.8 kOe for NiFe/Au and 1.7–0.9 kOe for NiFe/Cr to vary the precessional frequency and shed light on the damping mechanism, see Figures 4.2(c) and 4.4(c).

Here, the damping parameter for the un-irradiated Au capped NiFe was comparable with that of uncapped NiFe, suggesting insignificant spin-pumping effects. Ion-beam irradiation increases the precessional damping, which is associated with a broadening of the interfacial zone by intermixing between the NiFe and Au. This compositionally graded NiFeAu alloy extends over a few nanometers at the interface and may increase the damping by enhanced scattering and or modification of the spin-orbit interaction. The field dependent damping of the NiFe/Au was observed to decrease steadily with increasing frequency, indicating an extrinsic two-magnon type contribution to the damping that may be associated with increased disorder. This contrasts with the behavior observed for MBE grown Au on Fe, where the damping was enhanced by spin-pumping effects.[35] Enhanced scattering is expected to increase the electrical resistivity[36] and this was observed for the NiFe/Au bi-layer.[24] The precessional frequency falls with ion beam dose, but displays a small peak that is correlated in dose with a feature in the dose dependent magnetic moment.[28] The origin of this behavior is not currently understood.

Capping NiFe with Cr increased the α value by ~50% compared to uncapped NiFe. With increasing ion dose, the damping coefficient was reduced, falling to 0.0096 at the maximum dose, which is comparable with uncapped NiFe. The enhanced damping compared to uncapped NiFe could be an intrinsic effect associated with spin pumping across the interface or $d-d$ hybridization of the Fe and Cr at the interface that increases the d -band width of the NiFe in contact with the Cr layer, modifying the spin-orbit interaction. Alternatively, the increased damping could result from extrinsic two-magnon scattering linked to the coupling across the interface. However, the damping of NiFe/Cr was invariant with increasing precessional frequency for the doses investigated. This indicates an enhancement of the intrinsic damping, which contrasts with the effect of Cr on Fe observed for MBE grown samples[35] that identified an extrinsic two-magnon scattering contribution to the damping. Here, the enhancement may be associated with the thickness of the Cr layer or the interfacial structure. Both are modified by ion-beam irradiation, with the loss of some Cr from the surface by sputtering and increased interfacial intermixing, which could disrupt this spin-pumping or interface hybridization, respectively, thereby reducing the damping, ultimately towards to a single NiFe layer value. The precessional frequency of the Cr capped NiFe fell sharply with the lowest irradiation dose and changed little with further irradiation. This may also result from interfacial hybridization that increases the NiFe moment and hence the precessional frequency of the un-irradiated sample. Subsequent irradiation may degrade the moment and the precessional frequency would fall.

4.4. Summary

In summary, low-dose focused Ga^+ ion beam irradiation of ferromagnetic/non-magnetic thin-film bi-layers has demonstrated that the precessional magnetization behavior can be effectively tuned. For NiFe with a Au capping layer, the damping coefficient of the un-irradiated bi-layer was comparable with that of native NiFe, and the damping parameter increased with increasing ion beam dose. In contrast, capping NiFe with Cr increased the damping parameter compared to the native NiFe and the damping parameter then decreased with increasing ion beam irradiation dose. The combination of the low doses coupled with the high spatial resolution of the focused-ion-beam suggests this methodology may be applicable for locally modi-

fying the precessional magnetization behavior of ferromagnetic materials with feature sizes down to the nanoscale. This methodology may have applications to local control of damping for magnetic and spintronic device applications.

References

- [1] Keatley, P. S., Kruglyak, V., Gangmei, P. & Hicken, R. Ultrafast magnetization dynamics of spintronic nanostructures. *Philos. Trans. R. Soc. A* **369**, 3115 (2011).
- [2] Marrows, C. & Hickey, B. New directions in spintronics. *Philos. Trans. R. Soc. A* **369**, 3027 (2011).
- [3] Gilbert, T. L. A phenomenological theory of damping in ferromagnetic materials. *IEEE Trans. Magn.* **40**, 3443 (2004).
- [4] Bailey, W., Kabos, P., Mancoff, F. & Russek, S. Control of magnetization dynamics in Ni₈₁Fe₁₉ thin films through the use of rare-earth dopants. *IEEE Trans. Magn.* **37**, 1749 (2001).
- [5] Moore, T. A. *et al.* Magnetic-field-induced domain-wall motion in permalloy nanowires with modified Gilbert damping. *Phys. Rev. B* **82**, 094445 (2010).
- [6] Reidy, S. G., Cheng, L. & Bailey, W. E. Dopants for independent control of precessional frequency and damping in Ni₈₁Fe₁₉ (50 nm) thin films. *Appl. Phys. Lett.* **82**, 1254 (2003).
- [7] Woltersdorf, G. *et al.* Damping by Slow Relaxing Rare Earth Impurities in Ni₈₀Fe₂₀. *Phys. Rev. Lett.* **102**, 257602 (2009).
- [8] Rantschler, J. *et al.* Effect of 3d, 4d, and 5d transition metal doping on damping in permalloy thin films. *J. Appl. Phys.* **101**, 3911 (2007).
- [9] Ingvarsson, S., Xiao, G., Parkin, S. S. P. & Koch, R. H. Tunable magnetization damping in transition metal ternary alloys. *Appl. Phys. Lett.* **85**, 4995 (2004).
- [10] Fassbender, J. *et al.* Structural and magnetic modifications of Cr-implanted Permalloy. *Phys. Rev. B* **73**, 184410 (2006).
- [11] Dasgupta, V., Litombe, N., Bailey, W. E. & Bakhru, H. Ion implantation of rare-earth dopants in ferromagnetic thin films. *J. Appl. Phys.* **99**, 08G312 (2006).

- [12] Fassbender, J. & McCord, J. Control of saturation magnetization, anisotropy, and damping due to Ni implantation in thin Ni₈₁Fe₁₉ layers. *Appl. Phys. Lett.* **88**, 252501 (2006).
- [13] Park, D., Heo, K., Kim, W. & Choong, Y. The changes of the magnetic properties in ion irradiated Fe–Cr alloys. *Phys. Stat. Solidi* **4**, 4577 (2007).
- [14] Obry, B. *et al.* Microscopic magnetic structuring of a spin-wave waveguide by ion implantation in a Ni₈₁Fe₁₉ layer. *Appl. Phys. Lett.* **102**, 022409 (2013).
- [15] Fassbender, J. & McCord, J. Magnetic patterning by means of ion irradiation and implantation. *J. Magn. Magn. Mater.* **320**, 579 (2008).
- [16] Folks, L. *et al.* Localized magnetic modification of permalloy using Cr⁺ ion implantation. *J. Phys. D: Appl. Phys.* **36**, 2601 (2003).
- [17] Scheck, C. *et al.* Low Relaxation Rate in Epitaxial Vanadium-Doped Ultrathin Iron Films. *Phys. Rev. Lett.* **98**, 117601 (2007).
- [18] Bolse, W. Mechanisms of ion beam induced atomic mixing in solids. *Mater. Sci. Engg. A* **253**, 194 (1998).
- [19] Bonder, M. J. *et al.* Ion irradiation of Co/Pt multilayer films. *J. Appl. Phys.* **93**, 7226 (2003).
- [20] McCord, J. *et al.* Spatial manipulation of magnetic damping in ferromagnetic-antiferromagnetic films by ion irradiation. *Phys. Rev. B* **83**, 224407 (2011).
- [21] Fassbender, J., Ravelosona, D. & Samson, Y. Tailoring magnetism by light-ion irradiation. *J. Phys. D: Appl. Phys.* **37**, R179 (2004).
- [22] Kaminsky, W. M. *et al.* Patterning ferromagnetism in Ni₈₀Fe₂₀ films via Ga⁺ ion irradiation. *Appl. Phys. Lett.* **78**, 1589 (2001).
- [23] Faulkner, C., Atkinson, D., Allwood, D. & Cowburn, R. Rapid tuning of Ni₈₁Fe₁₉/Au bilayer magnetic properties by focused ion beam intermixing. *J. Magn. Magn. Mater.* **319**, 9 (2007).

- [24] Burn, D. *Domain wall behavior in ferromagnetic nanowires with interfacial and geometrical structuring*, Ph.D. thesis (Durham University, 2013); Burn, D., Hase, T. & Atkinson, D. Focused-ion-beam induced interfacial intermixing of magnetic bilayers for nanoscale control of magnetic properties. *J. Phys. Condens. Matter* **26**, 236002 (2014).
- [25] Pal, S. *et al.* Tunable magnonic frequency and damping in [Co/Pd]₈ multilayers with variable Co layer thickness. *Appl. Phys. Lett.* **98**, 082501 (2011).
- [26] Barman, A. *et al.* Size dependent damping in picosecond dynamics of single nanomagnets. *Appl. Phys. Lett.* **90**, 202504 (2007).
- [27] Starikov, A. A. *et al.* Unified First-Principles Study of Gilbert Damping, Spin-Flip Diffusion, and Resistivity in Transition Metal Alloys. *Phys. Rev. Lett.* **105**, 236601 (2010).
- [28] Arac, E. *et al.* Study of focused-ion-beam induced structural and compositional modifications in nanoscale bi-layer systems by combined grazing incidence x ray reflectivity and fluorescence. *J. Appl. Phys.* **111**, 044324 (2012).
- [29] Kamberský, V. Spin-orbital Gilbert damping in common magnetic metals. *Phys. Rev. B* **76**, 134416 (2007).
- [30] Gilmore, K., Idzerda, Y. U. & Stiles, M. D. Identification of the Dominant Precession-Damping Mechanism in Fe, Co, and Ni by First-Principles Calculations. *Phys. Rev. Lett.* **99**, 027204 (2007).
- [31] Gilmore, K., Idzerda, Y. U. & Stiles, M. D. Spin-orbit precession damping in transition metal ferromagnets (invited). *J. Appl. Phys.* **103**, 07D303 (2008).
- [32] Gerrits, T., Schneider, M. L. & Silva, T. J. Enhanced ferromagnetic damping in Permalloy/Cu bi-layers. *J. Appl. Phys.* **99**, 023901 (2006).
- [33] Tserkovnyak, Y., Brataas, A. & Bauer, G. E. W. Enhanced Gilbert Damping in Thin Ferromagnetic Films. *Phys. Rev. Lett.* **88**, 117601 (2002).
- [34] Urban, R., Woltersdorf, G. & Heinrich, B. Gilbert Damping in Single and Multilayer Ultrathin Films: Role of Interfaces in Nonlocal Spin Dynamics. *Phys. Rev. Lett.* **87**, 217204 (2001).

- [35] Woltersdorf, G., Buess, M., Heinrich, B. & Back, C. H. Time Resolved Magnetization Dynamics of Ultrathin Fe(001) Films: Spin-Pumping and Two-Magnon Scattering. *Phys. Rev. Lett.* **95**, 037401 (2005).
- [36] Ingvarsson, S. *et al.* Role of electron scattering in the magnetization relaxation of thin Ni₈₁Fe₁₉ films. *Phys. Rev. B* **66**, 214416 (2002).

Chapter 5

Tunable Magnetization Dynamics in Interfacially Modified Ni₈₁Fe₁₉/Pt Bi-layer Thin Film Microstructures

Interface modification for control of ultrafast magnetic properties using low-dose focused ion beam irradiation is demonstrated for bi-layers of two technologically important materials: Ni₈₁Fe₁₉ and Pt. Magnetization dynamics were studied using an all-optical time-resolved magneto-optical Kerr microscopy method. Magnetization relaxation, precession, damping and the spatial coherence of magnetization dynamics were studied. Magnetization precession was fitted with a single-mode damped sinusoid to extract the Gilbert damping parameter. A systematic study of the damping parameter and frequency as a function of irradiation dose varying from 0 to 3.3 pC/μm² shows a complex dependence upon ion beam dose. This is interpreted in terms of both intrinsic effects and extrinsic two-magnon scattering effects resulting from the expansion of the interfacial region and the creation of a compositionally graded alloy. The results suggest a new direction for the control of precessional magnetization dynamics, and open the opportunity to optimize high-speed magnetic devices.

5.1. Introduction

Controlling the magnetic properties of micro- and nano-scale magnetic structures is important for applications, such as magnetic data storage and sensors, and emerging technology concepts in spintronics[1] and magnonics[2-3]. This drives the search for engineered magnetic materials and metamaterials. In general ferromagnetic (FM) materials with low Gilbert damping are preferred in spin-transfer torque magnetic random access memory and magnonic devices, for reduced write-current and enhanced propagation of spin waves, respectively. On the other hand, for data storage and memory devices higher damping aids suppression of the magnetization precession during writing. Currently, to achieve control over spin waves[4]

lithographic patterning of magnonic crystals[5-8] was introduced, while for magnetic domain wall devices the behavior has been controlled by the lithographically defined shape[9] of nanowire structures and anisotropy[10] has been introduced by patterning magnetic films. Such patterning requires complicated nanofabrication methods, which, on a smaller scale may introduce defects that significantly affect the magnetic behaviour. Investigations of magnetic bi-layers and multilayers have revealed interesting phenomena like spin-dependent scattering[11] in giant magnetoresistance (GMR) multilayers, interlayer exchange coupling, interface hybridization, spin injection[12-13] and spin pumping[14], where the interface plays a crucial role in controlling the magnetization dynamics. Hence, interfacial engineering in ferromagnetic systems offers an exciting opportunity to both explore fundamental aspects of the interface physics and address the technological requirements for control of magnetization behavior as an alternative or complement to control by patterning. Precessional magnetization dynamics represents the transient response of the magnetization triggered by an external stimulus, such as a magnetic field pulse or a laser pulse. The magnetization vector follows a damped oscillatory trajectory in time-domain governed by the internal magnetization relaxation processes and the external magnetic field (H). The dynamical motion is phenomenologically described by Landau–Lifshitz–Gilbert (LLG) equation[15]

$$\frac{d\hat{m}}{dt} = -\gamma\hat{m} \times [H_{eff} + \frac{\lambda}{(\gamma m)^2} \frac{d\hat{m}}{dt}] \quad (5.1),$$

where, \hat{m} is the magnetization, γ is the gyromagnetic ratio, H_{eff} is the effective magnetic field and $\alpha = \lambda / \gamma m$ is the Gilbert damping coefficient. The relaxation of magnetization dynamics is governed by the damping parameter, α , which describes how rapidly magnetization equilibrates in absence of any stimulus. As introduced earlier, α plays an important role in technology, including magnetization switching in spin valves[16], spin-injection and detection[17], current-induced magnetization reversal[16], and spin wave propagation in magnetic media[18]. Despite significant research efforts and industrial need, the nature and origin of all the contributing factors to damping are not fully understood. A combination of spin-orbit interactions[19] and s - d scattering into ferromagnetic band electrons[20] provides some understanding of the origin of magnetic relaxation giving rise to intrinsic mechanisms for damping, while, extrinsic contributions, in particular the role of defects, via so-called two-magnon scattering[21], have also been shown to enhance α and leads to a shift in the precessional fre-

quency, f , for in-plane magnetized thin ferromagnetic films. This mechanism may be visualized by the generation of higher frequency spin waves that are degenerate with the FMR mode in the presence of dipolar coupling between spins. The defects scatter energy from the FMR mode into the spin waves leading to a relaxation with some de-phasing. In the case of bi-layered or multilayered thin films the situation is further complicated because the intrinsic damping in the system is sensitive to both electronic hybridization at the interface and spin pumping into non-magnetic (NM) layers. As outlined, a number of theoretical models exist for explaining damping analytically, however, experimental assessment is challenging, as it is difficult to distinguish the effects contributing to the experimentally observed damping.

In this work the role of interfacial structure on the damping of $\text{Ni}_{81}\text{Fe}_{19}(\text{NiFe})/\text{Pt}$ bi-layer films was studied by engineering the interface via exposure to low dose Ga^+ ion irradiation using a focused ion beam (FIB) system. The low dose regime principally leads to interfacial intermixing via ballistic cascade along with low levels of gallium implantation (up to $\sim 1\%$) and limited sputter loss from surface of the bi-layer. In chapter 4, FIB has already been used to locally manipulate magnetic properties like precession frequency and damping[22] by controlled intermixing with low-dose ion irradiation. Here, the variation of the effective damping and the precession frequency, and importantly, the spatial coherence of the dynamics were determined using a time-resolved magneto-optical Kerr effect microscope (TR-MOKE).

5.2. Sample Description

A bi-layer of $\text{NiFe}(10\text{ nm})/\text{Pt}(3\text{ nm})$ was grown by sputtering on a thermally oxidised $\text{Si}[100]$ substrate using an ultrahigh vacuum deposition system from a base pressure $\sim 1 \times 10^{-8}$ Torr. The bi-layer films were patterned by electron beam lithography into $30\ \mu\text{m}$ disks and were irradiated with irradiation dose (d) varying from 0 to $3.3\ \text{pC}/\mu\text{m}^2$. Figure 5.1(a) shows a schematic diagram of the sample. NiFe was chosen for its negligible anisotropies. Pt was selected as an important heavy metal with regard to its strong spin-orbit coupling[23] and significant proximity induced magnetic moment, although the role of this is currently an open question. Structurally, the as-deposited NiFe/Pt interface is shown to have a typical width of less than 1 nm, resulting from a combination of topological roughness and chemical intermixing as observed here by x-ray reflectivity. It has been shown in a previous detailed structural study of NiFe/Au that with higher ion dose the interface rapidly becomes broader, the capping layer

becomes very thin and the layer develops into a compositionally-graded alloy due to the intermixing of atoms of the heavy NM layer into the FM layer[24-25]. Pt also forms a protective layer preventing the oxidation of the NiFe.

5.3. Methods

5.3.1. Fabrication

A bi-layer of Ni₈₁Fe₁₉(10 nm)/Pt(3 nm) was grown by sputtering on a thermally oxidised Si[100] substrate using an ultrahigh vacuum deposition system from a base pressure $\sim 1 \times 10^{-8}$ Torr. Sputter deposition used Ar at a pressure $\sim 1 \times 10^{-3}$ Torr and the deposition rates were 0.01 nm/s and 0.02 nm/s for the NiFe and Pt, respectively. The bi-layered films were patterned by electron beam lithography using deposition and lift-off into 30 μm disks and were irradiated with 30 keV Ga⁺ ions at normal incidence using FEI Helios NanoLab 600 FIB system with the focused beam rastered scan over a circular area of $\sim 700 \mu\text{m}^2$. The irradiation dose (d) was varied from 0 to 3.3 pC/ μm^2 .

5.3.2. Measurement Technique

Time-resolved magnetization dynamics of the samples were measured using a custom built TR-MOKE microscope. An in-plane bias magnetic field (H) was applied at an angle of $\sim 5^\circ$ to the plane of the sample. The magnetization \hat{m} was aligned uniformly along the direction of H . An all-optical femtosecond laser-based pump-probe method was used to excite the magnetization dynamics and to probe the evolution of magnetization as a function of delay time with respect to the excitation. Details of the setup are described in chapter 3 and also in earlier literature[26]. Kerr images of the 30 μm disks were built-up by raster scanning the sample under the probe spot using an x-y-z piezoelectric scanning stage at fixed time delays and by measuring the Kerr rotation at each scan point. The experiments were performed at room temperature.

A two-color optical pump-probe setup was used with spatial and temporal resolutions of $\sim 1 \mu\text{m}$ and 100 fs, respectively. The sample was excited using a second harmonic ($\lambda_B = 400$ nm, fluence $\sim 17.0 \text{ mJ/cm}^2$, pulsewidth ~ 100 fs) of a mode locked Ti-sapphire pulsed laser (Tsunami, Spectra physics, pulsewidth ~ 80 fs). The fundamental laser beam ($\lambda_R = 800$ nm, fluence $\sim 2.1 \text{ mJ/cm}^2$) was used to probe the dynamics passing through a variable time delay.

The polar Kerr rotation was detected using a balanced photo diode detector, which completely isolates the Kerr rotation and reflectivity signals. The pump and probe beams were made collinear and focused on the central part of the sample through a microscope objective with numerical aperture, N.A. = 0.65. At the focal plane of the probe (diameter ~ 800 nm), i.e., on the sample surface, the pump beam was slightly defocused, and had a larger diameter (~ 1 μm) than the probe beam, which made it easier to overlap the pump and probe beams on the sample surface. The probe beam was centred on the pump beam so that slight misalignment during the course of the experiment does not affect the pump-probe signals. A large enough magnetic field was first applied at a small angle $\sim 5^\circ$ to the planes of the sample for saturating their magnetization. The magnetic field strength was then reduced to the bias field value ($H =$ component of bias field in the sample plane), which ensures that the magnetization still remains saturated along the bias field direction. The pump beam was chopped at 2 kHz frequency and a phase sensitive detection of total reflectivity and Kerr rotations were made using lock-in amplifiers. For obtaining the scanning Kerr images the sample was scanned under the focused laser spot by using a piezoelectric scanning stage (x-y-z) with feedback loop for better stability.

5.4. Results and Discussion

Figure 5.1(b) shows typical time-resolved Kerr rotation data obtained from a bi-layer disk irradiated with $d = 3.1$ $\text{pC}/\mu\text{m}^2$ measured under $H = 0.8$ kOe. Three different temporal regimes are identified. In region A ($t < 0$) a negative time delay simply shows steady magnetization signal due to H when the sample is probed prior to excitation. A change in the Kerr angle from this state shows a change in the magnetization from its initial uniform state. In region B ultrafast demagnetization occurs within about 500 fs as a result of the pulsed laser excitation, the Kerr signal recovers quickly (relaxation time τ_1) as the electronic thermal bath equilibrates with the lattice. This is followed by a slower relaxation with time constant τ_2 in region C where the lattice dissipates energy to the surrounding[27]. The solid curves are exponential fits to the relaxation in regions B and C. These relaxation processes are governed by the specific heats and the coupling between the different energy systems. A damped oscillatory signal was also observed in region C superimposed upon the decaying signal, and is due to the precession of magnetization that is described by equation 5.1.

5.4.1. Time-resolved Scanning Kerr Images

Figure 5.1(c) shows scanning Kerr images[28] of the same region of one of the irradiated disks at three different antinodes of the precession (time delays = 110 ps, 360 ps, 790 ps as indicated by the arrows in figure 5.1(b)). These images show the uniformity of the excitation within the circular structures and decreasing brightness (Kerr angle) with increasing time delay as the precession is damped. This indicates that any significant contribution to the damping from dephasing of multiple spin wave modes is ruled out and the damping is spatially uniform. Similar uniformity was observed for samples with other doses. This confirms that the magnetic changes due to irradiation were uniform over the sample and independent of the region probed. The effect of finite boundary or demagnetized region can also be excluded here since the sample size is much larger than the excitation and probed regions of about $1 \mu\text{m}^2$.

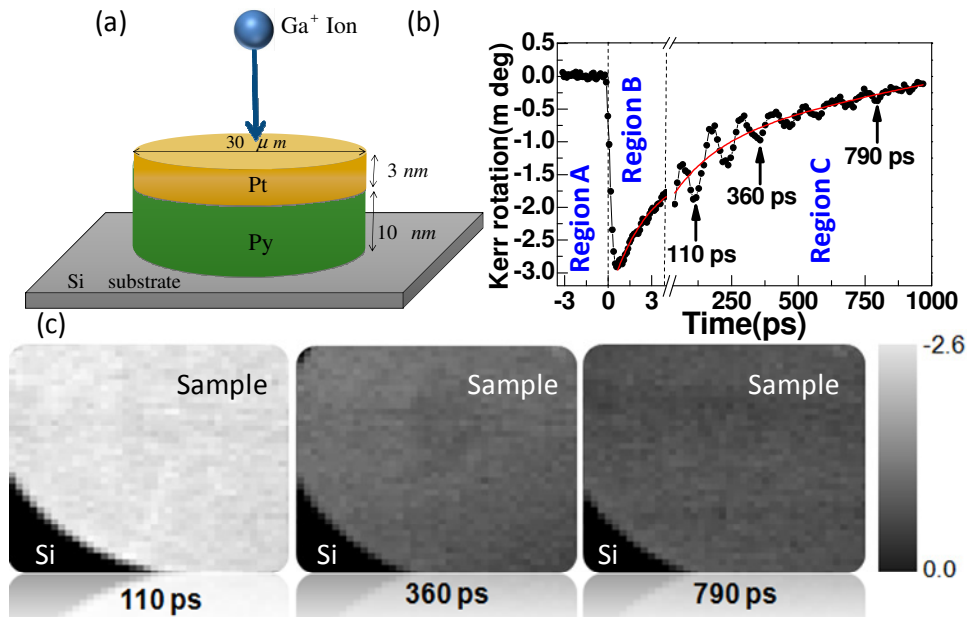


Figure 5.1. (a) Schematic illustration of ion beam irradiation of a bi-layer circular structure. (b) TR-MOKE trace from a sample irradiated with ion dose $d = 3.1 \text{ pC}/\mu\text{m}^2$. Note changes in the time base. (c) Time-resolved Kerr images of the sample at three time delays.

5.4.2. Precession Frequency and Damping

A bi-exponential background was subtracted from the TR-MOKE traces to isolate the damped precessional behavior. Precessional data for a bi-layer structure irradiated with $d =$

0.3 pC/ μm^2 and uncapped NiFe film at $H = 1.8$ kOe are presented in figure 5.2(a). In both cases a single frequency damped oscillation is clear and the decay is much faster for the bi-layer film. Similar single frequency damped oscillatory behavior was obtained for all of the samples here, see figure 5.1(c) for further examples. The time domain data were fitted with a damped sine curve

$$M(t) = M(0)e^{-\frac{t}{\tau}} \sin(2\pi ft - \phi) \quad (5.2),$$

where the relaxation time τ is related to the damping coefficient α by the relation $\tau = 1/2\pi f\alpha$, f is the precession frequency and ϕ is the initial phase of the oscillation. Examples of best fits to the experimental data are shown by the solid curves in figure 5.2(a), from which α values of 0.042 for the NiFe/Pt bi-layer and 0.015 for the uncapped NiFe layer were extracted. The uncapped value is consistent with typical values for NiFe film and the Pt capping increased the damping by almost a factor of 3. This large increase in damping may be attributed to spin pumping[29-30] into the Pt and enhanced dissipation associated with increased spin-orbit coupling (SOC)[23] at the NiFe/Pt interface. The precession frequency for NiFe/Pt (13.28 GHz) was slightly higher than for the uncapped NiFe (13.05 GHz), which may perhaps be attributed to an induced moment on the interfacial Pt atoms. Figure 2(b) shows a monotonic decrease of f with decreasing H for the NiFe/Pt system from the fast Fourier transform (FFT) power spectra and figure 5.2(c) shows f plotted as a function of H , and fitted with the Kittel formula for uniform precession, from which the saturation magnetization M_S was obtained as 833 emu/cc with the gyromagnetic ratio $\gamma = 0.0176$ GHz/Oe.

$$f = \frac{\gamma}{2\pi} \sqrt{H(H + 4\pi M_S)} \quad (5.3)$$

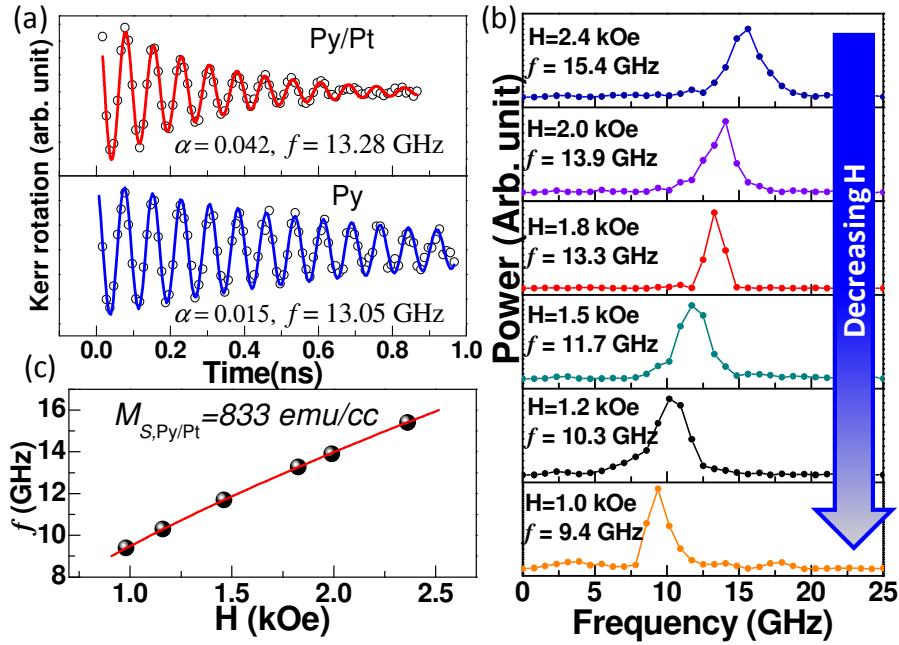


Figure 5.2. (a) Comparison of TR-MOKE traces between NiFe/Pt ($d = 0.3$ pC/ μm^2) and NiFe films. Symbols correspond to experimental data while the solid curves are fits to equation 5.2. (b) Power spectra of NiFe/Pt sample at different bias field values H . (c) Frequency vs. bias magnetic field for the NiFe/Pt ($d = 0.3$ pC/ μm^2) sample. Here the symbols represent experimental data points and the solid curve is a fit to equation 5.3.

The influence of interfacial engineering on the precession and damping of NiFe/Pt bi-layers is shown in figure 5.3(a). For the lowest irradiation dose ($d = 0.3$ pC/ μm^2) a value of $\alpha = 0.042$ was obtained, while for an intermediate dose, $d = 2.0$ pC/ μm^2 , α increased to a maximum of 0.060 before falling again to $\alpha = 0.052$ for the largest dose, $d = 3.3$ pC/ μm^2 .

In figure 5.3(b) the dependence of damping on the ion beam dose is plotted, where the top x -axis shows the number density of Ga^+ ions used during irradiation. The variation in α can be divided into two distinct regions. In region 1, α increases monotonically with increasing d reaching a peak between $d = 2$ - 2.4 pC/ μm^2 . At higher doses α falls rapidly at first followed by a slower decrease with further increase in d . To understand the observed behavior, the variation in the lower dose regime (region 1) for NiFe/Pt was compared with that of NiFe(10 nm)/Cu(3 nm) bi-layer in figure 5.3(c). In both cases α increased linearly with increasing d at similar rate of ~ 0.015 $\mu\text{m}^2/\text{pC}$, but with a constant higher offset of 0.019 in the case of the NiFe/Pt bi-layer. Significant spin-pumping and SOC associated with the Pt at the interface

can explain the origin of the shift. There are several studies related to the enhancement of α to spin pumping and SOC in the interfacial region, describing the Pt layer as a spin sink that absorbs spin waves from the adjacent FM layer[31-33]. The effect is insignificant in case of NiFe/Cu[33] which is supported by the observation that for NiFe/Cu α approaches 0.015 at $d = 0$, which is comparable with the damping coefficient of uncapped NiFe. SOC and spin pumping cannot explain the observed linear increase in α with dose that is common to both sets of samples. The doping from Ga is less than 1-2% and this is not expected to significantly affect the damping of pure NiFe[25]. However, with ion beam irradiation, NM atoms are displaced into the NiFe causing defects and structural changes that give rise to extrinsic two-magnon scattering, which causes an enhancement in α [34]. The defects introduced in the NiFe layer increase the width of intermixed region as the irradiation dose increases[24], resulting in a linear variation of α with d . This is supported by earlier literature in case of NiFe/Au bi-layers[22], where it was suggested that the enhanced α of NiFe/Au with irradiation was an extrinsic effect attributed to two-magnon scattering. This mechanism has been associated with defects, disorder or misfit symmetry breaking at the interface layer[25,35-36]. The dominance of two-magnon scattering as the mechanism for enhanced α with increasing d in region 1, is also supported by results from studies concerned with interface of an FM layer with Pt[25,35,37-41]. In figure 3(b) the variation of α with further increase of d shows a monotonic decrease in region 2. The shaded region indicates the dose region where α is expected to be maximum according to the trend of experimental data points. Structurally, ion beam irradiation leads predominantly to ballistic intermixing and some insight into the evolution of the NiFe/Pt interface may be gained from previous detailed x-ray structural analysis of FIB irradiated NiFe/Au bi-layers[24-25,40,42] since the process is dominated by momentum transfer and the atomic mass of Pt is close to that of Au. The interface in as-deposited NiFe/Au and NiFe/Pt has some small intrinsic width (~ 1 nm from XRR measurements) and with increasing irradiation dose the interface width increases linearly due to intermixing of the layers, creating an increasing thickness of compositionally-graded NiFePt alloy between the NiFe and Pt. Previous experimental analysis of the Au capped system showed that a dose of roughly $1 \text{ pC}/\mu\text{m}^2$ creates a graded alloy interlayer of ~ 4 nm and sputter loss of more than 1 nm of NM capping layer. Extending this to the NiFe/Pt system, and assuming continued linear intermixing, for a dose above $2 \text{ pC}/\mu\text{m}^2$ this would lead to the formation of a compositionally graded-alloy that extends through the NiFe layer thickness and the loss of most of the

pure NM capping layer[24-25,34]. Here, the compositionally-graded alloy region forms a continuous magnetic layer with the remaining NiFe part of the film. In addition the loss of pure Pt layer thickness due to sputtering of the Pt-rich surface region leads to a reduction of the SOC and interlayer spin diffusion contributing to the intrinsic α . As a result the effective α falls.

Further analysis of the variation of α with f is shown in figure 3(d). In the sample with minimum dose ($d = 0.3 \text{ pC}/\mu\text{m}^2$), α is independent of f , which is a signature of intrinsic damping. For doses of $d = 2.0$ and $3.3 \text{ pC}/\mu\text{m}^2$ α decreases steadily with f with similar slopes indicating an extrinsic contributions to the damping in both the cases. The extrinsic effect is dominant when H is weak (lower frequencies). At higher field, f is higher and the magnetization dynamics are strongly driven by the field itself and hence scattering is suppressed. Hence, the enhancement in α with decreasing f is a characteristic of two-magnon scattering effect. From the difference in slope in $\alpha(f)$ between $d = 0.3$ and $2.0 \text{ pC}/\mu\text{m}^2$ curves in figure 5.3(d), it is clear that the extrinsic damping develops with intermixing which supports our earlier explanation for linear variation of $\alpha(d)$ in region 1 of Figure 3(b) and the similar slope for $d = 2.0$ and $3.3 \text{ pC}/\mu\text{m}^2$ suggests the extrinsic contribution continues in region 2. This is because further irradiation beyond a certain dose does not increase the number of scattering defects in the pure NiFe layer due to formation of a thick interface region.

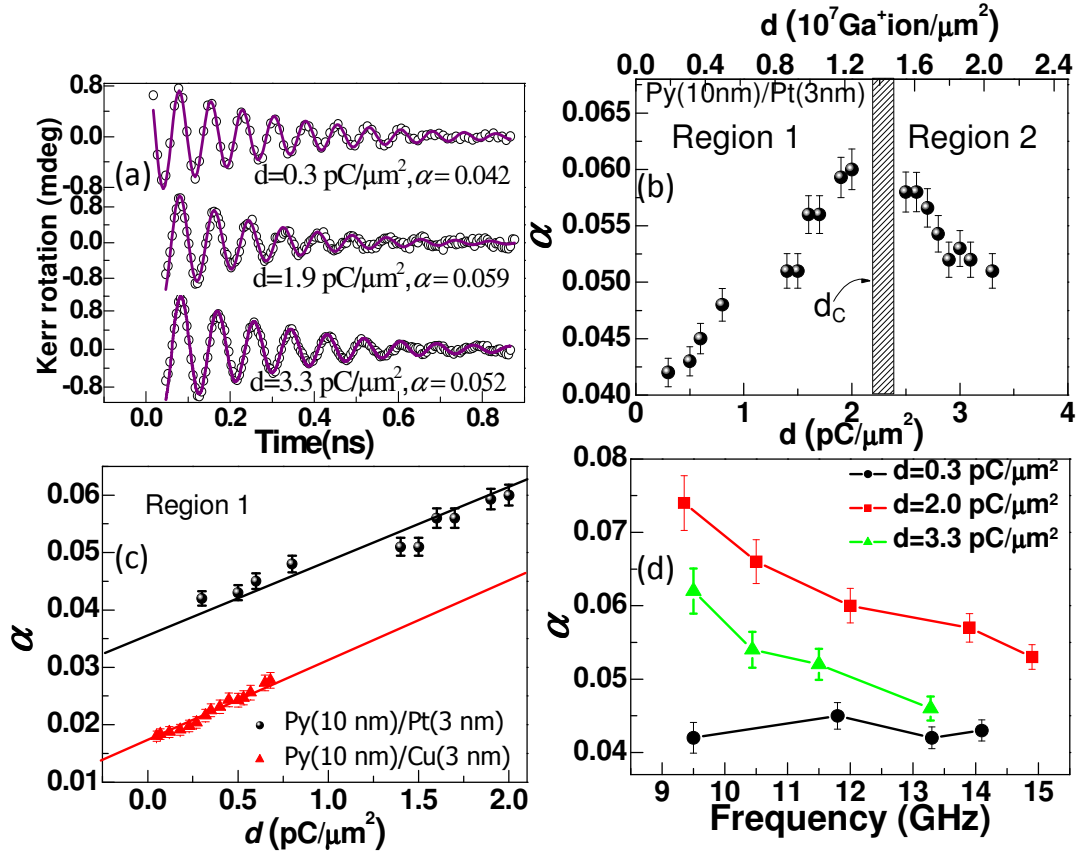


Figure 5.3. (a) TR-MOKE traces at three different doses. Here, symbols correspond to the experimental data and solid curves are fits to equation 5.2. (b) Damping is plotted as a function of dose. The shaded box represents the transition between two regions. (c) Variation of damping with dose in the lower dose regime for NiFe/Pt (filled circles) and NiFe/Cu (filled triangles). Here, symbols are the experimental results and solid lines are linear fits. The data shown in figure 5.3(a) - (c) correspond to $H = 1.8 \text{ kOe}$. (d) Variation of damping with precession frequency at three different doses.

Figure 5.4(a) shows FFT power spectra of the TR-MOKE data for three different doses. A clear decrease of f is observed with increasing dose. The variation of f with d is shown in Figure 5.4(b). First a large decrease of f of 1.3 GHz occurs as d increases from 0.3 to 2.0 $\text{pC}/\mu\text{m}^2$, while a smaller fall of 0.4 GHz occurs as d increases further from 2.0 to 3.3 $\text{pC}/\mu\text{m}^2$. The literature[43] shows a reduction of magnetic moment of Ni thin film with the concentra-

tion of Pt atoms. Hence, the decrease of f in region 1 is likely to be related to the reduction of moment due to the presence of Pt in the vicinity of Ni and Fe in the intermixed region. In region 2 a NiFe-Pt alloy is established throughout a large fraction of the original bi-layer. The precessional frequency is almost constant with increasing dose, because the probability of sputtered Pt atoms to reach the pure NiFe layer by traversing through the thick interface region is small. This effect is in agreement with the structural evolution discussed earlier.

5.4.3. Spin Relaxation Times

In figure 5.4(c) we plot the relaxation times τ_1 and τ_2 as a function of d . The relaxation times are obtained from the decaying part of the time-resolved Kerr rotation data as discussed earlier in figure 5.1(b). As mentioned earlier that τ_1 is related to the transfer of electron and spin energy to the lattice, while τ_2 is related to the transfer of lattice energy to the substrate and surroundings. The energy transfer rate depends on the specific heat of lattice (S). In other words τ_1 and τ_2 can be expressed in terms of S . Figure 5.4(c) shows both τ_1 and τ_2 increase with d . Specifically, the change is significant (larger than error) before and after $d = 2.0$ pC/ μm^2 . This is an indirect indication of a change in lattice configuration due to the formation of alloyed layer in region 2.

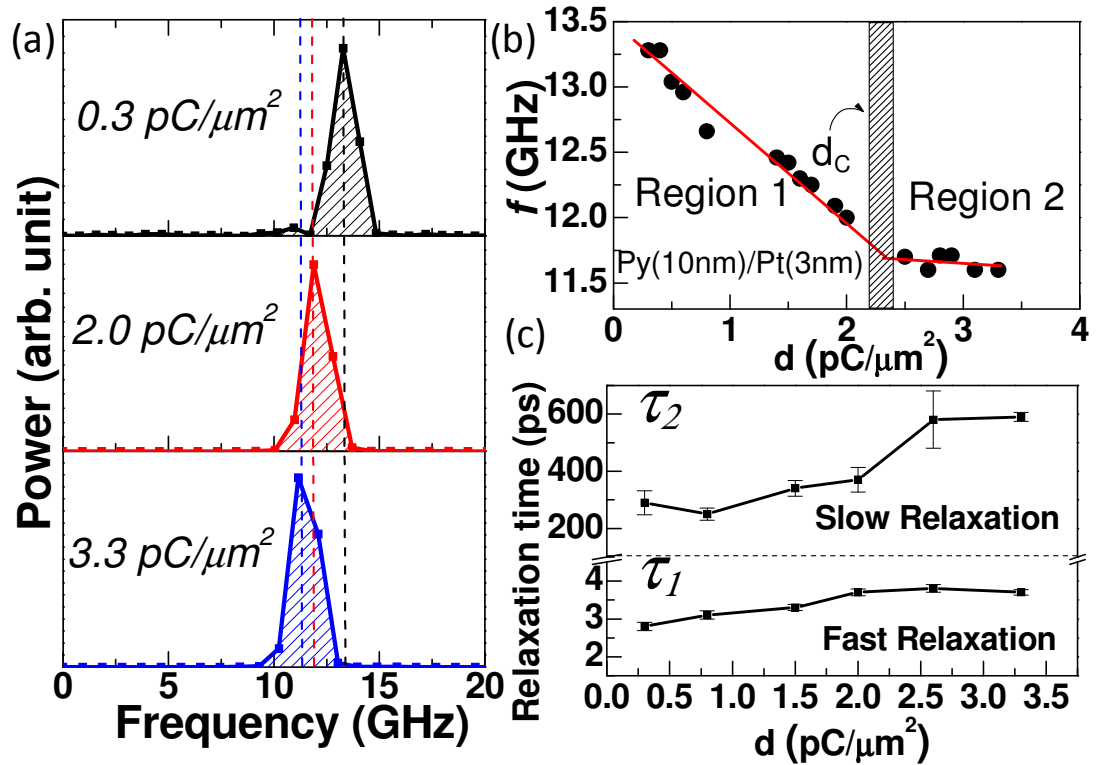


Figure 5.4. (a) FFT power spectra of the TR-MOKE data of ion irradiated NiFe/Pt samples at three different doses at $H = 1.8$ kOe. (b) Variation of frequency f as a function of dose at $H = 1.8$ kOe. Symbols are the experimental data and solid lines are linear fits. The shaded box represents the transition between two regions. (c) Magnetization relaxation times τ_1 and τ_2 are plotted as a function of dose. Here the symbols are obtained from experimental data while the solid lines are only guides to the eye.

5.5. Summary

In summary, the controlled modification of dynamic magnetic properties by low dose Ga^+ ion irradiation in NiFe/Pt bi-layer films has been demonstrated. TR-MOKE microscopy was used to study the variation of ultrafast magnetization dynamics including the ultrafast relaxation times, precession frequency and damping as a function of the irradiation dose. These parameters all show significant variation with dose, which has been divided into two regions. A low-

er dose region ($\leq 2.0 \text{ pC}/\mu\text{m}^2$); where the precessional frequency falls and the damping increases almost linearly with dose, and a higher dose region ($> 2.4 \text{ pC}/\mu\text{m}^2$), where the precessional frequency remains nearly unchanged while the damping decreases slowly. The damping of very low dose irradiated sample shows a large value as compared to uncapped NiFe layer due to the spin-orbit coupling and spin-pumping effects. Low dose irradiation causes dislocation of interface atoms leading towards defects and interface intermixing, which increases two-magnon scattering and the associated damping. With further increase of irradiation dose the interface region expands through the bi-layer leading to the formation of a compositionally graded alloy. In addition to that a progressive loss of the Pt layer by sputtering reduces the thickness of this spin-sink region below the spin-diffusion length, which in turn reduces the spin-orbit coupling and spin diffusion process and hence the damping of the system. The two relaxation times which are related to thermal conduction and lattice structural changes also show concurrent variation, confirming the mechanisms as discussed above. Such a controlled variation of damping and precession frequency by low dose local ion irradiation may be important for the development of various spintronic and magnonic devices with patterned static and dynamic magnetic properties.

References

- [1] Bader, S. D. & Parkin, S. S. P. in *Annual Review of Condensed Matter Physics* Vol. 1 (ed J. S. Langer) 71 (2010).
- [2] Kruglyak, V., Demokritov, S. & Grundler, D. Magnonics. *J. Phys. D: Appl. Phys.* **43**, 264001 (2010).
- [3] Kruglyak, V. V. & Hicken, R. J. Magnonics: Experiment to prove the concept. *J. Magn. Magn. Mater.* **306**, 191 (2006).
- [4] Stancil, D. D. & Prabhakar, A. *Spin waves*. (Springer, 2009).
- [5] Wang, Q. *et al.* Magnonic band gaps in two-dimension magnonic crystals with diffuse interfaces. *J. Appl. Phys.* **115**, 113904 (2014).
- [6] Saha, S. *et al.* Tunable magnetic anisotropy in two-dimensional arrays of Ni₈₀Fe₂₀ elements. *Appl. Phys. Lett.* **103**, 242416 (2013).
- [7] Mandal, R. *et al.* Effects of antidot shape on the spin wave spectra of two-dimensional Ni₈₀Fe₂₀ antidot lattices. *Appl. Phys. Lett.* **103**, 262410 (2013).

- [8] Kumar, D., Klos, J. W., Krawczyk, M. & Barman, A. Magnonic band structure, complete bandgap, and collective spin wave excitation in nanoscale two-dimensional magnonic crystals. *J. Appl. Phys.* **115**, 043917 (2014).
- [9] Komine, T., Murakami, I., Nagayama, T. & Sugita, R. Influence of Notch Shape and Size on Current-Driven Domain Wall Motions in a Magnetic Nanowire. *IEEE Trans. Magn.* **44**, 2516 (2008).
- [10] Jaafar, M. *et al.* Pattern-induced magnetic anisotropy in FePt thin films by ion irradiation. *Phys. Rev. B* **83**, 094422 (2011).
- [11] Baibich, M. N. *et al.* Giant Magnetoresistance Of (001)Fe/(001) Cr Magnetic Superlattices. *Phys. Rev. Lett.* **61**, 2472 (1988).
- [12] Takahashi, S. & Maekawa, S. Spin current, spin accumulation and spin Hall effect. *Sci. Technol. Adv. Mater.* **9**, 014105 (2008).
- [13] Ganguly, A. *et al.* Thickness dependence of spin torque ferromagnetic resonance in Co₇₅Fe₂₅/Pt bilayer films. *Appl. Phys. Lett.* **104**, 072405 (2014).
- [14] Kajiwara, Y. *et al.* Spin Pumping in Polycrystalline Magnetic Insulator/Metal Pt Films. *IEEE Trans. Magn.* **47**, 2739 (2011).
- [15] Gilbert, T. L. A phenomenological theory of damping in ferromagnetic materials. *IEEE Trans. Magn.* **40**, 3443 (2004).
- [16] Schumacher, H. W., Chappert, C., Sousa, R. C. & Freitas, P. P. Current-induced precessional magnetization reversal. *Appl. Phys. Lett.* **83**, 2205 (2003).
- [17] Ganguly, A. *et al.* Time-domain detection of current controlled magnetization damping in Pt/Ni₈₁Fe₁₉ bilayer and determination of Pt spin Hall angle. *Appl. Phys. Lett.* **105**, 112409 (2014).
- [18] Xi, H. & Xue, S. Spin-wave propagation and transmission along magnetic nanowires in long wavelength regime. *J. Appl. Phys.* **101**, 123905 (2007).
- [19] He, P. *et al.* Quadratic Scaling of Intrinsic Gilbert Damping with Spin-Orbital Coupling in L1(0) FePdPt Films: Experiments and Ab Initio Calculations. *Phys. Rev. Lett.* **110**, 077203 (2013).
- [20] Ingvarsson, S. *et al.* Role of electron scattering in the magnetization relaxation of thin Ni₈₁Fe₁₉ films. *Phys. Rev. B* **66**, 214416 (2002).
- [21] Arias, R. & Mills, D. L. Extrinsic contributions to the ferromagnetic resonance response of ultrathin films. *Phys. Rev. B* **60**, 7395 (1999).

- [22] King, J. A. *et al.* Local control of magnetic damping in ferromagnetic/non-magnetic bilayers by interfacial intermixing induced by focused ion-beam irradiation. *Appl. Phys. Lett.* **104**, 242410 (2014).
- [23] Mizukami, S., Ando, Y. & Miyazaki, T. Ferromagnetic resonance linewidth for NM/80NiFe/NM films (NM = Cu, Ta, Pd and Pt). *J. Magn. Magn. Mater.* **226**, 1640 (2001).
- [24] Burn, D., Hase, T. & Atkinson, D. Focused-ion-beam induced interfacial intermixing of magnetic bilayers for nanoscale control of magnetic properties. *J. Phys. Condens. Matter* **26**, 236002 (2014).
- [25] Burn, D. *Domain wall behaviour in ferromagnetic nanowires with interfacial and geometrical structuring*, Ph.D. thesis, Ch. 6 135-160 (Durham University, 2013).
- [26] Barman, A. & Haldar, A. in *Solid State Physics* Vol. 65 eds E. Camley Robert & L. Stamps Robert) 1-108 (Academic Press, 2014).
- [27] Laraoui, A. *et al.* Study of individual ferromagnetic disks with femtosecond optical pulses. *J. Appl. Phys.* **101**, 09C105 (2007).
- [28] Barman, A. *et al.* Imaging the dephasing of spin wave modes in a square thin film magnetic element. *Phys. Rev. B* **69**, 174426 (2004).
- [29] Nakayama, H. *et al.* Inverse Spin-Hall Effect Induced by Spin Pumping in Different Thickness Pt Films. *IEEE Trans. Magn.* **46**, 2202 (2010).
- [30] Rezende, S. M. *et al.* Enhanced spin pumping damping in yttrium iron garnet/Pt bilayers. *Appl. Phys. Lett.* **102**, 012402 (2013).
- [31] Tserkovnyak, Y., Brataas, A. & Bauer, G. E. Enhanced Gilbert damping in thin ferromagnetic films. *Phys. Rev. Lett.* **88**, 117601 (2002).
- [32] Rezende, S. *et al.* Enhanced spin pumping damping in yttrium iron garnet/Pt bilayers. *Appl. Phys. Lett.* **102**, 012402 (2013).
- [33] Mizukami, S., Ando, Y. & Miyazaki, T. Ferromagnetic resonance linewidth for NM/80NiFe/NM films (NM= Cu, Ta, Pd and Pt). *J. Magn. Magn. Mater.* **226**, 1640 (2001).
- [34] Rantschler, J. O. *et al.* Damping at normal metal/permalloy interfaces. *IEEE Trans. Magn.* **41**, 3523 (2005).

- [35] Blon, T. *et al.* Magnetic easy-axis switching in Co/Pt and Co/Au superlattices induced by nitrogen ion beam irradiation. *Nuclear Instruments & Methods in Physics Research Section B-Beam Interactions with Materials and Atoms* **257**, 374 (2007).
- [36] Najafabadi, R. & Srolovitz, D. J. Order-Disorder Transitions at and Segregation to (001) Ni-Pt Surfaces. *Surf. Sci.* **286**, 104 (1993).
- [37] Fassbender, J., Ravelosona, D. & Samson, Y. Tailoring magnetism by light-ion irradiation. *J. Phys. D: Appl. Phys.* **37**, R179 (2004).
- [38] Rantschler, J. O. *et al.* Effect of 3d, 4d, and 5d transition metal doping on damping in permalloy thin films. *J. Appl. Phys.* **101**, 033911 (2007).
- [39] Bonder, M. J. *et al.* Ion irradiation of Co/Pt multilayer films. *J. Appl. Phys.* **93**, 7226 (2003).
- [40] Arac, E. *et al.* Study of focused-ion-beam-induced structural and compositional modifications in nanoscale bilayer systems by combined grazing incidence x ray reflectivity and fluorescence. *J. Appl. Phys.* **111**, 044324 (2012).
- [41] Woltersdorf, G. *et al.* Damping by Slow Relaxing Rare Earth Impurities in Ni₈₀Fe₂₀. *Phys. Rev. Lett.* **102**, 257602 (2009).
- [42] Burn, D. M. & Atkinson, D. Control of domain wall pinning by localised focused Ga (+) ion irradiation on Au capped NiFe nanowires. *J. Appl. Phys.* **116**, 163901 (2014).
- [43] Parra, R. & Cable, J. Neutron study of magnetic-moment distribution in Ni-Pt alloys. *Phys. Rev. B* **21**, 5494 (1980).

Chapter 6

Role of Heavy Metal Capping Layer and Interface in Controlling the Damping of Ferromagnet/Nonmagnet Bi-layers

We have investigated variation of effective damping constant as a function of nonmagnetic heavy metal capping layer thickness in Pt/CoFeB and Ta/CoFeB bi-layer samples. The samples are excited electrically using rf current and spin torque ferromagnetic resonance linewidth is used for the extraction of damping constant. We found that damping constant decreases below a certain nonmagnetic layer thickness. The variation is explained by spin pumping effect and spin accumulation around the interface. The results are compared with Pt/CoFe and Ta/CoFe bi-layers for understanding the role of boron at the interface.

6.1. Introduction

Recently magnetic bi-layer thin films attract a considerable attention to research as it offers an opportunity for the development of spintronic[1], data storage and data transfer devices with added functionality due to its tunable magnetic property. The operations of these devices are primarily governed by the relaxation processes of the magnetic system. It is observed that the magnetization dynamics of a ferromagnetic material can be modified simply by adding[2] an adjacent nonmagnetic layer. In this case, the sample preparation technique is fairly straight forward as compared to the other technologies involving complicated nanofabrication processes. As a result, the bi-layer devices are less affected by instrumental limitations and hence, more acceptable for commercial applications due to its high quality to cost ratio.

When a bi-layer is created, an interface is formed at the boundary of two materials. The properties of the interface can have a significant impact on the overall magnetic behavior of the system which is often overlooked in experimental and theoretical analyses as well as

micromagnetic simulations. The interface can be associated with a number of interesting phenomena like spin injection[3-5], spin pumping[6-7], spin diffusion[8], orbital hybridization[9-11], spin orbit coupling[9], perpendicular magnetic anisotropy[9-10], two-magnon scattering[12-15] and proximity induced magnetization[16] with a rich physics involved in each of them. Hence, an improved understanding of magnetic relaxation processes of bi-layers is required with a careful consideration of these facts.

Although damping is a ferromagnetic material property, a nonmagnetic heavy metal adjacent to the ferromagnetic layer can enhance its value by spin pumping effect as seen in chapter 5. The efficiency of spin pumping depends on the spin absorption power of the nonmagnet associated with spin flip scattering process. In most of the cases the spin flip processes are considered to be intrinsic to the nonmagnetic metal, although it can be affected at smaller thicknesses, especially when comparable to the spin diffusion length of the material. Moreover, for simplicity the interface of a bi-layer is usually considered to be transparent for spin transport processes. However, the real situation can be far more complicated in presence of factors like spin accumulation, resistivity mismatch, strain, Rashba scattering, intermixing of atoms and defect induced translation symmetry breaking at the interface. Hence, investigation of spin pumping with nonmagnetic layer thickness and the role of interface in governing the process should be explored in detail.

In this work, we studied a systematic variation of damping relaxation as a function of both ferromagnetic and nonmagnetic layer thicknesses using spin torque ferromagnetic resonance (ST-FMR) technique[3]. Specifically, this work is attributed to the understanding of nonmagnetic layer thickness dependence of damping in magnetic bi-layers. The behavior of the damping constant is studied by using a combination of ferromagnetic (CoFe, CoFeB) and nonmagnetic (Ta, Pt) materials with different physical properties. The experimental results are explained by spin pumping with consideration of several interesting phenomena occurring at the interface.

6.2. Experimental

Nonmagnetic(NM)/ferromagnetic(FM) bi-layer films are grown on a thermally oxidized non-doped Si substrate by dc magnetron sputtering with continuously varying thickness using a linear motion shutter at the base pressure of 4×10^{-7} Pa and Ar gas pressure of 0.13 Pa. The

thicknesses of the ferromagnetic layers ($\text{Co}_{75}\text{Fe}_{25}$, $\text{Co}_{40}\text{Fe}_{40}\text{B}_{20}$) were varied between 3 and 10 nm, while the same for the nonmagnetic layers (Ta, Pt) were varied between 1.5 and 18 nm. A 2-nm thick Al_2O_3 is used as an insulating capping layer. The resistivities of Ta, Pt, $\text{Co}_{75}\text{Fe}_{25}$ and $\text{Co}_{40}\text{Fe}_{40}\text{B}_{20}$ were measured to be 162, 28, 15 and 194 $\mu\Omega\cdot\text{cm}$. Bi-layer films are patterned into rectangular shaped elements ($20 \times 60 \mu\text{m}^2$) using optical lithography and Ar-ion etching technique. A co-planar Ti (5 nm)/Au (150 nm) waveguide (20 μm wide central conductor with 50 Ω characteristic impedance) is deposited on top of each bi-layer patterns so that the patterned samples can act as a part of the waveguide. The schematic of a typical sample and the experimental arrangements are shown in figure 6.1 illustrating the broadening of FMR line-width (ΔH) due to spin pumping effect. A continuous rf ($f = 8 - 12$ GHz) signal with an output power of 10 dBm is applied along the length of the sample using a microwave analog signal generator. Resonance curve is obtained as a function of bias magnetic field H_{ext} varied from 0 – 1.8 kOe, applied at an angle of $\theta = 45^\circ$ in the plane of the sample. The effective damping constant[3,17] is calculated by using the expression $\Delta H = 2\pi f \alpha / \gamma$, where γ is the gyromagnetic ratio. In this power range the output signal amplitude is linear and hence the spin precession in the ferromagnetic layer falls in the small angle regime. The experiments are performed at room temperature.

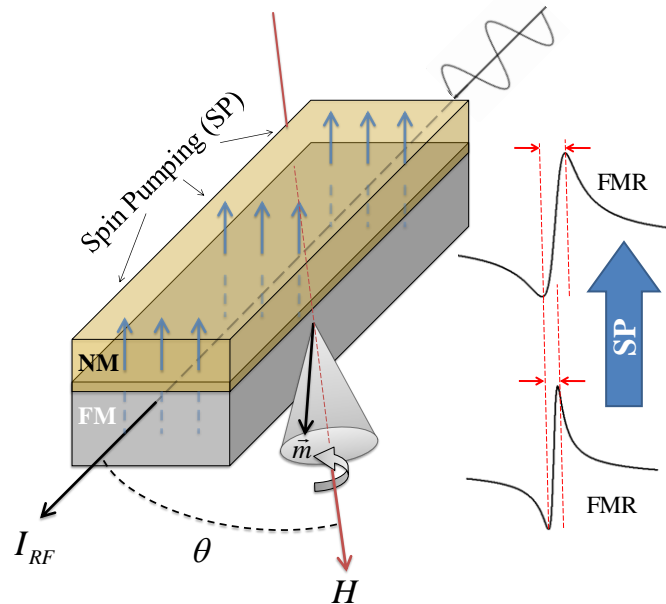


Figure 6.1. Schematic diagram of the experimental setup explaining increase in ferromagnetic resonance (FMR) line-width due to spin pumping effect.

6.3. Results and Discussion

Figure 6.2(a) shows variation of damping of CoFeB/Pt sample as a function of Pt layer thickness where the symbols indicate the experimental data points. We observe that damping constant shows smaller values at lower thicknesses of Pt which increases with thickness and gets saturated at higher thicknesses. The experiment is performed at four different thicknesses of CoFeB where we observe similar trend in the variation with Pt thickness. However, the damping values are higher for thinner CoFeB samples. Looking into the nonmagnetic layer thickness dependence of damping it can be said that Pt is a heavy metal which can absorb spin angular momentum from adjacent FM layer and act as a spin sink to the system. The precessing magnetization creates a non-equilibrium spin accumulation in the FM/NM interface which diffuses in the adjacent NM layers where it can dissipate by spin-flip processes[18-19] associated with the spin diffusion length of Pt layer. As a result when the thickness of the Pt layer is reduced to a value close to its spin diffusion length, the spin-flip process gets affected which essentially causes a drop in the spin dissipation rate. Hence, below a certain thickness an equilibrium spin accumulation starts to develop at the FM/NM interface which will oppose the spin pumping from FM to NM layer and thereby a reduction in damping.

This phenomenon has a noticeable similarity with the variation of spin injection as a function of normal metal thickness[5]. Let us consider the case where spin current is generated across the thickness of normal metal due to spin Hall effect (SHE) when a charge current is applied along its length. It is observed that the magnitude of spin current is reduced at lower thickness of Pt when it is comparable to its spin diffusion length (l_s)[20]. Due to a vertical gradient in the spin-dependent electron chemical potentials spin mixing occurs which gives rise to a counter flow of spin by effectively reducing the magnitude of the spin injection. Using the drift-diffusion analysis for a bilayer system and assuming a transparent interface one can obtain that the spin current density is proportional to $[1 - \text{sech}(d/l_s)]$. For simplicity, let us first consider spin pumping through a transparent interface. Thus, drawing an intuitive analogy between the two effects associated with momentum transfer in case of a bi-layers our experimental data points in figure 2(a) are fitted by equation 6.1 as shown by continuous lines.

$$\alpha_{eff} = \alpha_0 + \alpha_{SP}[1 - \text{sech}(d/d_{SF})] \quad (6.1).$$

Here, α_0 , α_{eff} and α_{SP} are the effective damping constants, intrinsic damping constant and enhanced damping constant due to spin pumping effect and d_{sf} is the length scale corresponding to the spin flip process in the NM layer. A good agreement between experimental data and theoretical fit has been observed. However, in case of spin pumping the role of ferromagnetic layer can be important. Figure 6.2(b) shows that d_{SF} decreases with FM layer thickness approaching a constant value ~ 2 nm which is comparable to l_S of Pt as obtained in reference 5. We think that at lower FM thickness d_{sf} becomes larger than l_S possibly because damping values get modified due to spin accumulation or development of strain at the interface. A detailed study can be a topic for further investigation.

Now, the Pt capping layer is replaced by Ta and the variation of damping is plotted with the NM layer thickness in figure 6.2(c). The experiment is repeated for different CoFeB layer thickness. A similar variation is observed as in case of Pt/CoFeB which is fitted by equation 6.1 although, the variation is smaller in this case. Here, spin accumulation at the interface is small because spin pumping is weaker in Ta as compared to Pt. Hence, estimation of d_{sf} (3 ± 1 nm) is associated with larger error.

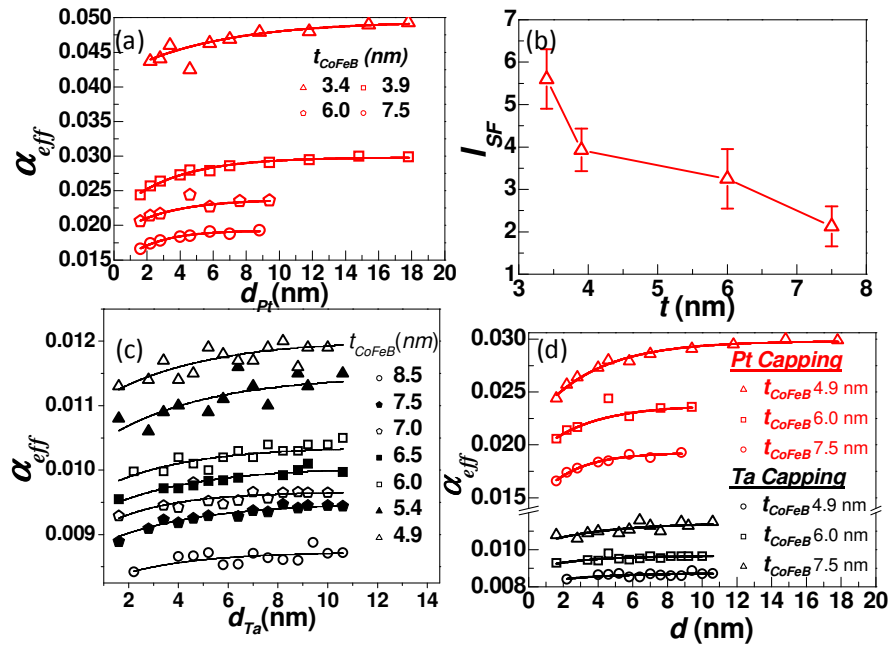


Figure 6.2. (a) Variation of damping in CoFeB/Pt system with Pt layer thickness and (b) spin diffusion length as a function of CoFeB layer thickness. (c) Variation of damping in CoFeB/Ta system with Ta layer thickness. (d) Comparison of damping variation between CoFeB/Pt and CoFeB/Ta with nonmagnetic layer thickness.

For the confirmation of the spin pumping effect as a key mechanism to describe the results above further investigation is performed. A variation of damping constant with CoFeB layer thickness t_{CoFeB} at a constant value of $d = 6$ nm. We observe that damping decreases with d similar to the observation of reference 18. To illustrate the nature of the variation we plotted damping as a function of $1/t$ as shown in figure 6.3(a) and found a linear dependence. The best fit straight lines are shown by the continuous lines. In this context it is worth noting that the line-width corresponding to spin pumping ΔH_{sp} follows the same $1/t$ dependence[6,21] as shown in equation 6.2

$$\alpha_{\text{eff}} = g\mu_B g_{\text{eff}}^{\uparrow\downarrow} / 4\pi M_s t_{\text{FM}} \quad (6.2),$$

where f is the frequency and $g_{\text{eff}}^{\uparrow\downarrow}$ is the effective spin mixing conductance. The slope is larger for Pt (0.1 nm) as compared to Ta (0.035 nm) although the ferromagnetic layer is the same. This is possible in presence of spin relaxation to the NM which is stronger in case of Pt. The observation suggests the presence of spin pumping effect in our sample. The frequency variation of line-width can also reveal important information about the nature of damping. In figure 6.3(b) we see that ΔH increases linearly with f for both CoFeB/Ta and CoFeB/Pt but with a larger slope in case of Pt. Such a linear variation can be observed in case of single ferromagnetic film. However, ferromagnetic layer is identical for both the samples. Hence, there must be some other origin which is responsible for the difference in slope. From earlier literature[6] it is known that line-width corresponding to spin pumping is also proportional to f . Therefore, the difference in slope can be attributed to different spin pumping efficiency of Pt and Ta. From these arguments we can confirm that in case of our sample spin pumping plays a crucial role and the effect is stronger for Pt.

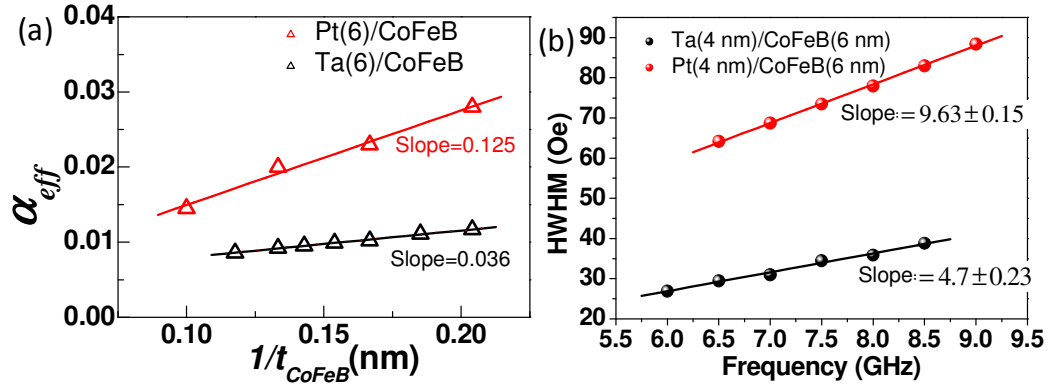


Figure 6.3. (a) Inverse of ferromagnetic layer thickness dependence of damping for CoFeB/NM systems (NM = Pt, Ta) and (b) variation of line-width with frequency for the same samples.

However, in case of a real samples interface is not completely transparent. In many cases interfacial layers are associated with some disorder, lattice mismatch and contact resistances which can influence the spin transport process. The transparency of the interface is quantitatively denoted by $g_{eff}^{\uparrow\downarrow}$. From equation 6.2 it can be easily seen that ΔH_{sp} is proportional to $g_{eff}^{\uparrow\downarrow}$ i.e., for a transparent interface spin pumping is high which causes broadening of FMR linewidth. The value of $g_{eff}^{\uparrow\downarrow}$ depends on the properties of the interface determined by the combination of material forming the interface. Here, we introduce CoFe in place of CoFeB which shows more crystalline property despite of its same magnetic composition (Co and Fe). Hence, a comparative study of damping in such magnetic bi-layers with different nonmagnetic capping may provide us a deeper insight into the problem. In figure 6.4(a) NM thickness dependence of damping constant for NM/FM samples, with NM = Pt, Ta and FM = CoFeB, CoFe, are compared. In the four combinations, the nature of variation shows a significant difference from each other. For Pt/CoFeB and Ta/CoFeB, the damping constant increases with d as we have seen earlier in figure 6.2(d). However, when CoFeB is replaced by CoFe, in case of Pt capping, damping constant is almost independent, while for Ta capping, it decreases with d . The results suggest that equation 6.1 is not sufficient to explain the four curves all to-

gether. Hence apart from spin pumping there must be some other effects governing the variation of damping which has been overlooked so far.

When a NM layer is deposited on top of a ferromagnetic layer having different lattice parameter, the lattices try to accommodate themselves to form a continuous crystalline structure across the interface for energy minimization. As a result strain is developed in the interface with the formation of a hybridized lattice below a critical thickness of the nonmagnetic capping known as coherent region. However, the coherency breaks above the critical thickness when the interface starts to accommodate lattice misfit by breaking the hybridization resulting in a reduction of damping and strain in the interface. In this region the strain effectively develops magnetoelastic interface anisotropy which is inversely proportional to the capping layer thickness[22]. As the damping constant is known to have a linear relation with the interface anisotropy[23], we would expect a $1/d$ dependence of the intrinsic damping constant. Thus equation 6.1 can be modified into equation 6.3 as follows:

$$\alpha_{eff} = \alpha_0 / d + \alpha_{sp}[1 - \text{sech}(d / d_{SF})] \quad (6.3).$$

Here, the first term accounts for the change in the intrinsic damping constant associated with the strain induced interface anisotropy, while the second term is related to the spin accumulation. With increasing d the first term causes a decrease in damping while the second term results in an increase and hence, the competition between the two determines the variation in the damping constant. In figure 6.4(a) all the experimental data are fitted with the modified equation. A good agreement between the experimental data and theoretical fit has been observed, which suggests the validity of our model.

With the help of this model expressed by equation 6.3, figure 6.4(a) can be understood as follows. We already discussed that Pt capping causes an overall increase in damping as opposed to Ta capping due to larger spin pumping effect. Here we compare the damping constant of two compositionally similar FM alloy CoFeB and CoFe having same NM capping layer as Pt to understand the role of B in this problem. In figure 6.4(a) we observe the overall damping constant is larger in case of CoFeB/Pt than in CoFe/Pt which is essentially the largest among the all four combinations of FM and NM. The CoFeB is amorphous[24-25] in nature due to the presence of boron which creates a diffused interface region with Pt. The role of boron diffusion[26-27] in the interface can be important in this case. On the contrary CoFe

is crystalline in nature[28] having a sharper interface with more prominent contact and resistivity mismatch. Hence, the larger value of damping in case of CoFeB/Pt may stem from larger spin conduction through the diffused interface. Further, we replace Pt by Ta and observe very similar value of damping in case of CoFeB and CoFe samples because spin pumping effect is weakly observed in case of Ta.

The nonmagnetic thickness dependence of damping of figure 4(a) can be categorized in two classes. First, is CoFeB/NM where the second term of equation 6.3 dominates describing reduction of damping constant with decreasing d due to spin accumulation. The other is CoFe/NM where the first term related to strain anisotropy is significant. For CoFe/Ta only the first term is important causing a slow decrease in α with d while for CoFe/Pt both the competing effects are equally present resulting in an invariance of α . Hence, from the discussion we understand that reduction of intrinsic damping due to strain at the interface is more relevant in case of CoFe samples due to its crystalline structure and sharp interface while interlayer spin transport processes are more favoured in CoFeB samples due to its diffused interface. The spin mixing conductance of the CoFeB(7.5 nm)/NM interface has been estimated using equation 6.2 which is found to be larger for NM = Pt(6) (34 nm^{-2}) as compared to Ta(6) obtained as 5 nm^{-2} . The values can be compared with earlier literature[19,29]. In figure 6.4(b) we compare damping constant as a function of $1/t$ for all the four samples. In all cases a linear variation is observed with different slopes. The slopes of the straight line fit reflect the spin pumping efficiency of the individual samples. The values are similar for Ta/CoFe and Ta/CoFeB samples whereas they are different for Pt/CoFe and Pt/CoFeB. The spin pumping effect itself is weak for Ta samples. As a result the difference in slopes between Ta/CoFe and Ta/CoFeB cannot be resolved. However, slope for Pt/CoFeB is larger than Pt/CoFe because CoFeB interface is more spin transparent. The result agrees with our earlier observation in figure 6.4(a).

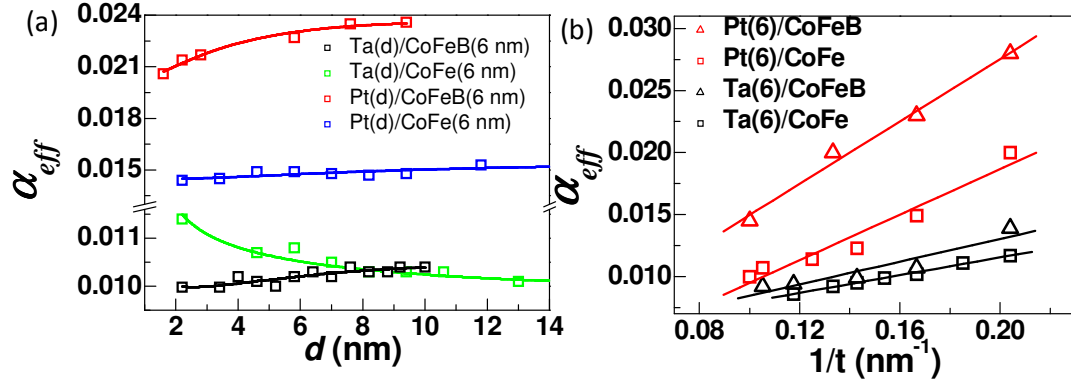


Figure 6.4. (a) NM layer thickness dependence of damping for the combination of FM (6 nm)/NM bi-layers, with FM = CoFe and CoFeB, NM = Pt, Ta. (b) Comparison of damping with inverse of FM layer thickness for those samples.

6.4. Summary

In summary, we perform spin torque ferromagnetic resonance experiment to study the variation of effective damping as a function of layer thicknesses in ferromagnet/nonmagnet bi-layers. The damping is essentially increased in presence of spin pumping however, at lower nonmagnetic layer thicknesses the effect is limited by interfacial spin accumulation leading to a continuous variation of damping with thickness. On the other hand, strain induced interface anisotropy causes a variation of damping with nonmagnetic layer thickness. A combined effect is described to explain the observed variation in different systems. We discuss the role of interface in governing the interlayer spin transport processes. It is found that CoFeB forms a more transparent interface than CoFe helping in spin pumping between the layers. Our study aims towards low cost optimization of magnetic devices.

References

- [1] Bader, S. & Parkin, S. Spintronics. *Annu. Rev. Condens. Matter Phys.* **1**, 71 (2010).
- [2] Mizukami, S., Ando, Y. & Miyazaki, T. Ferromagnetic resonance linewidth for NM/80NiFe/NM films (NM= Cu, Ta, Pd and Pt). *J. Magn. Magn. Mater.* **226**, 1640 (2001).

-
- [3] Liu, L., Moriyama, T., Ralph, D. & Buhrman, R. Spin-torque ferromagnetic resonance induced by the spin Hall effect. *Phys. Rev. Lett.* **106**, 036601 (2011).
- [4] Ganguly, A. *et al.* Time-domain detection of current controlled magnetization damping in Pt/Ni₈₁Fe₁₉ bilayer and determination of Pt spin Hall angle. *Appl. Phys. Lett.* **105**, 112409 (2014).
- [5] Ganguly, A. *et al.* Thickness dependence of spin torque ferromagnetic resonance in Co₇₅Fe₂₅/Pt bilayer films. *Appl. Phys. Lett.* **104**, 072405 (2014).
- [6] Rezende, S. *et al.* Enhanced spin pumping damping in yttrium iron garnet/Pt bilayers. *Appl. Phys. Lett.* **102**, 012402 (2013).
- [7] Dominguez, D. L. *et al.* High-resolution electron microscopy in spin pumping NiFe/Pt interfaces. *J. Appl. Phys.* **117** (2015).
- [8] Mizukami, S., Ando, Y. & Miyazaki, T. Effect of spin diffusion on Gilbert damping for a very thin permalloy layer in Cu/permalloy/Cu/Pt films. *Phys. Rev. B* **66**, 104413 (2002).
- [9] Grange, W. *et al.* Experimental and theoretical x-ray magnetic-circular-dichroism study of the magnetic properties of Co₅₀Pt₅₀ thin films. *Phys. Rev. B* **62**, 1157 (2000).
- [10] Nakajima, N. *et al.* Perpendicular magnetic anisotropy caused by interfacial hybridization via enhanced orbital moment in Co/Pt multilayers: magnetic circular x-ray dichroism study. *Phys. Rev. Lett.* **81**, 5229 (1998).
- [11] King, J. *et al.* Local control of magnetic damping in ferromagnetic/non-magnetic bilayers by interfacial intermixing induced by focused ion-beam irradiation. *Appl. Phys. Lett.* **104**, 242410 (2014).
- [12] Rantschler, J. O. *et al.* Damping at normal metal/permalloy interfaces. *IEEE Trans. Magn.* **41**, 3523 (2005).
- [13] Heinrich, B., Cochran, J. & Hasegawa, R. FMR line broadening in metals due to two-magnon scattering. *J. Appl. Phys.* **57**, 3690 (1985).
- [14] Hurben, M. & Patton, C. Theory of two magnon scattering microwave relaxation and ferromagnetic resonance linewidth in magnetic thin films. *J. Appl. Phys.* **83**, 4344 (1998).
- [15] Lenz, K. *et al.* Two-magnon scattering and viscous Gilbert damping in ultrathin ferromagnets. *Phys. Rev. B* **73**, 144424 (2006).

- [16] Ryu, K. S., Yang, S. H., Thomas, L. & Parkin, S. S. P. Chiral spin torque arising from proximity-induced magnetization. *Nat. Commun.* **5**, 3910 (2014).
- [17] Kondou, K. *et al.* Evaluation of spin Hall angle and spin diffusion length by using spin current-induced ferromagnetic resonance. *Appl. Phys. Express* **5**, 073002 (2012).
- [18] Tserkovnyak, Y., Brataas, A. & Bauer, G. E. Enhanced Gilbert damping in thin ferromagnetic films. *Phys. Rev. Lett.* **88**, 117601 (2002).
- [19] Rojas-Sánchez, J. C. *et al.* Spin Pumping and Inverse Spin Hall Effect in Platinum: The Essential Role of Spin-Memory Loss at Metallic Interfaces. *Phys. Rev. Lett.* **112**, 106602 (2014).
- [20] Liu, L., Buhrman, R. & Ralph, D. Review and analysis of measurements of the spin Hall effect in platinum. *arXiv:1111.3702* (2011).
- [21] Mosendz, O. *et al.* Detection and quantification of inverse spin Hall effect from spin pumping in permalloy/normal metal bilayers. *Phys Rev B* **82**, 214403 (2010).
- [22] Johnson, M., Bloemen, P., Den Broeder, F. & De Vries, J. Magnetic anisotropy in metallic multilayers. *Rep. Prog. Phys.* **59**, 1409 (1996).
- [23] Pal, S. *et al.* Tunable magnonic frequency and damping in [Co/Pd](8) multilayers with variable Co layer thickness. *Appl. Phys. Lett.* **98** 082501 (2011).
- [24] Yuasa, S., Suzuki, Y., Katayama, T. & Ando, K. Characterization of growth and crystallization processes in CoFeB/MgO/CoFeB magnetic tunnel junction structure by reflective high-energy electron diffraction. *Appl. Phys. Lett.* **87**, 2503 (2005).
- [25] Mukherjee, S. *et al.* Role of boron diffusion in CoFeB/MgO magnetic tunnel junctions. *Phys Rev B* **91**, 085311 (2015).
- [26] Kozina, X. *et al.* A nondestructive analysis of the B diffusion in Ta–CoFeB–MgO–CoFeB–Ta magnetic tunnel junctions by hard x-ray photoemission. *Appl. Phys. Lett.* **96**, 072105 (2010).
- [27] Miyajima, T. *et al.* Transmission electron microscopy study on the crystallization and boron distribution of CoFeB/MgO/CoFeB magnetic tunnel junctions with various capping layers. *Appl. Phys. Lett.* **94**, 122501 (2009).
- [28] Iwasaki, H. Magnetic Properties and Crystal Structures of Sputtered CoFe Films. *IEEE Trans. Magn. Jpn.* **5**, 515 (1990).
- [29] Tokaç, M. *et al.* Interfacial Structure Dependent Spin Mixing Conductance in Cobalt Thin Films. *Phys. Rev. Lett.* **115**, 056601 (2015).

Chapter 7

Thickness Dependence of Spin-torque Ferromagnetic Resonance in $\text{Co}_{75}\text{Fe}_{25}/$

Pt Bi-layer Films and Estimation of Spin Hall Angle of Pt

The spin Hall angle of Pt in $\text{Co}_{75}\text{Fe}_{25}/\text{Pt}$ bi-layer films was experimentally investigated by means of the spin-torque ferromagnetic resonance and the modulation of damping measurements. By comparing the present results with the $\text{Ni}_{80}\text{Fe}_{20}/\text{Pt}$ system, we found that the ferromagnetic layer underneath the Pt one greatly affects the estimation of the spin Hall angle. We also discuss the spin diffusion length of Pt and the ferromagnetic thickness dependence of the Gilbert damping coefficient.

7.1. Introduction

Existing technology of electronic data storage or data transfer devices driven by charge current may be replaced by a technology that solely deals with the spin degree of freedom of an electron, known as spintronics[1]. For a pure spin current[2] there are many advantages like no net flow of charge and hence no stray Oerstead field, minimum power dissipation, tunable magnetic damping[3-6], by which one can achieve loss-less propagation of electromagnetic waves in magnetic media[3], or reduction of noise due to thermal fluctuation[5] in nanomagnetic devices. Hence, a great deal of research is going on to increase the conversion efficiency between charge current and spin current known as spin Hall angle[6-8] (θ_{SH}) for applications in spintronic devices. Spin current can be generated by different techniques including nonlocal electrical injection from ferromagnetic contacts in multi-terminal structures, optical injection using circularly polarized light, spin pumping from a precessing ferromagnet and also by spin Hall effect[3,6-7,9-12] (SHE). The SHE does not require any ferromagnet

(FM) or external bias field to generate the spin current. However, injected spin current can affect the magnetization dynamics of an adjacent FM layer, from which one can quantify θ_{SH} . Hence, in case of FM and nonmagnetic metal (NM) bi-layer structures, the magnetic properties of the FM layer, thickness of the FM and NM layers, and interface properties can play crucial roles in determining θ_{SH} . As a matter of fact, there is a large inconsistency in the estimated θ_{SH} [6,8,13-14] of a standard SHE material Pt. The values reported by several groups differ even by an order of magnitude. Thus, it is very important to investigate the origin of this inconsistency, for which a systematic study of θ_{SH} for different materials and thicknesses are required. In this work, we have studied the SHE of $\text{Co}_{75}\text{Fe}_{25}/\text{Pt}$ bi-layer films using the spin-torque induced ferromagnetic resonance (ST-FMR)[6-7] and modulation of damping (MOD) measurements.[6] The latter is done by applying a dc current in the bi-layer system. This dc current produces an additional torque in FM layer either parallel or anti parallel to the Gilbert damping thereby modifying the effective damping. Here, $\text{Co}_{75}\text{Fe}_{25}$ is chosen as the FM layer as it has a smaller anisotropic magnetoresistance (AMR) effect than $\text{Ni}_{80}\text{Fe}_{20}$. Consequently, for this sample, contributions from other effects to θ_{SH} are expected to become more prominent compared to the AMR effect.

7.2. Experimental Details

Thin films of $\text{Co}_{75}\text{Fe}_{25}$ ($t=0-17$ nm)/Pt($d=0-20$ nm)/ Al_2O_3 (2 nm) are grown on a non-doped Si substrate by dc/rf magnetron sputtering in a wedge shape using a linear motion at the base pressure of 4×10^{-7} Pa and Ar gas pressure of 0.13 Pa. Al_2O_3 is used as an insulating capping layer. The resistivities of Pt and $\text{Co}_{75}\text{Fe}_{25}$ are measured to be 28.0 and 15.2 $\mu\Omega\cdot\text{cm}$ while the measured AMR is about 1.0% for the 10 nm thick CoFe film, which is smaller than that of $\text{Ni}_{80}\text{Fe}_{20}$ (about 1.6%). The bi-layer films are patterned into rectangular shaped elements ($20 \times 60 \mu\text{m}^2$) using optical lithography and Ar-ion etching technique. A co-planar Ti(5 nm)/Au(150 nm) waveguide is deposited on top of each sample element so that the sample can act as a part of the waveguide. The schematic of a sample and the circuit diagram of the experimental setup are shown in figure 7.1(a). A constant rf (8–12 GHz) signal with an output power of 10 dBm is applied along the length of the sample using a microwave analog signal generator [model No. MXG N5183A]. An external bias magnetic field ($H_{ext} = 0-1.8\text{kOe}$) is also applied at an angle of 45° within the plane of the sample. In this power range

the output signal amplitude is linear with power, and hence, the spin precession in the ferromagnetic layer is in the small angle regime. All the experiments are performed at room temperature.

7.3. Underlying Theory

The current applied in the bi-layer film is divided in two parts flowing into the two adjacent layers depending on their resistances. The stray Oersted field generated due to the current in the Pt layer induces a FMR, which is antisymmetric with respect to the resonant magnetic field. On the other hand, due to the spin orbit interaction and impurity scattering[2] charge carriers with opposite spin polarities are scattered in opposite directions in the Pt layer. Consequently, spin current is generated perpendicular to the charge current due to the SHE and is injected[2] into the adjacent CoFe layer. As a result of the injected spin current, another FMR is induced in the CoFe layer, which is symmetric in nature. The AMR of the precessing magnetization gives rise to an electrical resistance oscillating at the same frequency as the applied rf current. The oscillating resistance and current together produce a measurable dc voltage due to the spin-torque diode effect[7] as given by equation 7.1

$$V = -\frac{1}{4} \frac{dR}{d\theta} \frac{\gamma I_{FM} \cos \theta}{\Delta 2\pi (df / dH_{ext})_{H_{ext}=H_0}} [S F_S(H_{ext}) + A F_A(H_{ext})] \quad (7.1),$$

where I_{FM} is the current in FM layer, $F_A(H_{ext}) = F_S(H_{ext}) \frac{H_{ext} - H_0}{\Delta}$ is a Lorentzian derivative,

which is anti-symmetric at resonant field, $F_S(H_{ext}) = \frac{\Delta^2}{\Delta^2 + (H_{ext} - H_0)^2}$ is the Lorentzian function,

which is symmetric at resonant field, Δ is the half width at half maximum, H_0 is the resonant field, S and A are the weight factors for the symmetric and anti-symmetric FMR, θ is the angle between current and magnetization, R is the resistance, f is the frequency, and γ is the gyromagnetic ratio.

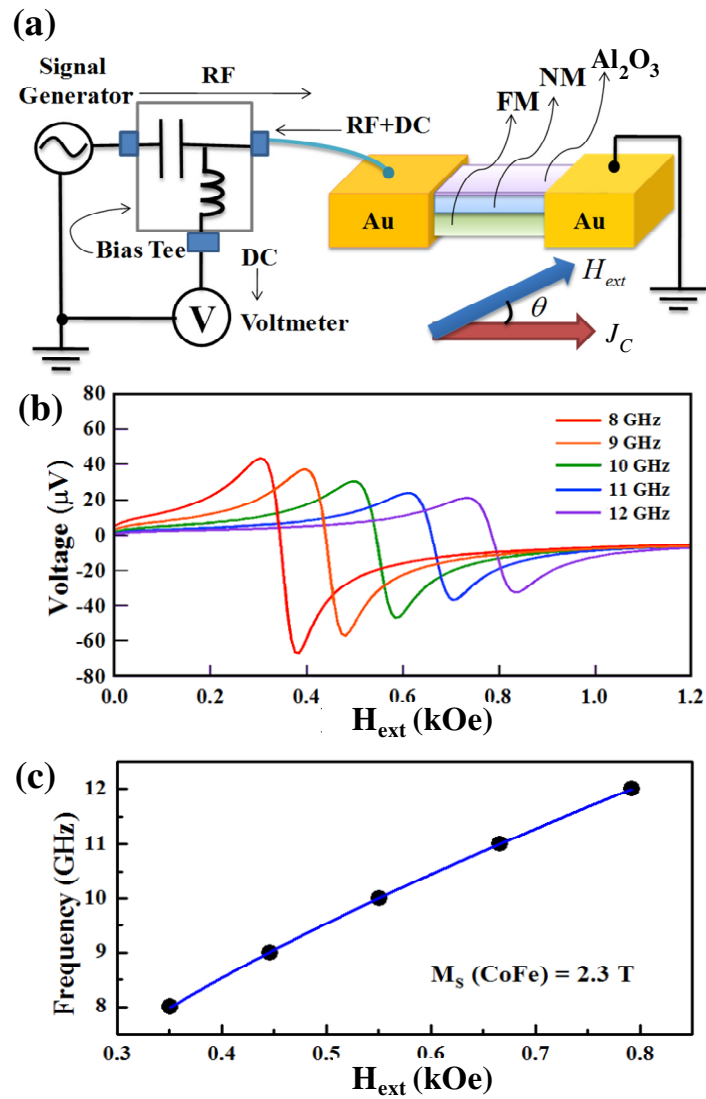


Figure 7.1. (a) Schematic illustration of the experimental setup and the sample along with the directions of the applied rf current and bias magnetic field; (b) FMR spectra measured at different excitation frequencies (f); and (c) variation of resonance frequency (f) with the bias magnetic field for CoFe (6.5 nm)/Pt (5.8 nm) sample and the extraction of saturation magnetization from the Kittel fit.

The effective damping coefficient α_{eff} [6-7] of the sample is related to the line-width by $\Delta = \frac{2\pi f \alpha_{eff}}{\gamma}$ while S and A are proportional to the spin current density J_S and charge current density J_C , respectively[4,7], in the Pt layer as given by equation 7.2

$$\begin{aligned} S &= \frac{\hbar J_s}{2e\mu_0 M_s t} \\ A &= H_{rf} \left[1 + \left(\frac{M_{eff}}{H_{ext}} \right)^{1/2} \right] \\ &\approx \frac{J_c d}{2} \left[1 + \left(\frac{M_{eff}}{H_{ext}} \right)^{1/2} \right] \end{aligned} \quad (7.2),$$

where e is the charge of electron, μ_0 is the free space permeability, M_s is the saturation magnetization, H_{rf} is the field due to rf current and M_{eff} is the effective magnetization including magnetic anisotropy. Since the magnetic anisotropy is small for ferromagnetic thin films, we can approximate M_{eff} as M_s . Hence, the ratio between spin current and charge current densities (J_s / J_c) can be summarized from equation 7.2 as given in equation 7.3[3,6].

$$\frac{J_s}{J_c} = td \frac{S}{A} \frac{e\mu_0 M_s}{\hbar} \sqrt{1 + \left(\frac{M_{eff}}{H_{ext}} \right)} \quad (7.3)$$

We have processed the measured FMR spectra to isolate the symmetric and asymmetric contributions and thereby estimated the (J_s / J_c) value, which we termed as the ST-FMR results in this paper.

On the other hand, if a dc charge current is applied to the sample in addition to the rf charge current, a dc spin current is generated in the NM layer perpendicular to the charge current. This produces a spin transfer torque[6,14-15] (STT) in the FM layer, acting along the $(\hat{m} \times \hat{\sigma} \times \hat{m})$ direction, where \hat{m} is the magnetization vector and $\hat{\sigma}$ is the injected spin moment. The STT is collinear with the damping torque and either increases or decreases the effective value of damping depending on the polarity of $\hat{\sigma}$. The STT is incorporated as the last term in the Landau–Lifshitz– Gilbert equation as given by equation 7.4 below

$$\frac{d\hat{m}}{dt} = -\gamma[\hat{m} \times (H_{eff} + H_{rf})] + \alpha(\hat{m} \times \frac{d\hat{m}}{dt}) + \frac{\hbar}{2e\mu_0 M_s t} J_s (\hat{m} \times \hat{\sigma} \times \hat{m}) \quad (7.4),$$

where H_{eff} is the effective magnetic field and α is the Gilbert damping. Hence, by tuning the applied dc charge current we can externally control the effective damping of the FM material (MOD) as estimated from the FMR line-width. According to the theory of spin torque, this modulation is related to the injected spin current density and relative orientation of magnetic moment with current as given by equation 7.5

$$\Delta\alpha = (\alpha - \alpha_0) = \frac{\sin\theta}{(H_{ext} + M_{eff})\mu_0 M_s t} \frac{\hbar J_s}{2e}, \quad (7.5),$$

where α_0 is the Gilbert damping with zero dc current and $\Delta\alpha$ is the MOD. Hence, by calculating the rate of MOD, $\Delta\alpha / J_c$ we can evaluate J_s / J_c from equation 7.5. This, in turn, gives another estimate of θ_{SH} . This measurement technique is referred to as MOD measurement in this paper.

7.4. Results and Discussion

Figure 7.1(b) shows the typical ST-FMR spectra for a CoFe(6.5 nm)/Pt(5.8 nm) bi-layer film excited at different rf frequencies (f) from 8 to 12 GHz. The obtained f vs. resonant field curve is well fitted with Kittel formula[7] for in-plane magnetized samples given by equation 7.6, as shown in figure 7.1(c)

$$f = \frac{\gamma}{2\pi} \sqrt{H_{ext}(H_{ext} + 4\pi M_s)}. \quad (7.6).$$

From the fit, we obtained $\gamma = 1.76 \times 10^{11}$ rad/(s.T) and $4\pi M_s = 2.3$ T, which is more than two times larger compared to commonly used Permalloy (Ni₈₀Fe₂₀, hereafter Py) (~1 T).

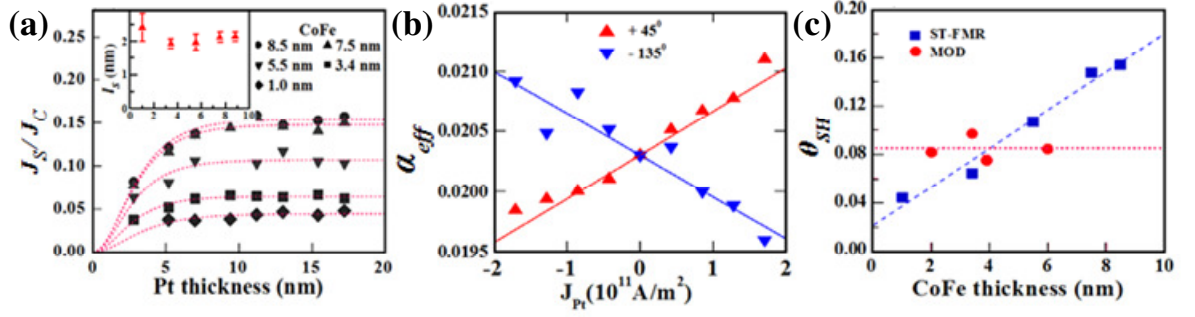


Figure 7.2. (a) Variation of J_s / J_c as a function of Pt thickness in CoFe/Pt bi-layers with different CoFe thickness. Inset shows the variation of spin diffusion length (l_s) of Pt with CoFe thickness. (b) MOD as a function of current density in the Pt layer for two different orientations of the bias magnetic field in CoFe(3.4 nm)/Pt(5.8 nm) bi-layer. (c) Comparison of θ_{SH} as a function of CoFe thickness obtained from ST-FMR and MOD measurements.

In figure 7.2(a) we plot J_s / J_c values obtained from the ST-FMR measurement as a function of Pt thickness. J_s / J_c is found to be constant for thick Pt films, while it decreases as we lower the thickness and approaches towards zero at zero thickness limit. This behavior can be well explained by equation 7.7

$$\frac{J_s}{J_c} = \theta_{SH} \left[1 - \operatorname{sech} \left(\frac{d}{l_s} \right) \right] \quad (7.7),$$

where θ_{SH} is the characteristic spin Hall angle and l_s is the spin diffusion length[7] of the nonmagnetic layer, which is Pt in our case. From the fitted curve l_s is found to be 2 ± 0.2 nm, which is almost independent of CoFe thickness as shown in the inset of figure 7.2(a). We should note here that the spin diffusion length estimated using equation 7.7 is a characteristic length for bi-layer films, which is essentially different from the one obtained from nonlocal spin valve measurements[16] or from weak anti-localization measurements[17] where Pt is not directly in contact to FM. More details about the spin diffusion length will be discussed elsewhere.

On the other hand, in the MOD measurement, the effective value of damping shows a linear variation with the dc charge current density in the Pt layer as shown in figure 7.2(b). When

the bias field angle is reversed from 45° to -135° the slope of the curve only changes sign while keeping its magnitude unaffected. This clearly shows that MOD must have a magnetic origin. Moreover, the slope of the graph in figure 7.2(b) is also an important measurable quantity, from which we can calculate $\Delta\alpha/J_C$ and hence J_S/J_C using equation 7.5, which gives an estimate of θ_{SH} .

In figure 7.2(c) we compare the values of θ_{SH} as a function of CoFe thicknesses obtained from ST-FMR as well as the MOD measurement. We should note that the θ_{SH} values from ST-FMR measurement shown in figure 7.2(c) are the characteristic value of θ_{SH} obtained from the fitted curves of figure 7.2(a). It monotonically increases with the CoFe thickness and the data points are well fitted by a straight line. At zero thickness limit θ_{SH} comes out to be $2.2\% \pm 0.8\%$. In contrary from the MOD measurement we obtain a θ_{SH} value of $8.5\% \pm 0.9\%$, which is almost independent of CoFe thickness. To investigate this behavior we compare the results of ST-FMR and MOD measurements of CoFe/Pt with those from $\text{Ni}_{80}\text{Fe}_{20}(\text{Py})/\text{Pt}$ system as shown in figures 7.3(a) and 7.3(b), respectively. In case of ST-FMR measurement, as shown in figure 7.3(a), we again observe a linear increase of θ_{SH} with Py layer thickness but with a smaller slope. What is interesting to note is that at zero thickness limit both of the curves converge to the same value ($2.2\% \pm 0.4\%$ in case of Py/Pt[7]). These results indicate that for finite values of t , θ_{SH} has a clear dependence of ferromagnetic material whereas at $t \rightarrow 0$ it no longer depends on the type of ferromagnet. Hence, the $t \rightarrow 0$ limit closes with the actual measure of θ_{SH} of the NM layer, which is an intrinsic property of that material.

We have analyzed the reason for the dependence of θ_{SH} on the FM material and its thickness as follows. (i) First, we apply an rf current in a single CoFe layer[18] and found an ST-FMR like spectrum at the same resonance frequency as observed for the bi-layer system as shown in figure 7.3(c). This behaviour is unexpected as the current density inside the CoFe layer should be uniform as the thickness of the CoFe layer is smaller than the microwave skin depth. However, there is a possibility that nucleation and propagation of non uniform spin waves[18] around the FM wire edges may give rise to a dc voltage inside the FM layer.

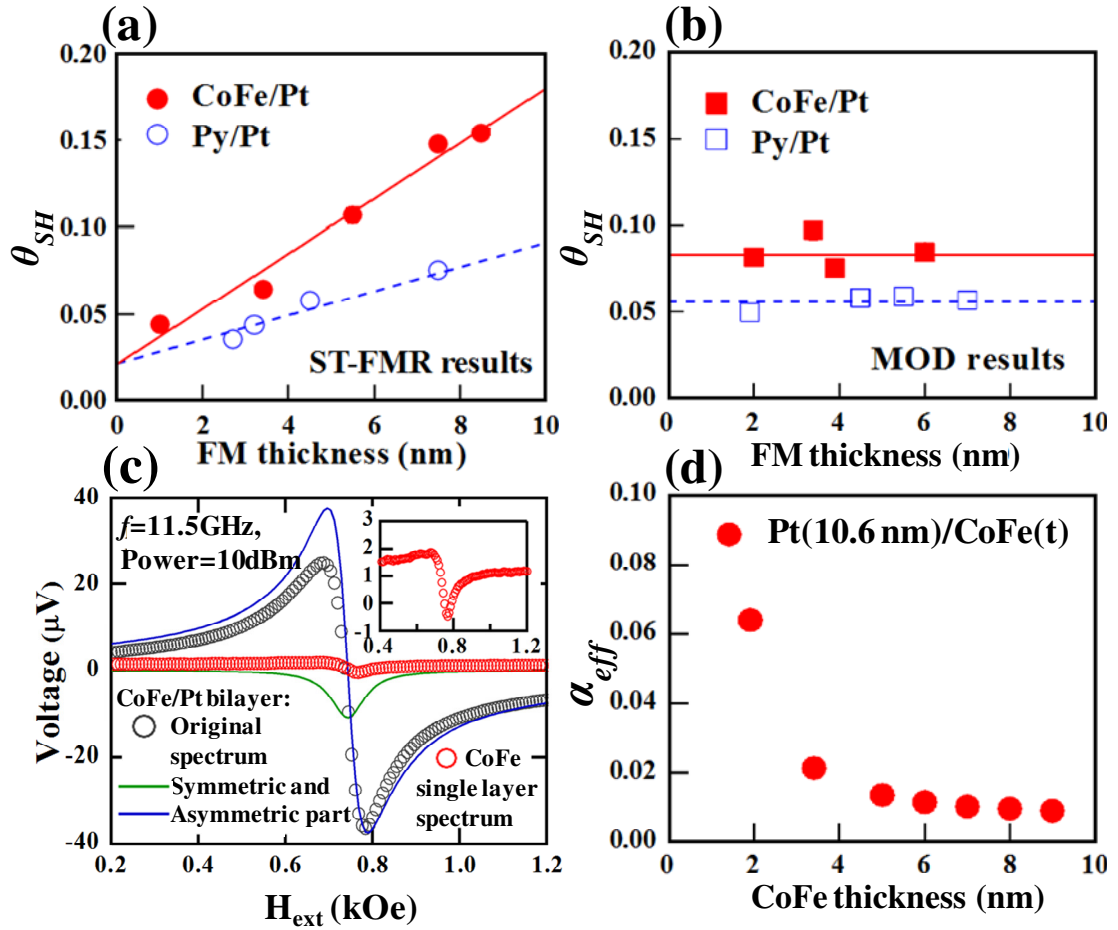


Figure 7.3. FM layer thickness dependency of θ_{SH} in CoFe/Pt and Py/Pt systems obtained from (a) ST-FMR measurement and (b) MOD measurement ($d = 5.8$ nm). (c) ST-FMR spectrum of CoFe(4.7 nm)/Pt(7 nm) bi-layer film is shown by black circle. Green and blue solid lines are the symmetric and asymmetric components, respectively. Red circles in the main graph as well as in inset show ST-FMR like spectrum in single CoFe(4.7 nm) layer. (d) CoFe thickness dependency of effective damping coefficient α_{eff} . For the Py/Pt system, the ST-FMR data in figure 7.3(a) and the MOD data in figure 7.3(b) are taken from references 7 and 19, respectively.

In case of a FM/NM bi-layer samples similar voltage can also be generated in the FM layer, which further modifies the spectrum shape and thereby the value of θ_{SH} . This effect is expected to increase with the FM layer thickness as the demagnetization region increases with thickness, which may give rise to a monotonic increase in θ_{SH} as shown in figure 7.3(a). However, the contribution of nonuniform spin wave is very small in the CoFe/Pt bi-layer film. This is because the output voltage of ST-FMR like spectrum in single CoFe layer is much smaller than the FMR spectrum in CoFe/Pt bi-layer film as shown in figure 7.3(c). (ii) The other possibility is the generation of inverse spin Hall effect[8,16] (ISHE) in the bi-layer sample due to the spin pumping effect. The corresponding voltage is determined by the cone angle[8] of spin precession, which is inversely proportional to the spectrum line-width or the effective value of damping at the point of resonance. Figure 7.3(d) shows that α_{eff} sharply decreases with the CoFe thickness, indicating greater ISHE at higher FM layer thickness. This effect eventually modifies the original ST-FMR spectrum such that θ_{SH} also increases with the FM layer thickness. Again, the ISHE voltage is related to the spin mixing conductance ($g_{eff}^{\uparrow\downarrow}$)[8] which is directly proportional to M_s . As the M_s value of CoFe (2.3 T) is larger than that of Py (1.0 T), the former shows a faster modification of spectrum with thickness and also a greater slope in figure 7.3(a). Additionally, the ratio of ISHE voltage to ST-FMR voltage in the CoFe/Pt system is larger than that of the Py/Pt system, because of a smaller AMR effect in CoFe than Py, which is also responsible for the difference in the slopes.

On the other hand, figure 7.3(b) shows that in the MOD measurement there is no variation of θ_{SH} with respect to the FM thickness both for CoFe/Pt and Py/Pt bi-layers. For the CoFe/Pt system, θ_{SH} is found to be $8.5\% \pm 0.9\%$ which is larger than that for the Py/Pt system $5.6\% \pm 0.4\%$ [19]. These values are not in good agreement with those found from the ST-FMR measurement, which is $\sim 2.2\%$ for both systems. In the MOD measurement, ISHE does not affect the value of θ_{SH} because the rate of change of spectrum line-width with dc charge current density ($\Delta\alpha / J_C$) is important rather than the exact spectrum shape. ISHE directly affect the amplitude ratio of S and A but not the line-width of the original spectrum. This explains why θ_{SH} obtained from MOD measurement is almost independent of FM layer thickness.

However, the exact reason behind the inconsistency between the values of θ_{SH} obtained from the ST-FMR and MOD measurements is not very clear. We believe, in MOD measurements, thermally generated spin waves in the FM layer may cause line broadening, due to which θ_{SH} comes out to be larger compared to that from the ST-FMR measurement. On the other hand, the difference in θ_{SH} between the CoFe/Pt and Py/Pt systems obtained from MOD measurement may be caused by the difference in $g_{eff}^{\uparrow\downarrow}$ between CoFe/Pt and Py/Pt. The $g_{eff}^{\uparrow\downarrow}$ of CoFe is $4.0 \times 10^{19} \text{ m}^{-2}$ which is larger than that of Py ($2.6 \times 10^{19} \text{ m}^{-2}$).

Finally, the observed variation in α_{eff} with the CoFe layer thickness (t) shown in figure 7.3(d) may be interpreted as follows. Due to the Co 3d-Pt 5d hybridization[20] at the interface atoms of the bi-layer sample, d -band width for Co reduces, resulting in an increase in the spin-orbit coupling and thereby the damping coefficient α_{eff} . However, the nonlinear variation of α_{eff} with t implies that in addition to the interface hybridization effect, the spin pumping effect may also have an influence in determining the α_{eff} vs. t variation.

7.5. Summary

In summary, we presented the thickness dependence of θ_{SH} in $\text{Co}_{75}\text{Fe}_{25}/\text{Pt}$ bi-layer using the ST-FMR and MOD measurement and compared the results with those from the Py/Pt bilayers. From the ST-FMR measurements, we found that the intrinsic value of θ_{SH} for Pt does not depend on the material and thickness of the adjacent FM layer. However, due to the large influence of some extrinsic effects such as ISHE, the measured θ_{SH} value strongly depends on the FM material and its layer thickness. The MOD measurement gives higher value of θ_{SH} , which is independent of the FM layer thickness but depends on the FM material and the reason of this inconsistency is not very clear. We also found that the effective value of Gilbert damping sharply increases with the decreasing CoFe thickness probably due to a combination of the Co 3d-Pt 5d hybridization at the interface and the spin pumping effect.

7.6. References

- [1] Bader, S. & Parkin, S. Spintronics. *Annu. Rev. Condens. Matter Phys.* **1**, 71 (2010).

- [2] Takahashi, S. & Maekawa, S. Spin current, spin accumulation and spin Hall effect. *Sci. Technol. Adv. Mater.* **9**, 014105 (2016).
- [3] Ando, K. *et al.* Electric Manipulation of Spin Relaxation Using the Spin Hall Effect. *Phys. Rev. Lett.* **101**, 036601 (2008).
- [4] Demidov, V. E. *et al.* Control of Magnetic Fluctuations by Spin Current. *Phys. Rev. Lett.* **107**, 107204 (2011).
- [5] Demidov, V. E. *et al.* Magnetic nano-oscillator driven by pure spin current. *Nat Mater* **11**, 1028 (2012).
- [6] Liu, L., Moriyama, T., Ralph, D. C. & Buhrman, R. A. Spin-Torque Ferromagnetic Resonance Induced by the Spin Hall Effect. *Phys. Rev. Lett.* **106**, 036601 (2011).
- [7] Kondou, K. *et al.* Evaluation of spin Hall angle and spin diffusion length by using spin current-induced ferromagnetic resonance. *Appl. Phys. Express* **5**, 073002 (2012).
- [8] Mosendz, O. *et al.* Quantifying Spin Hall Angles from Spin Pumping: Experiments and Theory. *Phys. Rev. Lett.* **104**, 046601 (2010).
- [9] Demidov, V., Urazhdin, S., Edwards, E. & Demokritov, S. Wide-range control of ferromagnetic resonance by spin Hall effect. *Appl. Phys. Lett.* **99**, 172501 (2011).
- [10] Kato, Y., Myers, R., Gossard, A. & Awschalom, D. Observation of the spin Hall effect in semiconductors. *Science* **306**, 1910 (2004).
- [11] Liu, L. *et al.* Spin-torque switching with the giant spin Hall effect of tantalum. *Science* **336**, 555 (2012).
- [12] Zhang, S. Spin Hall effect in the presence of spin diffusion. *Phys. Rev. Lett.* **85**, 393 (2000).
- [13] Azevedo, A. *et al.* Spin pumping and anisotropic magnetoresistance voltages in magnetic bilayers: Theory and experiment. *Phys. Rev. B* **83**, 144402 (2011).
- [14] Liu, L., Buhrman, R. & Ralph, D. Review and analysis of measurements of the spin hall effect in platinum. *eprint arXiv:1111.3702* (2011).
- [15] Yan, P., Wang, X. S. & Wang, X. R. All-magnonic spin-transfer torque and domain wall propagation. *Phys. Rev. Lett.* **107**, 177207 (2011).
- [16] Morota, M. *et al.* Indication of intrinsic spin Hall effect in *4d* and *5d* transition metals. *Phys. Rev. B* **83**, 174405 (2011).
- [17] Niimi, Y. *et al.* Experimental Verification of Comparability between Spin-Orbit and Spin-Diffusion Lengths. *Phys. Rev. Lett.* **110**, 016805 (2013).

- [18] Yamaguchi, A. *et al.* Rectification of radio frequency current in ferromagnetic nanowire. *Appl. Phys. Lett.* **90**, 182507 (2007).
- [19] Kasai, S. *et al.* Modulation of effective damping constant using spin Hall effect. *Appl. Phys. Lett.* **104**, 092408 (2014).
- [20] Mizukami, S. *et al.* Gilbert damping in perpendicularly magnetized Pt/Co/Pt films investigated by all-optical pump-probe technique. *Appl. Phys. Lett.* **96**, 2502 (2010).

Chapter 8

Time-domain Detection of Current Controlled Magnetization Damping in Pt/Ni₈₁Fe₁₉ Bi-layer and Determination of Pt Spin Hall Angle

The effect of spin torque from the spin Hall effect in Pt/Ni₈₁Fe₁₉ rectangular bi-layer film was investigated using time-resolved magneto-optical Kerr microscopy. Current flow through the stack resulted in a linear variation of effective damping up to $\pm 7\%$, attributed to spin current injection from the Pt into the Ni₈₁Fe₁₉. The spin Hall angle of Pt was estimated as 0.11 ± 0.03 . The modulation of the damping depended on the angle between the current and the bias magnetic field. These results demonstrate the importance of optical detection of precessional magnetization dynamics for studying spin transfer torque due to spin Hall effect.

8.1. Introduction

Utilizing spin current[1] for manipulating magnetization in non-magnetic (NM)/ferromagnetic (FM) bi-layer films is of considerable interest for low power consumption in spintronic devices. Spin current generated via the spin Hall effect[1-3](SHE) in large spin-orbit coupling NM materials has drawn significant attention due to its technological potential and fundamental interest. To understand the effect of spin current due to SHE, it is important to estimate the conversion efficiency between charge current and spin current which is referred as spin Hall angle (SHA)[4-8]. The accuracy of the SHA determined for various materials is still debated due to the large variation in the values reported by different groups for the same material. For example, the estimated value of the SHA for Pt[5,7,9-11] varies over a wide range (0.0037 to 0.16) as mentioned in other reports.[4-5,8,11-12].

In general, the spin-torque-induced ferromagnetic resonance technique[4,6] (ST-FMR) has been used to estimate the value of SHA. With the ST-FMR technique, a NM/FM bi-layer film is excited using rf current and a response is detected in the form of a dc voltage from the magnetic layer using the spin torque diode effect[13-14]. However, it is known that the ST-FMR spectrum shape can be modified[7] by inverse spin Hall effect[15-17] (ISHE) and line-width broadening can also result from thermal spin waves. These effects may contribute to a significant error in the estimation of the SHA. As an alternative to the ST-FMR technique, optical excitation and detection method for determining SHA looks very promising, which has not been explored so far. Here, time-resolved magneto-optical Kerr effect (TR-MOKE) microscopy[18] was used to investigate the magnetic damping and its modulation due to spin Hall spin torque in Pt/Ni₈₁Fe₁₉ bi-layer stack. The advantage of implementing TRMOKE was that the damping was measured directly in time domain within the highly localized probe area ($\sim 1 \mu\text{m}^2$) due to focused laser spot.[19] It excluded any inhomogeneities or variation due to larger area averaging and provided better estimates of damping[19]. A further advantage is that the modal composition of the magnetization oscillations can be observed in the time domain and the damping for each mode can be assessed. Another benefit of using TR-MOKE was it did not require any additional fabrication of waveguide on the sample and only dc current was passed through the sample. Estimates of the value of the spin Hall angle for the Pt layer were obtained from the experiment which are comparable with those found in some of the existing literature.[4-5,7-8].

8.2. Experimental Details

Thin film stacks of Pt(6.8 nm)/Ni₈₁Fe₁₉(12.7 nm)/MgO(2.4 nm) were grown on a thermally oxidized Si [100] substrate by dc/rf magnetron sputtering. The base pressure of the chamber was $\sim 1 \times 10^{-7}$ Torr, and the deposition used Ar gas at 1.14×10^{-3} Torr. The MgO layer was an insulating protective capping layer. The sample dimensions of $5 \times 1.5 \text{mm}^2$ were obtained by deposition through a rectangular shadow mask. Pt contact pads (15nm thick) were deposited at the two ends along the length of the sample for electrical connections. The resistivities of the Pt and Ni₈₁Fe₁₉ were measured to be 15.0 and 36.0 $\mu\Omega$ cm, respectively. A dc charge current (I_{dc}) was applied along the length of the sample using a variable dc current source. An in-plane bias magnetic field H was applied at an angle θ with respect to the long axis of the

sample. Due to negligibly small magnetocrystalline anisotropy of $\text{Ni}_{81}\text{Fe}_{19}$ thin film, the magnetization M was uniformly aligned along the direction of the bias magnetic field. Figure 8.1 shows a schematic of the sample and measurement arrangement. A 400 nm laser with 17.0 mJ/cm^2 of fluence and $\sim 100 \text{ fs}$ pulse-width was used to excite the magnetization dynamics in the sample while a 800 nm laser with 2.1 mJ/cm^2 of fluence and $\sim 80 \text{ fs}$ pulse-width probed the sample at different time delays with respect to excitation. The experiments were performed at room temperature.

8.3. Theory

The direct current flowing in the bi-layer sample was expected to be distributed between $\text{Ni}_{81}\text{Fe}_{19}$ and Pt layers as determined by the resistivity of each layer. Due to strong spin orbit interaction and impurity scattering within the Pt, electrons with opposite spin polarity would be deflected in opposite directions, leading to spin accumulation at the interfaces and giving rise to a spin current due to the SHE. Spin current injected[1] from the Pt into the adjacent $\text{Ni}_{81}\text{Fe}_{19}$ layer can exert a torque upon the magnetization which is referred to as the spin transfer torque (STT). This transfer of angular momentum to the magnetization modifies the magnetization relaxation, τ and can thereby modify the effective magnetic damping α .

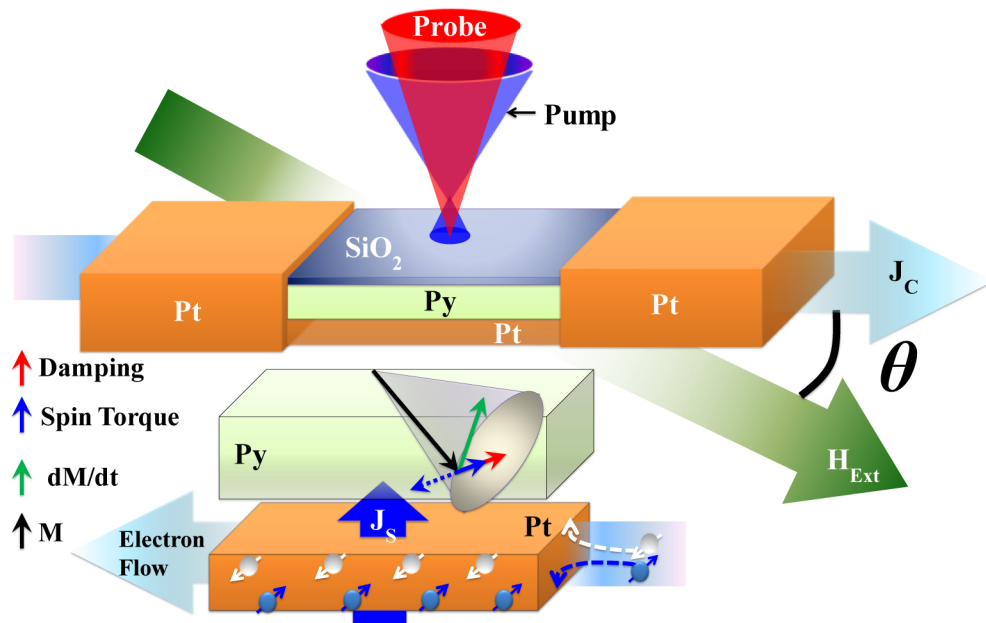


Figure 8.1. Schematic diagram of the sample and the experimental geometry.

The polarization of spin current, $\hat{\sigma}$, is determined by $\hat{J}_c \times \hat{n}$, where \hat{J}_c is the applied charge current density and \hat{n} is the normal vector to the interface plane. The interaction between spin current and magnetization has been described by the modified Landau Lifshitz Gilbert equation[7] (LLG equation)

$$\frac{d\hat{m}}{dt} = -\gamma(\hat{m} \times H_{eff}) + \alpha(\hat{m} \times \frac{d\hat{m}}{dt}) + \frac{\hbar}{2e\mu_0 M_s t} J_s (\hat{m} \times \hat{\sigma} \times \hat{m}) \quad (8.1),$$

where the last term incorporates the STT[20-22]. The direction of STT is determined by $(\hat{m} \times \hat{\sigma} \times \hat{m})$ and acts collinearly with the effective damping, α and can increase or decrease the effective value of α depending on the polarity of $\hat{\sigma}$. This modulation of the damping can be related to the injected spin current density and the relative orientation of magnetic moment with respect to current by the following equation:[5]

$$\Delta\alpha = (\alpha - \alpha_0) = \frac{\hbar\gamma J_s \sin\theta}{2eM_s t 2\pi f} \quad (8.2),$$

where α_0 is the original damping with zero dc current, $\Delta\alpha$ is the change in the damping (MOD), and J_s is the spin current density. The spin Hall angle, θ_{SH} , is given by J_s / J_c , defined as

$$\frac{J_s}{J_c} = \frac{4f\pi e t M_s \Delta\alpha}{\hbar\gamma J_s \sin\theta} \quad (8.3).$$

Hence, by estimating the rate of MOD ($\Delta\alpha / J_c$) experimentally, we can evaluate J_s / J_c using equation 8.3.

8.4. Results and Discussion

Figure 8.2(a) shows the time-resolved Kerr rotation data obtained from Pt/Ni₈₁Fe₁₉ bi-layer film at H~1.4 kOe, $\theta = 0^\circ$ and $I_{dc} = 0$. The data can be divided into three different temporal regions. Region I ($t < 0$) shows negative time delay where the sample is probed before excitation and the sample shows steady magnetization due to external bias magnetic field. Region II (up to few tens of ps) shows a sharp demagnetization (500 fs) and a subsequent fast relaxation due to spin lattice relaxation. This is followed by a slower relaxation in region III and precession of magnetization around its new equilibrium.

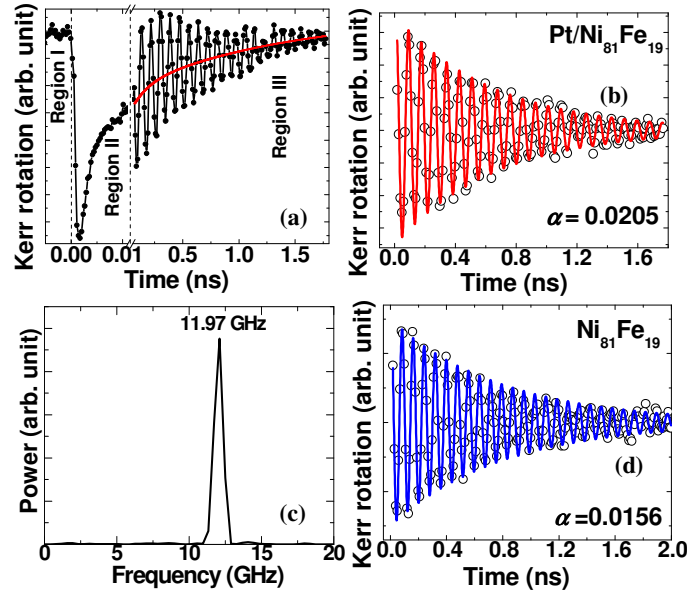


Figure 8.2. (a) Time-resolved Kerr rotation data for Pt/Ni₈₁Fe₁₉ bi-layer film at H~1.4 kOe, $I_{dc}=0$ and at $\theta=0^\circ$. (b) Precessional part of the time-resolved data. (c) Fast Fourier transform (FFT) spectrum of figure 8.2(b). (d) Time-resolved Kerr rotation data from a single Ni₈₁Fe₁₉ layer of equal dimensions as that in the bi-layer film.

In Region III, heat is diffused to the substrate and to the surrounding and the precession was slowly damped. The analysis here mainly concentrates on region III, which is the region of interest for estimating α . The solid line in figure 8.2(a) is the bi-exponential background of the damped oscillation shown in region III from which relaxation times of 1.4 ps and 1.43 ns were obtained. Figure 8.2(b) shows the precessional data with the background subtracted. A single mode oscillation decaying with time was typically observed. The time-resolved data were fitted with a damped harmonic function from which α was estimated as $\alpha = 1/(2\pi f\tau)$ where f is the frequency of oscillation and τ is the relaxation time corresponding to oscillation of magnetization. Figure 8.2(c) shows the fast Fourier transform (FFT) spectrum of the data in figure 8.2(b) from which f was determined to be about 12.0 GHz. From figure 8.2(b), α was found to be about 0.021. Figure 8.2(d) shows the time evolution of magnetization dynamics of Ni₈₁Fe₁₉ film of same dimensions. From this, we found α to be about 0.016. The enhanced value of α for Pt/Ni₈₁Fe₁₉ bi-layer stack in comparison to a single

$\text{Ni}_{81}\text{Fe}_{19}$ layer may be explained by considering additional loss due to spin pumping into the Pt layer, as well as due to the $d-d$ hybridization[23] at the Pt/ $\text{Ni}_{81}\text{Fe}_{19}$ interface.

The effect of the magnetic field on the magnetization dynamics of the Pt/ $\text{Ni}_{81}\text{Fe}_{19}$ bi-layer is shown in figure 8.3. Figure 8.3(a) shows the TR-MOKE data at various H values, and figure 8.3(b) shows the corresponding FFT power spectra. The precessional frequency f values obtained from figure 8.3(a) are plotted as function of H in figure 8.3(c). The experimental data points can be fitted using the Kittel formula

$$f = \frac{\gamma\sqrt{H(H + 4\pi M_s)}}{2\pi} \quad (8.4).$$

A value for M_s of 770 emu/cc was obtained from fitting and a value for the gyromagnetic ratio $\gamma \sim 0.0185 \times 10^{11}$ Hz/T. Figure 8.3(d) shows a plot of α as a function of frequency f . It is observed that α remains almost constant over a range of frequency between 8.5 to 15 GHz, from which it is inferred that in this sample, extrinsic phenomena[24], such as two magnon scattering, do not contribute to the effective damping.

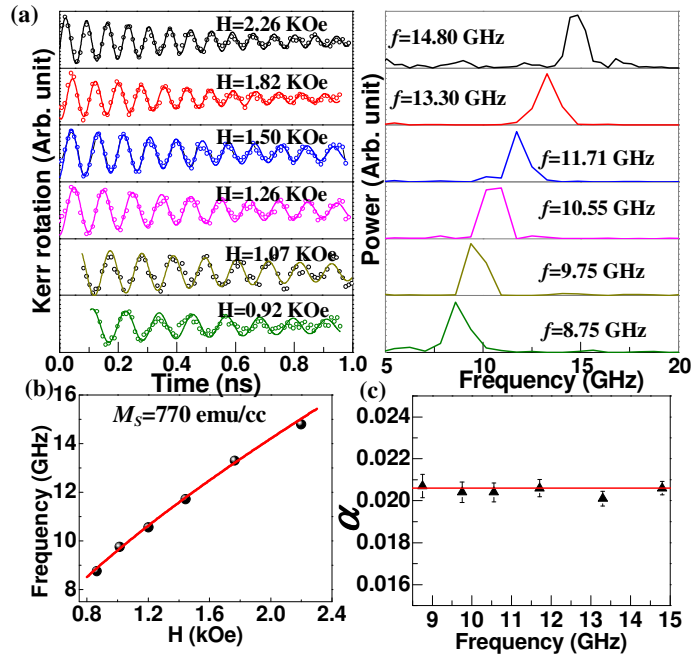


Figure 8.3. (a) Time-resolved Kerr rotation for Pt/ $\text{Ni}_{81}\text{Fe}_{19}$ bi-layer film at different bias field values (H) at $I_{dc} = 0$ and $\theta = 0^\circ$. (b) The corresponding FFT spectra. (c) Variation of experimental precession frequency (f) with H (symbol) and fit to the Kittel formula (solid line).

(d) Variation of α as a function of f .

In order to investigate the effect of spin torque on damping, a dc current was passed through the stack. Figure 8.4(a) shows the time-resolved magnetization precession at different current densities (J_C) varying from $-1.1 \times 10^{10} \text{ A/m}^2$ to $+1.1 \times 10^{10} \text{ A/m}^2$ with a magnetic field, $H \sim 1.2 \text{ kOe}$ applied at an angle of $\theta = 90^\circ$ to the current flow. A variation in α of up to $\pm 7\%$ as compared to its intrinsic value was observed for positive and negative values of J_C up to $1.1 \times 10^{10} \text{ A/m}^2$. Significantly, for positive J_C , the damping α decreases whereas for negative J_C , α increases. The observed sensitivity of MOD on the sign of J_C suggests that the origin is related to the injected spin current due to SHE from the Pt layer, which depends on the current polarity.

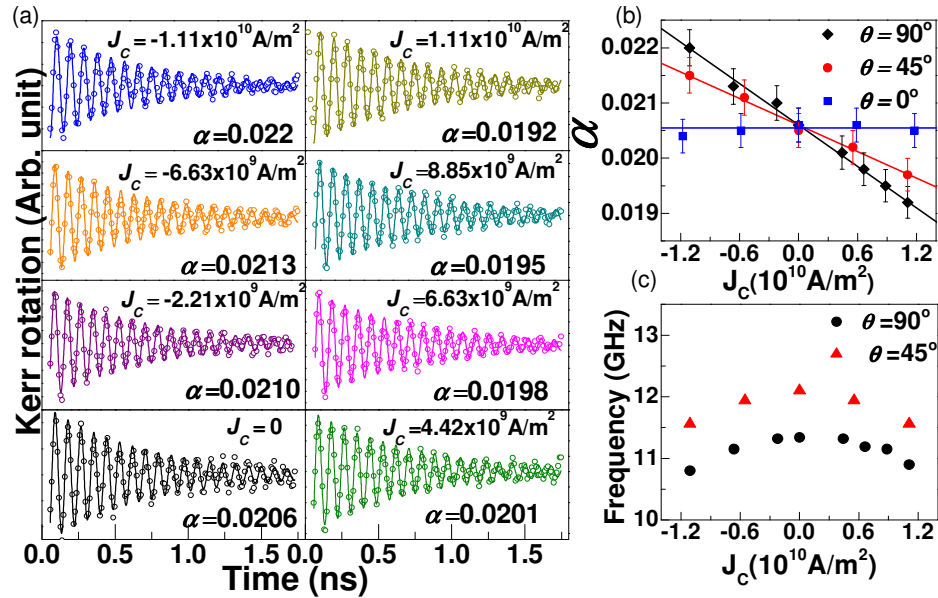


Figure 8.4. (a) Time-resolved magnetization precession at different dc charge current densities, J_C , for $\theta = 90^\circ$ obtained from the TR-MOKE experiment. Symbols represent the experimental data points, and solid lines are the theoretical fits. (b) The variation of α with J_C for magnetic fields oriented at angle $\theta = 0^\circ$, 45° and 90° with respect to the current direction. (c) Variation of the precessional frequency f with J_C for $\theta = 45^\circ$, and 90° .

Joule heating produced by the application of a dc current would only induce an increase in α with respect to its zero current value and show no polarity dependence. Thus, the results suggest that Joule heating has a negligible influence on the magnetization dynamics in the Pt/Ni₈₁Fe₁₉ bi-layer. In figure 8.4(b), the variation of effective value of α with J_C is shown for $H \sim 1.2$ kOe where the field is orientated at $\theta = 0^\circ, 45^\circ$ and 90° with respect to the current axis. At $\theta = 0^\circ$, α remains almost constant for all J_C , indicating that there is no net torque on the magnetization. More interestingly, for $\theta = 45^\circ$ and 90° , a clear linear MOD is observed. The slopes of the linear fit to the current density dependence of MOD determined for $\theta = 90^\circ$ and 45° are $1.24 \times 10^{-13} \text{ m}^2/\text{A}$ and $8.14 \times 10^{-14} \text{ m}^2/\text{A}$, indicate that the MOD depends not only on the polarity of J_C but also on magnetization orientation with respect to the current. The above observations further support the notion of spin torque acting on the Ni₈₁Fe₁₉ layer due to SHE from Pt layer leads to MOD. By extracting the values of $\Delta\alpha / J_C$ obtained from figure 8.4(b) for $\theta = 45^\circ$ and 90° , and using in equation 8.3, we estimate spin Hall angle, θ_{SH} , to be 0.11 ± 0.02 and 0.11 ± 0.03 respectively. From these values, an average value for θ_{SH} 0.11 ± 0.03 is calculated which is within the upper bound (< 0.16) of the values reported in the literature.[4-5,7-8] Here, the observed value of θ_{SH} is on the higher side which may be related to some aspect specific to the sample (transparency of the Pt/NiFe interface, Pt microstructure, substrate, etc.) as well as the different methodology (TR-MOKE) used to estimate the same. Figure 8.4(c) shows the variation of frequency as a function of J_C . A decrease (red shift) in the precessional frequency, f , with increasing magnitude of J_C was observed and was more or less symmetric with respect to zero current. Previously, a red shift in frequency with J_C was explained by considering the reduction in effective magnetization of the material because of magnetic fluctuation[25] due to Joule heating. However, the change in f with current should not affect α as is shown in figure 8.3(c) or the estimation of θ_{SH} .

8.5. Summary

In summary, using an all-optical excitation and detection technique, the magnetization dynamics in a Pt/Ni₈₁Fe₁₉ bi-layer was studied. A spin transfer torque was indicated in Ni₈₁Fe₁₉ via a current dependent modulation of the effective damping which is attributed to the spin

Hall effect from the Pt underlayer. A linear modulation of the damping up to $\pm 7\%$ was observed as a function of current density, to an experimental limit of 1.11×10^{10} A/m². An average spin Hall angle for Pt was estimated from analysis of the data to be about 0.11 ± 0.03 . A larger modulation of damping may be observed by increasing the current density, allowing the determination of θ_{SH} with greater precision. These results will help in understanding the role of spin Hall effect in affecting magnetization dynamics.

References

- [1] Takahashi, S. & Maekawa, S. Spin current, spin accumulation and spin Hall effect. *Sci. Technol. Adv. Mater.* **9**, 014105 (2008).
- [2] Demidov, V. E., Urazhdin, S., Edwards, E. R. J. & Demokritov, S. O. Wide-range control of ferromagnetic resonance by spin Hall effect. *Appl. Phys. Lett.* **99**, 172501 (2011).
- [3] Zhang, S. Spin Hall Effect in the Presence of Spin Diffusion. *Phys. Rev. Lett.* **85**, 393 (2000).
- [4] Liu, L., Moriyama, T., Ralph, D. C. & Buhrman, R. A. Spin-Torque Ferromagnetic Resonance Induced by the Spin Hall Effect. *Phys. Rev. Lett.* **106**, 036601 (2011).
- [5] Liu, L., Buhrman, R. & Ralph, D. Review and analysis of measurements of the spin hall effect in platinum. *arXiv:1111.3702* (2011).
- [6] Ganguly, A. *et al.* Thickness dependence of spin torque ferromagnetic resonance in Co75Fe25/Pt bi-layer films. *Appl. Phys. Lett.* **104**, 072405 (2014).
- [7] Ando, K. *et al.* Electric Manipulation of Spin Relaxation Using the Spin Hall Effect. *Phys. Rev. Lett.* **101**, 036601 (2008).
- [8] Kondou, K. *et al.* Evaluation of spin Hall angle and spin diffusion length by using spin current-induced ferromagnetic resonance. *Appl. Phys. Express* **5**, 073002 (2012).
- [9] Azevedo, A. *et al.* Spin pumping and anisotropic magnetoresistance voltages in magnetic bi-layers: Theory and experiment. *Phys. Rev. B* **83**, 144402 (2011).
- [10] Mosendz, O. *et al.* Quantifying Spin Hall Angles from Spin Pumping: Experiments and Theory. *Phys. Rev. Lett.* **104**, 046601 (2010).
- [11] Kimura, T. *et al.* Room-Temperature Reversible Spin Hall Effect. *Phys. Rev. Lett.* **98**, 156601 (2007).

- [12] Kimura, T. *et al.* Erratum: Room-Temperature Reversible Spin Hall Effect [*Phys. Rev. Lett.* **98**, 156601 (2007)]. *Phys. Rev. Lett.* **98**, 249901 (2007).
- [13] Suzuki, Y. & Kubota, H. Spin-torque diode effect and its application. *J. Phys. Soc. Jpn.* **77**, 031002 (2008).
- [14] Tulapurkar, A. *et al.* Spin-torque diode effect in magnetic tunnel junctions. *Nature* **438**, 339 (2005).
- [15] Ando, K. *et al.* Angular dependence of inverse spin-Hall effect induced by spin pumping investigated in a NiFe/Pt thin film. *Phys. Rev. B* **78**, 014413 (2008).
- [16] Harii, K. *et al.* Inverse spin-Hall effect and spin pumping in metallic films. *J. Appl. Phys.* **103**, 07F311 (2008).
- [17] Nakayama, H. *et al.* Inverse spin-Hall effect induced by spin pumping in different thickness Pt films. *IEEE Trans. Magn.* **46**, 2202 (2010).
- [18] A. Barman and A. Haldar, in *Solid State Physics*, edited by R. E. Camley and R. L. Stamps (Academic Press, Burlington, 2014), Vol. 65, pp. 1–108.
- [19] Neudecker, I. *et al.* Comparison of frequency, field, and time domain ferromagnetic resonance methods. *J. Magn. Magn. Mater.* **307**, 148 (2006).
- [20] Kasai, S. *et al.* Modulation of effective damping constant using spin Hall effect. *Appl. Phys. Lett.* **104**, 092408 (2014).
- [21] Liu, L. *et al.* Spin-torque switching with the giant spin Hall effect of tantalum. *Science* **336**, 555 (2012).
- [22] Yan, P., Wang, X. S. & Wang, X. R. All-Magnonic Spin-Transfer Torque and Domain Wall Propagation. *Phys. Rev. Lett.* **107**, 177207 (2011).
- [23] Pal, S. *et al.* Tunable magnonic frequency and damping in [Co/Pd]₈ multilayers with variable Co layer thickness. *App. Phys. Lett.* **98**, 082501 (2011).
- [24] King, J. *et al.* Local control of magnetic damping in ferromagnetic/non-magnetic bilayers by interfacial intermixing induced by focused ion-beam irradiation. *Appl. Phys. Lett.* **104**, 242410 (2014).
- [25] Demidov, V. E. *et al.* Control of Magnetic Fluctuations by Spin Current. *Phys. Rev. Lett.* **107**, 107204 (2011).

Chapter 9

Role of Interface in Current Induced Modulation of Damping in Ion Irradiated Ni₈₁Fe₁₉/Pt Bi-layers

The damping of a ferromagnetic layer can be modulated by injecting spin current from an adjacent nonmagnetic heavy metal layer. Hence, in many experiments related to spin Hall effect, modulation of damping is used as a standard technique to measure the transverse spin current converted from applied charge current in heavy metals. However, the modulation of damping is highly dependent on the spin transparency of the interface. In this work we controllably modify the interface by intermixing atoms using low dose gallium ion irradiation and study the effect of modified interface transparency on the spin current induced modulation of damping. Our aim is to investigate the role of interface in determining the efficiency of spin injection. We found that the modulation is linear with the applied charge current for as deposited film interface and the rate of modulation decreases with the increased irradiation dose. At a higher irradiation dose greater than $2 \text{ pC}/\mu\text{m}^2$, a nonlinear modulation of damping replaces the linear modulation. Our experimental results are interpreted by considering possible factors associated with the structural changes developed in the sample by irradiation.

9.1. Introduction

Spintronics[1] shows a lot of promises as an upcoming technology for the replacement of our present semiconductor based electronics due to its high stability, energy efficiency and signal quality. The driving force for spintronic devices is pure spin current. This is basically a charge less flow of spin angular momentum which can exert torque on magnetization. Spin current can be generated from conventional charge current in non-magnetic heavy metals having strong spin orbit coupling. This is called spin Hall effect[2-3]. The conversion ratio is constant for a particular material which is known as spin Hall angle[2]. Recently a lot of re-

search efforts have been dedicated to the estimation of spin Hall angle[4-13] because it quantifies spin current in a known reference frame of charge current. Spin current cannot be measured directly by electrical meters like charge current, but the effect of spin current can be realized by the modification of magnetization dynamics of an adjacent ferromagnetic layer. Hence, many of such experiments involve ferromagnetic/nonmagnetic thin film bi-layers[4-5,11]. However, the main concern of this research lies in a different point. Although many groups have observed similar effects of spin current (generated by spin Hall effect) on magnetization, the values of spin Hall angle for a particular system reported by different groups are largely different from each other. For example, in case of Pt the value varies significantly[4,6-7,9,11,14-15]. The anomaly might have some fundamental origin underlying in the spin transport between the layers which is often overlooked by considering a fully transparent interface. Hence, it is important to investigate the role of interface in spin injection process to resolve the ambiguity related to the amplitude of spin current.

Recent report by W. Zang *et al.*[9] shows that spin torque induced ferromagnetic resonance is sensitive to the interface. When a thin buffer layer is inserted between ferromagnetic and nonmagnetic layer, the value of spin Hall angle changes. It varies as a function of buffer layer thickness and the nature of variation depends on the buffer material.

In our study the interface of Ni₈₁Fe₁₉/Pt bi-layer stack is modified by low dose Ga⁺ ion irradiation using focussed ion beam. The irradiation causes intermixing of atoms near the interface leading to the formation of a compositionally graded alloy and broadening of the interface[16-17]. Magnetization dynamics is studied by an all-optical time resolved magneto-optical Kerr effect microscope. The rate of modulation of damping is used as a measure of spin injection efficiency. Here, damping is investigated as a function of the applied charge current for various irradiation dose. Finally, we discuss a unique technique for local spin injection with controlled amplitude ratio which can modulate local magnetization dynamics, spin waves and have useful applications in spintronic devices.

9.2. Sample Preparation

To study the effect of interface first we require a bi-layer sample with high quality interface. For that thin film bi-layer of Ni₈₁Fe₁₉(7 nm)/Pt(10 nm) is grown on a thermally oxidised non doped Si[100] substrate by dc/rf magnetron sputtering using a ultrahigh vacuum deposition system (Mantis). The deposition conditions are carefully optimized to obtain good quality

interface for as deposited film. The deposition is performed at a base pressure of $\sim 7 \times 10^{-8}$ Torr and Ar pressure of 1.1×10^{-3} Torr. The Ar flow rate is maintained at 18 sccm and the deposition rates for $\text{Ni}_{81}\text{Fe}_{19}$ and Pt are 0.01 nm/s and 0.021 nm/s, respectively. The bi-layer is deposited in a rectangular shape between two electrodes using a shadow mask during deposition. The electrode pads of Pt (3nm)/Au (30 nm) are deposited for applying dc charge current along the length of the sample. The purpose of the Pt under layer in the electrode is a good adhesion of Au with the substrate. The sample is locally irradiated in $15 \mu\text{m} \times 15 \mu\text{m}$ square areas having edge to edge separation of $20 \mu\text{m}$ between the square patterns. The irradiation dose (d) varies from 0-5 pC/ μm^2 . Figure 9.1 shows the schematic diagram of the sample and figure 9.2 shows the microscopic image of irradiation spot. It is interesting to note that the contrasts are different for different irradiation dose (see figure 9.2). In our sample a highly irradiated rectangular spot is used as a marker for its good contrast.

Earlier in chapters 5 and 8 we have discussed the reason for preferring $\text{Ni}_{81}\text{Fe}_{19}$ and Pt as two materials forming a bi-layer in our spin transport studies. The first one is a soft ferromagnetic material with its negligible anisotropies. Hence we can avoid unnecessary complication related to anisotropy while studying the magnetization dynamics of the system. The second one is a popular nonmagnetic heavy metal known for its strong spin Hall effect, proximity induced magnetic moment and spin pumping effect [10]. Usually, the as-deposited $\text{Ni}_{81}\text{Fe}_{19}$ /Pt interface is shown to have a typical width of less than 1 nm, resulting from a combination of topological roughness and chemical intermixing as observed earlier by x-ray reflectivity[10,16]. It has been observed in a previous detailed structural study of $\text{Ni}_{81}\text{Fe}_{19}$ /Au that with higher ion dose the interface rapidly becomes broader due to intermixing of atoms, the individual layers becomes thinner and the layer develops into a compositionally-graded alloy due to the intermixing of atoms of the heavy metal layer into the ferromagnetic layer[10,16-17]. In our case Pt also acts as a protective capping layer for the sample.

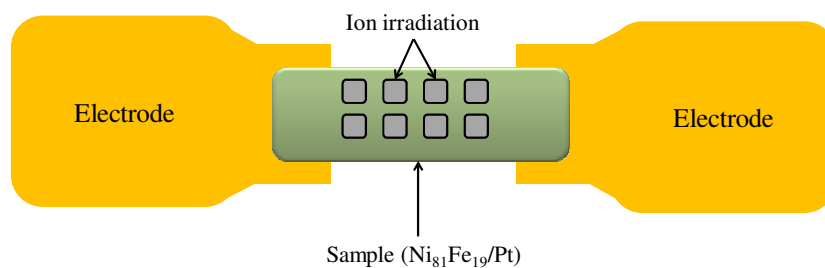


Figure 9.1. Schematic diagram of the ion irradiated Ni₈₁Fe₁₉/Pt bi-layer sample.

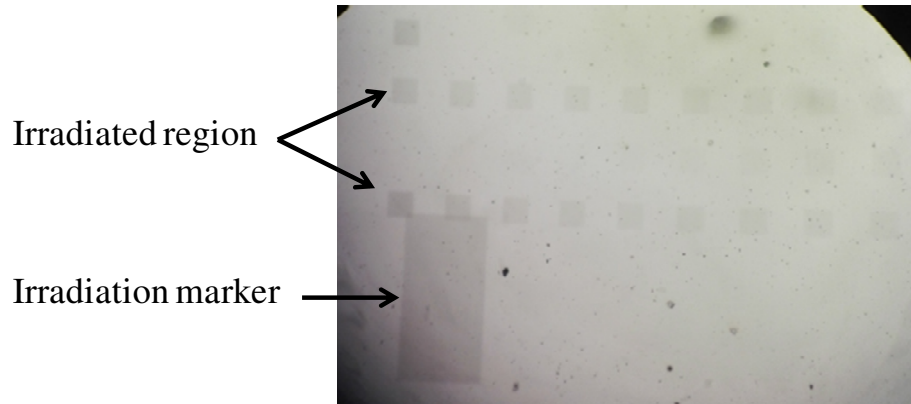


Figure 9.2 Microscopic image of ion irradiated spots on the sample.

9.3. Experimental Technique

The experiment is performed using an all-optical time-resolved Kerr microscopy which is based on local excitation and detection technique. A 400 nm laser beam with 40 mJ/cm² of fluence and ~100 fs pulse-width is used to excite the magnetization dynamics in the sample while a 800 nm laser with 2.5 mJ/cm² of fluence and ~80 fs pulse-width probe the dynamics at different time delays with respect to the excitation. Both the beams are focussed onto the sample through a microscope objective with spot sizes of of ~1 μm for the pump and ~800 nm for the probe beam. The details of the experimental setup are discussed in chapter 2. A dc charge current (I) is applied along the length of the sample using a variable dc current source. To connect the dc current source with the sample we used thin stainless steel wires, one end of which is connected to the sample electrode by silver paste and the other end is soldered on a small copper strip fixed with the sample holder. The copper strip is directly connected to the source meter. In such arrangement strain does not develop in the wires which are loosely connected to the electrodes keeping the electrical connection steady during the movement of the sample holder (see figure 9.3). An in-plane bias magnetic field H is applied perpendicular to the long axis of the sample. Due to negligibly small magnetocrystalline anisotropy of Ni₈₁Fe₁₉ thin film, the magnetization M is uniformly aligned along the direction of the bias magnetic field. Now the time-resolved magnetization data is taken by focussing the pump and probe spots on a particular dose region and the experiment is performed at different applied dc charge current ranging from -0.24 A to +0.24 A. The charge current magnitude is limited

by the Joule heating of the sample, which may cause a number of spurious effects ranging from a movement and consequent defocusing of the pump and probe spots on the sample to an unwanted variation in frequency and damping. Subsequently, the laser spot is moved to different dose regions by moving the sample holder using a piezoelectric scanning stage to perform the similar current dependent magnetization dynamics measurement. A photograph of the experimental arrangement is shown in figure 9.4. All the experiments are performed at room temperature.

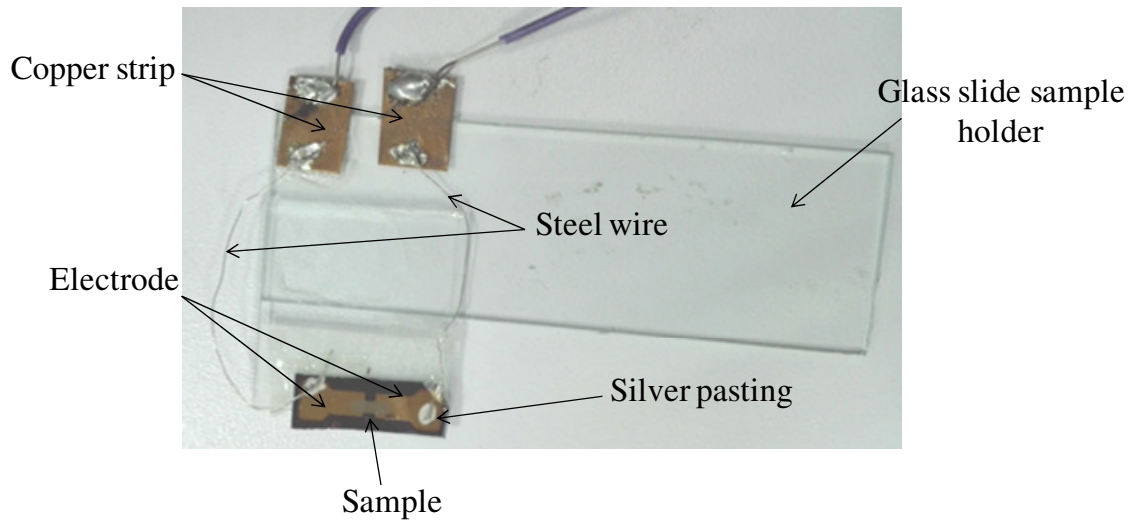


Figure 9.3. Photographic image of the sample with electrical connection arranged on a sample holder.

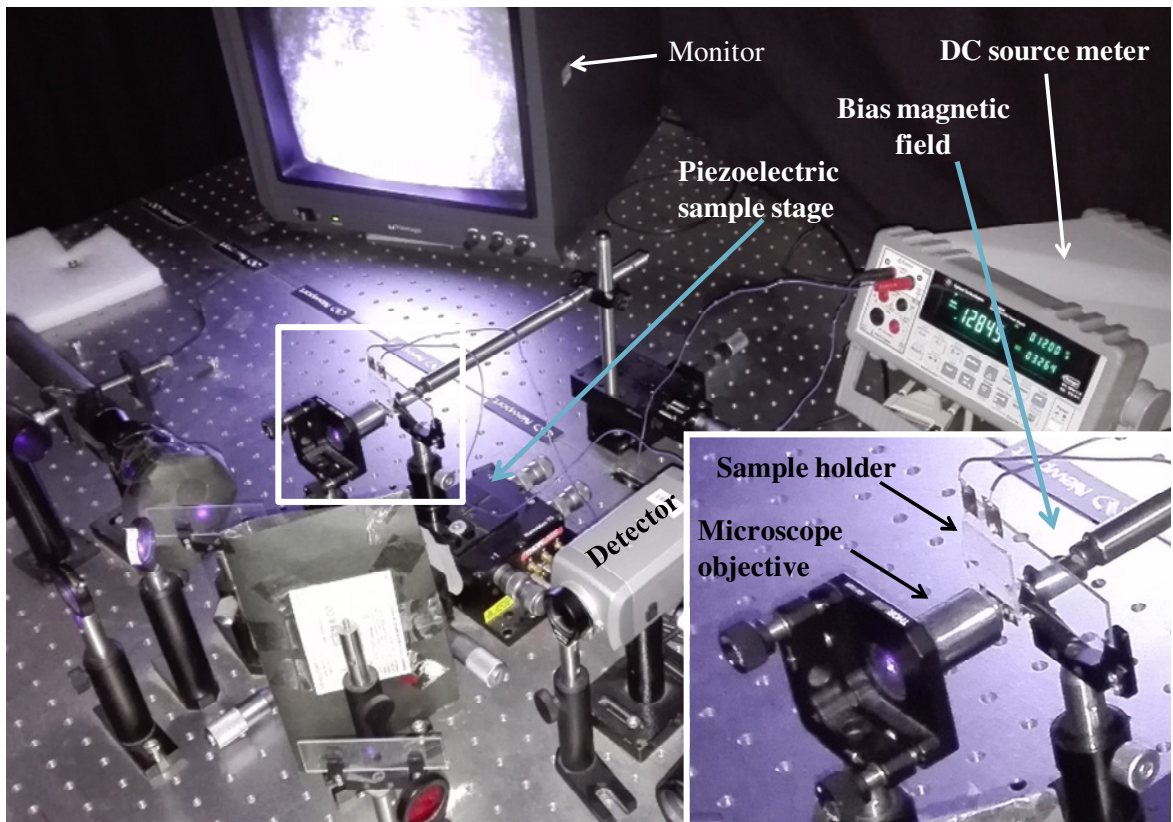


Figure 9.4. Photograph of the excitation and detection part of the TR-MOKE setup illustrating the experimental arrangement for this experiment.

9.4. Results

First we measure the time-resolved magnetization dynamics from unirradiated sample as a reference. As usual the time-resolved Kerr rotation data shows a negative delay, zero delay followed by ultrafast demagnetization, two step relaxation and a precession of magnetization superposed on the slower relaxation part of the dynamics. Figure 9.5(a)-(e) shows background subtracted time-resolved Kerr rotation data for different applied current measured at a bias magnetic field of ~ 1.4 kOe. We have observed single mode oscillations for all applied currents. The black circles denote the experimental data points which are fitted by damped sinusoid as shown by solid red curves. Damping values have been extracted as a fitting parameter. In our study we can consider figure 9.5(c) as the simplest case where we measured magnetization dynamics of a thin film bi-layer without applied current and irradiation. That means we neither have any effect from spin current nor have a modified interface affecting

spin transport processes. In such case the damping value is obtained as 0.02. The value increases with the application of positive current and decreases for negative current.

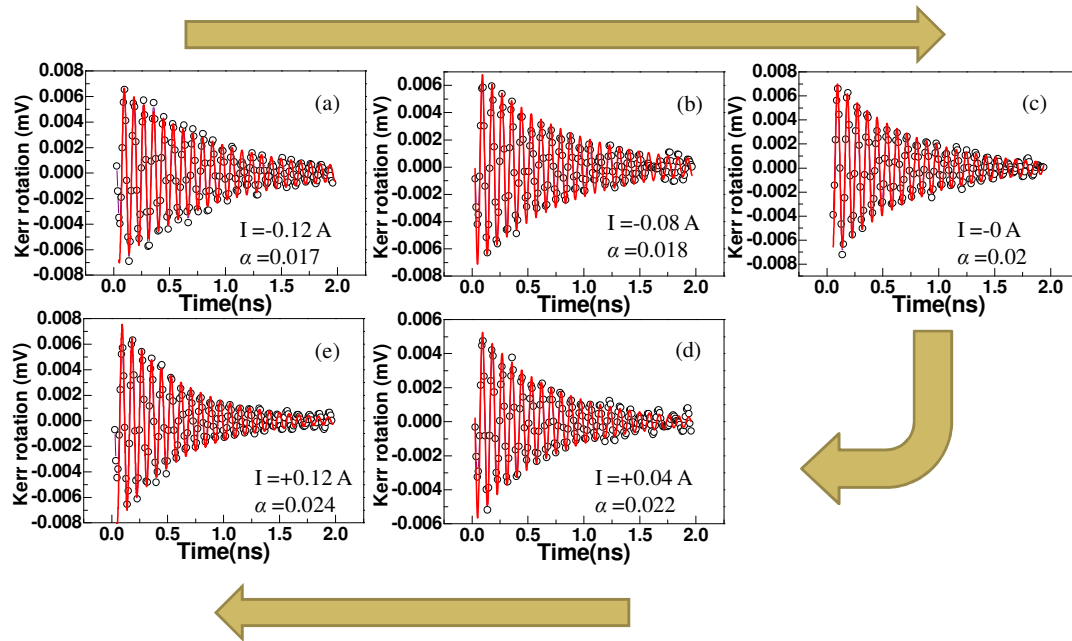


Figure 9.5. (a-e) Time-resolved Kerr rotation data for unirradiated $\text{Ni}_{81}\text{Fe}_{19}/\text{Pt}$ bi-layer at different applied current. The black circles denote experimental data points and the red lines are the fitted data.

The extracted damping constant is plotted as a function of current in figure 9.6, which shows a clear linear variation. From the slope of the variation in figure 9.6 we have obtained an overall 35% modulation as the current changes from -0.12 A to +0.12 A, with a rate of 0.03 A^{-1} .

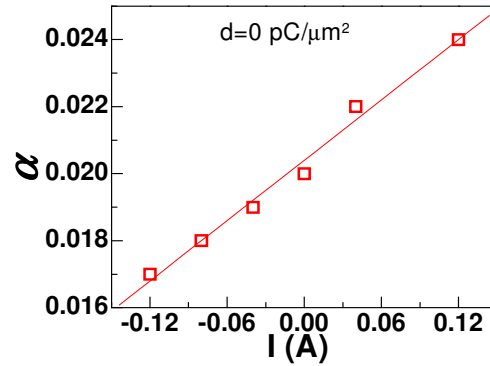


Figure 9.6. Damping is plotted as a function of applied current for un-irradiated Ni₈₁Fe₁₉/Pt bi-layer sample.

We next focus on the irradiated samples. The time-resolved Kerr rotation data for the sample with dose $d = 0.08 \text{ pC}/\mu\text{m}^2$ at different values of applied current are shown in figure 9.7 (a)-(e) and the extracted damping values are plotted as a function of current in figure 9.8. A similar variation of damping with applied current is observed as obtained in case of un-irradiated part of the sample. However, the rate of modulation is reduced by a factor of two as opposed to the unirradiated sample. In this case a maximum modulation of about 32% is observed as the applied current is varied from -0.24 A to +0.24 A. The modulation rate obtained by fitting the data points of figure 9.8 with a straight line is 0.016 A^{-1} .

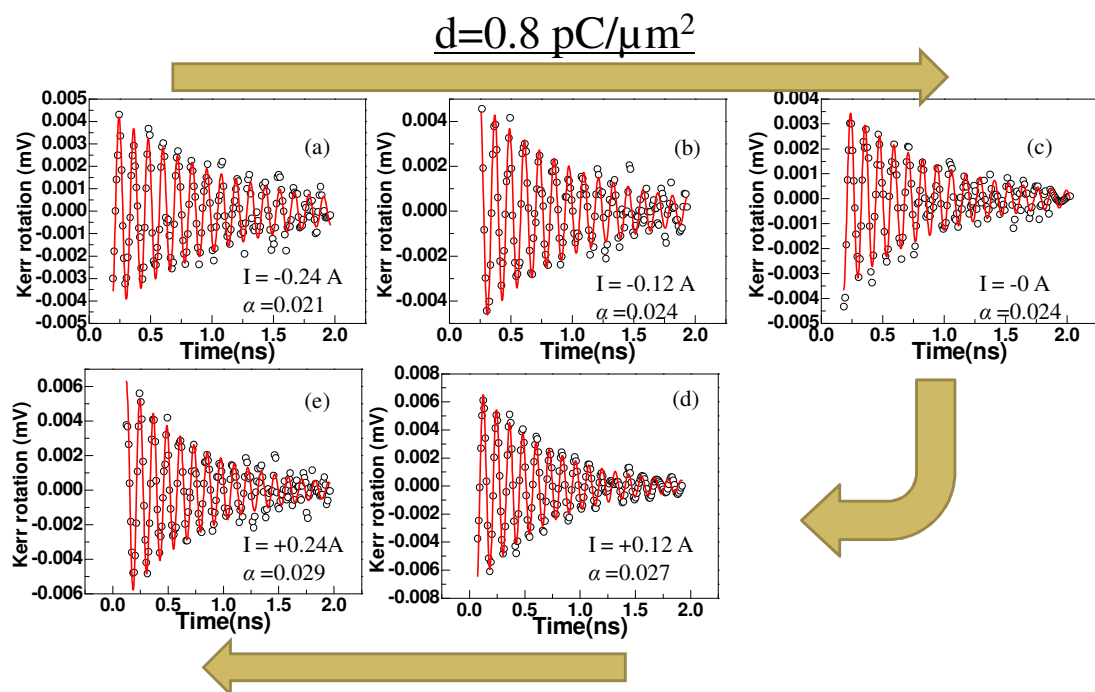


Figure 9.7 (a-e) Time-resolved Kerr rotation data of $\text{Ni}_{81}\text{Fe}_{19}/\text{Pt}$ bi-layer at an irradiation dose $d = 0.8 \text{ pC}/\mu\text{m}^2$ for different applied current. The black circles denote experimental data points and the red lines are the fitted data.

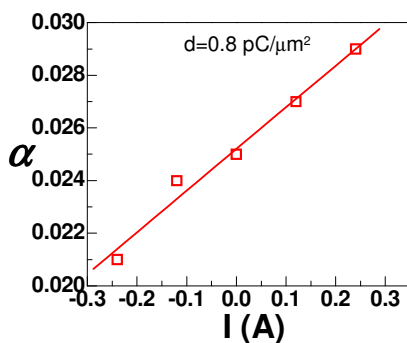


Figure 9.8. Damping is plotted as a function of applied current for the sample with irradiation dose $d = 0.8 \text{ pC}/\mu\text{m}^2$.

However, as the irradiation dose increases to a higher value of $d = 2 \text{ pC}/\mu\text{m}^2$ the asymmetric linear modulation of damping with applied current disappears and the damping values are

found to be almost invariant with current. Figures 9.9(a)-(e) show time-resolved Kerr rotation data for various values of applied current and figure 9.9(f) shows the variation of damping with current for $d = 2 \text{ pC}/\mu\text{m}^2$. No detectable variation between the damping values are observed beyond the error bars in figure 9.9(f).

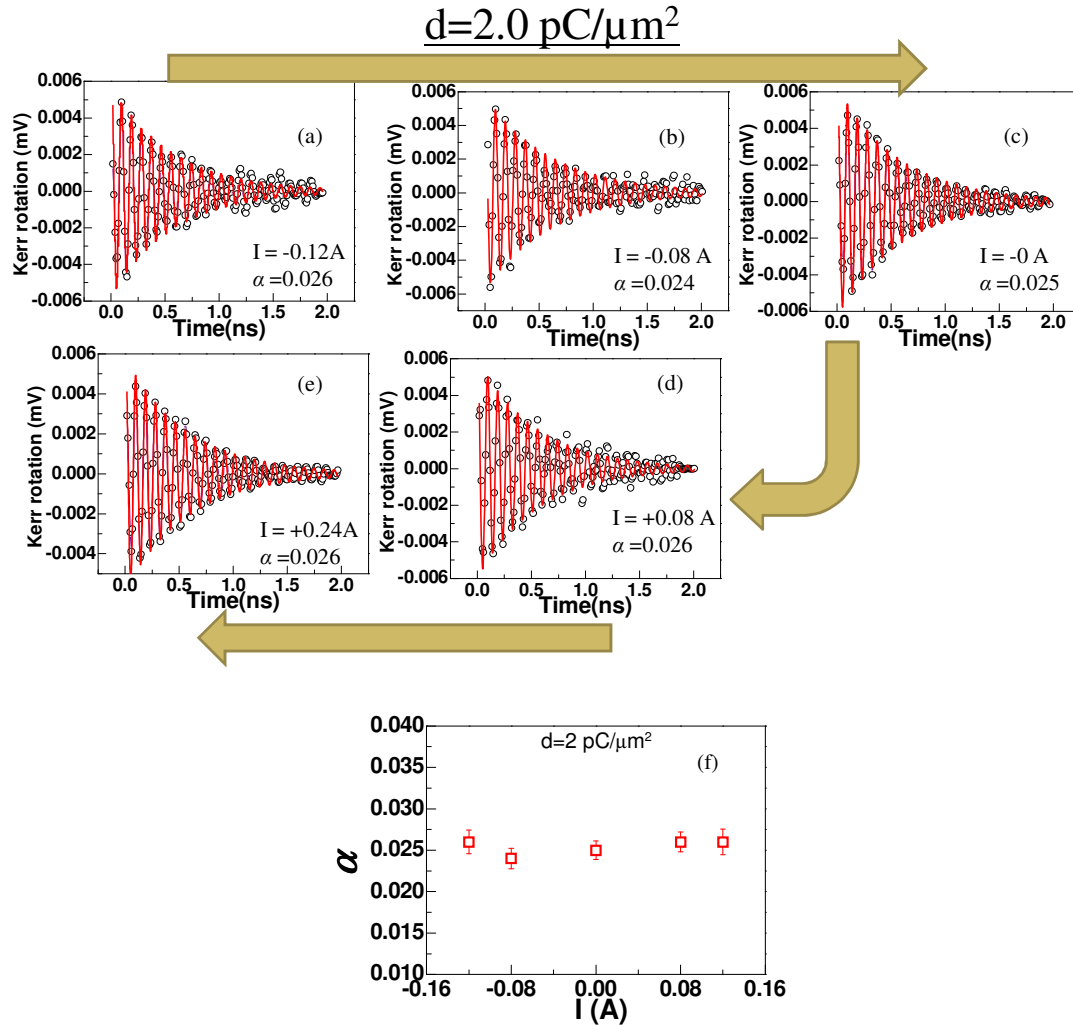


Figure 9.9. (a-e) Time-resolved Kerr rotation data of $\text{Ni}_{81}\text{Fe}_{19}/\text{Pt}$ bi-layer for an irradiation dose of $d = 2 \text{ pC}/\mu\text{m}^2$ for different applied current. The black circles denote experimental data points and the red lines are the fitted data. (f) Variation of damping as a function of applied current corresponding to figure 9.9 (a-e).

We further repeated the experiment for even higher irradiation doses. Figure 9.10 and 9.11 shows time-resolved Kerr rotation data and corresponding modulation of damping with current measured at irradiation dose of $d = 3.6 \text{ pC}/\mu\text{m}^2$ and $5 \text{ pC}/\mu\text{m}^2$, respectively. Here, we observe a significant change in the nature of variation of damping with applied current. Figures 9.10(g) and 9.11(g) show damping increases for both positive and negative applied currents which mean the variation is independent of the polarity of the charge current as opposed to the case of spin torque induced modulation of damping. In addition, this non-linear variation is larger for $d = 5 \text{ pC}/\mu\text{m}^2$ than that for $d = 3.6 \text{ pC}/\mu\text{m}^2$. In figure 9.11 (e) it is observed that the variation of damping with applied current is not linear but nearly parabolic associated with a small asymmetric component with respect to zero current.

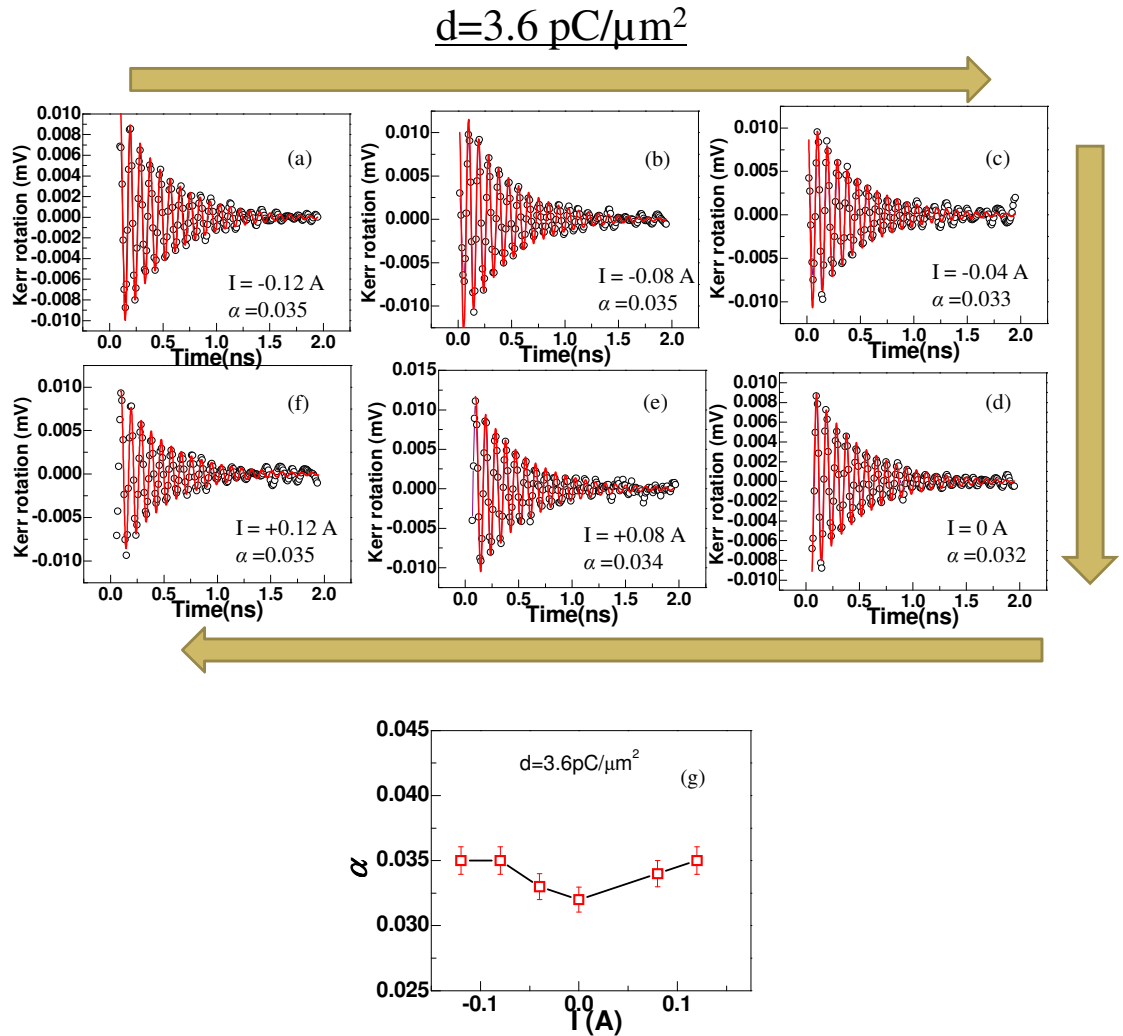


Figure 9.10. (a-f) Time-resolved Kerr rotation data of $\text{Ni}_{81}\text{Fe}_{19}/\text{Pt}$ bi-layer for irradiation dose $d = 3.6 \text{ pC}/\mu\text{m}^2$ for different applied current. The black circles denote experimental data points and the red lines are the fitted data. (g) Variation of damping as a function of applied current corresponding to figure 9.10 (a-f).

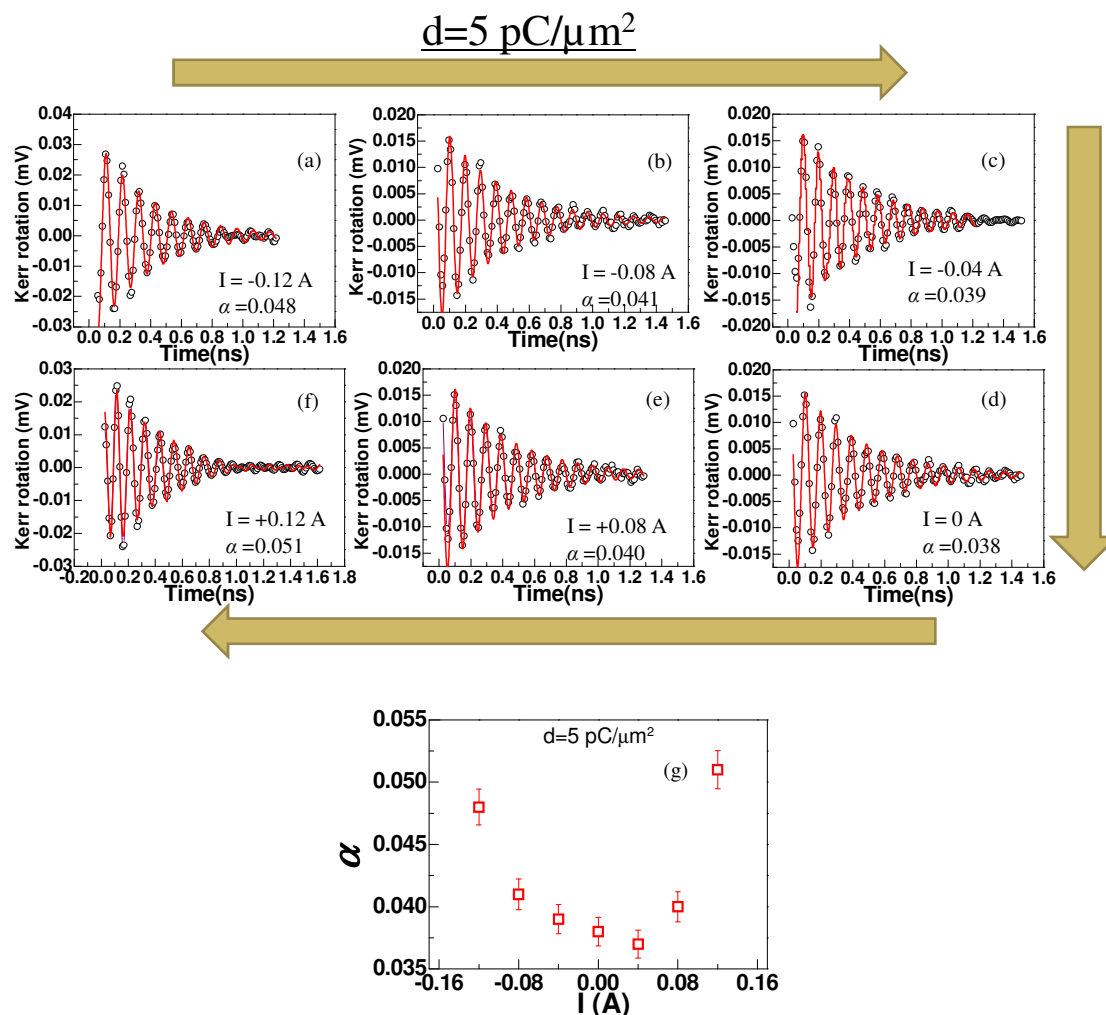


Figure 9.11. (a-f) Time-resolved Kerr rotation data of $\text{Ni}_{81}\text{Fe}_{19}/\text{Pt}$ bi-layer for irradiation dose $d = 5 \text{ pC}/\mu\text{m}^2$ for different applied current. The black circles denote experimental data points and the red lines are the fitted data. (g) Variation of damping as a function of applied current corresponding to figure 9.11 (a-f).

9.5. Discussion

From our earlier work and recent literature[14,19] we understand that in case of un-irradiated $\text{Ni}_{81}\text{Fe}_{19}/\text{Pt}$ bi-layer sample the modulation of damping in the NiFe layer is originated from transfer of angular momentum due to spin current injection from the Pt layer as a result of spin Hall effect. This exerts a spin transfer torque (STT) on the precessing magnetization in the NiFe layer. In that case the magnetization dynamics can be described by incorporating a STT term into the Landau–Lifshitz–Gilbert equation as discussed earlier in chapter 2 section 2.19 (equation 2.76). The STT acts collinearly with the damping torque. Depending on the polarity of spin current it can be either parallel or anti-parallel to the damping torque. In the former situation it enhances the damping while in the latter it compensates and reduce the damping. Hence, the asymmetric nature of variation of damping for positive and negative applied current as observed in figure 9.6 suggests that the STT due to injected spin current in the NiFe layer dominates the variation of damping at $d = 0 \text{ pC}/\mu\text{m}^2$. However, we have observed that this modulation of damping is very much dependent on ion irradiation dose. With the increase in irradiation dose the rate of STT induced modulation of damping decreases. The modulation rate is highest (0.03 A^{-1}) in the un-irradiated sample, reduces drastically to 0.016 A^{-1} for $d = 0.8 \text{ pC}/\mu\text{m}^2$ and further reduces to about zero for $d = 2 \text{ pC}/\mu\text{m}^2$ (i.e., there is no significant variation of damping with current). Low dose ion irradiation causes intermixing of atoms localized in the interface region. This essentially reduces the spin injection efficiency from Pt to the $\text{Ni}_{81}\text{Fe}_{19}$ layer and thereby the spin torque induced rate of modulation of damping. When the irradiation dose increases further a different type of modulation starts to occur where damping increases for both positive and negative current (figure 9.10 (g) and 9.11 (g)). This modulation increases with dose and the variation is nonlinear with current. The nonlinear behavior is more prominently observed for $d = 5 \text{ pC}/\mu\text{m}^2$ as compared to $d = 3.6 \text{ pC}/\mu\text{m}^2$ due to its larger variation of damping. This type of modulation can be originated from the Joule heating[20]. Ion irradiation with higher dose introduces defects and disorders in the sample resulting in an increase of resistance and consequent Joule heating while applying current. When the temperature of the sample increases thermal fluctuation of magnetization is enhanced resulting in an increase of damping in the system. The variation is nonlinear and does not depend on the polarity of current because Joule heating is proportional to the square of the applied current. In figure 9.11(g) we can see the variation of damping with current for the highest dose is not fully symmetric with respect to zero current but has a small

asymmetric component associated with it. A clear quantitative understanding about the source of this small asymmetry requires a detailed structural characterization which is out of the scope of this thesis. However, it can be qualitatively explained by STT induced modulation of damping. Now the immediate question comes is why the STT induced modulation of damping reappears in this case ($d = 5 \text{ pC}/\mu\text{m}^2$) after disappearing at $d = 2 \text{ pC}/\mu\text{m}^2$? The answer may lie in the structural deformation developed in the sample by a high dose irradiation. Earlier in chapter 7 equation 7.5 we have seen that the STT induced modulation of damping is inversely proportional to the ferromagnetic layer thickness. At higher dose values, the intermixed region at the interface gets broadened resulting in a significant reduction of the pure ferromagnetic layer thickness and this may result in an enhanced rate of modulation for $d = 5 \text{ pC}/\mu\text{m}^2$. Moreover, as the resistivity of $\text{Ni}_{81}\text{Fe}_{19}$ and Pt are comparable the current density is more or less uniform along the thickness. Irradiation with higher dose (e.g., $d = 5 \text{ pC}/\mu\text{m}^2$) may significantly increase sputtering of atoms from the top surface. It may cause an effective reduction of the sample thickness in the irradiated region and a consequent increase of local current density for a constant applied current resulting in a detectable amount of STT induced asymmetric modulation of damping for $d = 5 \text{ pC}/\mu\text{m}^2$.

9.6. Summary and Future Prospective

In summary, in this chapter we deal with two different effects at the interface of a ferromagnet/heavy metal bi-layer. The first one is the spin current injection from the heavy metal layer to the ferromagnetic layer due to spin Hall effect and the second one is interface intermixing due to ion irradiation. A dc charge current produces a transverse spin current in Pt which gets injected into the adjacent $\text{Ni}_{81}\text{Fe}_{19}$ layer and influences its magnetization dynamics by exerting STT. It causes a linear modulation of damping which can be positive or negative depending on the polarity of the charge current. On the other hand, ion irradiation causes intermixing of atoms around interface and the intermixed region gets broadened with irradiation dose by the formation of a compositionally graded alloy between the layers. It may also cause sputtering of atoms from the top surface at a very high dose. The influence of these two effects on the magnetization dynamics reveals interesting results. For un-irradiated sample the rate of STT induced modulation is the highest which decreases with increased irradiation dose and then disappears due to the reduced spin transparency of the interface. Further increase in irradiation dose increases the disordered region thickness around the interface

resulting in Joule heating induced nonlinear and symmetric modulation of damping. At very high dose the symmetric variation may contain a small asymmetric part for which responsible factors are significant reduction of pure Ni₈₁Fe₁₉ layer thickness due to intermixing and increased current density due to the reduction of sample thickness by sputtering.

The study suggests a unique technique for amplitude controlled local spin injection. If we pattern a ferromagnet/heavy metal bi-layer thin film with different irradiation dose the amplitude of the transverse spin current will depend on the local irradiation. This will enable spin current excitation and STT induced magnetization reversal and modulation of magnetization precession in selected regions of an adjacent ferromagnet with a determined amplitude ratio. For example, local damping of un-irradiated part of the sample can be selectively made larger or smaller with respect to the irradiated part just by changing the polarity of the bias dc. The knowledge can be applied to guide spin waves or domain walls along preferred directions depending on the polarity of current and irradiation. The research shows a new direction towards the construction of on-chip spintronic, logic and data transfer devices.

References

- [1] Bandyopadhyay, S. & Cahay, M. *Introduction to spintronics*. (CRC press, 2015).
- [2] Takahashi, S. & Maekawa, S. Spin current, spin accumulation and spin Hall effect. *Sci. Technol. Adv. Mater.* **9**, 014105 (2008).
- [3] Dyakonov, M. & Khaetskii, A. in *Spin Physics in Semiconductors* **157**, 211 (Springer Science & Business Media, 2008).
- [4] Liu, L., Moriyama, T., Ralph, D. & Buhrman, R. Spin-torque ferromagnetic resonance induced by the spin Hall effect. *Phys. Rev. Lett.* **106**, 036601 (2011).
- [5] Mosendz, O. *et al.* Detection and quantification of inverse spin Hall effect from spin pumping in permalloy/normal metal bi-layers. *Phys. Rev. B* **82**, 214403 (2010).
- [6] Kimura, T. *et al.* Room-temperature reversible spin Hall effect. *Phys. Rev. Lett.* **98**, 156601 (2007).
- [7] Kimura, T. *et al.* Erratum: Room-Temperature Reversible Spin Hall Effect [Phys. Rev. Lett. 98, 156601 (2007)]. *Phys. Rev. Lett.* **98**, 249901 (2007).
- [8] Kondou, K. *et al.* Evaluation of spin Hall angle and spin diffusion length by using spin current-induced ferromagnetic resonance. *Appl. Phys. Express* **5**, 073002 (2012).

- [9] Zhang, W. F. *et al.* Role of transparency of platinum-ferromagnet interfaces in determining the intrinsic magnitude of the spin Hall effect. *Nat. Phys.* **11**, 496 (2015).
- [10] Ganguly, A. *et al.* Tunable magnetization dynamics in interfacially modified Ni₈₁Fe₁₉/Pt bi-layer thin film microstructures. *Sci. Rep.* **5**, 17596 (2015).
- [11] Ganguly, A. *et al.* Thickness dependence of spin torque ferromagnetic resonance in Co₇₅Fe₂₅/Pt bi-layer films. *Appl. Phys. Lett.* **104**, 072405 (2014).
- [12] Liu, L. *et al.* Spin-torque switching with the giant spin Hall effect of tantalum. *Science* **336**, 555 (2012).
- [13] Mosendz, O. *et al.* Quantifying spin Hall angles from spin pumping: Experiments and theory. *Phys. Rev. Lett.* **104**, 046601 (2010).
- [14] Ganguly, A. *et al.* Time-domain detection of current controlled magnetization damping in Pt/Ni₈₁Fe₁₉ bi-layer and determination of Pt spin Hall angle. *Appl. Phys. Lett.* **105**, 112409 (2014).
- [15] Kouta, K. *et al.* Evaluation of Spin Hall Angle and Spin Diffusion Length by Using Spin Current-Induced Ferromagnetic Resonance. *Appl. Phys. Express* **5**, 073002 (2012).
- [16] Burn, D. *Domain wall behaviour in ferromagnetic nanowires with interfacial and geometrical structuring*, Ph.D. thesis, Ch. 6 135-160 (Durham University, 2013).
- [17] Burn, D., Hase, T. & Atkinson, D. Focused-ion-beam induced interfacial intermixing of magnetic bi-layers for nanoscale control of magnetic properties. *J. Phys. Condens. Matter* **26**, 236002 (2014).
- [18] Mizukami, S., Ando, Y. & Miyazaki, T. Ferromagnetic resonance linewidth for NM/80NiFe/NM films (NM = Cu, Ta, Pd and Pt). *J. Magn. Magn. Mater.* **226**, 1640 (2001).
- [19] Ando, K. *et al.* Electric manipulation of spin relaxation using the spin Hall effect. *Phys. Rev. Lett.* **101**, 036601 (2008).

Chapter 10

Evolution of Damping in Ferromagnetic/ Nonmagnetic Thin Film Bi-layers As a Function of Nonmagnetic Layer Thickness

The evolution of damping in Co/Pt, Co/Au, and Ni₈₁Fe₁₉/Pt bi-layers was studied with increasing nonmagnetic(NM) heavy-metal layer thicknesses in the range $0.2 \text{ nm} \leq t_{\text{NM}} \leq 10 \text{ nm}$, where t_{NM} is the NM layer thickness. Magnetization precession was measured in the time domain using time-resolved magneto-optical Kerr effect magnetometry. Fitting of the data with a damped sinusoidal function was undertaken in order to extract the phenomenological Gilbert damping coefficient α . For Pt-capped Co and Ni₈₁Fe₁₉ layers a large and complex dependence of α on the Pt layer thickness was observed, while for Au capping no significant dependence was observed. It is suggested that this difference is related to the different localized spin-orbit interaction related to intermixing and to d-d hybridization of Pt and Au at the interface with Co or Ni₈₁Fe₁₉. Also, it was shown that damping is affected by the crystal structure differences in FM thin films and at the interface, which can modify the spin-diffusion length and the effective spin-mixing conductance. In addition to the intrinsic damping an extrinsic contribution plays an important role in the enhancement of damping when the Pt capping layer is discontinuous. The dependence of damping on the nonmagnetic layer thickness is complex but shows qualitative agreement with recent theoretical predictions.

10.1. Introduction

Precessional magnetization dynamics are fundamental to magnetic field and current-driven magnetization processes and underpin switching behaviour in applications such as magnetic data storage, where data writing depends on the magnetic damping. Precessional damping plays an important role in a number of emerging technologies, including magnonics and spin

transfer torque magnetoresistive random access memory (STT-MRAM) devices. Understanding and controlling damping in thin film systems therefore continues to drive research in this field. It has been demonstrated that damping can be enhanced in both bulk ferromagnetic (FM)[1-4] and multilayered systems[5-8] and many studies have addressed the fundamental origin of damping both experimentally and theoretically[1,3,9-15]. Both Co and Ni₈₁Fe₁₉ have attracted a lot of attention due to their common application in magnetic devices. More recently, the influence of heavy-metal (NM) over layers on the damping in adjacent ferromagnetic (FM) layers has attracted a lot of research interest. In such bi-layer systems there are several mechanisms that may lead to the enhancement of damping. Spin-orbit coupling (SOC) and interfacial *d-d* hybridization enhance the intrinsic damping, while extrinsic enhancement of the damping can arise from two-magnon scattering processes, linked to roughness and defects at the interface region[1,3,11-21]. The total precessional damping is a sum of the intrinsic and extrinsic contributions.

In the case of bi-layer and multilayer thin films, the strong SOC of the heavy metal layer leads to enhanced damping because of enhanced coupling of the electron spin with the lattice at the interface. This will facilitate the propagation and dissipation of transverse spin current generated by precession in the ferromagnetic layer. NM layers can therefore act as an absorber or sink for spin current pumped across the interface[3,14]. The spin-current pumped into the adjacent NM layer may either dissipate in the NM layer or diffuse back into the FM layer. This depends on the spin diffusion length (λ_{sd}) and the effective spin-mixing conductance ($g_{\uparrow\downarrow}^{eff}$) across the interface[8]. The *d-d* electron hybridization of the FM/NM layer occurs at the interface and is therefore influenced by topological roughness and intermixing. These factors may also increase the local density of states at the Fermi energy or decrease the bandwidth in the interface region[3,11,13,17,21]. The specific electronic behavior depends on the materials involved and the damping has been studied in variety of systems, including Au, MgO, Cu, and Ta (NM) overlayers on FM layers of Co, CoFeB, and Ni₈₁Fe₁₉[3,8,16,22].

Moving on to extrinsic damping contributions, two-magnon scattering refers to the scattering of uniform magnetization precession into pairs of magnons with nonzero wave vectors[3,16,22]. This can occur when the symmetry of the system is disturbed by structural defects like film roughness and intermixing[1,3,21] and will enhance the effective damping

of the magnetization precession. Increased intermixing will also enhance the effective spin-mixing conductance[8,21-22], and modifying the interface will affect all of the mechanisms mentioned above[4,23]. It is therefore of great interest to study the evolution of precessional magnetic damping in FM/NM bi-layers as the interface develops as a function of the NM thickness.

A recent theoretical study of FM/NM bi-layers by Barati *et al.*[3] reported the dependence of damping with increasing thickness of the NM layer, assuming an ideal flat interface. This predicted that for NM layers the damping depends on the specific material and the layer thickness. In particular, for the case of Co/Pt bi-layers the magnetic damping was found to increase by more than two times with the addition of a few monolayers of Pt. This theoretical analysis motivates the experimental study of precessional damping as a function of NM capping layer thickness in this work. The experimental study requires well-controlled thin film deposition and also structural analysis in order to establish precise layer thicknesses, interface width, and FM crystal structure.

10.2. Formalism for Analysis of Damping

The measured effective magnetic damping α_{eff} can be written as the sum of the bulk, intrinsic and extrinsic contributions,

$$\alpha_{eff} = \alpha_0^{int} + \alpha_{ext} \quad (10.1),$$

Where α_0^{int} and α_{ext} are the total intrinsic and extrinsic damping coefficients of the system, respectively. Furthermore, α_0^{int} can be expressed such that

$$\alpha_{eff} = \frac{G_0}{\gamma M_s} + \frac{\alpha_s}{t_{FM}} + \alpha_{ext} \quad (10.2),$$

where G_0 is the bulk Gilbert damping parameter, γ is the gyromagnetic ratio, M_s is the saturation magnetization, t_{FM} is the ferromagnetic layer thickness, and α_s is the interface contribution to the effective damping[3,12,24].

The thickness dependence of the damping enhancement may be explained by a mixture of spin-pumping, $d-d$ hybridization, and two-magnon scattering effects. In this study α_{eff} was measured as a function of the NM layer thickness.

10.3. Experimental Details

The common and widely utilized ferromagnetic materials Co and Ni₈₁Fe₁₉ were studied with NM capping layers of Pt and Au. Bi-layer thin films were deposited by UHV magnetron sputtering from a base pressure $\sim 1 \times 10^{-8}$ torr on to thermally oxidized silicon substrate with a 100 nm SiO₂ layer. The complete structure was Si/SiO₂/FM/NM and the FM layer was deposited directly on the SiO₂. The selected Co layer thicknesses were either 4 or 10 nm and for the Ni₈₁Fe₁₉ films the thickness was 7 nm. The thicknesses were chosen to maximize the interaction between the films and the incident optical probe. The thinnest capping layers may permit partial oxidation of the FM surface, but adding a further capping layer would make the physical system more complex, which could confuse the results. The study aimed to examine the sub nanometer thickness effect of specific NM materials on the damping. Capping layer thicknesses were varied from 0.2 to 10 nm. Dynamic magnetization behaviour was studied *ex situ* using time-resolved magneto-optical Kerr effect (TR-MOKE) magnetometry using an all-optical pump-probe technique. More details about the TR-MOKE system can be found elsewhere[25-27]. Structural analysis was carried out using a Bede-D1 diffractometer with a CuK α source for grazing incidence x-ray reflectivity (XRR) to study layer thicknesses and interfacial structure and for x-ray diffraction (XRD) to analyze crystal structure; more information can be found elsewhere[28-29]. True specular XRR data were obtained by subtraction of the measured forward diffuse scatter and was modeled with simulations generated using the GenX code, which uses a differential evolution algorithm with the Parrat recursive mechanism to simulate the XRR data[30]. XRD results were analyzed to determine the out-of-plane lattice parameter.

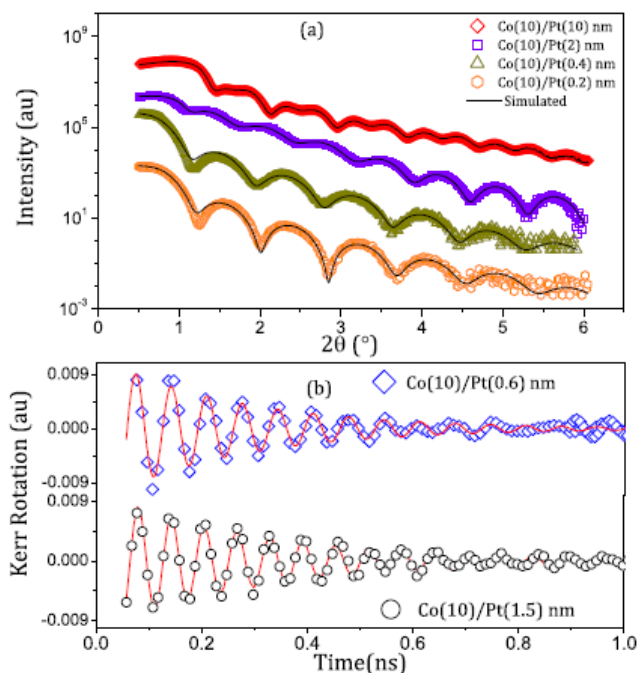


Figure 10.1. (a) Examples of x-ray reflectivity data and the best-fitting simulations for Co (10 nm)/Pt (t_{Pt}). (b) Background subtracted time-resolved magneto-optic Kerr rotation data for Co/Pt with two different Pt layer thicknesses and the best-fitting damped sinusoids.

10.4. Results

Figure 10.1(a) shows examples of the XRR data obtained from selected samples and the corresponding best-fitting simulations. From the numerical analysis structural parameters were derived, including the layer thicknesses and interface roughness. Table 10.1 shows the thickness and roughness of selected FM/NM bi-layers. These data were selected because they indicate the width of the FM/NM interfacial region when the NM metal forms a complete layer over the FM layer. The interface width includes topological roughness and intermixing. The interface width is important as it provides an indication of the thickness at which the NM capping layer changes from island-like coverage to continuous coverage of the FM layer. The structural analysis shows that both Pt and Au form a continuous layer on Co at a thickness greater than ~ 0.7 nm, while for Ni₈₁Fe₁₉ the NM capping layer becomes continuous at a thicknesses above ~ 0.9 nm. This difference in roughness between the two FM materials may stem from the crystal structure, which XRD shows is fcc for the Ni₈₁Fe₁₉ and hcp for the Co[3,15,22]. The Au and the Pt are both fcc. For Au and Pt capping of Co, the interfacial

roughness is very similar; however, details of the local atomic arrangement are likely to differ, Co and Pt are miscible while Co and Au are immiscible[31]. The growth of Au or Pt capping layers onto a FM thin film layer begins with the formation of localized islands of the NM material; these expand and develop into a continuous capping layer as the NM thickness increases.

Table 10.1. Structural properties for selected Co/Au, Co/Pt, and NiFe/Pt bi-layers samples extracted from XRR measurements: FM layer thickness, t_{FM} ; NM layer thickness, t_{NM} ; and interface width at FM/NM interface.

Sample structure	$t_{\text{FM}}(\text{nm})$	$t_{\text{NM}}(\text{nm})$	Interface width(nm)
Co(10nm)/Au(4nm)	9.44 ± 0.05	3.5 ± 0.04	0.61 ± 0.11
Co(10nm)/Pt(2nm)	9.56 ± 0.09	2.8 ± 0.05	0.66 ± 0.07
Ni ₈₁ Fe ₁₉ (7nm)/Pt(1nm)	7.24 ± 0.11	0.94 ± 0.08	0.92 ± 0.05

Figure 10.1(b) shows typical TR-MOKE data for selected samples following removal of the ultrafast demagnetization and subtraction of a background signal by fitting with a bi-exponential function. The background signal represents the initial recovery of magnetization following an optically induced demagnetization and is characterized by two relaxation times of the order of 1 and 20 ps. The shorter time scale is related to electronic thermal bath dissipation to the lattice. The longer time scale is associated with dissipation of energy between the lattice and surroundings, which decreases with the addition of the capping layer. Returning to the figure, the TR-MOKE data illustrates the magnetic precession, which show that FM-NM bi-layers with certain NM capping thickness are damped faster. The figure also shows the best-fitting curves, which indicate a single-mode damped precession behaviour representing the Landau-Lifshitz-Gilbert relation from which the damping coefficient was obtained.

Figures 10.2(a) and 10.2(c) show the variation of α_{eff} with Pt and Au layer thickness. It shows that α_{eff} increases significantly for both Co/Pt and Ni₈₁Fe₁₉/Pt layers as the Pt capping layer thickness increases and peaks around 0.7–0.8 nm for Co/Pt and 0.6 nm for Ni₈₁Fe₁₉/Pt. However, in the case of Co/Au, α_{eff} is nearly constant across the entire Au thickness range. Also, it should be noted that the bulk damping coefficient for hcp Co is 0.011; however, here the uncapped or the partially capped Co and Ni₈₁Fe₁₉ are likely to be partially oxidized and this may enhance α_{eff} from the bulk value. The interfacial width shown in Table 10.1 for Ni₈₁Fe₁₉/Pt may explain the increase in α_{eff} up to a capping layer thickness of 0.6 nm, but the available damping data is limited to thicknesses up to 1 nm.

The thickness dependence of the capping layer on α_{eff} for Co/Pt and Ni₈₁Fe₁₉/Pt may be divided into three different regions. With initial increasing Pt thickness the damping first increases rapidly (region I) and then peaks (region II) before falling back to a lower constant level (region III). These different regions are discussed in more detail later. Figure 10.2(b) shows the precessional frequency, f , and the saturation magnetization, M_s , as a function of NM layer thickness for the Co/Pt bi-layer. A noticeable similarity of the Pt thickness dependence between M_s and f is observed. In particular, both M_s and f increase rapidly with Pt thickness between 0.6 and 0.8 nm.

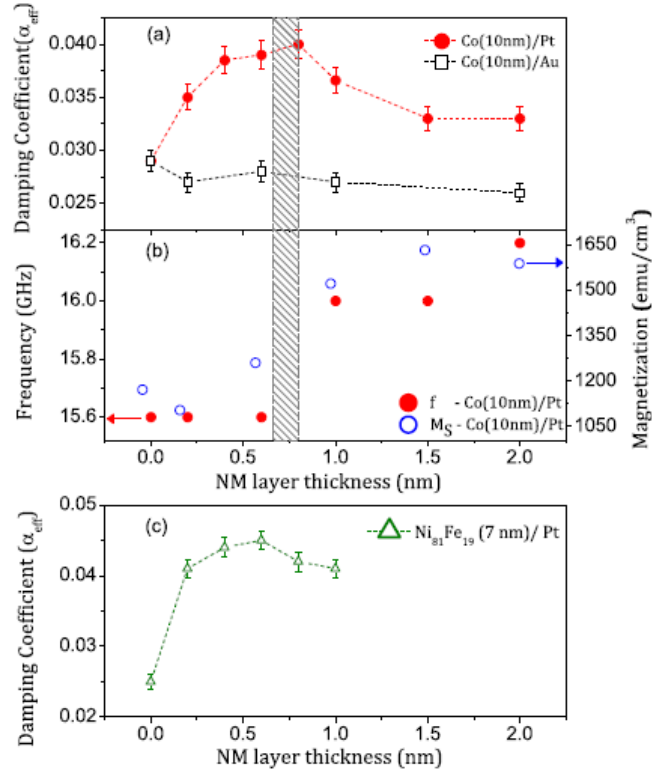


Figure 10.2. [(a) and (c)] α_{eff} as a function of t_{NM} for Co/Pt and Ni₈₁Fe₁₉/Pt, respectively. (b) Frequency and saturation magnetization as a function of t_{NM} and ~ 1.4 kOe of magnetic field strength; it shows a similar trend in their variations. The shaded bar indicates the Pt thickness where the Pt became continuous.

In order to understand the damping mechanisms further a series of TR-MOKE measurements were undertaken at different bias fields in order to look for a dependence on the precessional frequency, which can inform on the nature of the damping. Figure 10.3 shows examples of plots of α_{eff} as a function of f for a discontinuous (0.6 nm) and continuous (2 nm) Pt capping layer on Co. In the case of the discontinuous Pt layer the damping falls linearly with the increase in precessional frequency, while the damping remains almost constant with frequency for the continuous Pt-capped Co bi-layer. For a continuous Pt capping layer on Ni₈₁Fe₁₉ the damping is also constant as a function of precessional frequency.

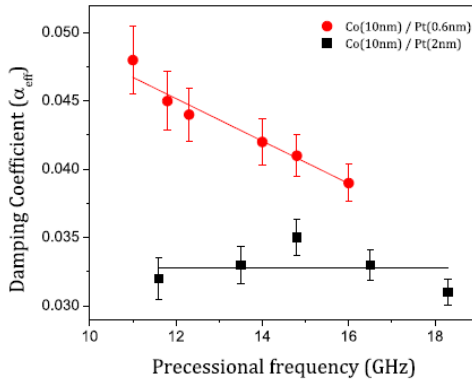


Figure 10.3. Damping coefficient α_{eff} as a function of precessional frequency for 10 nm Co films capped with 0.6 nm and 2 nm Pt. The extrinsic damping decreases with the increasing Pt thickness until reaches to negligible extrinsic effect at $t_{NM} = 2$ nm.

10.5. Discussion

The complex dependence of α_{eff} with NM layer thickness described in Figures 10.2(a) and 10.2(c) with three characteristic regions can be understood by considering several intrinsic and extrinsic effects occurring at the interface of the FM and NM layers. It is known that $d-d$ hybridization, spin-pumping, and two-magnon scattering are the effective factors for damping enhancement in FM/NM thin films[3-4,11,13,17,21,23]. The experimental results are in agreement with a recent theoretical study[3] where damping increases with increasing Pt capping layer thickness up to a broad peak followed by a decrease to constant value with further increases in thickness. In the experimental work the Co structure is hcp, but fcc in the theoretical; however, a key point is that Pt and Au have fcc structure, which allows direct comparison[32].

The possible intrinsic contributions to the enhancement of the damping in region I can be attributed to $d-d$ hybridization and spin-pumping in the case of the Pt capping layer. Hybridization causes changes in the electronic structure in the interface, whereas spin-pumping allows absorption of angular momentum from the precessing magnetization, giving rise to an enhancement of damping. Both effects are intrinsic in nature.

However, the effect of spin pumping should be very limited over the studied thickness range of Pt, as it is comparable or below the spin-diffusion length, λ_{sd} [12,33-35]. Hence, $d-d$

hybridization mainly contributes to the intrinsic enhancement of the damping. The availability of $5d$ electrons in the NM layer and the opportunity for hybridization with the $3d$ electrons in the FM at the interface is a key mechanism which enhances the damping. This agrees with previous studies of FM-NM interfaces including the recent theoretical work of Barati *et al.*[1-3,11-21]. Extrinsic contributions to the damping can be attributed to two-magnon scattering, which is related to local variations linked to topological roughness, defects, and impurities at the interface. For discontinuous Pt it is suggested that variations in local electronic properties of the Pt capped and uncapped regions leads to local variation of intrinsic damping, which gives rise to extrinsic damping via two-magnon scattering. The precessional frequency dependence of the damping data (see figure 10.3) shows a linear increase in damping with the decreasing frequency for the discontinuous Pt layer, which clearly indicates that extrinsic effects are present in the system when the capping layer is discontinuous.

Following the initial rapid increase in region I, the damping reaches a broad peak in region II. From the structural analysis it is observed that the second region falls into the thickness range where a continuous Pt capping layer is just forming. Beyond this thickness a complete Pt layer is established.

In region III damping falls from its maximum and slowly stabilizes to an intermediate value with increasing Pt thickness. The independence of the damping on applied field indicates the mechanism here is predominantly intrinsic when the Pt is continuous. The decrease in the damping from the peak primarily represents a reduction in the extrinsic contribution that largely vanishes for higher thicknesses of Pt. Further details of this mechanism in terms of the local arrangement of atoms at the interface are discussed later. It is interesting to observe that the final value of α_{eff} is larger than the uncapped ($t_{NM} = 0$) value for both Co and $Ni_{81}Fe_{19}$. The reason for this is that although at higher thicknesses of Pt the extrinsic contribution is negligible, intrinsic effects from the interface are the dominant contribution to the damping. Theoretical analysis[3] shows some reduction in the intrinsic damping from the peak, along with periodic oscillations due to the formation of quantum well states. Oscillations are not observed in the experiment as the t_{NM} range is too small, but also any oscillations would be lost due to interfacial roughness.

Regarding the mechanism for extrinsic damping, it is suggested that two-magnon scattering is a result of local variation of $d-d$ hybridization of the Co and Pt when the capping layer is discontinuous, leading to localized variations of the intrinsic damping. The miscibility of the NM material changes the local structure. In the case of Pt this can produce Co-Pt clusters or islands at the surface[22], while for Au this leads to the formation of Au islands on Co in the low-thickness regime[31]. For thin Pt, where the capping layer is incomplete, the formation of clusters or islands at the surface acts to break the translational symmetry leading to regions with higher and lower intrinsic damping due to the distribution of Co-Pt. This is also supported by a study which showed that SOC for Pt is stronger when it is 2D rather than 3D, which increases the local damping of the Co-Pt islands[36]. This inhomogeneous magnetic surface can, therefore, give rise to an extrinsic contribution to the enhancement of the damping. When the Pt capping layer completely covers the Co the interface region is more uniform and the extrinsic contribution vanishes[2-3,12,18].

It is worth noting that the experimental data [Figure 10.2(b)] for the precessional frequency and the saturation magnetization, M_s , of the Co/Pt system shows an increase in the net magnetic moment as the Pt capping increases. This may be attributed to a proximity induced magnetization (PIM) in Pt[12]. The role of PIM in damping remains a matter of debate[19]. Also, it can be seen that M_s for the uncapped Co is lower than expected for bulk Co, which may be related to oxidation of the uncapped Co surface. This is supported by the significant increase in M_s when t_{Pt} reaches 0.6 nm where the Pt cap would restrict the oxidation of the Co surface. However, PIM cannot explain the large additional M_s when t_{Pt} reaches to 2 nm except the case when Co/Pt thin film have hcp crystal structure, which agrees with XRD in of this study and also with the recent published research[15].

Comparing the Pt and the Au layers, greater miscibility of Pt is an additional factor affecting the damping and is supported by the XRR structural analysis[31]. As a result, two-magnon scattering is also lower in case of Co/Au. Furthermore, Au has a lower density of electrons in d band states at the Fermi level compared to Pt[37], which therefore contributes very weakly to the intrinsic damping. For $Ni_{81}Fe_{19}/Pt$, the capping layer thickness dependence of the damping shows similar behaviour to Co/Pt. However, it can be seen from figures 10.2(a) and 10.2(c) that α_{eff} for $Ni_{81}Fe_{19}/Pt$ is higher at lower Pt thickness. This may be related to a slightly larger topological roughness and different FM crystal structure, as shown by the structural analysis. The larger enhancement of the damping for the $Ni_{81}Fe_{19}$, as compared to

Co, may be explained by a higher spin-mixing conductance across the interface for fcc rather than hcp FM interfacial structure[15,38]. This is supported by the experimental XRD results showing hcp Co and fcc $\text{Ni}_{81}\text{Fe}_{19}$ in the FM/NM bi-layers.

Bringing together the structural analysis and the discussion of the damping mechanisms the interpretation of the NM capping layer thickness dependence of the ferromagnetic damping is summarized in figure 10.4, where the structural changes associated with the thickness dependence of the damping are illustrated for regions, I, II, and III.

Figure 10.4 also shows a comparison between the experimental damping data and the theoretical analysis of Co/Pt and Co/Au by Barati *et al.*[3]. The general trends of rapidly increasing damping to a peak followed by a small reduction and then leveling out of the damping with increasing film thickness are broadly similar between the theory and experiment results. Figure 10.4(b) shows some reduction in the intrinsic damping from the peak. In figure 10.4(a) oscillations are not observed as the t_{NM} range is too small, but overall there is good agreement between the Barati *et al.* study and this work.

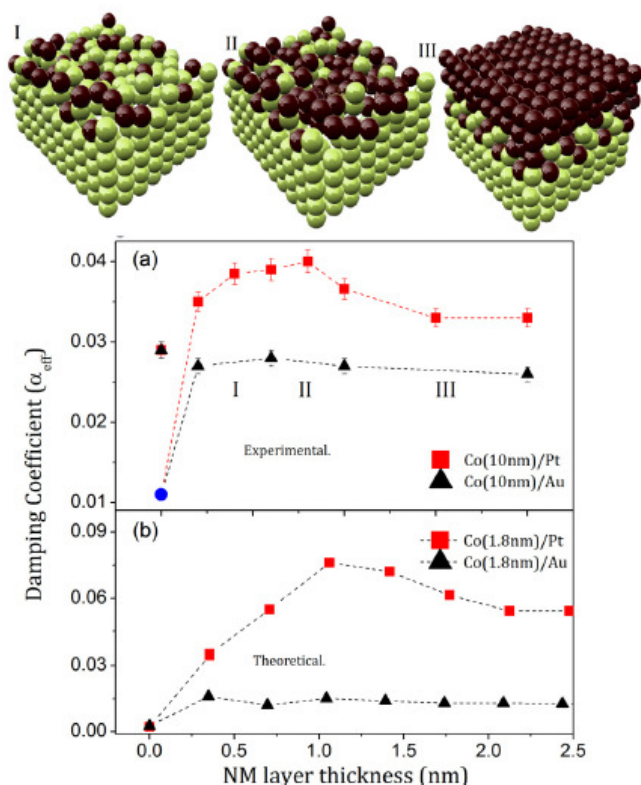


Figure 10.4. Schematic illustration of the growth of discontinuous to continuous NM capping layer. (a) Experimental damping data for Co/Pt and Co/Au as a function of t_{NM} . The circular point is a literature value for pure cobalt. (b) Theoretical variation in damping data for Co/Pt and Co/Au adapted from reference 3. as a function of t_{NM} .

Finally, the spin-mixing conductance has been estimated for both Co/Pt and Ni₈₁Fe₁₉/Pt from the damping data obtained for samples with the thickest Pt layer, where the Pt has formed a complete capping layer and measurements indicate that the mechanism for the enhanced damping is intrinsic. The spin-mixing conductance is related to the change in damping according to:

$$\Delta\alpha = \alpha_{eff} - \alpha_0 = \frac{g\mu_B}{4\pi t_{FM} M_{eff}} g_{\uparrow\downarrow}^{eff} \quad (10.3),$$

where g is the Landé ‘ g ’ factor, μ_B is the Bohr magneton, M_{eff} is the effective saturation magnetization, and $g_{\uparrow\downarrow}^{eff}$ is the effective spin-mixing conductance. Taking literature values for the damping in bulk hcp Co as 0.011[21] and fcc Ni₈₁Fe₁₉ as 0.010[30] and saturation magnetization as obtained experimentally, the effective spin-mixing conductance was estimated from the observed saturation enhancement to the damping. For Co/Pt a value of 38 nm⁻² was obtained for the spin-mixing conductance, which is comparable with the value recently observed experimentally[19]. In the case of Ni₈₁Fe₁₉/Pt a value of 125 nm⁻² was obtained. This is notably higher than the value obtained for Co/Pt and it is suggested that this may be related to the different crystallographic structures at the interface with the Pt. This is supported by recent work on Co/Ir where the Co structure at the interface was either hcp or fcc[15].

10.6. Conclusion

In conclusion, precessional magnetization damping has been studied in different FM/NM bilayer thin films with a gradually increasing capping layer thickness starting from the sub-monolayer regime. For Pt capping of Co and Ni₈₁Fe₁₉ the Pt thickness-dependent damping shows an increase followed by a peak and a modest fall to constant value that is higher than

the bulk values for Co and Ni₈₁Fe₁₉. Structural analysis using x-ray reflectivity and x-ray diffraction were used to characterize the interface and the crystallographic structure and aid the interpretation. Both intrinsic and extrinsic mechanisms are invoked to explain the observed magnetic precessional damping behavior. Extrinsic effect occurs when the Pt capping layer is incomplete as it leads to variation in *d-d* hybridization leading to inhomogeneities in damping which can act to create two-magnon scattering. This extrinsic damping is lost when the Pt layer became continuous over the FM. Finally the effective spin-mixing conductance was estimated for Ni₈₁Fe₁₉/Pt and Co/Pt. The analysis indicates that the effective spin-mixing conductance is higher in Ni₈₁Fe₁₉/Pt than Co/Pt and it is suggested that this may be linked to the crystal structure type and the interface properties. The results provide further insight into the mechanism of damping variation in FM/NM bi-layer when the interfacial region is gradually formed.

References

- [1] Lenz, K. *et al.* Two-magnon scattering and viscous Gilbert damping in ultrathin ferromagnets. *Phys. Rev. B* **73**, 144424 (2006).
- [2] Rantschler, J. *et al.* Effect of 3d, 4d, and 5d transition metal doping on damping in permalloy thin films. *J. Appl. Phys.* **101**, 3911 (2007).
- [3] Barati, E., Cinal, M., Edwards, D. & Umerski, A. Gilbert damping in magnetic layered systems. *Phys. Rev. B* **90**, 014420 (2014).
- [4] Ganguly, A. *et al.* Tunable Magnetization Dynamics in Interfacially Modified Ni₈₁Fe₁₉/Pt Bi-layer Thin Film Microstructures. *Sci. Rep.* **5**, 17596 (2015).
- [5] Tserkovnyak, Y., Brataas, A. & Bauer, G. E. W. Enhanced Gilbert Damping in Thin Ferromagnetic Films. *Phys. Rev. Lett.* **88**, 117601 (2002).
- [6] Chen, K. & Zhang, S. Spin Pumping in the Presence of Spin-Orbit Coupling. *Phys. Rev. Lett.* **114**, 126602 (2015).
- [7] Woltersdorf, G., Buess, M., Heinrich, B. & Back, C. H. Time Resolved Magnetization Dynamics of Ultrathin Fe(001) Films: Spin-Pumping and Two-Magnon Scattering. *Phys. Rev. Lett.* **95**, 037401 (2005).
- [8] Liu, Y. *et al.* Interface Enhancement of Gilbert Damping from First Principles. *Phys. Rev. Lett.* **113**, 207202 (2014).
- [9] Malinowski, G. *et al.* Control of speed and efficiency of ultrafast demagnetization by direct transfer of spin angular momentum. *Nat. Phys.* **4**, 855 (2008).

- [10] Zhang, G. P. *et al.* Paradigm of the time-resolved magneto-optical Kerr effect for femtosecond magnetism. *Nat. Phys.* **5**, 499 (2009).
- [11] Kyuno, K., Ha, J. G., Yamamoto, R. & Asano, S. Magnetoelastic contribution to the interface anisotropy of Pd/Co metallic multilayers. *Phys. Rev. B* **54**, 1092 (1996).
- [12] Sun, Y. *et al.* Damping in Yttrium Iron Garnet Nanoscale Films Capped by Platinum. *Phys. Rev. Lett.* **111**, 106601 (2013).
- [13] Nakajima, N. *et al.* Perpendicular Magnetic Anisotropy Caused by Interfacial Hybridization via Enhanced Orbital Moment in Co/Pt Multilayers: Magnetic Circular X-Ray Dichroism Study. *Phys. Rev. Lett.* **81**, 5229 (1998).
- [14] Urban, R., Woltersdorf, G. & Heinrich, B. Gilbert Damping in Single and Multilayer Ultrathin Films: Role of Interfaces in Nonlocal Spin Dynamics. *Phys. Rev. Lett.* **87**, 217204 (2001).
- [15] Tokaç, M. *et al.* Interfacial Structure Dependent Spin Mixing Conductance in Cobalt Thin Films. *Phys. Rev. Lett.* **115**, 056601 (2015).
- [16] Iihama, S. *et al.* Gilbert damping constants of Ta/CoFeB/MgO(Ta) thin films measured by optical detection of precessional magnetization dynamics. *Phys. Rev. B* **89**, 174416 (2014).
- [17] Barman, A. *et al.* Ultrafast magnetization dynamics in high perpendicular anisotropy [Co/Pt]_n multilayers. *J. Appl. Phys.* **101**, 9D102 (2007).
- [18] Hickey, M. C. & Moodera, J. S. Origin of Intrinsic Gilbert Damping. *Phys. Rev. Lett.* **102**, 137601 (2009).
- [19] Rojas-Sánchez, J. C. *et al.* Spin Pumping and Inverse Spin Hall Effect in Platinum: The Essential Role of Spin-Memory Loss at Metallic Interfaces. *Phys. Rev. Lett.* **112**, 106602 (2014).
- [20] Mizukami, S. *et al.* Gilbert damping in perpendicularly magnetized Pt/Co/Pt films investigated by all-optical pump-probe technique. *Appl. Phys. Lett.* **96**, 2502 (2010).
- [21] Pal, S. *et al.* Tunable magnonic frequency and damping in [Co/Pd]₈ multilayers with variable Co layer thickness. *Appl. Phys. Lett.* **98**, 082501 (2011).
- [22] Blon, T. *et al.* Magnetic easy-axis switching in Co/Pt and Co/Au superlattices induced by nitrogen ion beam irradiation. *Nucl. Instrum. Methods B* **257**, 374 (2007).
- [23] King, J. *et al.* Local control of magnetic damping in ferromagnetic/non-magnetic bilayers by interfacial intermixing induced by focused ion-beam irradiation. *Appl. Phys. Lett.* **104**, 242410 (2014).

- [24] Gilbert, T. L. A phenomenological theory of damping in ferromagnetic materials. *IEEE Trans. Magn.* **40**, 3443 (2004).
- [25] Keatley, P. S., Kruglyak, V., Gangmei, P. & Hicken, R. Ultrafast magnetization dynamics of spintronic nanostructures. *Philos. Trans. R. Soc. Lond. A* **369**, 3115 (2011).
- [26] Conger, R. L. & Moore, G. H. Direct Observation of High-Speed Magnetization Reversal in Films. *J. Appl. Phys.* **34**, 1213 (1963).
- [27] Barman, A. & Haldar, A. in *Solid State Physics* Vol. 65 eds E. Camley Robert & L. Stamps Robert) 1-108 (Academic Press, 2014).
- [28] Bowen, D. K. & Tanner, B. K. *High Resolution X-ray Diffractometry and Topography* (CRC Press, Boca Raton, FL, 2005); *X-ray Metrology in Semiconductor Manufacturing* (CRC Press, Boca Raton, FL, 2006).
- [29] Björck, M. & Andersson, G. GenX: an extensible X-ray reflectivity refinement program utilizing differential evolution. *J. Appl. Crystallogr.* **40**, 1174 (2007).
- [30] Parratt, L. G. Surface studies of solids by total reflection of X-rays. *Phys. Rev.* **95**, 359 (1954).
- [31] Baker, H. ASM Handbook, Vol. 3: Alloy Phase Diagrams, edited by H. Baker, Materials Park, OH: ASM International, 1992 (1992), pp. 1.1–1.29.
- [32] Umerski, A. (personal communication).
- [33] Mizukami, S., Ando, Y. & Miyazaki, T. Effect of spin diffusion on Gilbert damping for a very thin permalloy layer in Cu/permalloy/Cu/Pt films. *Phys. Rev. B* **66**, 104413 (2002).
- [34] Mizukami, S., Ando, Y. & Miyazaki, T. Magnetic relaxation of normal-metal (NM)/80NiFe/NM films. *J. Magn. Magn. Mater.* **239**, 42 (2002).
- [35] Ruiz-Calaforra, A. *et al.* The role of the non-magnetic material in spin pumping and magnetization dynamics in NiFe and CoFeB multilayer systems. *J. Appl. Phys.* **117**, 163901 (2015).
- [36] Huda, M. N., Niranjana, M. K., Sahu, B. R. & Kleinman, L. Effect of spin-orbit coupling on small platinum nanoclusters. *Phys. Rev. A* **73**, 053201 (2006).
- [37] Fadley, C. & Shirley, D. Electronic densities of states from X-ray photoelectron spectroscopy. *J. Res. Natl. Bur. Stand. A* **74**, 543 (1970).
- [38] Huang, J. *et al.* Epitaxial growth and characterization of (100) and (110) permalloy films. *J. Cryst. Growth* **171**, 442 (1997).

Chapter 11

Summary and Future Prospective

11.1. Summary

In this thesis, we made a detailed investigation on controlled magnetization dynamics in ferromagnetic/nonmagnetic bi-layer systems using various techniques. The purpose of choosing such a bi-layer system is simple. We tried to control the dynamical magnetization properties which are useful for device applications. Hence, we must have a ferromagnetic layer in our system on which magnetization dynamics has to be investigated. On the other hand a nonmagnetic metal usually does not possess any magnetization, except small proximity induced magnetization, to contribute in the dynamical processes as a ferromagnet does. However, earlier study reveals that a lot of spintronic physics is associated with nonmagnetic metals which can be used for the transfer of spin angular momentum under certain experimental conditions. Interestingly, the structure for the famous giant magnetoresistance effect also consists of alternative ferromagnetic and nonmagnetic layers. In our study we take that advantage of the interlayer spin angular momentum transport between the nonmagnetic and ferromagnetic layers for tuning the magnetization dynamics of our bi-layer system. In addition to that we attempted to locally control the precession frequency and damping behavior of a ferromagnet by focused ion irradiation. In doing so we used a nonmagnetic capping layer, which may contribute to the variation of damping by a variety of ways ranging from interface roughness, hybridization, proximity induced magnetization and spin pumping effect. The local low dose ion irradiation has been used to control the interface properties in pursuit of obtaining a variation of the precession frequency and damping.

The experiments are performed using time resolved magneto-optical Kerr effect (TR-MOKE) and spin-torque ferromagnetic resonance (ST-FMR) technique. The dc and rf magnetron sputtering, e-beam evaporation, optical lithography, reactive ion etching and focused ion beam are used for sample preparation. Scanning electron microscope, atomic force micro-

scope, X-ray reflectivity, vibrating sample magnetometer, static magneto-optical Kerr effect and electrical meters are used for basic characterization of the samples.

In this thesis, injection of spin current using spin Hall effect, intermixing of atoms by low dose ion irradiation, selection of suitable combination of materials and variation of individual layer thicknesses in nanometer and sub-nanometer length scale are used as key techniques for the modulation of damping and frequency of our system. In some cases spin pumping effect is found to have a significant role in the enhancement of damping, specifically when the nonmagnetic material is a heavy metal like Pt. It is also observed that interface plays a crucial role in this study. In a nutshell, the physical phenomena or factors like spin pumping, spin Hall effect, inverse spin Hall effect, spin diffusion, extrinsic two-magnon scattering, spin transparency of the interface, formation of alloy, strain, hybridization at the interface and translation symmetry breaking induced scattering have been discussed in this thesis for explaining our experimental observation.

Chapter 1 gives the introduction. It is all about the history of magnetism and the evolution of spintronics, its present aspects and future possibilities which forms the background of this thesis. In chapter 2 relevant theories of spintronics and magnetism have been discussed. The third chapter is dedicated to the experimental techniques used in this thesis which includes sample preparation, characterization and detection techniques.

In chapters 4 and 5 ferromagnetic/non-magnetic bi-layers with engineered interface have been studied. The interface is controllably modified by energetic gallium ions using focused ion beam. The magnetization dynamics is studied using TR-MOKE. Precessional frequency, damping and picoseconds magnetization relaxation processes have been investigated as a function of irradiation dose. The chapters reveal exciting information about interface engineering which can be used for controlling magnetic systems.

Chapter 6 describes investigation of damping obtained from the line-width of the ST-FMR spectra. Here the individual layer thickness of the bi-layer is varied systematically to study its effect on damping. Two different nonmagnetic metal (Pt and Ta) are used for studying the effect of spin pumping. CoFe and CoFeB are used as ferromagnet to investigate the role of boron in determining the spin transparency of the interface.

Chapters 7 and 8 are dedicated to study the spin current induced changes on magnetization and determination of Pt spin Hall angle which is debated over a long time. Chapter 7 describes an all-electrical global measurement while chapter 8 is devoted to all-optical TR-MOKE microscopy which is a local measurement technique. In chapter 7 we also determine spin diffusion length of Pt. We also compare spin Hall angle obtained from modulation of damping and spectrum shape analysis. Finally, we conclude that modulation of damping as a more elegant method for the determination of spin Hall angle. Hence, in chapter 8 we follow the modulation of damping technique by using an all-optical technique, which is a better method for extraction of damping and hence we claim that the spin Hall angle of Pt determined by this technique is more reliable.

Chapter 9 is interesting because the problem that defines the chapter is basically a superposition of chapter 5 and 8. Here, we see a combined effect of spin injection and interface modification in NiFe/Pt bi-layer. Here spin current is created by spin Hall effect and injected into the ferromagnet through an ion irradiated interface. Spin-torque induced modulation of damping is studied as a function of irradiation dose using TR-MOKE technique.

Finally, Chapter 10 studies about nonmagnetic layer thickness dependence of damping, frequency and structural properties at the interface using TR-MOKE and XRR technique. The specialty of the problem is the capping layer thickness which varies between sub-nanometer to nanometer length scale. The most interesting point of this investigation is the magnetization and structural changes developed when clusters of nonmagnetic atoms start forming a continuous capping layer on top of a ferromagnetic thin film.

11.2. Future Prospective

Today we are living in a digital era. Starting from industry, research, medical system to agriculture every aspect of life now relies on computers, or instruments that perform logical operations and store data. People all around the world are now using personal gadgets with individual online accounts forming network with other people but hardly caring to think about how much memory and energy we consume to maintain the whole system. With the increasing popularity of this digital lifestyle there is an exploding growth of demand for memory and logical devices. However, our resource is slowly reaching its limit. So, we must look for smarter alternative technologies to circumvent the inevitable crisis.

From the recent trend of research it has been observed that people are trying to establish spin current as a driving force for future computers due to certain advantages like energy efficiency, high performance and stability. In that case all the data storage, logic and data transfer components of our electronic gadgets needs to be replaced by spintronic ones. So in the first step conversion of spin current from charge current and a proper estimation of the conversion factor is important. But that is not the sole requirement to fulfil our dream for constructing those devices. We have to go a long way for that. The devices usually use the magnetic properties of ferromagnetic metals for their operation. So the obvious question comes whether we can control the magnetic devices using spin current or not. If yes, then how can that be done in the most energy- and cost-efficient ways? The thesis is devoted to find an answer to some of these questions. Here, we describe a number of techniques involving spin current, structural changes of a ferromagnetic system or the combination of the two for tuning magnetic properties. The knowledge can be helpful for the construction and optimization of magnetic memory and logic devices.

The technique described in this thesis shows its usefulness in manipulating magnetization dynamics. More precisely it can modulate precessional frequency, damping and ultrafast relaxation processes of a magnetic system. The technique can be used for local modification of magnetic properties which opens a new hope for constructing nanoscale printed spintronic circuit where data storage, data transfer and logical operation can be performed simultaneously on a single thin film structure. Similarly, spin Hall effect induced spin injection, structural modification at the interface of a ferromagnetic bi-layer or multilayer wire, Rashba effect in inversion asymmetric structure or a combination of the above can be used for external bias field free control of domain wall motion, vortex and skyrmion dynamics which can add a new dimension to this research field. Our study is also useful for spin current induced magnetization reversal and microwave assisted magnetic recording.

In this thesis, the study of spin current injection is mostly confined in systems with negligible or in-plane anisotropic structures for simplicity of understanding. Now the study can be extended further in case of samples with out-of-plane or tilted anisotropy. This can be helpful to develop a new scheme for perpendicular or even simultaneous in-plane and out-of-plane recording for high storage density. The research can lead us closer to the construction of spin Hall effect based STT-MRAM and logic devices which can be a smarter alternative to our

present volatile random access memory and semiconductor based logic system. In addition to spin transfer torque described in this thesis, current induced spin orbit torque can be used manipulate magnetization in ferromagnetic metals lacking inversion symmetry which can give a new direction to research.

Antiferromagnets are considered as a potential candidate for high density data storage. They are magnetic microscopically with their alternate moments. However, if we consider macroscopically, they have zero net moment. Hence, the information stored in the moments remain safe from unwanted fields in the environment and the neighbouring moments do not magnetically interact even when they are very close to each other. Hence, the effect of spin current in antiferromagnet can be an interesting topic for investigation.

Apart from that the effect of spin current and interface engineering in Dzyaloshinskii-Moriya interaction, spin Hall effect with non uniform distribution of current density, spin injection in patterned magnetic media, complete compensation of magnetization damping by spin Hall effect, interface modelling in multi-layers are few of many follow-up problems related to this thesis which can be carried out in future.

In short, the thesis made a detailed investigation on controlled magnetization properties of ferromagnetic/non-magnetic bi-layers using electrical and optical technique. The study aims towards an energy efficient technology for the construction of high performance spintronic and magnonic devices and opens a lot of new scope for future research.